# Clouds and Hazes in Saturn's Troposphere and Stratosphere

Cécile T. G. MERLET




Submitted for the degree of Doctor of Philosophy

Lady Margaret Hall, Trinity Term 2013

Atmospheric, Oceanic and Planetary Physics

Department of Physics

University of Oxford

To Marie-Christine, Patrick and François.

Atmospheric, Oceanic and Planetary Physics

Department of Physics

University of Oxford

Trinity Term 2013

# CLOUDS AND HAZES IN SATURN'S TROPOSPHERE AND STRATOSPHERE

This thesis is submitted in partial fulfillment of the requirements for the degree of Doctor of Philosophy in Physics at the University of Oxford. The research and the writing embodied in the thesis are entirely my own work except where otherwise stated.

Word count = 63,185

Page count = 250

Cécile Thérèse Geneviève MERLET

Lady Margaret Hall, Oxford



# Abstract

Clouds and Hazes in Saturn's Troposphere and Stratosphere

Cécile Thérèse Geneviève MERLET, Lady Margaret Hall

Submitted for the degree of Doctor of Philosophy in Physics, Trinity Term 2013

The cloud and haze properties in the troposphere and stratosphere of Saturn are investigated in this thesis by analysing Cassini/VIMS spectra at 0.8-3.5 $\mu$m and 4.5-5.1 $\mu$m. The aerosol properties are derived from VIMS data by using the retrieval tool NEMESIS developed at the University of Oxford. Near-infared VIMS data between 4.5 and 5.1 $\mu$m are mainly sensitive to deeper tropospheric levels down to approximately 5 bar. At such pressure levels, thermochemical models predict the formation of condensed clouds made of ammonia and ammonium hydrosulphide ices, although none of these species has been spectrally detected so far. In addition, phosphine and ammonia are responsible for most of the gaseous absorption at these wavelengths. Therefore, the cloud properties and gas distributions can be retrieved from VIMS near-infared spectra. In this thesis, the analysis of limb-darkening data at 4.5-5.1 $\mu$m is performed in order to constrain the aerosol properties in Saturn's atmosphere. The best-fitting model consists of a scattering cloud between 2 and 3 bar, and a scattering haze layer which can be placed anywhere between 10 and 500 mbar. The composition is still poorly constrained for both the deep cloud and haze layer. The haze physical and optical properties can however be independently retrieved from VIMS near-infrared spectra at shorter wavelengths in the 0.8-3.5 $\mu$m spectral range. Saturn's hazes in the troposphere and stratosphere reflect the sunlight at 0.8-3.5 $\mu$m. The properties and vertical structure of tropospheric and stratospheric hazes are then investigated from VIMS reflection spectra in the near-infared. The latitudinal variation of haze properties is compared to a thermal feature known as "the temperature knee", corresponding to a local increase of temperature right below the tropopause. The north-south temperature variations in the troposphere are obtained from the analysis of thermal infrared data measured with the Composite InfraRed Spectromete (CIRS) instrument on board Cassini. Finally, VIMS near-infrared data at 0.8-3.5 and 4.5-5.1 $\mu$m are combined in order to obtain a cloud and haze model coherent with both wavelength ranges.

# Acknowledgements

I would like to first thank all the members of the Atmospheric, Oceanic and Planetary Physics (AOPP) division at the University of Oxford for providing me the intellectual means of carrying out my D.Phil project over the last four years. More specifically, I have been honoured to work under the supervision of Pr. Patrick Irwin within the gas giant team. I would like to thank him sincerely for his guidance and support at all stages of my project. I have also enjoyed the interaction with the other members of the team, including Leigh Fletcher, Jane Hurley, James Sinclair, Dane Tice, Jaemin Lee and Joanna Barstow. Their feedbacks have been very useful for my project and I have benefited a lot from the numerous dicussions we had over the weekly planetary seminars and informal meetings. I will also not forget Sarah, Simon, Xiaoming, Tahir, Corwin, Andy, Benjamin, Liam, Ian and Steffen who have contributed to make my presence in AOPP a very enjoyable moment.

Special thanks to my parents, Marie-Christine and Patrick, and my dear brother, François, for their constant moral support and sincere interest throughout my studies. They provided me with the intellectual awakening which has led me to all the different stages of my academic career and ultimately towards the doctoral journey.

These last few years in Oxford would not have been the same without my affiliation to my college, Lady Margaret Hall. I would like to thank my college advisor, David Andrews, and the other members of the academic and administrative staff, including Allan Doig, Sarah Bates, Glynis Beckett and Emma Welton for always being very helpful to me when it was necessary.

When the brain had to slightly quiet itself, Oxford offered me all kinds of thrilling escapes. I am particularly grateful to the caving and the gliding clubs. Thanks to them, my week-ends during my first two years were never spent on the ground, and I can say it was worth every bruises. My attempt at shooting wass less successful, but Oxford has taught me to always give it a go.

I have been lucky enough to meet many bright personalities from various cultures and backgrounds, who have now become more than just acquaintances. So my last thanks would go to my numerous international friends who will recognise themselves. You all are very dear to me.

# Table of Contents

**List of Figures** **ii**

**List of Tables** **iii**

**1 Introduction** **1**

1.1 Saturn in the Solar System . . . . . 1

1.2 Saturn's atmospheric science overview . . . . . 6

1.2.1 Composition and chemistry . . . . . 6

1.2.2 Thermal structure . . . . . 10

1.3 Aerosols in Saturn's troposphere and stratosphere . . . . . 12

1.4 Thesis themes . . . . . 16

**2 VIMS and CIRS infrared observations of Saturn** **19**

2.1 Cassini-Huygens space mission to Saturn . . . . . 19

2.1.1 A brief historical survey . . . . . 19

2.1.2 Mission overview . . . . . 21

2.1.3 Journey to Saturn . . . . . 22

2.1.4 Technical capabilities . . . . . 23

2.2 The Visual and Infrared Mapping Spectrometer (VIMS) . . . . . 25

2.2.1 The VIMS team . . . . . 25

2.2.2 Instrument description . . . . . 25

2.2.3 Science objectives . . . . . 28

2.3 Calibration of VIMS data . . . 30
2.4 Overview of the Composite InfraRed Spectrometer (CIRS) . . . 32

**3 Modelling Saturn's infrared spectra 35**
3.1 Radiative transfer model . . . 35
3.1.1 Radiative transfer equation . . . 35
3.1.2 The RADTRANS model . . . 39
3.2 Retrieval code: NEMESIS . . . 43
3.3 Scattering model . . . 45

**4 Limb-darkening analysis of Saturn's near-infrared thermal emission 51**
4.1 Saturn's thermal emission at 5 $\mu$m . . . 51
4.2 Fitting strategy . . . 56
4.2.1 Reference atmosphere . . . 56
4.2.2 Sensitivity analysis . . . 63
4.3 Degeneracies of Saturn's 5-$\mu$m window . . . 67
4.4 Limb-darkening analysis . . . 74
4.4.1 Methodology . . . 74
4.4.2 Limb-darkening retrievals . . . 80
4.4.3 North-south limb-darkening analysis . . . 98
4.5 Summary . . . 101

**5 Saturn's hazes from VIMS near-infrared reflection spectra 103**
5.1 Saturn's spectrum at 0.8-3.5 $\mu$m . . . 103
5.2 Modelling VIMS near-infrared reflection spectra . . . 108
5.2.1 Reference atmosphere . . . 108
5.2.2 Aerosol-free atmosphere . . . 109
5.3 Optical and physical properties of Saturn's hazes . . . 110
5.3.1 Strategy . . . 110
5.3.2 Results at a latitude of 20°S . . . 112
5.3.3 Retrieval of aerosol properties from individual reflection speaks . . . 116

5.3.4 Testing the viewing geometry . . . 119
5.3.5 Results at all latitudes . . . 125
5.4 Haze vertical structure . . . 130
5.4.1 Variations with optical and physical parameters . . . 130
5.4.2 Testing the *a priori* profile . . . 132
5.4.3 Sensitivity to pressure levels . . . 135
5.4.4 Opacity clearing . . . 139
5.5 Latitudinal variations . . . 141
5.6 Temporal variations . . . 145
5.7 The temperature knee: a correlation with the tropospheric haze ? . . . 149
5.7.1 Overview . . . 149
5.7.2 Temperature structure from CIRS infrared spectra . . . 150
5.7.3 Sensitivity of the temperature knee to the retrieval strategy . . . 152
5.7.4 Comparison of haze distribution with the thermal structure . . . 154
5.8 Haze particle candidates . . . 157
5.8.1 Comparison with laboratory measurements of the refractive index . . . 157
5.8.2 Comparison with photochemical models . . . 160
5.9 Summary . . . 165

**6 Consistency of the reflected sunlight and 5-$\mu$m analysis 167**

6.1 Methodology: $\sigma$ tests . . . 167
6.2 Parameterisation of the tropospheric haze at 5 $\mu$m . . . 170
6.3 Tropospheric model at 20°S . . . 180
6.3.1 Cloud composition . . . 180
6.3.2 Retrievals for an ammonia and ammonium hydrosulphide clouds . . . 184
6.4 Tropospheric model at all latitudes . . . 189
6.4.1 $\sigma_N$ tests . . . 189
6.4.2 Retrievals at all latitudes for an ammonia and ammonium hydrosulphide cloud 197
6.5 Summary . . . 202

**7 Conclusions and future work** **205**

7.1 Thesis results . . . . . 205

7.1.1 5-$\mu$m limb-darkening analysis . . . . . 206

7.1.2 Saturn's haze properties . . . . . 208

7.1.3 Saturn's haze and cloud model consistent with the reflection and 5-$\mu$m VIMS data . . . . . 210

7.2 Next steps . . . . . 212

**Bibliography** **213**

# List of Figures


1.1 The gas giants in the Solar System . . . . . 1

1.2 Hydrocarbon abundances in Saturn's stratosphere . . . . . 9

1.3 Saturn's thermal structure in the upper troposphere and middle stratosphere from Cassini/CIRS data . . . . . 11

1.4 Thermochemical equilibrium model of cloud formation in Saturn's troposphere . . . 13

1.5 Photochemical model of the haze formation models in Saturn's troposphere and stratosphere . . . . . 15

2.1 Historical survey . . . . . 20

2.2 The Cassini cruise trajectory to Saturn. . . . . 23

2.3 Both Sides View of the Cassini Spacecraft. . . . . 24

2.4 The VIMS instrument . . . . . 26

2.5 Calibration of VIMS data. . . . . 31

2.6 The CIRS instrument . . . . . 32

3.1 Propagation of Radiation . . . . . 36

3.2 Henyey-Greenstein Phase Functions . . . . . 47

4.1 VIMS image and several spectra of Saturn in the 5-$\mu$m window . . . . . 53

4.2 Altitude Sensitivity of Saturn's Thermal Emission Spectra . . . . . 55

4.3 Reference gaseous composition in Saturn's troposphere and stratosphere . . . . . 59

4.4 Absorption spectra between 4.6 and 5.1 $\mu$m of radiatively active gases in the troposphere 60

4.5 Sensitivity analysis of Saturn's 5-$\mu$m window to retrieved atmospheric parameters in NEMESIS . . . . . 64
4.6 Retrieval of cloud base pressure and aerosol particle size for a compact ammonia cloud 68
4.7 Retrieval of cloud base pressure and aerosol particle size for a purely absorptive ammonia cloud at various latitudes between 30°S and 60°N . . . . . 71
4.8 Retrieval of aerosol properties for a compact ammonium hydrosulphide cloud and a grey aerosol layer made of purely absorptive and scattering aerosol particles. . . . . 73
4.9 Limb-darkening observation scheme . . . . . 75
4.10 Limb-darkening observation of Saturn. . . . . 79
4.11 Limb-darkening analysis for one compact ammonia and ammonium hydrosulphide cloud models . . . . . 82
4.12 Limb-darkening analysis for one compact grey cloud model . . . . . 83
4.13 Limb-darkening analysis for an extended ammonia cloud made of purely absorptive aerosol particles. . . . . 87
4.14 Limb-darkening analysis for an extended ammonia cloud made of scattering aerosol particles. . . . . 88
4.15 Ammonia volume mixing ratio and aerosol vertical profile for an extended ammonia cloud made of scattering aerosol particles retrieved from limb-darkening observations. 89
4.16 Limb-darkening analysis for a two compact aerosol layer model in the non-scattering and scattering cases . . . . . 94
4.17 Limb-darkening analysis for a continuous aerosol opacity model in the scattering case 96
4.18 Extinction coefficients and single scattering albedos of ammonia, ammonium hydrosulphide and grey particles in the 4.6-5.1 $\mu$m wavelength range . . . . . 97
4.19 Limb-darkening analysis at various latitudes for one and two compact aersosol layers 100

5.1 VIMS near-infrared reflection images and spectrum of Saturn. . . . . 104
5.2 Comparison of VIMS and SpeX near-infrared reflection spectra of Saturn . . . . . 106
5.3 Two-way transmission weighting functions for an aerosol-free atmosphere . . . . . 107
5.4 Vertical distribution of gases in Saturn's reference atmosphere for the analysis of VIMS reflection spectra . . . . . 108

5.5 Effects of Rayleigh scattering by tropospheric and stratospheric gases on Saturn's near-infared reflection spectrum . . . 109
5.6 Optical and physical parameters of Saturn's hazes from the analysis of VIMS near-infrared reflection spectrum . . . 114
5.7 Retrieval of the complex refractive index and aerosol particle size from the individual reflection peaks . . . 118
5.8 VIMS cubes used for the sensitivity analysis of the haze optical and physical parameters to the viewing geometry . . . 120
5.9 Retrieval of the haze optical and physical properties at a latitude of 20°S for different values of the solar and emission angles . . . 124
5.10 Goodness-of-fit as a function of the aerosol particle size, real refractive index and imaginary refractive index. . . . 129
5.11 Haze vertical structure derived from VIMS near-infrared reflection data . . . 131
5.12 Sensitivity of the retrieved haze vertical profile to the *a priori* value . . . 133
5.13 Sensitivity of the retrieved haze vertical profile to the *a priori* error . . . 134
5.14 Sensitivity of Saturn's near-infrared reflection spectrum to the haze pressure levels . 137
5.15 Validity of the opacity clearing . . . 140
5.16 VIMS image at 0.93 $\mu$m and viewing geometry for the study of latitudinal variations of the haze structure in Saturn's troposphere and stratosphere . . . 142
5.17 North-south variations of haze vertical distribution in 2007 . . . 144
5.18 VIMS images at 1.07 $\mu$m used for the retrieval of haze properties in 2004-2012. . . . 146
5.19 Latitudinal variation of haze concentration in 2004-2012 . . . 148
5.20 Temperature, lapse rate and curvature profiles in Saturn's troposphere and stratosphere at 30°S . . . 151
5.21 Sensititivity of the temperature knee to the retrieval strategy . . . 153
5.22 The 2005 curvature maps retrieved from FP1 and FP1+FP3 spectra . . . 155
5.23 The curvature map compared to the haze contour profile . . . 157
5.24 Known complex refractive indexes from laboratory measurements of tropospheric species . . . 159
5.25 Comparison of the haze vertical structure with Saturn's photochemical model . . . 163

5.26 North-South distributions of phosphine and ammonia. . . . . 164

6.1 Update of the retrieval strategy at 4.6-5.1 $\mu$m using the results from the analysis at 0.8-3.5 $\mu$m. . . . . 167

6.2 Aerosol reference model used for the limb-darkening analysis at 5-$\mu$m . . . . . 170

6.3 Limb-darkening analysis at 5 $\mu$m for a compact ammonia cloud and a haze vertical structure derived from VIMS data at 0.8-3.5. . . . . 171

6.4 Effect of haze properties at 4.6-5.1 $\mu$m on the retrieved parameters . . . . . 174

6.5 Standard deviation between the two haze vertical distributions at 0.8-3.5 $\mu$m ($C^1$(p)) and 4.6-5.1 $\mu$m ($C^2$(p)) for different optical and physical properties of Saturn's hazes at 5 $\mu$m . . . . . 178

6.6 $\sigma_N$ maps as a function of the haze parameters at 0.8-3.5 $\mu$m and 4.6-5.1 $\mu$m . . . . . 179

6.7 $\sigma_N$ tests for various compositions of the deep tropospheric cloud . . . . . 182

6.8 Limb-darkening analysis of Saturn's 5-$\mu$m window for a deep cloud made of ammonia and ammonium hydrosulphide particles . . . . . 185

6.9 VIMS near-infrared cubes and haze distribution in February 2006 used in the update of the 5-$\mu$m analysis at all latitudes. . . . . 190

6.10 $\sigma_N$ tests at multiple latitudes . . . . . 194

6.11 Minimum $\sigma_N$ values for various cloud compositions and latitudes. . . . . 196

6.12 Limb-darkening analysis of Saturn's 5-$\mu$m window at latitudes in the range 60°S-60°N for a scattering ammonia and ammonium hydrosulphide clouds. . . . . 198

# List of Tables


1.1 Saturn's observational parameters. . . . . 5

2.1 Summary of VIMS specifications . . . . . 27

2.2 CIRS specifications summary . . . . . 33

3.1 Reference atmosphere in RADTRANS . . . . . 42

4.1 Effects of the parametrisation of phosphine vertical profile on Saturn's 5-$\mu$ window . 66

4.2 VIMS spectral cubes selected for the limb-darkening analysis of Saturn's thermal emission spectra . . . . . 76

4.3 Comparison of the ammonia VMR retrieved for a scattering grey cloud with tropospheric ammonia abundances from previous studies . . . . . 85

4.4 Viewing geometries of VIMS limb-darkening data at various latitudes between 50°S and 50°N . . . . . 99

5.1 Best-fitting scattering albedo and phase function parameters . . . . . 116

5.2 List of VIMS observations used for testing the sensitivity of retrievals to the viewing geometry . . . . . 121

5.3 Viewing geometries of VIMS data at various latitudes between 60°S and 60°N used for the analysis of Saturn's near-infrared reflection spectra . . . . . 125

5.4 Best-fitting values of aerosol properties at all latitudes from VIMS near-infrared reflection spectra . . . . . 126

5.5 List of VIMS observations used for the study of the haze temporal variations . . . . . 145

6.1 Retrieved parameters at 4.6-5.1 $\mu$m for low and high $\sigma_N$ values. . . . . 187
6.2 Viewing geometries of VIMS data at various latitudes between 60°S and 60°N used for the update of the 5-$\mu$m analysis. . . . . 192
6.3 Retrieved parameters at 4.6-5.1 $\mu$m for an ammonia cloud and an ammonium hydrosulphide cloud . . . . . 201

Chapter 1

# Introduction

*This introductory chapter is fully based on a literature review.*

## 1.1 Saturn in the Solar System

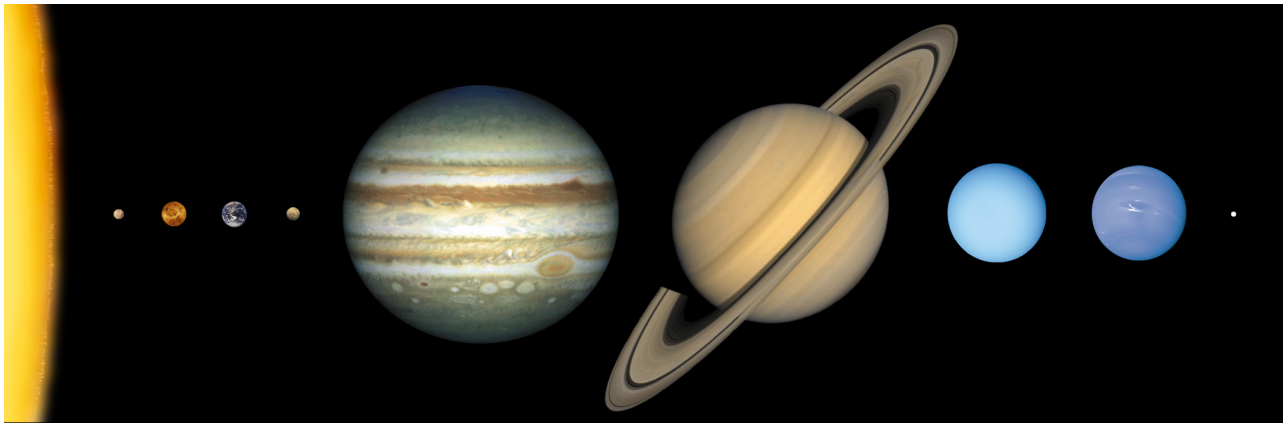


Figure 1.1: The gas giants in the Solar System. The telluric and gas giant planets, shown here in true colors, have their relative sizes to scale but not their relative distances to the Sun. Credit: NASA/JPL.

The Solar Sytem was formed only a few gigayears after the Big Bang which current measurements of the cosmological constant estimate at 13.7 Ga[1] ago (Spergel *et al.*, 2007). Many galaxies, including the Milky Way, may have formed as quickly as a few hundred million years after the Big Bang. Pasquini *et al.* (2007) estimated the lower limit of the Milky Way's age at approximately 13.4 Ga. The Sun and its circumstellar disc originated from an interstellar medium cloud through either gravitational collapse or collapse triggered by a shockwave from a supernova (Boss, 2007). Primitive meteorites containing early condensable materials from the circumstellar disc were collected

[1] 1 Ga = 1 gigayear or gigaanum = $10^9$ years

on Earth and radiometric dating led to an age estimation of the planet formation at 4.567 $\pm$ 0.6 Ga (Amelin *et al.*, 2002). The formation times of telluric planets can be estimated from isotopic dating of terrestrial and lunar samples, and also of meteorites. Such materials are however not available for gas giants, and so observations of other star systems combined with theoretical models of giant planet formation are used instead to constrain the formation times of giant planets. Recent studies suggest that gas giants form very quickly from a planetary disc in less than $10^7$ years, before the gas is removed from the disc (Espaillat *et al.*, 2007; Meyer *et al.*, 2007).

Two models are in competition for the formation of gas giants; they are usually referred to as the Gas Instability (GI) model and the Core Nucleated Accretion (CNA) model. The CNA model is currently more accepted by researchers although both models are being continuously developed. In the GI model, non-linear instabilities within the circumstellar disc lead to the formation of self-graviting clumps, precursors of gas giants (Cameron, 1978; Durisen *et al.*, 2007). Theoretical predictions of the GI model are generally in good agreement with an early formation of gas giants in the planetary disc's lifetime, however they are in contradiction with the enrichment in heavy elements over solar abundances observed on all the giant planets. Also the GI model does not account for the formation of telluric planets in the Solar System and other planetary systems. The CNA model was extended to gas giants from Safronov theories describing the formation of telluric planets in planetary accretion discs (Safronov, 1967, 1991; Safronov and Ruskol, 1994). In this model, gas giant formation starts with the growth of a core of rock and ice in the vicinity of the gas giants. When the core reaches a critical mass, it can accrete gas from the local nebula until disappearance of gas in the giant planet's forming region. The CNA model leads to non solar abundances of heavy elements on Jupiter and Saturn as expected from observational constraints (Estrada *et al.*, 2009). This model can also explain the formation of the four telluric planets, Mercury, Venus, Earth and Mars. This model predicts formation times of $10^8$ to $10^9$ years or longer (Wetherill, 1980, 1993) in contradiction with the $10^7$ years estimation. However, recent CNA models, developed by Hubickyj *et al.* (2005) and Lissauer *et al.* (2009) where the formation times of gas giants are strongly dependent on the mass of solid core and the opacity of the accreted gas, are capable of forming gas giants in $\sim$ 1-12$\times 10^6$ years.

Recent models of planet formation suggest that gravitational interactions with the circumstellar disc resulted in the migration of the young gas giants from where they were originally formed (Goldreich and Tremaine, 1980; Ward, 1986, 1997; Goldreich *et al.*, 2004). Indeed, such interactions

can affect the orbital energy and angular momentum of gas giants, so that they may move radially through the circumstellar disc, a process known as planet migration. Observations of gas giants in other planetary systems show that they migrated inwards from their forming regions at a closer distance to their stars. Indeed most gas giants discovered in other planetary systems are found within 1 AU[2] of their star, although gas giants are not expected to form so close to a star (Bodenheimer *et al.*, 2000; Ida *et al.*, 2004). The gas giants in the Solar System are located further away from the Sun, suggesting that planetary migration induced by the circumstellar disc may have played a negligible role. Indeed, Jupiter, Saturn, Uranus and Neptune are at a mean distance from the Sun of respectively 5.2, 9.5, 19.2 and 30.1 AU (Cox, 2000). However, the gas giants themselves can cause other planets to move away from their forming region. Once formed, a gas giant can create instabilities in the circumstellar disc through orbital resonances, and as a result affects the orbit of other gas giants. This phenomenon, often referred to as planet-induced migration, further complicates gas giant formation scenarii. To date, the most recent model taking into account planet-migration effects was developed at the Nice Observatory in France and is known as the Nice model (Gomes *et al.*, 2005; Morbidelli *et al.*, 2005; Tsiganis *et al.*, 2005; Levison *et al.*, 2007, 2008). This model suggests that gas giants in the Solar System formed originally at a close distance from each other with the order between Uranus and Neptune being reversed. The gas giants then separated to their current location after Jupiter and Saturn reached a 1:2 mean motion resonance leading to a perturbation of the gas giant orbits.

The process described above led to the formation of eight planets in the Solar System: the four telluric planets, Mercury, Venus, Earth and Mars, and the four giant planets, Jupiter, Saturn (gas giants), Uranus and Neptune (ice giants). Note that Pluto was recategorised as a dwarf planet in 2006 by the International Astronomical Union. The formation process and subsequent evolution of each planet resulted in planetary bodies of various physical parameters and chemical properties. As seen in Fig. 1.1, planets in the Solar System differ greatly in size, shape, oblateness and obliquity. The giant planets are significantly larger than the four telluric planets, with Jupiter being the largest planet. The telluric planets are the closest to the Sun in the Solar System and are orbiting at a distance between 0.4 and 1.5 AU from the Sun, whereas giant planets are located between 5.2 and 30.1 AU from the Sun. The gap between telluric and giant planets is filled by a region containing numerous asteroids known as the asteroid belt.

[2]One Astronomical Unit (AU) is the mean Sun-Earth distance of about 149,597,870.7 km (Cox, 2000)

Many natural satellites are also present in the Solar System, with almost all of them orbiting gas giants. The Moon orbiting the Earth is the only natural satellite amongst the telluric planets. Jupiter, Saturn, Uranus and Neptune have respectively 66, 62, 27 and 13 natural satellites orbiting around them. With a radius of 2,575 kilometres (Cox, 2000), Titan is Saturn's largest satellite and it is also the only natural satellite in the Solar System with a dense atmosphere. Telluric planets are made mainly of a metallic core surrounded by a silicate mantle while giant planets are mostly composed of gaseous and liquid substances. There are also notable differences between the giant planets, especially between Jupiter and Saturn on the one hand, and Uranus and Neptune on the other. Jupiter and Saturn, also referred to as gas giants, are made essentially of hydrogen and helium although planetary models suggest that both planets possess a rocky core surrounded by an intermediate layer of liquid hydrogen and liquid helium (Lissauer, 1993; Guillot, 1999; Boss, 2002; Hubbard *et al.*, 2002). Uranus and Neptune have more astrophysical ices such as water, methane, hydrogen sulphide and ammonia even though their outer atmospheres are also made primarily of hydrogen and helium. Thus, Uranus and Neptune are referred to as ice giants. Their bluish color results from the presence of methane in their upper atmosphere. Giant planets contain more than 99% of the mass of all planets and make up the majority of angular momentum in the entire Solar System. As a result, giant planets are likely to have played a significant role in the formation and subsequent evolution of the entire Solar System. The knowledge of these systems is essential in order to constrain planetary formation theories. Because of their composition, it is not surprising that many studies of giant planets have focused on their atmospheres. This thesis addresses some key aspects in Saturn's atmosphere, and so properties of the ringed planet are reviewed below (the planet's main properties are listed in Table 1.1 and compared with Earth).

During planetary formation in the Solar System, gas giants accreted most of the mass from the circumstellar disc, thus they are significantly more massive than telluric planets. With a mass of $5.685 \times 10^{26}$ kg, Saturn is 95.3 times heavier than Earth despite the significantly lower density of the ringed planet ($\rho = 0.70$ g·cm$^{-3}$) . As a result, Saturn's volume is 763.6 times larger than Earth leading to an important difference in size between the two planets (see Fig. 1.1). Note that although gas giants are the most massive planets in the solar system, they only account for around 0.1 % of the solar mass. Saturn orbits at 9.54 times the Earth-sun distance, and so the large volume of the planet makes it visible to the naked eye. Saturn is significantly more oblate than the Earth due to

| *Parameters* | *Saturn* ♄ | *ratio* $\frac{[Saturn]}{[Earth]}$ |
|---|---|---|
| Semimajor axis of orbit (2000.0)[a] | $1.427\times10^9$ km | 9.54 |
| Mass | $5.685\times10^{26}$ kg | 95.16 |
| Volume | $82{,}713\times10^{10}$ km$^3$ | 763.6 |
| Mean density | 0.70 g·cm$^{-3}$ | 0.13 |
| Sidereal orbital period | 29.42 yr | 29.42 |
| Mean daily motion | 0.033° | 0.0034 |
| Mean orbit velocity | 9.67 km·s$^{-1}$ | 0.32 |
| Orbital eccentricity (2000.0) | 0.054 | 3.24 |
| Inclination to ecliptic (2000.0) | 2.48° | N.A. |
| Equatorial radius $R_e$ | 60,268 km | 9.45 |
| Polar radius $R_p$ | 54,362 km | 8.5 |
| Oblateness $(R_e - R_p)/R_e$ | 0.098 | 288.2 |
| Inclination of equator to orbit | 26.73° | 1.14 |
| Sidereal day (System III)[b] | III $10^h39^m24^s$ | 0.44 |
| Surface gravity at 1 bar[c] | 10.44 | 1.06 |
| Surface acceleration at 1 bar[d] | 8.96 | 0.92 |
| Escape velocity | 35.5 km·s$^{-1}$ | 3.2 |
| Planetary albedo | 0.34 | 1.12 |
| Solar irradiance | 14.90 W·m$^{-2}$ | 0.011 |
| Emitted/absorbed flux ratio | 1.78 | 1.0 |
| Number of natural satellites | 62 | 62 |

Table 1.1: Saturn's observational parameters compared with Earth. Sources: Cox (2000) and Irwin (2003).

[a] Data are given with respect to the mean ecliptic and equinox of J2000.0 at the epoch J2000 (JD 2451545.0).

[b] In the System III reference frame, the period of Saturn's kilometric radiation is used to infer its bulk rotation period. The value given here is inferred from Voyager measurements. More recently, a period up to 7 minutes longer than Voyager's value has been obtained from Cassini data (Read *et al.*, 2009).

[c] Equatorial gravitational acceleration at the 1 bar level, not including the effects of rotation.

[d] Effective equatorial gravitational acceleration at the 1 bar level, including the effects of rotation.

a fast rotation. Indeed, a Saturnian sidereal day in the System III coordinate system is estimated at $10^h39^m24^s$ from Voyager measurements at kilometric wavelengths. Jupiter and Saturn have the shortest sidereal rotation period among all other planets in the Solar System. Because of its lower density, Saturn is however more oblate than Jupiter. Saturn has a notable system of rings made almost entirely of water ice. The three other gas giants are also surrounded by ring systems, although not as extensive as the rings of Saturn. All gas giants except Uranus have an effective temperature superior to their radiating temperature defined as the temperature of a black body in thermal equilibrium with similar size of the gas giant and at equal distance from the Sun. Therefore, gas giants still have a residual internal heat source. The ratio of emitted over absorbed radiation for Saturn is equal to 1.78. Saturn's internal heat source is likely to be due to internal differentiation of helium (Conrath *et al.*, 1989; Li *et al.*, 2012 ). Temperatures in Saturn's atmosphere are not high enough to dissolve helium molecules and so instead they form droplets falling through the planet's interior. During this process, helium molecules accumulate gravitational potential energy which is then converted into thermal energy released outwards. Therefore, the atmospheres of Jupiter, Saturn, and Neptune are meteorologically active due to convection driven by their internal heat source. Because of the low conductivity and viscosity of hydrogen, Saturn's internal heat is transported outwards by convection. Saturn's surface gravitational acceleration at 1 bar is comparable to the value measured on Earth. Studies of Saturn's gravity field have suggested the presence of a dense core made of ices and rocks at the center of the planet (Guillot, 1999, 2005). Finally, most models of the interior of Saturn include a metallic hydrogen envelope between the dense core and the gaseous atmosphere.

## 1.2 Saturn's atmospheric science overview

### 1.2.1 Composition and chemistry

As mentioned in the previous section, Saturn's gaseous atmosphere is primarily composed of hydrogen and helium, and so these two molecules contribute most to the total molecular mass in Saturn's atmosphere. Conrath *et al.* (1984, 2000) obtained a helium-to-hydrogen mixing ratio in the range 0.11-0.16 from Voyager/IRIS data in the far-infrared. Because Saturn's far-infrared spectra are also sensitive to the thermal structure and ortho/para distribution of molecular hydrogen, the helium abun-

dance cannot be determined more precisely from IRIS measurements. The molecular hydrogen exists in two different quantum states, the ortho state and the para state. Ortho-hydrogen molecules have odd rotational quantum numbers, and para-hydrogen molecules have even rotational quantum numbers. In the deep atmosphere, where $T > 300$ K, the fraction of para-hydrogen ($f_p$) should approach its equilibrium value ($f_{pe}$) equal to 0.25. The equilibrium para-hydrogen fraction increases as the temperature falls. Therefore, an air parcel rising quickly in the troposphere retains a smaller value of its para-hydrogen fraction ($f_p$) than the equilibrium value ($f_{pe}$) at higher altitudes. Assuming that chemical equilibration is slow enough in comparison with dynamical transport, the ortho/para-hydrogen ratio can be used to trace the circulation in Saturn's troposphere (Conrath *et al.*, 1998).

The atmosphere of Saturn is enriched in heavy elements, that is to say in elements heavier than helium, relative to the Sun. The knowledge of heavy element abundances in Saturn's atmosphere is essential to constrain models of the formation and evolution of the planet. The enrichment in carbon can be inferred from the measurements of methane volume mixing ratio. Methane ($CH_4$) is thermodynamically stable, well-mixed and does not condense in Saturn's atmosphere, thus it can be used as a tracer for carbon abundance. The most accurate measurement of methane volume mixing ratio is obtained by Fletcher *et al.* (2009). They derived a value of $(4.7 \pm 0.2)\times10^{-3}$ from four $CH_4$ rotational lines at 96-136 $\mu$m observed for the first time with the CIRS instrument on board the Cassini spacecraft. These lines are well isolated from other absorption lines which allows a precise determination of methane abundance. The methane volume mixing ratio obtained by Fletcher *et al.* (2009) implies a carbon enrichment of 10.4 over the solar abundance assuming that carbon is almost entirely tied up in methane. The solar composition from Grevesse *et al.* (2007) is used in this introduction to convert volume mixing ratios into enrichment in heavy elements relative to the Sun.

Most nitrogen and sulphur molecules are tied up respectively in ammonia ($NH_3$) and hydrogen sulphide ($H_2S$). Estimation of ammonia and hydrogen sulphide volume mixing ratios are complicated by the possible condensation of ammonia, ammonium hydrosulphide ($NH_4SH$) and water ($H_2O$) in the troposphere down to the 20-bar level (see Fig. 1.4). Indeed, retrieving ammonia and hydrogen sulphide abundances in gas phase implies probing below the cloud layers. Only spectral observations in the centimetre range between 6 and 70 cm can probe so deep in the troposphere. However, radiances at such wavelengths have large uncertainities of around 20%. Also, laboratory measurement of absorption coefficients are limited at these wavelengths. Briggs and Sackett (1989) found a deep ($\sim$

25 bar) ammonia volume mixing ratio of $(4.8 \pm 1)\times10^{-4}$ from their Very Large Array and Arecibo centimetre observations, corresponding to a nitrogen enrichment of 4.5 times the solar abundance. Their analysis of the 2-6 cm range of Saturn's spectrum concluded on a hydrogen sulphide ($H_2S$) volume mixing ratio of $4.1\times10^{-4}$ leading to a sulphur enrichment of 17 times the solar abundance. Hydrogen sulphide is expected to combine with ammonia to form an ammonium hydrosulphide cloud between 4 and 6 bar, leading to a lower ammonia volume mixing ratio of 0.7 to $1.1\times10^{-4}$ above the cloud. The ammonia abundance at pressure levels of a few bars obtained by Briggs and Sackett (1989) are consistent with more recent results from de Graauw *et al.* (1997), Orton *et al.* (2000) and Burgdorf *et al.* (2004). Fletcher *et al.* (2011) retrieved larger ammonia volume mixing ratios up to $\sim 4.5\times10^{-4}$ at the equator between $\pm 5^{\circ}$ latitude from Cassini/VIMS measurements, although values in the range 1.2-2.2$\times10^{-4}$ were obtained at higher latitudes. In addition to condensation, the photolysis of ammonia in the upper troposphere (Hurley *et al.*, 2012) also depletes the ammonia volume mixing ratio at higher altitudes (Kerola *et al.*, 1997; Kim *et al.*, 2006). The Infrared Space Observatory (ISO) detected tropospheric water at 5 $\mu$m. At such short wavelenths, ISO probes at pressure levels between 2 and 4 bar where water vapour is expected to condense out. Stratospheric water was also detected with Herschel observations in the sub-millimetre (Fletcher *et al.*, 2012). The deuterium-to-hydrogen (D/H) ratio is particularly relevant to constrain the fraction of solids to gases accreted at the time of Saturn's formation. The D/H ratio can be directly derived from the $HD/H_2$ ratio. Griffin *et al.*, (1996) obtained a ratio of $2.3\times10^{-5}$ from the measurements of the HD R(1) rotational line at 56 $\mu$m with the ISO Long Wavelength Spectrometer. The D/H ratio can also be obtained by comparing the ratio of deuterated methane $CH_3D$ to methane. The most convincing results fall in the range 1.1-2.0$\times10^{-5}$ (Noll and Larson, 1991; Lellouch *et al.*, 2001; Fletcher *et al.*, 2009b). The disequilibrium species phosphine ($PH_3$), germane ($GeH_4$) and arsine ($AsH_3$) have been detected at 5 $\mu$m. These species are transported by convection from around 300-500 bar to upper tropospheric levels, thus their abundances highly exceed the values predicted by thermochemical equilibrium. Noll and Larson (1990) estimated the $GeH_4$ and $AsH_3$ volume mixing ratios in the upper troposphere at respectively $3.5\times10^{-10}$ and $2.6\times10^{-9}$. Fletcher *et al.* (2009) obtained a phosphine volume mixing ratio of $6.4\times10^{-6}$ from CIRS measurements. Photolysis of phosphine depletes its volume mixing ratio in the upper troposphere (Weisstein and Serabyn, 1994; Orton *et al.*, 2000) with an estimated

fractional scale height[3] of 0.27 (Fletcher *et al.*, 2009a). However, no photochemical products have been spectrally detected to date. Photolysis of germane (Graauw *et al.*, 1997) and arsine (Bézart *et al.*, 1989) might also deplete these molecules in the upper troposphere. Carbon monoxide (CO) might also originate from Saturn's interior such as phosphine, germane and arsine. However, another scenario involving an external oxygen influx might also explain the presence of carbon monoxide in the planet's atmosphere (Winkelstein *et al.*, 1993). Noll and Larson (1991) obtained a tropospheric volume mixing ratio of $(1.0 \pm 0.3)\times10^{-9}$ by analysing high-resolution spectra in the 4.5-5.0 $\mu$m wavelength range at the IRTF.

Photochemical reactions in Saturn's stratosphere lead to the formation of various hydrocarbons. Methane is photodissociated by ultraviolet photons to produce CH, $CH_2$ and $CH_3$ radicals. These radicals react with other atmospheric molecules to form heavy hydrocarbons. To date, the following hydrocarbons have been observed: acetylene ($C_2H_2$), ethylene ($C_2H_4$), ethane ($C_2H_6$), propane ($C_3H_8$), methylacetylene ($CH_3C_2H$), diacetylene ($C_4H_2$) and benzene ($C_6H_6$). The radical $CH_3$ has also been detected. Vertical profiles of stratospheric hydrocarbons, derived from both photochemical models and various observations in the infrared and ultraviolet, are shown in Fig. 1.2.

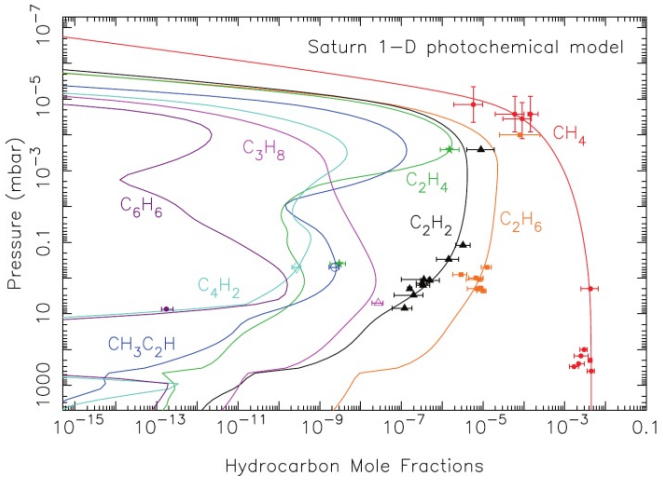



Figure 1.2: Hydrocarbon abundances in Saturn's upper troposphere and stratosphere. The lines represent abundance profiles from the 1-D steady-state photochemical model of Moses and Greathouse (2005). The symbols represent various empirical data in the infrared and ultraviolet. $CH_4$: Festou and Atreya (1982), Smith *et al.* (1983), Courtin *et al.* (1984), Tomasko and Doose (1984), Trafton (1985), Killen (1988), Karkoschka and Tomasko (1992) and Kerola *et al.* (1997) ; $C_2H_6$: Courtin *et al.* (1984), Noll *et al.* (1986), Sada *et al.* (1996), Moses *et al.* (2000) and Sada *et al.* (2005) ; $C_2H_2$: Courtin *et al.* (1984), Noll *et al.* (1986a), Chen *et al.* (1991), Moses *et al.* (2000) and Sada *et al.* (2005) ; $C_2H_4$: Bézard *et al.* (2002) ; $C_3H_8$: Greathouse *et al.* (2003) ; $C_4H_2$: Moses *et al.* (2000) ; $C_6H_6$: Bézard *et al.* (2001) ; $CH_3C_2H$: Moses *et al.* (2000).

[3]Ratio of phosphine scale height to the scale height of the bulk atmosphere

### 1.2.2 Thermal structure

The current knowledge of Saturn's thermal structure in the troposphere and stratosphere comes from radio occultation and thermal infrared sounding. Radio occultation measurements provide higher vertical resolution while thermal infrared mapping data have better latitudinal and longitudinal coverage. Orton and Ingersoll (1980) were among the first to map Saturn's thermal structure from the infrared radiometer (IRR) on board Pioneer 11. More recently, Fletcher *et al.* (2007) used Cassini/CIRS thermal spectra from 10-1400 $cm^{-1}$ to retrieve north-to-south temperatures in the upper troposphere and middle stratosphere during southern summer (see Fig. 1.3). The tropopause at around 80 mbar separates out the troposphere at lower altitudes from the stratosphere at higher altitudes. The stratosphere is stably stratified and temperature increases with altitude while temperature increases with depth in the troposphere. The upper troposphere down to 400-500 mbar is also stably stratified, but becomes convective at higher pressure levels. The limit between the stably stratified and convective atmosphere is known as the radiative-convective (RC) boundary. In the upper troposphere above the RC boundary, heat transfers through radiation and the temperature gradient increases with depth. Below the RC boundary, heat transfers through convection and the lapse rate becomes nearly dry adiabatic (Lindal *et al.*, 1985; Fletcher *et al.*, 2007). The thermal structure in Saturn's stratosphere is driven by solar heating and the solar-driven circulation, and as a result north-to-south variations in stratospheric temperatures are observed (Tukunaga *et al.*, 1978). In particular, the temperature map in Fig. 1.3 shows that the summer southern pole of Saturn at 1 mbar was around 40 K warmer than the northern pole during the Cassini prime mission in 2004-2008. The north-to-south variation in temperature weakens as the pressure increases until it disappears below the RC boundary. A local increase of temperature below the tropopause was retrieved initially from Voyager/IRIS spectra at near-equatorial and southern latitudes (Hanel *et al.*, 1981). This feature, referred to as a temperature "knee", was also derived from CIRS data (Fletcher *et al.*, 2007). The knee was observed only in the summer hemisphere of Saturn and might undergo seasonal variations. A few scenarios might explain the presence of the temperature knee in Saturn's upper troposphere, including local heating by the tropospheric haze. The latter hypothesis will be adressed in this thesis since VIMS and CIRS spectral ranges can be used to model both the haze distribution and the thermal structure in Saturn's upper troposphere.

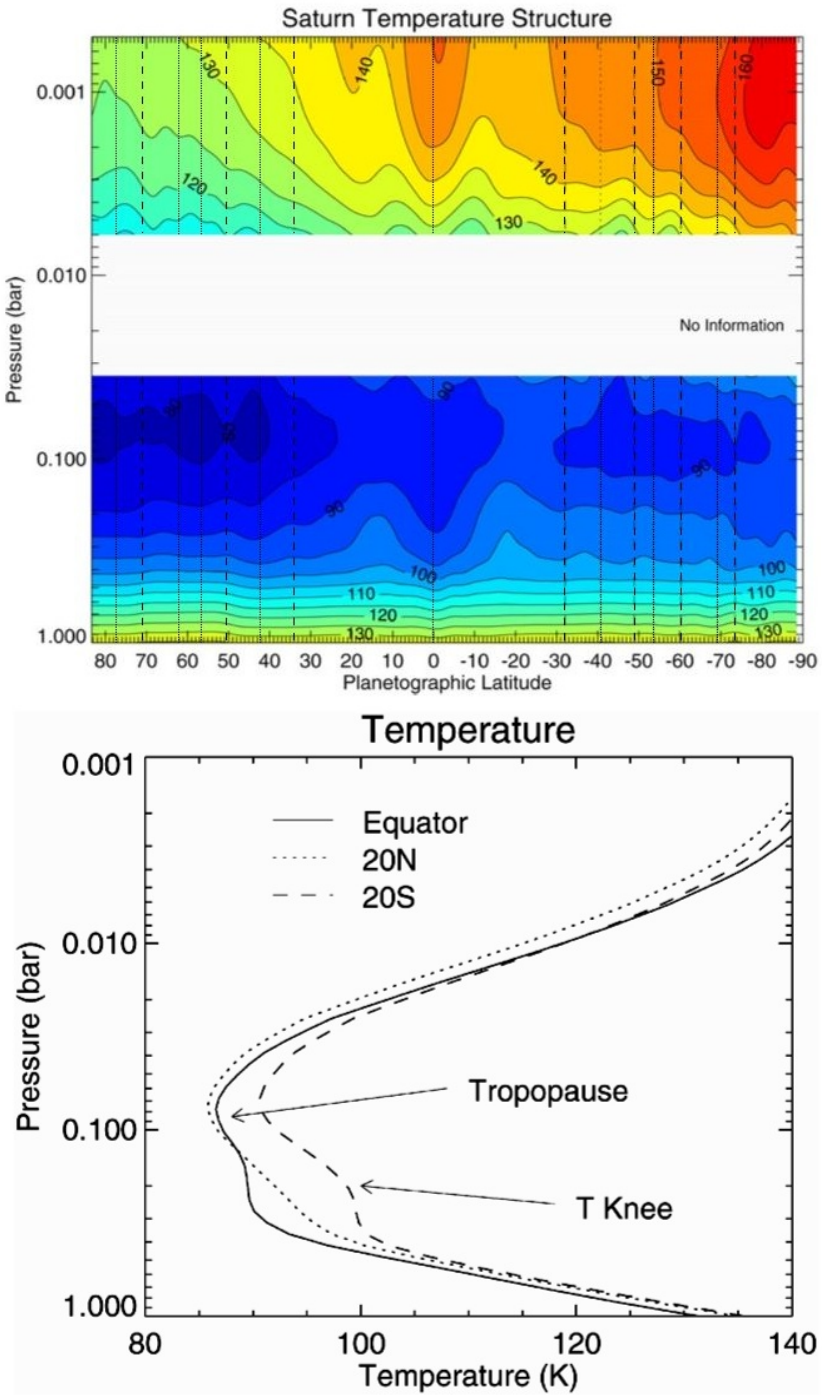



Figure 1.3: Temperature map (*top*) and vertical profiles (*bottom*) in Saturn's upper troposphere and middle stratosphere from Cassini/CIRS data (Fletcher *et al.*, 2007). Temperatures are retrieved from nadir observations during the prime mission of Cassini (2004-2008). This epoch coincides with summer conditions in the southern hemisphere. There is no information on temperatures between 5 and 50 mbar since CIRS thermal spectra are not sensitive to these pressure levels. The dotted and dashed lines on the temperature map correspond respectively to the prograde (eastwards) and retrograde (westwards) jets (Sánchez-Lavega *et al.*, 2000; Porco *et al.*, 2005). Vertical profiles are shown for three latitudinal bands at 20°S, the equator and 20°N. A local increase of temperature below the tropopause, referred to as a temperature knee, was retrieved in the southern hemisphere and at the equator. Such a feature was not observed in the winter northern hemisphere.

## 1.3 Aerosols in Saturn's troposphere and stratosphere

The terms aerosol, cloud and haze will be often used throughout this thesis. The term aerosol will refer to any set of fine solid particles or liquid droplets in suspension within an atmospheric gas. As a result, this term comprises many different types of atmospheric *objects*, such as clouds, hazes, mist and dust. The liquid or solid aerosol particles have sizes typically in the range 100nm-10$\mu$m. In this work, only two types of aerosol will be considered: clouds and hazes. The underlying physics for the formation of clouds and hazes is based mainly on thermochemical equilibrium models and photochemical models respectively. Both processes are described below for Saturn's atmosphere.

Thermochemical equilibrium models predict the formation of clouds in Saturn's troposphere where oxygen, nitrogen and sulphur are expected to combine with hydrogen in gas phase. The equilibrium cloud condensation models (ECCM) were first developed for Jupiter by Lewis (1969), and extended later to the other gas giants by Weidenschilling and Lewis (1973), Atreya and Romani (1985), Atreya (1986) and Atreya *at al.* (2005). In the ECCM, clouds form above a pressure level where the partial pressure and the saturation vapor pressure of the condensible volatile are equal. This defines the cloud base level. The extension of the cloud is defined as the height, in kilometres or pressures, between the cloud base and the cloud top.In convective clouds, the cloud top is defined as the level of neutral buoyancy.

The formation of cloud droplets is based on two micophysical processes: homogeneous nucleation and heterogeneous nucleation. In homogeneous nucleation, small droplets initially form in the supersaturated atmosphere in order to trigger the cloud formation process. The curvature of these droplets cause the vapour pressure over the droplets to rise. As a result, higher actual vapour pressure is required for the nucleation process to carry on and form cloud droplets. In heterogeneous nucleation, the intial small droplets are made of a different substance from the cloud particles. This reduces the saturation vapour pressure required for the formation of cloud droplets which makes the heterogeneous nucleation a more favourable process.

The thermochemical equilibrium models are dependent on the the atmospheric composition, especially the abundances of potential condensates, as well as the thermal structure. Note that condensation releases latent heat and so modifies the lapse rate, hence the thermal structure in the troposphere. The cloud structrure and density predicted by the ECCM for Saturn are shown in Fig. 1.4

assuming a 5-times enrichment in solar condensible volatile abundances. Three clouds made of ammonia ($NH_3$), ammonium hydrosulphide ($NH_4SH$) and water ($H_2O$), are expected to form at around 2, 6 and 20 bar respectively (Atreya *at al.*, 2005). The water cloud combines with ammonia into an aqueous solution at 20 bar, and extends up to the 9-bar level until only water ice remains within the cloud. Hydrogen sulphide ($H_2S$) has not been remotely detected yet in either Saturn or Jupiter, but was detected *in situ* in Jupiter by the Galileo probe. This could be explained by the condensation of hydrogen sulphide into tropospheric clouds. Models predict that $H_2S$ would not condense in Saturn's troposphere, but instead it would combine with ammonia to form ammonium hydrosulphide[4] through the chemical reaction:

$$NH_3(g) + H_2S(g) = NH_4SH(s)$$

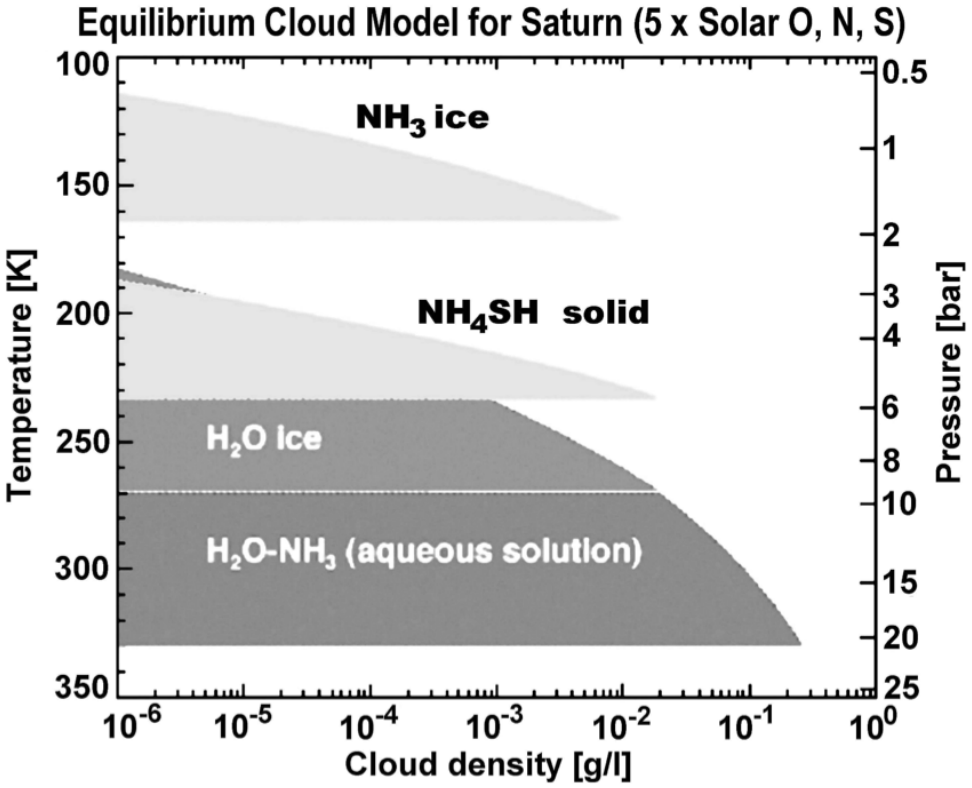



Figure 1.4: Thermochemical equilibrium model of the cloud formation in Saturn's troposphere from Atreya and Wong (2004). Ratios of N/H, S/H and O/H have 5-times solar condensible volatile abundances and the cloud concentrations represent upper limit values.

Note that local meteorology or microphysical processes are not taken into account in the thermochemical equilibrium models, even though they might affect the possible location of the clouds

[4]hydrogen sulphide and ammonia can also combine into ammonium sulphide ($[NH_4]_2S$) although the ECCM predict that an ammonium hydrosulphide cloud is more likely to form.

as observed on Jupiter (West *et al.*, 2009). It is surprising that no ammonia ice features have been spectrally detected so far, even though laboratory measurements have shown evidence of ammonia spectral lines throughout the near-infrared and at 9.4 and 26 $\mu$m (Martonchik *et al.*, 1984). A very few ammonia ice features have been detected on Jupiter in newly-forming cloud regions (Brooke *et al.*, 1998; Baines *et al.*, 2002; Wong *et al.*, 2004). However, ammonia clouds are expected to cover a wider area of the Jovian troposphere and so spectral detection of ammonia ice is expected at most latitudes and longitudes. Several phenomena might explain the suppression of ammonia ice features in Saturn and Jupiter's spectra. Brooke *et al.* (1998) suggested that large aerosol particles (radius $\geq$ 10 $\mu$m) might absorb so much radiation in the band wings that ammonia ice lines would overlap the other absorption lines. A similar process might also occur for large ammonia ice particles in Saturn's troposphere. The shape of aerosol particles might modify ammonia ice features. In particular, non-spherical particles of size smaller than the radiation wavelength might diminish ammonia spectral lines formed when surface modes dominate electro-magnetic resonances (Huffman and Bohren, 1980). Another factor could be the contamination of the ammonia cloud by water or ammonium hydrosulfide brought from deeper tropospheric levels or either a contamination by a photochemical haze located above the cloud (Tomasko *et al.*, 1984; West *et al.*, 1986).

Most models of the formation of tropospheric and stratospheric hazes involve photochemical processes and bombardment by energetic particles, as well as microphysical reactions such as the nucleation, coagulation and sedimentation of haze particles. Simplified photochemical paths such as those shown in Fig 1.5 suggest that polycyclic aromatic hydrocarbons (PAHs) and diphosphine ($P_2H_4$) are likely to be the main haze components with a smaller contribution from the other photochemical products ($C_{2n+2}H_2$, HCP). The photochemistry of ammonia leading to the formation of hydrazine ($N_2H_4$) is not expected to play an important role on Saturn because of the low volume mixing ratio of ammonia in the planet's upper troposphere and stratosphere. In most photochemical models, diphosphine is produced by the photolysis of phosphine (Atreya and Wong, 2004; West *et al.*, 2009). In these models, the more complex chemical scheme leading to the formation of PAHs involves H-abstraction of benzene ($C_6H_6$) by UV photolysis or reaction with molecular hydrogen, followed by addition of acetylene ($C_2H_2$). An admixture of PAHs and diphosphine sedimenting out to the troposphere might contaminate the ammonia cloud, and so make the spectral detection of such a cloud impossible. Auroral particles might have a significant role in initiating the photolysis of

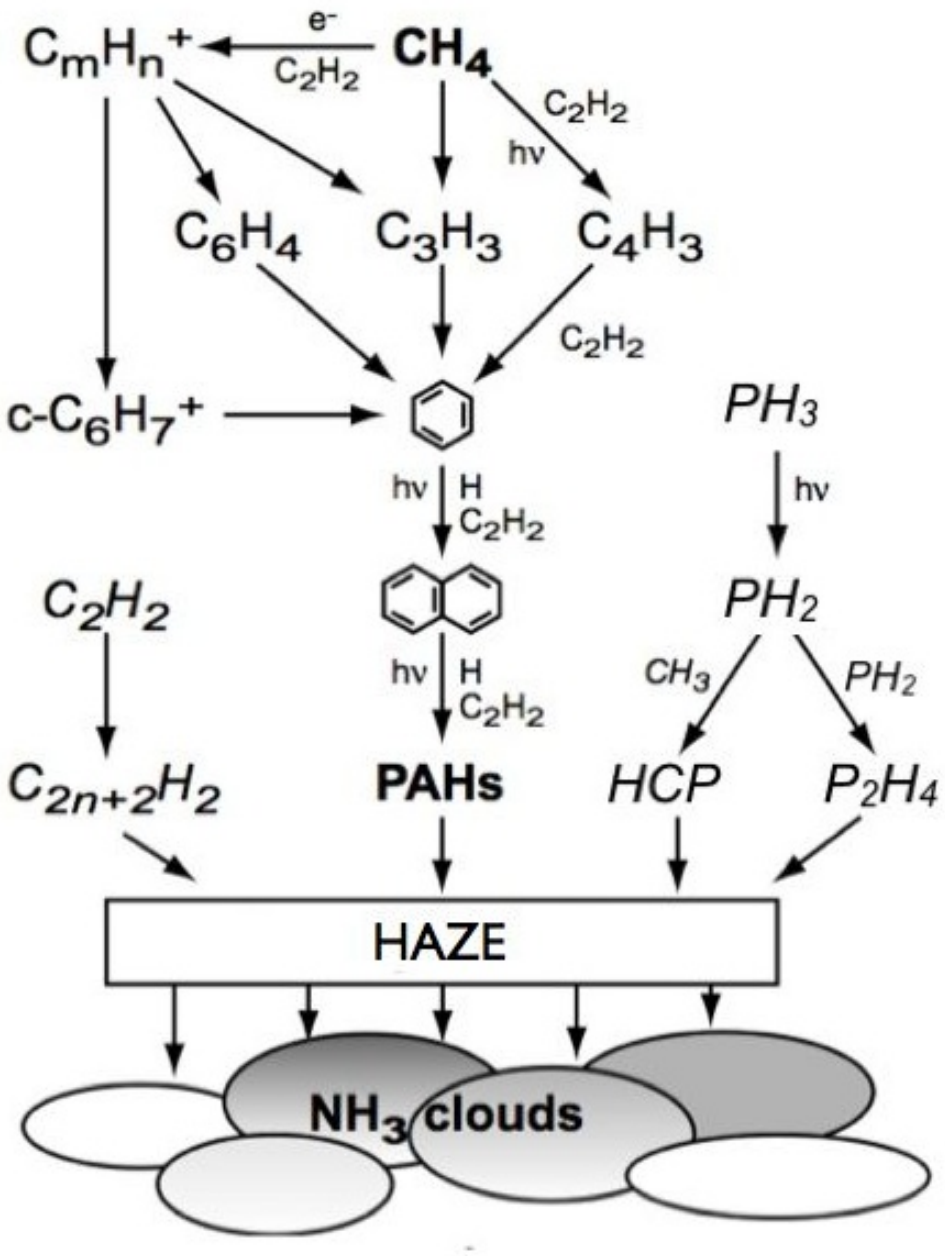



Figure 1.5: Photochemical model of the haze formation in Saturn's troposphere and stratosphere. The photochemical model was originally developed for Jupiter and adapted to Saturn's atmosphere (Wong *et al.*, 2003; Atreya and Wong, 2004).

methane leading to the formation of benzene and heavier ring components in the upper stratosphere, resulting in an enhancement of PAHs haze particles in polar regions. On the other hand, photolysis of phosphine would occur in the lower stratosphere or the troposphere where phosphine abundances are high enough to initiate the production of diphosphine. As for ammonia ice, no spectral lines of solid diphospine has been identified so far. However, stellar occultation measurements with the Cassini/VIMS instrument led to the detection of a hydrocarbon haze in the stratosphere (Nicholson

*et al.*, 2006).

Aerosols in Saturn's troposphere and stratosphere take part in many atmospheric processes, such as the energy balance, the interaction with thermal radiation and solar flux, as well as the photochemical and microphysical reactions. Also, aerosols can be used as passive tracers of the wind motions. In conclusion, thermochemical and photochemical theories predict the formation of tropospheric clouds made of ammonia, ammonium hydrosulphide and water, as well as upper tropospheric and stratospheric hazes composed of polycyclic aromatic hydrocarbons and diphosphine. However, only a hydrocarbon haze has been spectrally detected in the stratosphere so far. A few factors listed in this section are likely to challenge the direct detection of cloud and haze components. Instead, indirect methods based on the analysis of the interaction between aerosol particles and radiation have been used to study the cloud and haze properties in Saturn's atmosphere. In particular, this thesis focuses on the interaction of aerosols with both near-infrared thermal emission (4.6-5.1 $\mu$m) and near-infrared sunlight (0.8-3.5 $\mu$m).

## 1.4 Thesis themes

The analysis of Saturn's near-infrared spectra measured with the Cassini/VIMS instrument was carried out in order to study the properties of aerosols in the troposphere and stratosphere of the planet. In chapter 2, the main stages of the Cassini space mission are reviewed, as well a the technical capabilities and science objectives of the VIMS instrument. Correlations between the haze structure and a thermal feature referred as to the "temperature knee" are also investigated in this thesis. Saturn's temperature profiles are obtained from thermal measurements with Cassini/CIRS. Therefore, a description of the CIRS instrument is also included in chapter 2. VIMS data processing and calibration were performed with the Planetary Data System available to the whole scientific community. This was compared in chapter 2 to the other main calibration pipeline developed at the University of Arizona. CIRS calibrated data were already available to the scientific team at the University of Oxford.

The radiance emitted at the top of Saturn's atmosphere can be described by the radiative transfer (RT) equation. The RT equation is a function of key atmospheric parameters, such the temperature, gas composition and aerosol opacity. This is the main equation used in this thesis to model Saturn's

infrared spectra measured with VIMS or CIRS. The mathematical form of the RT equation is obtained in chapter 3. Saturn's infared spectra are modelled with the the numerical code RADTRANS, developed at the University of Oxford. RADTRANS is a RT algorithm which calculates Saturn's emitted radiance for a given atmospheric profile. Such a profile should include the relevant atmospheric parameters defined at all pressure between a bottom and top pressure levels. However, VIMS and CIRS measure Saturn's infared radiation and so the RT equation needs to be inverted in order to obtain useful information on the atmospheric structure. The inversion is performed by a retrieval algorithm, NEMESIS which is also described in chapter 3. RADTRANS can compute the radiance emitted by any planetary atmosphere where scattering opacity sources are present. The scattering model assumed in the numerical code is assessed at the end of chaper 3.

Chapter 4 focuses on the analysis of Saturn's 5-$\mu$m window at nighttime. VIMS near-infrared spectra in the 4.6-5.1 $\mu$m wavelength range sound at deep tropospheric levels where clouds are expected to form from thermochemical equilibrium theories. Gaseous absorption, mainly from phosphine and ammonia, also contributes to the shape of Saturn's spectra in the near-infrared. The cloud properties and gas abundances are retrieved with NEMESIS from single VIMS spectra in chapter 4. The retrieval problem turns out to be highly degenerate, and so many cloud models are found to match VIMS data quite well. As a result, a similar analysis but for limb-darkening data is undertaken in chapter 4. Indeed, the cloud properties can be constrained by considering VIMS spectra of the same latitude and longitude onto the surface of the planet, but measured at different emission angles. Chapter 4 concludes on the sensitivity of Saturn's 5-$\mu$m window to the haze layer located above the cloud forming region. However, the haze properties are poorly constrained at 5 $\mu$m and so VIMS spectra at shorter wavelengths are analysed in chapter 5 in order to derive the optical and physical properties, as well as the vertical structure of Saturn's tropospheric and startospheric hazes.

Saturn's reflection spectra at 0.8-3.5 $\mu$m measured with VIMS are used in chapter 5 to constrain the aerosol distribution in the upper troposphere and lower troposphere of the planet. The north-south variations of Saturn's haze properties are also considered in this chapter. The hypothesis of a "temperature knee" formed by the absorption of sunlight radiation by the tropospheric haze is assessed. Therefore, Saturn's thermal structure in the troposphere is derived from CIRS spectra in the far-infrared. In the last section of chapter 5, the retrieval results from the analysis of VIMS reflection spectra are compared to theoretical models in order to determine the haze composition.

Such theoretical models include laboratory measurements of the refractive index and photochemical models.

In chaper 6, the haze properties derived from the analysis of VIMS spectra at 0.8-3.5 $\mu$m are included in the cloud model used in chapter 4 to simulate Saturn's 5-$\mu$m window. The limb-darkening analysis at 5-$\mu$m is then updated by fixing the haze structure obtained in the previous chapter. Finally, chapter 6 concludes on a coherent model of the haze and cloud structure by combining results from the analysis of VIMS spectra at 0.8-3.5 and at 4.6-5.1 $\mu$m.

Chapter 2

# VIMS and CIRS infrared observations of Saturn

*This chapter is based partly on a literature review of the Cassini-Huyguens space mission, and the VIMS and CIRS instrumentations. The VIMS calibration software was developed by the VIMS team globally and I used this software in order to calibrate the data described in this thesis.*

## 2.1 Cassini-Huygens space mission to Saturn

*"The primary goal of Cassini-Huygens is to conduct an in-depth exploration of the Saturnian System", NASA (1989)*

### 2.1.1 A brief historical survey

Visible to the naked eye, Saturn was observed before the beginning of Christianity by the most ancient civilisations as a moving point on the sphere of fixed stars[1]. Nevertheless, it is really with the start of telescopic astronomy in 1609 that Saturn was seen not as an ordinary planet but as a much more complex system. In July 1610, Galileo pointed his telescope, an instrument with an aperture of around 2cm, 20× magnification and imperfect optics, at Saturn and noted that the planet was triple. He shared his discovery with Johannes Kepler in the most cryptic way by the use of an anagram: "*smaismrmilmepoetaleumibunenugttauiras*". Several months later, Kepler decoded the anagram but came up with the wrong solution and then published it. He thought that Galileo had observed two

[1] The very first recorded observations of Saturn were made by the Assyrian and Babylonian civilisations in ∼ 800 BC.

moons orbiting Mars. Although it was not what Galileo was trying to say, Kepler turned out to be correct since the two moons of Mars, Phobos and Deimos, were discovered by Asaph Hall in 1877. Combined in the right order, the letters of Galileo's anagram finally revealed their true meaning: *Altissinum planetum tergeminum observavi* [I have observed the highest planet to be triple-bodied]. Galileo observed that the lateral bodies were large and motionless with respect to Saturn, and so he concluded that they were unlikely to be satellites orbiting around the planet. It is only early in 1655 that the Dutch astronomer Christiaan Huygens correctly interpretated Galileo's observations with the discovery of Saturn's rings. Like Galileo, he used an anagram to publish his ring theory in *De Saturni luna observation nova* (1656). However, Christiaan Huygens's ring theory became generally known to the whole scientific community only in 1659 with the publication of *Systema Saturnium*. He also discovered, in March 1655, Saturn's largest moon, Titan. A few years later, the Italian-French astronomer Giovanni Domenico Cassini would discover the satellites Iapetus (1671), Rhea (1672), Tethys (1684) and Dione (1684), as well as the division between the A ring and B ring of Saturn (1675).

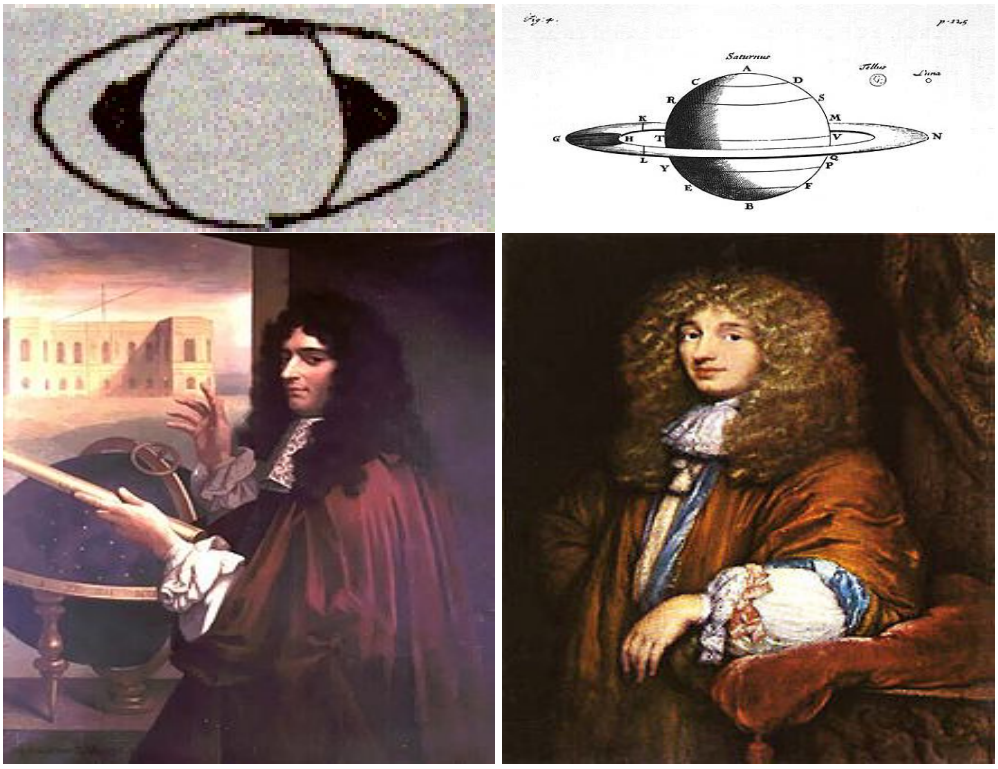



Figure 2.1: *Top-left*: Saturn as sketched by Galileo in 1616. *Top-right*: Christiaan Huygens's drawing of Saturn published in *The Celestial worlds discovered* (1698). *Bottom-left*: Portrait of Giovanni Domenico Cassini (1625-1712). *Bottom-right*: Portrait of Christiaan Huygens (1629-1695).

### 2.1.2 Mission overview

The development of modern astronomy and space exploration since about 1960 has made it possible to enhance our knowledge of the Saturnian system. The first space missions to Saturn, Pioneer 11 (1979), Voyager 1 (1980) and 2 (1981), only flew rapidly by the planet, as well as its moons and rings. They provided a unique insight into the Saturnian system, but they also raised many new questions to planetary scientists. Following the Galileo mission to Jupiter (1995-2000), the Cassini-Huygens mission to the ringed world was the next logical step.

The Cassini-Huygens spacecraft is a joint NASA/ESA/ASI[2] interplanetary mission aimed at studying the Saturnian system. The mission was first suggested in June 1982, 15 years before the launch of the spacecraft, when the Space Science Committee of the European Science Foundation and the Space Science Board of the National Academy of Sciences formed a joint working group to enhance cooperation in planetary science between the United Sates and Europe. In 1989, the Cassini-Huygens mission was formally approved. In the same year, NASA and ESA called for scientific investigation proposals. In 1990, NASA and ESA announced a list of 17 instruments selected for the overall mission. However, an instrument capable of measuring Titan's upper atmospheric properties was missing in the selection, leading to a second call of opportunity in 1991. A year later, the Ion and Neutral Mass Spectrometer (INMS) was selected as the $18^{th}$ instrument on board the spacecraft.

The spacecraft is made of two components: the Cassini orbiter, which surveys Saturn, its moons and its rings, and the Huygens probe, which landed on Titan's surface on 14 January 2005. NASA provided the Cassini orbiter, the launch vehicule, the mission operations and the telecommunication systems via the Deep Space Network (DSN). The development of the Huygens probe was carried out by ESA. The Italian Space Agency was in charge for the supply of the orbiter's hardware systems, as well as instruments for both the orbiter and the probe. Other scientific groups and industrial partners of NASA and ESA also contributed to the Cassini-Huygens mission by providing instruments for the orbiter and the probe. The flight operations of the Cassini orbiter and the Huygens probe are carried out respectively from the Mission Control Center at the Jet Propulsion Laboratory (JPL) in Pasadena, California, and from the ESA's European Operations Centre in Darmstadt, Germany.

[2]The ASI is the Italian Space Agency (Agenzia Spaziale Italiana)

### 2.1.3 Journey to Saturn

The Cassini-Huygens spacecraft was launched on 15 October 1997 at 08:55 UTC from Cape Canaveral Air Force Station complex 40, Florida, using a Titan IV/B-Centaur rocket and two Solid Rocket Motor Upgrades (SRMU) attached to the lower stage of the vehicle (Matson *et al.*, 2002). A 20-metre-long payload fairing sat on top of the rocket to protect the spacecraft during its trip through the Earth's lower atmosphere. The two SRMUs were first separated from the spacecraft, followed then by the payload fairing and centaur rocket within less than 10 minutes after the launch.

On its way to Saturn, the spacecraft performed four gravity assist flybys of Venus on 26 April 1998 and 24 June 1999, Earth on 18 August 1999, and Jupiter on 30 December 2000 in order to propel the spacecraft on its way to Saturn (see Fig. 2.2). Calibration, checkout and maintenance of instruments were performed during the gravity assist trajectory. A few science observations were also carried out during this phase of the mission especially on Jupiter. The Cassini-Huygens spacecraft reached Saturn's satellite Phoebe on 11 June 2005, 19 days before successfully entering Saturn's orbit on 1 July 2004 at an altitude of only 0.3 Saturn radii ($\sim$ 18 000 km). The spacecraft was then at the closest distance to Saturn ever reached by the Cassini-Huygens mission, and so the planet orbit insertion phase represented a unique opportunity for science observations at high spatial resolution. In particular, the spacecraft at such a short distance from the planet passed through the rings of Saturn within a region almost free of debris. The Saturn orbit insertion manoeuvre lasted 97 minutes and was the beginning of numerous orbital tours around the ringed planet.

During the first four years of the mission, also known as the *prime mission*, Cassini orbited 74 times around Saturn, executed close targeted flybys of Titan ($\times$45), Enceladus ($\times$4), Phoebe, Hyperion, Dione, Rhea and Iapetus, and made distant flybys of other major moons. The Huygens probe was released from the Cassini orbiter on 25 December 2004, and entered Titan's upper atmosphere 20 days later. The *prime mission* ended on 30 June 2008 and was extended until September 2010 under the name of *Cassini equinox mission* as the mission coincided with Saturn's equinox. During the two years of extended mission, the Cassini orbiter performed 28 close Titan flybys, 12 close icy moons flybys and 64 orbits around Saturn. The mission is currently known as the *extended-extended mission* or the *solstice mission*, and will end at the summer soltice of Saturn's northern hemisphere on 15 September 2017. This last mission should consist of 54 Titan flybys, 23 close icy flybys and

156 orbits of Saturn. The Cassini mission will end on 15 September 2017 with the orbiter's descent through Saturn's atmosphere.

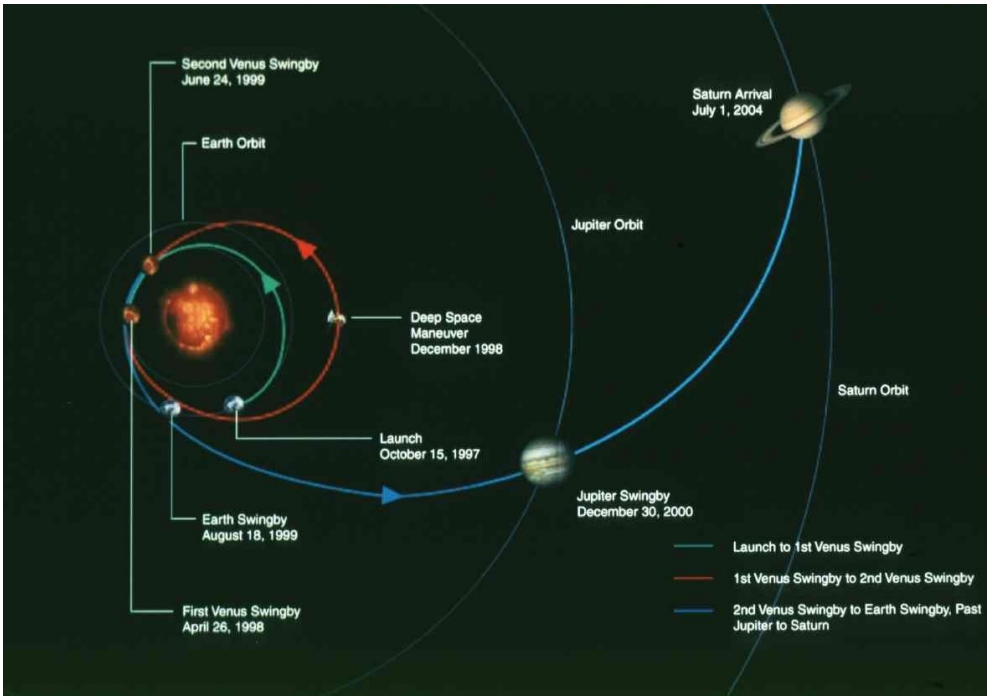



Figure 2.2: The Cassini cruise trajectory to Saturn. Credit: NASA/JPL.

### 2.1.4 Technical capabilities

With a total mass at launch of 5,636 kg[3] and height of 6.87 m, Cassini-Huygens is one of the largest interplanetary spacecraft ever built, and the third heaviest one after the two Soviet Union spacecrafts Phobos[4]. The main sections of the Cassini orbiter are mounted on top of each other. They include the propellant tanks, the engines, the twelve-bay electronic compartment, the 4-metre-diameter high-gain antenna, and two low-gain antennas (see Fig. 2.3). The three-metre Huygens probe was initially attached to the side of the orbiter. Three Radioisotope Thermoelectric Generators (RTG) provide electric power to the spacecraft. RTGs convert the heat generated by the natural radioactive decay of plutonium ($^{238}$Pu) into electricity. The temperature of the spacecraft is regulated by several means including insulation and blankets, shade from the antenna, electric and radio-isotope heaters, and reflective coatings. The Cassini-Huygens spacecraft communicates with Earth via the high-gain antenna and one of the low-gain antennas. The instruments on board the three-axis-stabilised orbiter

[3]The total mass includes the propellant mass at launch of 3,132 kg.

[4]The two spacecrafts Phobos 1 and 2 were sent to Mars and its moons, Phobos and Deimos, in July 1988. They each weighed 6,220 kg with their orbital insertion hardware attached.

are fixed and so their pointing at scientific targets is effected by turning the spacecraft. This can be done by using either the reaction wheels or one of the 0.5-Newton thrusters at the bottom of the stack. The data are stored in two solid-state recorders with a memory capacity of two gigabits each.

The Cassini-Huygens spacecraft is equipped with 18 science instruments, which have been designed to meet 27 science investigations. Six instruments mounted on the orbiter undertake *in situ* measurements of the plasma, dust and magnetic field in the Saturnian system: CAssini Plasma Spectrometer (CAPS), Cosmic Dust Analyze (CDA), Ion and Neutral Mass Spectrometer (INMS), MAGnetometer (MAG), Magnetospheric IMaging Instrument (MIMI) and Radio and Plasma Wave Science (RPWS). The other 6 instruments on the orbiter consist of remote sensing instruments operating at optical and radio wavelengths: Composite InfraRed Spectrometer (CIRS), Imaging Science Subsystem (ISS), UltraViolet Imaging Spectrograph (UVIS), Visible and Infrared Mapping Spectrometer (VIMS), RADAR, and Radio Science Subsystem (RSS). The Huygens probe carried 6 science instruments: Gas Chromatograph and Mass Spectrometer (GCMS), Aerosol Collector and Pyrolyzer (ACP), Descent Imager and Spectral Radiometer (DISR), Huygens Atmospheric Structure Instrument (HASI), Doppler Wind Experiment (DWE) and Surface Science Package (SSP).

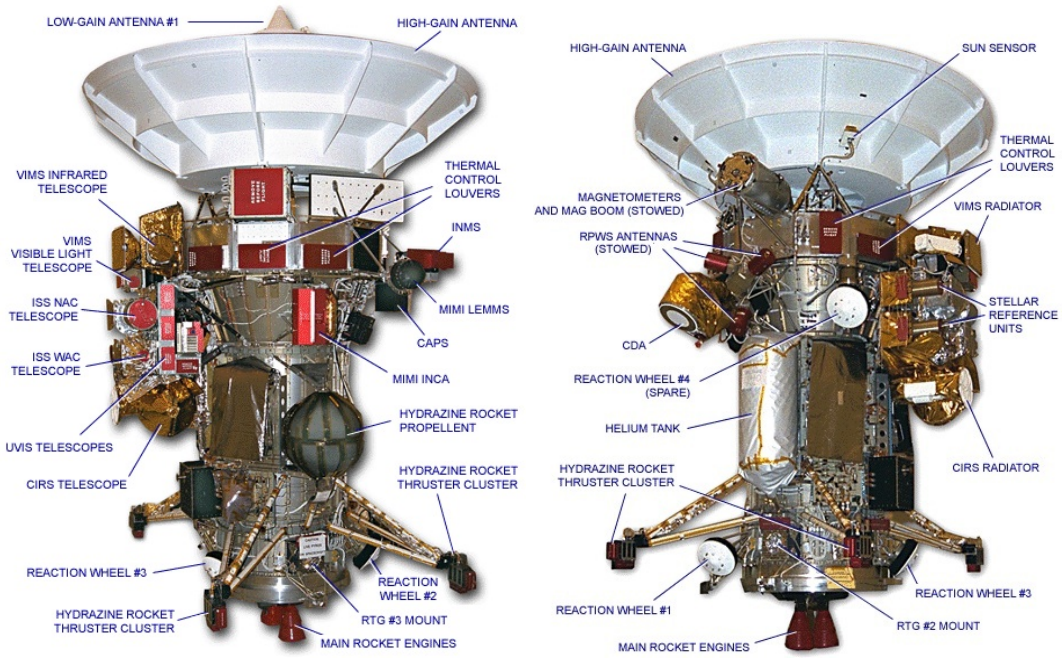



Figure 2.3: Views from both sides of the Cassini orbiter.

## 2.2 The Visual and Infrared Mapping Spectrometer (VIMS)

### 2.2.1 The VIMS team

The Visual and Infrared Mapping Spectrometer (VIMS) is a remote sensing instrument on board the Cassini orbiter involving engineering and science teams in the United States, France and Italy. After the selection of the instrument in November 1990, NASA/JPL took responsibility of the overall management, and was joined soon after by laboratories in France and Italy. The visible channel of VIMS instrument was designed and built in Florence, Italy by the Officine Galileo in contract with ASI. On the other hand, the infrared channel was designed and built at JPL which also conducted the calibration, test and integration of the instrument. The Institut d'Astrophysique Spatiale in Orsay, France provided the data compressors and buffers. The VIMS engineer team consisted of around 50 members responsible for designing and building the VIMS instrument. The VIMS Science team formed on 5 November 1990, after the announcement of the instruments selected for the Cassini orbiter. Both the VIMS engineer and science teams worked together to design, build-up and determine the science objectives of VIMS investigation of Saturn's system.

### 2.2.2 Instrument description

VIMS is a dual imaging spectrometer measuring scattered and emitted light from surfaces and atmospheres in the 0.35-5.1 $\mu$m wavelength range (Reininger *et al.*, 1994; Miller *et al.*, 1996). It consists of two distinct instruments in the visible and near-infrared: VIMS-VIS and VIMS-IR. VIMS data consist of 64$\times$64 pixel images. Each pixel corresponds to a spectrum with 352 wavelengths, 96 in the visible and 256 in the infrared. As a result, images produced by the VIMS instrument are often referred to as "image cubes". VIMS-VIS operates in the 0.35-1.05 $\mu$m spectral range, and can reach a maximum spectral and spatial resolution of respectively 1.46 nm and 167 $\mu$rad in the high-resolution mode. In the normal mode VIMS-VIS operates at a resolution of 7.3 nm (5 pixel summing) and 500 $\mu$rad (3$\times$3 pixel summing). The VIMS-VIS total field of view (FOV) is 42$\times$42 mrad in the lower resolution mode, however the visible channel covers an effective FOV of 32$\times$32 mrad in order to match the infrared channel's capabilities. Radiation emitted in the visible from targeted sources is collected by a scanning telescope and then focused onto a grating spectrometer. Spectral images in

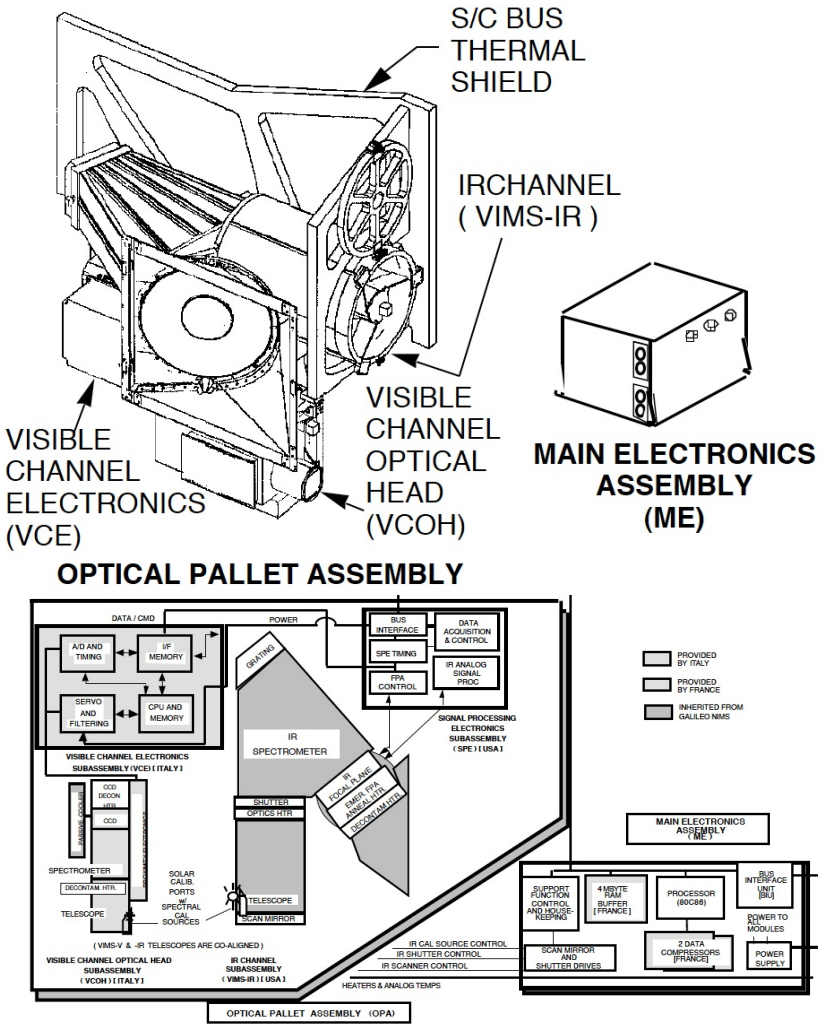



Figure 2.4: The VIMS layout (*Top*) and functional block diagram (*Bottom*).

the visible are then stored on a 256 $\times$ 512 frame transfer Charge-Coupled Device (CCD). Visible data are acquired in "push-broom" mode, meaning that data are stored in one row at a time before the scan mirror moves to the next row. The image on each row is dispersed by a spectrometer, so that the image can be viewed in the 96 visible wavebands.

The infrared channel VIMS-IR covers the 0.85-5.1 $\mu$m wavelength range. The instrument has a maximum spectral resolution of 16.6 nm and covers an effective FOV of 500 $\mu$rad. The infrared foreoptics consist of a 23-cm diameter telescope and a secondary mirror which can be scanned in two orthogonal directions. Therefore, a linear array instead of a 2D detector can be used to image the light dispersed by the infrared spectrometer. The VIMS-IR is equipped with a $1 \times 256$ array of InSb infrared detectors to store dispersed radiation in the infrared. The infrared detector operates in "whiskbroom mode" so that only one single spatial pixel is viewed by exposure. The infrared spectrometer disperses the pixel image on the linear array so that each of the 256 detectors corresponds

to the image at a specific waveband. VIMS main specifications for both the visible and infrared channels are listed in Table 2.1.

The detectors and optics of the visible and infrared channels, as well as the electronics, are thermally isolated from the Cassini spacecraft and cooled down in order to reduce the effects of noise. With a temperature ranging between approximately 60 and 77 K, the infrared focal plane is the coolest part of the VIMS instrument. The visible detector is cooled down to between 233 and 253 K. The optics in the visible and the infrared operate repectively from 263 to 293 K, and from 130 to 160 K. Temperatures of the main electronic assembly range between 253 and 323 K.

| SPECIFICATIONS | VISIBLE CHANNEL | INFRARED CHANNEL |
|---|---|---|
| Waveband number | 96 | 256 |
| Spectral range | 0.35 to 1.05 $\mu$m | 0.85 to 5.1 $\mu$m |
| Spectral resolution | 7.3 nm | 16.6 nm |
| Inst. Field Of View (IFOV) | 167 $\times$ 167 $\mu$rad | 250 $\times$ 500 $\mu$rad |
| Effective IFOV per pixel | 500 $\times$ 500 $\mu$rad | 500 $\times$ 500 $\mu$rad |
| Total field of view (64 $\times$ 64 pixels) | 32$\times$32 mrad | 32$\times$32 mrad |
| Typical integration time | 80 ms | 13 ms |
| Detector type | Si 512 $\times$ 256 (2D) | InSb 1 $\times$ 256 (1D) |
| Detector temperature | 233-253 K | 60-77 K |
| Optics temperature | 263-293 K | 130-160 K |
| Electronics temperature | 253-323 K | 253-323 K |
| Quantum efficiency | 0.13-0.41 | $> 0.7$ |
| Readout noise | 10e- | $<$ 500e- |
| Dark current | 40 pA/cm$^2$ at 22°C | 3 pA/cm$^2$ at 64 K |

Table 2.1: Summary of VIMS specifications (Brown *et al.*, 2004; Baines *et al.*, 2011)

VIMS-VIS and VIMS-IR are mounted together on the same optical pallet assembly, along with their signal processing package and a bus thermal shield, so that the two spectrometers are optically aligned (see Fig. 2.4). The instrument's main electronics are mounted on a separate pallet. Data from both the visible and infrared channels are combined into the electronics, and so a single spectrum is produced simultaneously in the whole 0.35-5.1 $\mu$m wavelength range.

The VIMS instrument can operate in "image", "point" and "line" modes. Point and line modes measure respectively one point and one single line in space. Point modes are mainly used for occultation studies while line modes are particularly useful for fast object flybys. Images can be acquired in three different pixel sizes: $1\times1$, $12\times12$ or $64\times64$. Only VIMS data measured in image mode are considered in this thesis. VIMS performs spectral imaging in five different observation modes at various spectral and spatial resolutions to study the atmosphere of Saturn. High spectral and high spatial resolution observations within 25 Saturn radii are used to investigate specific targets such as belts, zones, storms, etc. Full-disk spectral images of the planet at a high spectral resolution are acquired utilising the moderate-spatial resolution of VIMS. A third mode consists of measuring nighttime spectra of Saturn with the infrared channel only. This is particularly useful to survey the deep tropospheric clouds and trace gaseous constituents such as phosphine and ammonia. Long-integration measurements with VIMS-IR are used to detect weak emissions, including methane fluorescence from daytime observations, and $H_3^+$ from nighttime observations. Typical integration times for VIMS-VIS and VIMS-IR are 80 and 13 ms respectively. Finally, the VIMS instrument can detect lighting emissions while operating in the high-speed photometry mode at nighttime. The sources of errors in VIMS data are discussed in section 2.3 along with the data processing and calibration.

### 2.2.3 Science objectives

The VIMS instrument has been measuring the spectrum of Saturn at various latitudes and longitudes, and for many emission, solar and azimuthal angles. Therefore, it allows us not only to map atmospheric features all over the surface of Saturn, but also to constrain numerical models by considering a specific area of the planet observed at different viewing geometries. VIMS can also perform measurements of Saturn's spectrum at a very high spatial resolution. Thus the instrument capabilities has made it possible to track distinctive features in the planet's atmosphere, such as the recent 2010-2011 storm in the northern hemisphere (Baines *et al.*, 2011). The list of science objectives targeted by the VIMS instrument is extensive (Brown *et al.*, 2004). In particular, VIMS observations of Saturn's atmosphere have been expected to provide new insights on:

*i.* The structure of clouds and hazes in the troposphere and stratosphere, as well as their optical

and physical properties. Thermal near-infrared spectra of Saturn at 4.5-5.1 $\mu$m are sensitive to the deep tropospheric clouds while reflection spectra at shorter wavelengths (0.8-3.5 $\mu$m) can be used to study tropospheric and stratospheric hazes located above the cloud layers. Combined with stellar occultation measurements, reflection spectra are expected to provide a new insight on stratospheric hazes.

*ii.* The nature of tropospheric aerosols by spectral detection of cloud features, especially ammonia and water ice features. Ammonia ice spectral lines have been identified on Jupiter by the infrared spectral imager NIMS on board the spacecraft Galileo, however such a detection is still missing on Saturn.

*iii.* The distribution of gas species, including condensables such as ammonia and disequilibrium species such as phosphine from nightside thermal spectra. These species absorb the thermal radiation emitted from the deep atmospheric layers of Saturn. Therefore the VIMS-IR instrument offers a unique opportunity to map gas species over latitude and longitude, and look for seasonal trends.

*iv.* The bolometric bond albedo. As a key parameter in the energy balance of Saturn, it constrains the magnitude of the internal heat source of the planet.

*v.* The role of solar energy in the dynamics of the planet.

*vi.* The three-dimensional distribution and measurement of lighting using the high-speed photometry observation mode.

*vii.* The stratospheric temperature profiles from occultation measurements.

*viii.* Tropospheric wind fields by tracking ammonia clouds both in the horizontal and vertical directions.

*iix.* Polar aerosols and their link to magnetospheric phenomena.

Only the infrared channel of the VIMS instrument is considered in this thesis. In particular, the points (*i*) and (*iii*) in the list above are addressed in the next chapters. VIMS spectra in the two wavelength ranges 0.8-3.5 and 4.6-5.1 $\mu$m are analysed in order to study the haze and cloud properties in the troposphere and stratosphere of Saturn. VIMS infrared data are also sensitive to the distribution of phosphine and ammonia in gas phase. Therefore, the tropospheric abundance of these species is also derived from VIMS infrared spectra.

## 2.3 Calibration of VIMS data

VIMS raw cubes can be downloaded directly from the Planetary Data System (PDS) which stores scientific data from most NASA planetary missions. VIMS uncalibrated and unprocessed data are received by the VIMS operation system and are stored into archive volumes containing the raw spectral images, the instrument pointing and navigation, as well as the calibration files and software. Raw data units are data numbers (DN) defined as the number of counts per second measured by VIMS detectors. VIMS data were released for the first time to the whole scientific community on 1 July 2005. To date (16th February 2014) there are 52 volumes available on the PDS.

The data calibration was performed for the infrared channel by using the calibration pipeline provided by the PDS. The calibration files and software are stored in the same directories as the raw VIMS data. The first step in the calibration process is to substract the background noise from the data and flag any saturated pixels. Then the software flatfields the infrared spectral cubes. The last step is to divide the data by the exposure time and convert the signal originally in electron/second (DN) units into radiance units. This step is achieved by multiplying first the raw data by the instrument performance model in photons/DN, and then by the factor $f$ given by:

$$f = \frac{h \cdot c}{\lambda \cdot A \cdot \Omega \cdot \Delta_\lambda}$$

where $h$ is the Planck constant, $c$ is the speed of light, $\lambda$ is the wavelength in microns, $A$ is the aera of the primary mirror in square centimeters, $\Omega$ is the solid angle subtended by a pixel in steradians and $\Delta_\lambda$ is the width of the spectel. This step converts VIMS raw data into specific energy.

The software ISIS (Integrated Software for Imagers and Spectrometers) was used to add all the backplane data in the cubes, which provide information on the geometry of observations such as the phase angle, emission angle, solar incidence angle, as well as the latitude, longitude, pixel resolution and line resolution (See Gaddis *et al.* (1997), Torson and Becker (1997), and Anderson *et al.* (2004) for information on the ISIS software). In addition, the VIMS team at the University of Arizona developed continuously their own calibration pipeline. However this version of the pipeline is not available to the whole scientific community and so only a few cubes calibrated with the updated algorithm were released. Extensive testing was made to compare VIMS data calibrated with the PDS and the University of Arizona pipelines. By using a new version of the flatfield files created in 2009

by the VIMS operation team, both pipelines provide identical calibrated data as seen in Fig. 2.5. The new flatfield files were incorporated into the PDS pipeline to calibrate all VIMS data.

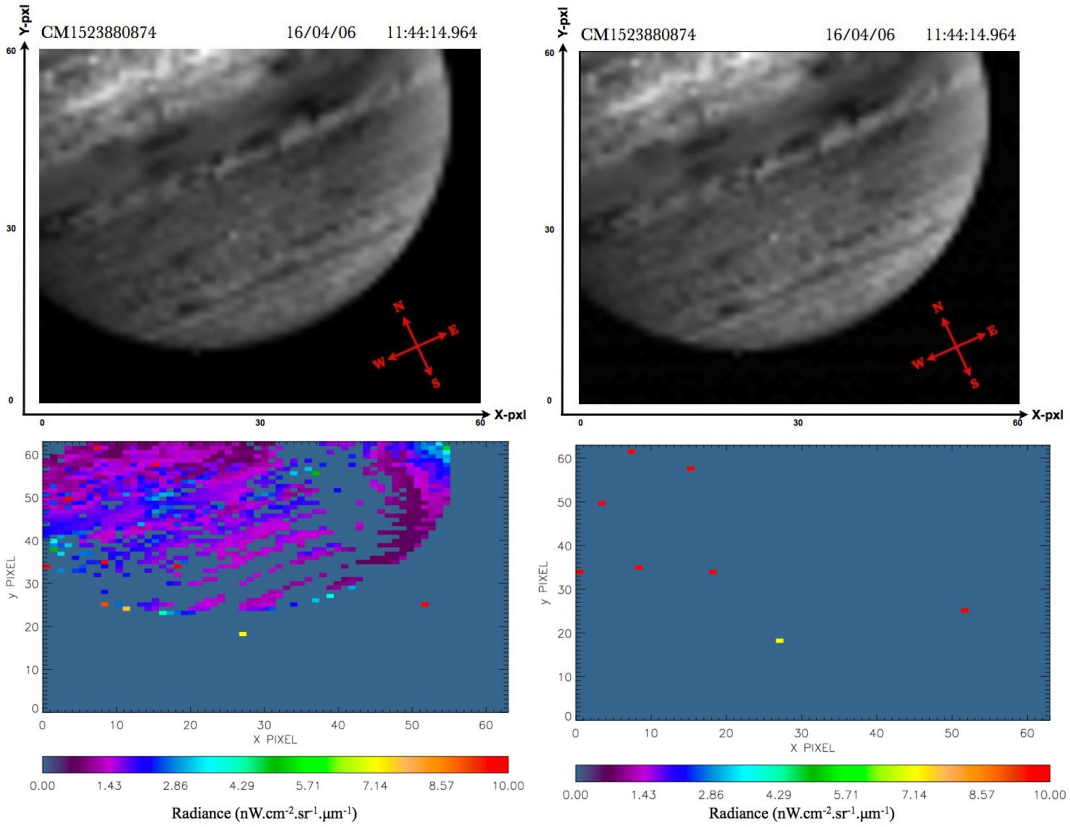



Figure 2.5: Calibrated (*top-left*) and uncalibrated (*top-right*) VIMS images CM1523880874 at 5.02 $\mu$m acquired on 16 April 2006 at $11^h44^m14.964^s$. Comparison of radiances in nW.cm$^{-2}$.sr$^{-1}$.$\mu$m$^{-1}$ at 5.02 $\mu$m calibrated with the University of Arizona pipeline and the PDS pipeline using the old (*bottom-left*) and new (*bottom-right*) flatfield files.

The spectral cubes are provided without measurement errors. The photon noise has been estimated to be less than 1 DN, which corresponds to a relative error on the flux of around 0.1%. However, folding in all of the other errors (especially, absolute calibration errors and the instrument response), the measurement errors are more likely to be around a few percent. In particular, the measurement errors should be at least as large as the solar irradiance uncertainty in the near-infrared. Colina *et al.* (1996) estimated this error to be around 3-5% of the solar flux. The measurement errors are greater where water absorbs in particular since the calibration was done on Earth where water exists (Kevin Baines, November 2009. *personal communication*, NASA/JPL). Therefore, it is generally agreed to set up VIMS data errors after calibration at 10% of the flux (Sromovsky *et al.*, 2010).

## 2.4 Overview of the Composite InfraRed Spectrometer (CIRS)

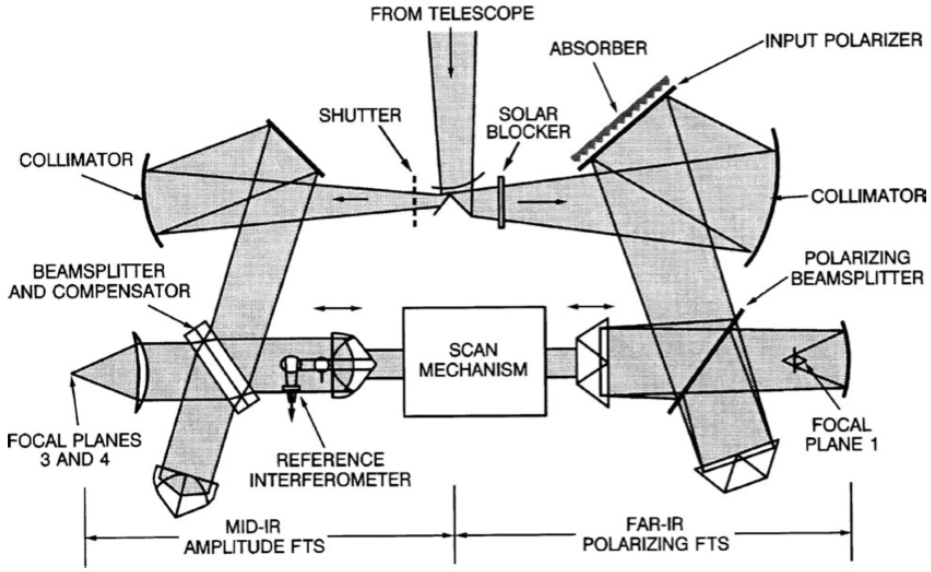



Figure 2.6: The CIRS instrument

The Composite InfraRed Spectrometer (CIRS) is an infrared remote-sensing Fourier transform spectrometer mounted on the Cassini orbiter, measuring thermal emission between 10 and 1400 $cm^{-1}$, that is to say between 7 $\mu$m and 1 mm (Flasar *et al.*, 2004). The instrument properties are summarised in Table 2.2. CIRS is made of two interferometers in the far- and mid-infrared sharing a common 50.8-cm diameter Cassegrain telescope and a scan mechanism (see Fig. 2.6). The incident radiation is first divided between the two interferometers by a field splitting mirror. Then, the infrared radiation passes through a beamsplitter in each spectrometer. Finally, the output beams are focused on the detector focal planes with an on-axis mirror in the far-infrared and a germanium lens in the mid-infrared. The CIRS instrument operates at a spectral resolution ranging between 0.5 and 15 $cm^{-1}$. The far-infrared interferometer is a polarisation interferometer with a focal plane FP1, operating at wavenumbers between 10 and 600 $cm^{-1}$. FP1 consists of two thermopile detectors with a large field of view of 3.9 mrad. The mid-infrared interferometer is a Michelson interferometer with two focal plane arrays, FP3 and FP4, operating at wavenumbers greater than 600 $cm^{-1}$. The two focal plane arrays are made of 10 HgCdTe detectors with a small field of view of 0.273 mrad per pixel. FP3 and FP4 are cooled down by a passive cooler radiating to space at an operating temperature ranging between 75 and 80 K. The other parts of the CIRS instrument, including the telescope and the FP1 focal plane, operate at a temperature of 170 K.

| SPECIFICATIONS | FAR-IR | MID-IR |
|---|---|---|
| Spectral range | 10 to 600 $cm^{-1}$ | 600 to 1400 $cm^{-1}$ |
| Spectral resolution | 0.5 to 15.5 $cm^{-1}$ | 0.5 to 15.5 $cm^{-1}$ |
| Pixel field of view | 3.9 × 3.9 mrad | 273 × 273 $\mu$rad |
| Interferometer type | polarising | Michelson |
| Integration time | 2-50 s | 2-50 s |
| Focal planes | FP1 | FP3 and FP4 |
| Detector type | thermopile | HgCdTe |
| Pixel number | $2^a$ | 1 × 10 |

Table 2.2: CIRS specifications summary

[a] one single large field of view but two different polarisations

The CIRS instrument can operate in five major observation modes aimed at specific scientific goals, listed below.

*i. Composition integrations (COMPSIT):* In this mode, spectral observations are made within 45 $R_S$ (1 $R_S$ = one Saturnian radius). The far-infrared and mid-infrared focal planes cover respectively 10° and 0.8° of latitude, and spectra are generally averaged over longitude. The composition integration spectra of Saturn are measured at the high resolutions of either 0.5 or 1.0 $cm^{-1}$ and for long integration times. This mode is used to map the spatial distribution of $H_2O$ in FP1, and $CO_2$, $CH_3C_2H$ (methylacetylene) and $C_4H_2$ in FP3. $PH_3$ can be mapped both in FP1 and FP3. This mode is also particularly useful to retrieve isotopic ratios, such as [HD]/[$H_2$], [$CH_3D$]/[$CH_4$], [$^{13}CH_4$]/[$^{12}CH_4$] and [$^{13}C^{12}CH_6$]/[$C_2H_6$].

*ii. Mid-IR nadir maps (MIRMAP):* Mid-infrared spectra are measured at low emission angles in FP3 and FP4 within $\sim$ 30 $R_S$. The spatial resolution of 0.5° latitude is therefore slightly higher than in the composition integration mode. The maps are acquired with a spectral resolution of 3 $cm^{-1}$. The mid-infrared nadir map mode is particularly relevant for the study of Saturn's thermal structure in the tropopause region and the middle stratosphere. $PH_3$, $C_2H_6$ and $C_2H_2$ can also be mapped in this mode.

*iii. Far-IR nadir maps (FIRMAP):* Far-infrared observations are made in FP1 at 16-20 $R_S$, resulting in a latitudinal resolution of 4-5°. Far-IR maps are acquired at the lowest spectral resolution equal

to 15.5 $cm^{-1}$. In this mode, the temperature in the troposphere down to approximately the 1-bar level can be mapped over all latitudes and longitudes.

*iv. Regional nadir maps (REGMAP):* This mode is very similar to the mid-infrared nadir map mode described in *ii*. However, observations in FP3 and FP4 are executed at a higher latitudinal resolution between 0.2° and 0.3°. FPI pixel resolution is about 3° in this mode. At such spatial resolutions, the spacecraft orbits Saturn at approximately 12-15 $R_S$.

*v. Limb maps (LIMBMAP):* In this mode, only measurements in FP3 and FP4 are carried out since the field of view in FP1 is too large for limb observations. The spatial resolution is about one atmospheric scale-height ($\sim$ 60 km) for limb observations near periapsis. Mid-infrared limb data are acquired at a spectral resolution of 15.5 $cm^{-1}$. This mode is used to map the temperature at 0.01-10 mbar, as well as the stratospheric distribution of methane.

FIRMAP spectra are analysed in this thesis in order to study the thermal structure of Saturn in the upper troposphere. Indeed, a local increase of temperature below the tropopause known as the "temperature knee" has been derived from Voyager/IRIS (Hanel *et al.*, 1981) and CIRS (Fletcher *et al.*, 2007) measurements. However, the physical origin of this feature is still pretty uncertain. Fletcher *et al.* (2007) suggested that local heating due to the absorption of sunlight radiation by the troposheric haze might contribute significantly to the change in temperature below the tropopause. This assumption is addressed in this thesis.

VIMS and CIRS instruments measure the radiance emitted from Saturn's atmosphere. The radiation interacts with various sources of opacity in the planet's atmosphere, such as gases and aerosols. therefore, VIMS and CIRS data provide key information on Saturn's atmospheric properties. In particular, VIMS and CIRS data are sensitive to troposheric and stratospheric levels. The interaction between radiation and Saturn's atmosphere is decribed by the radiative transfer equation in the next chapter. The radiative transfer and retrieval algorithms RADTRANS and NEMESIS are used to model Saturn's infrared spectra and derive the relevant atmospheric parameters. Both numerical codes are also reviewed in the next chapter, as well as the scattering model assumed throughout this thesis.

Chapter 3

# Modelling Saturn's infrared spectra

*The numerical models described in this chapter were initially developed by Pr. Patrick Irwin. The codes are being continuously updated by all members of the gas giant team at Oxford University.*

## 3.1 Radiative transfer model

### 3.1.1 Radiative transfer equation

In this thesis, the analysis of Saturn's infrared spectra was carried out using the infrared channel of the VIMS instrument and the CIRS instrument on board Cassini-Huygens. The interaction between Saturn's infrared emission and atmospheric properties is described by radiative transfer (RT) theories. In Saturn's atmosphere, infrared radiation is affected by emission, absorption and scattering from gases and aerosols. On-board spacecraft instruments, such as VIMS and CIRS, measure the radiance emitted at the top of the planet's atmosphere. The fundamental quantities in radiation theories are first described before coming up to the radiative transfer equation. The radiance $I_{\tilde{\nu}}$ is defined as the flux of energy propagating from a point $P$ on the planet in a given line-of-sight $\vec{S}$ per unit time $dt$, per unit wavenumber[1] $d\tilde{\nu}$, per unit solid angle $d\omega_S$ and per unit area $d\pi_S$ (see Fig. 3.1).

Thus, the infinitesimal energy transported $dE_{\tilde{\nu}}$ is given by:

$$dE_{\tilde{\nu}} = I_{\tilde{\nu}}(P,\vec{S})\, d\tilde{\nu}\, d\omega_S\, d\pi_S\, dt.$$

[1]The radiative equation is given here in terms of wavenumber, although the equation can also be expressed as a function of wavelength.

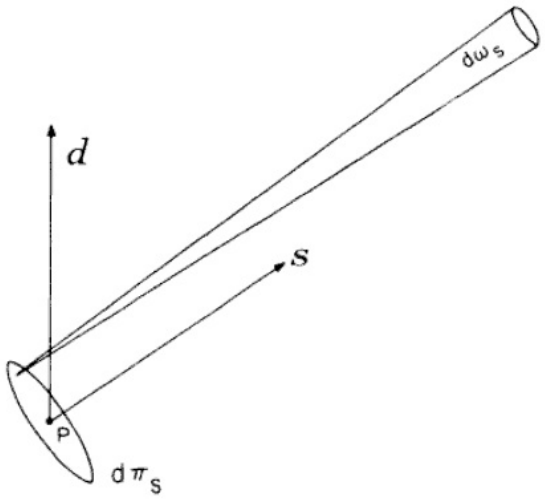



Figure 3.1: Sketch showing the propagation of radiation emitted at a point $P$ from a surface $d\pi_S$ on the planet in the direction $\vec{S}$ within a solid angle $d\omega_S$.

The total energy emitted from the whole surface of the planet is obtained by integrating $dE_{\tilde{\nu}}$ over each of the four integration ranges. The interaction between $I_{\tilde{\nu}}$ and Saturn's troposphere and stratosphere consists of two processes : extinction and emission. Thus the total radiance can be separated into one extinction and emission terms:

$$dI_{\tilde{\nu}} = dI_{\tilde{\nu}}^{extinction} + dI_{\tilde{\nu}}^{emission}.$$

The extinction term comprises both absorption and scattering by Saturn's opacity sources. It is described by Lambert's law, which states that the change of radiance along an optical path $ds$ is proportional to the attenuation coefficient $e_{\tilde{\nu}}$ and the radiance itself:

$$dI_{\tilde{\nu}}^{extinction} = -e_{\tilde{\nu}} I_{\tilde{\nu}} ds.$$

The emission term may be written:

$$dI_{\tilde{\nu}}^{emission} = e_{\tilde{\nu}} J_{\tilde{\nu}} ds,$$

where $J_{\tilde{\nu}}$ is the source function. Note that the source function is here defined so that the proportional term $e_{\tilde{\nu}} ds$ is the same as in the extinction term. Therefore, the source function is given by:

$$J_{\tilde{\nu}} = I_{\tilde{\nu}} \frac{dI_{\tilde{\nu}}^{emission}}{dI_{\tilde{\nu}}^{extinction}}.$$

The sum of the extinction and emission terms gives :

$$dI_{\tilde{\nu}}(P,\vec{S}) \;=\; -e_{\tilde{\nu}}\,ds\,[I_{\tilde{\nu}}(P,\vec{S}) - J_{\tilde{\nu}}(P,\vec{S})],$$

and hence

$$\boxed{-\frac{1}{e_{\tilde{\nu}}}\frac{dI_{\tilde{\nu}}(P,\vec{S})}{ds} \;=\; I_{\tilde{\nu}}(P,\vec{S}) - J_{\tilde{\nu}}(P,\vec{S}).}$$

The equation above is the radiative transfer (RT) equation, also known as the Schwarzschild equation. The method used to solve the RT equation depends of the physical conditions in which radiation and matter interact. In some cases, there are no analytical solutions to the RT equation, and so numerical methods must be applied to solve it. Lambert's law of absorption also states that the attenuation coefficient $e_{\tilde{\nu}}$ is equal to the product of the mean number density $n$ with the extinction coefficient $k_{\tilde{\nu}}$, and as a result the change of radiance is given by

$$dI_{\tilde{\nu}} = -I_{\tilde{\nu}}\,k_{\tilde{\nu}}\,n\,ds.$$

Consider a thick slab of atmosphere where $s_0$ and $s_1$ are respectively the start and end of the path, with radiant intensity $I_{\tilde{\nu}0}$ incident upwards from $s_0$. This radiation will be attenuated before reaching $s_1$ and thus the upward radiation at the top of the atmosphere from the base is given by integrating $dI_{\tilde{\nu}}$ between $s_0$ and $s_1$:

$$I_{\tilde{\nu}1} = I_{\tilde{\nu}0}\,\exp\left(-\int_{s_0}^{s_1} k_{\tilde{\nu}}(s)\,n(s)\,\mathrm{d}s\right)$$

which may also be expressed as

$$I_{\tilde{\nu}1} = I_{\tilde{\nu}0}\,\exp\left(-\tau_{\tilde{\nu}}(s_0,s_1)\right) = I_{\tilde{\nu}0}\,T_{\tilde{\nu}}(s_0,s_1)$$

where $\tau_{\tilde{\nu}}$ is the optical thickness (or optical depth if measured downwards from the top of the atmosphere) and $T_{\tilde{\nu}}(s_0,s_1)$ the transmittance or transmission function between $s_0$ and $s_1$. Now the thin slab at a coordinate $s$ along the optical path and of thickness $ds$ will also emit thermal radiation. For a thin slab in the troposphere and stratosphere, temperatures are uniform enough and molecular collisions are sufficiently rapid to assume local thermodynamic equilibrium[2]. Thus, from Kirchoff's law of thermal radiation the emissivity of the radiance emitted by the thin layer is equal to:

$$dI_{\tilde{\nu}} = k_{\tilde{\nu}}(s)\,n(s)\,B(\tilde{\nu},T(s))\,ds$$

[2]It can be shown that local thermodynamic equilibrium applies to vibrational and rotational modes of most radiatively active gases for pressures higher than 1 mbar (Andrews, 2000).

where $T(s)$ is the temperature and $B(\tilde{\nu}, T(s))$ the Planck function defined as:

$$B(\tilde{\nu}, T(s)) = \frac{2h\tilde{\nu}^3}{c^2\left(\exp\left(\frac{h\tilde{\nu}}{kT}\right) - 1\right)}$$

where $h$ is the Planck constant, $c$ the speed of light and $k$ the Boltzmann constant.

This radiance is itself attenuated by overlying layers before reaching the top of the atmosphere and thus the contribution to the total radiance at the top of the atmosphere $I_{\tilde{\nu}1}$ from a thin slab at a coordinate $s$ along the optical path is:

$$dI_{\tilde{\nu}1}(s) = k_{\tilde{\nu}}(s)n(s)B(\tilde{\nu}, T(s))\exp\left(-\int_s^{s_1} k_{\tilde{\nu}}(s')n(s')\,\mathrm{d}s'\right)ds$$

or alternatively

$$dI_{\tilde{\nu}1}(s) = B_{\tilde{\nu}}dT_{\tilde{\nu}}(s, s_1).$$

Thus, summing the contributions from all the layers, the total radiance reaching the top of the atmosphere at the end of the optical path $s_1$ is:

$$I_{\tilde{\nu}1} = I_{\tilde{\nu}0}T_{\tilde{\nu}}(s_0, s_1) + \int_{T_{\tilde{\nu}}(s_0,s_1)}^{1} B_{\tilde{\nu}}(s)\,\mathrm{d}T_{\tilde{\nu}}(s, s_1)$$

or alternatively

$$I_{\tilde{\nu}1} = I_{\tilde{\nu}0}T_{\tilde{\nu}}(s_0, s_1) + \int_{s_0}^{s_1} B_{\tilde{\nu}}(s)\frac{dT_{\tilde{\nu}}}{ds}\,\mathrm{d}s$$

which also can be written as

$$\begin{aligned} I_{\tilde{\nu}1} &= I_{\tilde{\nu}0}T_{\tilde{\nu}}(s_0, s_1) + \int_{s_0}^{s_1} B_{\tilde{\nu}}(s)K_{\tilde{\nu}}(s)\mathrm{d}s \\ &= I_{\tilde{\nu}0}T_{\tilde{\nu}}(s_0, s_1) + \int_{s_0}^{s_1} C_{\tilde{\nu}}(s)\mathrm{d}s \end{aligned}$$

where $K_{\tilde{\nu}} = \dfrac{dT_{\tilde{\nu}}}{ds}$ is the transmission weighting function, and $C_{\tilde{\nu}}(s) = B_{\tilde{\nu}}(s)K_{\tilde{\nu}}(s)$ is commonly known as the contribution function.

Considering that atmospheric properties are well-known between $s_0$ and $s_1$ and assuming black body emission and scattering as source functions, the transmittance between the bottom and top layers, as well as the contribution functions for each atmospheric layer can be calculated, and as

a result the radiance emitted at the top of the atmosphere can be estimated. The radiative transfer model RADTRANS was used in this thesis to simulate the radiation emitted from Saturn's atmosphere at infrared wavelengths assuming a reference model where all the relevant amospheric properties are defined.

### 3.1.2 The RADTRANS model

RADTRANS is a radiative transfer, or forward, numerical code which computes the synthetic spectrum emitted at the top of a reference atmosphere for scattering and non-scattering conditions. A few radiative transfer algorithms already exist, however they have been generally developed for Earth observations (Snell *et al.*, 1995; Berk *et al.*, 1998; Stamnes *et al.*, 1998). RADTRANS applies to any planetary conditions although it will be specifically used here to model the interaction of Saturn's troposphere and stratosphere with infrared radiation.

Before running RADTRANS, it is necessary to define an atmospheric model for Saturn's atmosphere. The main input parameters of the model are listed in Table 3.1. The troposphere and stratosphere are split into individual layers equally spaced in logarithm pressure. The top and bottom layers of the reference atmosphere are carefully chosen so that the pressure range covers all levels contributing to Saturn's infrared radiation. At each pressure level in the model, the temperature, the volume mixing ratio of all radiatively active gases present in Saturn's atmosphere, the para/ortho hydrogen ratio, the aerosol concentration and the fractional cloud cover are specified. The optical properties of aerosols, characterised by the extinction cross-section, the scattering albedo and the scattering phase functions at each wavelength, are also included in the model. Finally, the absorption coefficients of each individual spectral line must be added into the forward model in order to compute Saturn's transmittance in the troposphere and stratosphere. Line data are stored in line databases, such as HITRAN and GEISA (Rothman *et al.*, 2009; Jacquinet-Husson *et al.*, 2005). The individual absorption lines must be computed for all pressure levels and temperatures considered in Saturn's atmospheric model. As a result, line-by-line numerical codes are very slow, and so band and correlated-*k* methods are used instead in the retrieval model, where many computations must be performed. Since scattering by aerosol particles is not possible in the band model, the correlated-*k* method (Lacis and Oinas, 1991) is chosen for the computation of Saturn's infared spectra. In the radiative transfer equation,

the mean transmittance, or transmission function, of an optical path can be written as:

$$\bar{T}_{\tilde{\nu}} = \exp\left(-m\sum_{i=1}^{N} k_i(\tilde{\nu})\right)$$

where $N$ is the number of absorbers, $m$ is the mean column density[3] in $\mathrm{cm}^{-2}$ and $k_i(\tilde{\nu})$ is the absorption spectrum of the $i^{th}$ absorber in $\mathrm{cm}^2$ (Irwin *et al.*, 2008). The transmission must then be integrated over a particular wavelength range. For example, the transmission in the wavenumber interval $[\tilde{\nu}_0,\tilde{\nu}_0+\Delta\tilde{\nu}]$ is given by:

$$\bar{T} = \frac{1}{\Delta\tilde{\nu}}\int_{\tilde{\nu}_0}^{\tilde{\nu}_0+\Delta\tilde{\nu}} \exp\left(-m\sum_{i=1}^{N} k_i(\tilde{\nu})\right) d\tilde{\nu}.$$

In the line-by-line model, the transmission $\bar{T}_{\tilde{\nu}}$ is calculated for each of the $\Delta\tilde{\nu}/d\tilde{\nu}$ infinitesimal intervals. Since $k_i(\tilde{\nu})$ varies rapidly with wavenumber, $d\tilde{\nu}$ must be sufficiently small in order to resolve the individual line shapes. In the correlated-$k$ model, the transmission is expressed in the alternative form:

$$\bar{T} = \int_0^{\infty} f(k)\, exp(-km)\, dk$$

where $f(k)\,dk$ is the fraction of the wavenumber range occupied by absorption coefficients between $k$ and $k+dk$. The cumulative function $g(k)$ defined as:

$$g(k) = \int_0^{k} f(k)\, dk$$

is a smooth, single-valued, monotonically increasing function between 0 and 1, therefore the inverse function $k(g)$ exists and the transmission can be further simplified to

$$\bar{T} = \int_0^{1} exp(-k(g)\, m)\, dg.$$

$k(g)$, also known as the $k$-distribution function, varies smoothly with wavenumber allowing faster numerical integration than in the line-by-line model. The integral above can be estimated by considering only a few quadrature points between 0 and 1, and thus:

$$\bar{T} = \sum_{i=1}^{N} exp(-k_i\, m)\, \Delta g_i$$

[3]The mean column density is the number density integrated along the optical path

where $k_i$ is the $k$-distribution value at the $i^{th}$ quadrature point and $\Delta g_i$ is the corresponding weight. In a real atmosphere, the transmission varies with height, and so the total transmission should be evaluated at each homogeneous level. Assuming that the reference atmosphere can be split into M homogeneous layers, the total transmission at the top of the atmosphere is given by:

$$\bar{T} = \sum_{i=1}^{N} exp\left(-\sum_{j=1}^{M} k_{ij} m_j\right) \Delta g_i$$

where $m_j$ is the density of the $j^{th}$ layer, and $k_{ij}$ is the $k$-distribution value of the $j^{th}$ layer at the $i^{th}$ quadrature point. If $P$ absorbing gases have overlapping lines, the transmission at each layer is approximated by:

$$\bar{T} = \sum_{i1=1}^{N} \sum_{i2=1}^{N} ... \sum_{iP=1}^{N} exp - (k_{i1} m_1 + k_{i2} m_2 + ... + k_{iP} m_2) \Delta g_{i1} \Delta g_{i2} ... \Delta g_{iP}$$

or equally:

$$\bar{T} = \prod_{j=1}^{P} \sum_{i_j=1}^{N} \left[exp - (\sum_{j=1}^{P} k_{i_j} m_j)\right] \left[\prod_{j=1}^{P} \Delta g_{i_j}\right]$$

where $k_{ij}$ and $m_j$ are the $k$-distribution value at the $i^{th}$ quadrature and density of respectively the $j^{th}$ gas. Irwin *et al.* (2008) estimated the accuracy of the correlated-$k$ method with a line-by-line calculation. They found that this method is accurate to better than 5% for 10-20 quadrature points.

Atmospheric properties in Saturn's troposphere and stratosphere are then implemented into the model as a function of pressure or equivalently as a function of height. However, Saturn is observed at various emission angles and so what matters in the radiative transfer equation is the optical path of radiation through the atmosphere to the position of observation. Therefore, the algorithm calculates the mean atmospheric properties as seen at the emission angle. Then, the transmission and contribution functions can be estimated, and finally RADTRANS calculates Saturn's synthetic spectrum as measured at a specific viewing geometry. Assuming an atmospheric model of Saturn's troprophere and stratosphere, the synthetic spectrum of the planet at a given latitude and longitude in the infrared can be calculated for a particular viewing geometry and then directly compared to a spectrum measured by ground-based or space facilities in similar conditions. The atmospheric model can be varied until the synthetic spectrum matches the observations. This can be done numerically by the means of a retrieval algorithm. In this thesis, the numerical code NEMESIS was used to derive atmospheric properties from Saturn's infrared spectra in the troposphere and stratosphere of the planet.

| PARAMETER | DEFINITION |
|---|---|
| $p$ | *Pressure level:* the reference atmosphere is split into a finite number of atmospheric layers between a bottom and top levels specified in the model. All the pressure levels are equally spaced in logarithm scale. For each layer at a specific pressure, atmospheric properties are assumed to be uniform throughout the layer. |
| $T$(p) | *Temperature profile* |
| $f_p$(p) | *Para/ortho hydrogen ratio*: A hydrogen molecule with a para state has an even total angular momentume $J$. Ortho hydrogen molecules are characterised by an odd value of $J$. |
| $vmr$(p) | *Volume mixing ratio:* ratio of the number density of the gas to the total number density of the atmosphere. Up to 44 radiatively active gases are available in RADTRANS. |
| $\rho_a$(p) | *Aerosol concentration:* specific density in number of particles per gram. This quantity is converted by the algorithm to units of particles per cm$^2$ and then multiplied by the cross-section. At the end, the optical path is estimated for each layer of the atmospheric model |
| $k(g)$ | *k-distribution table:* They are calculated for each gas present in the atmospheric model at a range of representative temperatures and pressures. RADTRANS can also compute synthetic spectra using line-by-line or band models. However, the first model makes the calculation significantly slower while the second one is incompatible with multiple-scattering. |
| $f_a$(p) | *Fractional cloud cover:* fraction of aerosols covering each vertical level. |
| $x_{ext}(\lambda)$ | *Extinction cross-section:* in the model, the cross-section in cm$^2$ for each particle type can be specified for each wavelength. |
| $\omega(\lambda)$ | *Scattering albedo:* ratio of scattering coefficient to total extinction coefficient for each particle type. The scattering albedo is a function of wavelength. |
| $\{g, f_1, f_2\}(\lambda)$ | *Scattering phase functions:* see section 3.3. |

Table 3.1: Parameters of the reference atmosphere used in RADTRANS to compute Saturn's synthetic spectra at infrared wavelengths.

## 3.2 Retrieval code: NEMESIS

As for RADTRANS, the retrieval model **N**on-linear Optimal **E**stimator for **M**ultivariat**E** Spectral analy**SIS** (NEMESIS) can be generally applied to any planetary atmosphere (Irwin *et al.*, 2007). Although the code was originally developed to analyse thermal spectra of Saturn and Titan measured by the CIRS instrument on board the Cassini orbiter, it can be used to retrieve atmospheric properties from any ground-based or space observations from visible to microwave wavelengths.

The first task of NEMESIS is to calculate the synthetic spectrum for a specific wavelength range assuming a reference planetary atmosphere. This is done with the radiative transfer, or forward, model RADTRANS. The synthetic spectrum is then directly compared to the measured spectrum of the planet, and the retrieval, or inversion, model adjusts the reference atmosphere in order to minimise the discrepancies between the synthetic and measured spectra.

A few iterations need to be applied to the retrieval model in order to converge to a solution. Typically, this is achieved with NEMESIS after about ten iterations. At each iteration, the synthetic spectrum and the rate of change of modelled radiances with atmospheric properties must be evaluated. This allows the retrieval model to modify the reference atmosphere in a way that improves the fit to the observations within the measurement errors. This process requires a fast forward model, and so the correlated-*k* method is used here since it allows faster calculation of the retrieval code in multiple-scattering conditions.

NEMESIS can retrieve a scale factor of a vertical profile, as well as a continuous profile with a given number of vertical points. In the first case, least-squares methods are efficient enough to provide a very precise solution to the retrieval problem. The algorithm NEMESIS retrieves continuous profiles by using the technique of optimal estimation detailed by Rodgers (2000). This technique consists in minimising a cost function ($\phi$) given by:

$$\phi = (\vec{y_m} - \vec{y_n})^T S_\varepsilon^{-1} (\vec{y_m} - \vec{y_n}) + (\vec{x_n} - \vec{x_0})^T S_x^{-1} (\vec{x_n} - \vec{x_0})$$

where $\vec{y_m}$ is a vector of dimension $N_Y$ representing the measured spectrum; $\vec{y_n}$ represents the modelled spectrum also with dimension $N_Y$ calculated from a reference atmosphere characterised by a trial vector $\vec{x_n}$ of dimension $N_X$. Thus, $N_X$ variables are retrieved with NEMESIS . The state vector $\vec{x_0}$ contains a first-guess of the continuous profile to be retrieved, and will be referred to as the *a priori*

state vector. $\vec{x_0}$ has the same dimension as $\vec{x_n}$ equal to $N_X$. $S_\varepsilon$ and $S_x$ are respectively the measurement and *a priori* covariance matrices. $S_\varepsilon$ contains both the measurement and forward modelling errors, while $S_x$ contains the errors on the *a priori* profile. Once a choice of *a priori* errors has been made, $S_x$ is defined as follows for continuous profiles (Rodgers, 2000):

$$\begin{cases} S_{ii} &= a_i \\ S_{ij} &= (a_i a_j)^{1/2} \exp\left(-\dfrac{\ln|p_i/p_j|}{c}\right), i \neq j \end{cases}$$

where $a_i$ and $a_j$ are the *a priori* errors associated with the $i^{th}$ and $j^{th}$ elements of the *a priori* vector $\vec{x_0}$, $p_i$ and $p_j$ are the $i^{th}$ and $j^{th}$ pressure levels, and $c$ is the correlation length. The correlation length is the number of atmospheric scale heights over which the vertical profile is correlated. A value of 1.5 is generally adopted for Saturn (Fletcher *et al.*, 2007; Irwin *et al.*, 2008). By minimising the cost function, the retrieval code reduces the discrepancies between the measured and modelled spectra while staying close enough to the *a priori* profile to obtain a realistic solution to the retrieval problem. Such a solution should provide a new set of atmospheric parameters constrained equally by the measurement and *a priori* errors.

Practically, the diagonal elements $S_{ii}$ of the covariance matrix $S_x$ are first estimated by testing various values in the retrieval model and select the ones which better balance the measurement errors. Then, the non-diagonal elements $S_{ij}$ can me calculated as a function of the diagonal elements, pressure levels and correlation factor. As the cost function $\phi$ is minimised at each iteration step, the new trial vector $\vec{x_{n+1}}$ at the next step must be calculated as follows:

$$\vec{x_{n+1}} = \vec{x_0} + S_x K_n^T (K_n S_x K_n^T + S_\varepsilon)^{-1} (\vec{y_m} - \vec{y_n} - K_n(x_0 - x_n))$$

where $K_n$ is the $N_Y \times N_X$ Jacobian, or functional derivative, matrix which contains the rate of change of the $N_Y$ measurements with respect to each of the $N_X$ elements in the trial vector $\vec{x_n}$. However, the Jacobian can vary significantly between each iteration, and as a result lead to unstable solutions for the new trial vector $\vec{x_{n+1}}$. Therefore, NEMESIS uses a modified trial vector $\vec{x'_{n+1}}$ given by:

$$\vec{x'_{n+1}} = \vec{x_n} + \frac{x_{n+1} - x_n}{1 + \lambda} \text{ (Press } \textit{et al.}\text{, 1992).}$$

The parameter $\lambda$ is fixed to 1.0 at the first iteration. The cost function $\phi$ is recalculated at the new iteration step $n+1$ for the trial vector $\vec{x'_{n+1}}$. If $\phi$ decreases, then $\lambda$ is multiplied by a factor 0.3.

However, this parameter is multiplied by 10 if $\phi$ increases. This step ensures that the trial vector $\vec{x'_{n+1}}$ converges smoothly to a solution at the last iteration. The retrieval errors are contained in the matrix $S$ given by:

$$S = (S_x^{-1} + K_n^T S_\varepsilon^{-1} K_n)^{-1} \text{ (Rodgers, 2000).}$$

## 3.3 Scattering model

In planetary atmospheres, particles are sufficiently far away from each other to be considered as independent scatterers. Therefore, Saturn's atmosphere can be treated as a sum of small volume elements with individual scattering properties (Hansen *et al.*, 1974). The theory describing light scattering within these small volume elements is known as single scattering. Light scattering in the entire atmosphere is then computed by a multiple scattering algorithm. In this work, scattering will refer to multiple scattering since it is mostly used in the radiative transfer model. Rayleigh scattering and Mie scattering are both implemented in NEMESIS.

**Rayleigh scattering**

Rayleigh scattering applies to particles with size smaller than the wavelength of the incident radiation. This condition implies that individual particles can be treated as being in a homogeneous external electric field. Another condition for Rayleigh scattering to apply is that the ratio between the wavelength and the absolute value of the complex refractive index should be larger than the particle size. A dipole moment proportional to the incident electic field is induced in the particle. The second condition means that the time of polarisation in response to incident radiation is short compared to the period of the incident wave. The Rayleigh phase matrix[4] is as follows (Chandrasekhar, 1950):

$$\begin{pmatrix} \frac{3}{4}(1+\cos^2\alpha) & -\frac{3}{4}\sin^2\alpha & 0 & 0 \\ -\frac{3}{4}\sin^2\alpha & \frac{3}{4}(1+\cos^2\alpha) & 0 & 0 \\ 0 & 0 & \frac{3}{2}\cos\alpha & 0 \\ 0 & 0 & 0 & \frac{3}{2}\cos\alpha \end{pmatrix}$$

[4]Radiation polarised by Rayleigh scatterers is represented by a phase matrix in the I, Q, U, and V Stokes vectors. The solution is given here for isotropic Rayleigh particles.

where the phase angle $\alpha$ is the angle between the incident and emission angles. The angle $\alpha$ takes values in the range 0-180°, where $\alpha = 0°$ and $\alpha = 180°$ describe respectively forward and backward scattering. Rayleigh scattering theory is particularly relevant for understanding light scattering by molecular gases. In Saturn's atmosphere, Rayleigh scattering by the gaseous $H_2$-He can be important at bluer wavelengths in the visible (Del Genio *et al.*, 2009). However, Rayleigh scattering is negligible at longer wavelengths and Saturn's infrared spectra are instead dominated by Mie scattering.

**Mie scattering**

Light scattering by spherical particles with size of the same order of the incident wavelength is described by Mie theory. The Mie phase function is a function of the size distribution and complex refractive index of particles. The refractive index carries important information on the optical and physical properties of particles, and their interaction with radiation. The real and imaginary parts of the index represent respectively the phase velocity of radiation in the medium composed of the scatterers, and the absorption of radiation by the scatterers.

Mie scattering theory provides an analytical solution for spherical particles interacting with plane waves, therefore scatterers are modelled as single spheres in the numerical code. NEMESIS computes the radiation absorbed and scattered by spherical particles with various size distributions. In this thesis, the scatterers are assumed to have a standard gamma size distribution $n(r)$ as a function of the radius $r$:

$$n(r) \propto r^{(1-3b)/b} \exp(-\frac{r}{ab}),$$

where $a$ and $b$ are respectively the mean radius and the variance. Note that Mie theory only describes particles with spherical shapes. Knowledge of the microphysical processes in Saturn's atmosphere can be greatly enhanced by such a theory since a rough particle radius and variance can be both estimated from remote sensing observations. However, equilibrium thermochemical models of Saturn's atmopshere predict the formation of ammonia ices with non-spherical shapes. In this work, the use of a spherical shape for aerosol particles is in good agreement with the data observations, however future effort should be put on developing radiative transfer algorithms consistent with non-spherical particles for gas giants.

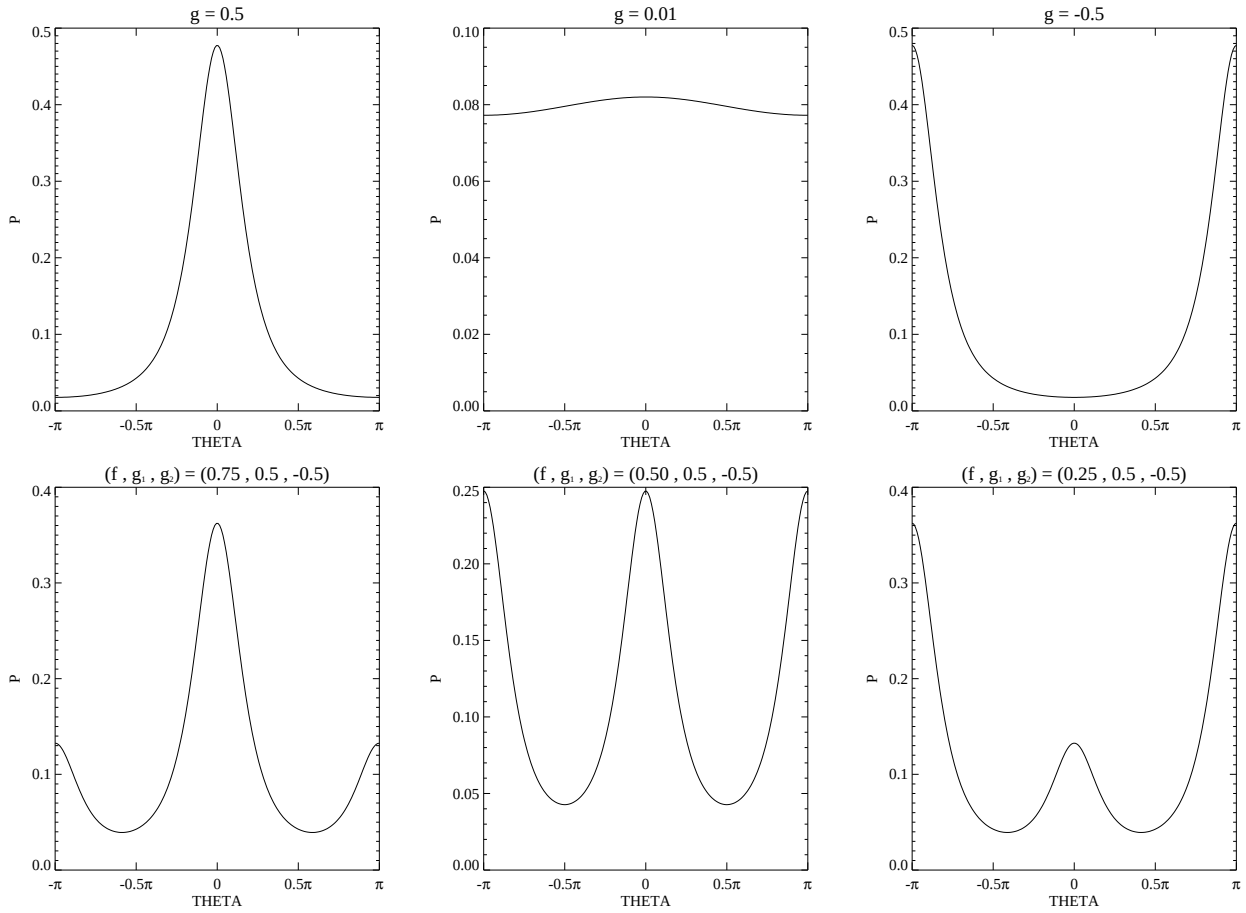



Figure 3.2: Henyey-Greenstein phase functions. *Top*: Simple Henyey-Greenstein functions for forward ($g = 0.5$), isotropic ($g = 0.01$), and backward scattering ($g = -0.5$). *Bottom*: Combined Henyey-Greenstein functions. The three phase functions have both forward and backward peaks with variable relative strengths. By tuning the values for $f$, $g_1$, and $g_2$, a wide range of phase functions can be modelled including the specific case where both forward and backward scattering are simultaneously present. Note that for $f = 0, 1$, the phase functions are identical to the single Henyey-Greenstein functions.

The Mie phase function is calculated by NEMESIS and then fitted with the Henyey-Greenstein function in order to make the computation of radiance by the retrieval code more efficient. The Henyey-Greenstein phase function is given by:

$$p(\theta) = \frac{1}{4\pi} \frac{1-g^2}{(1+g^2-2g\cos\theta)^{3/2}},$$

where $\theta$ is the scattering angle[5] and $g$ the asymmetry factor.

The simple Henyey-Greenstein function can account for forward, backward, and isotropic scattering (see Fig. 3.2). However, this function cannot properly model by itself all the possible phase functions observed for atmospheric particles. In particular, none of the simple Henyey-Greenstein

[5]Here the definition of the Henyey-Greenstein function implies that forward scattering occurs for $\theta \in [-\frac{\pi}{2}, \frac{\pi}{2}]$, and backward scattering for $\theta \in [-\pi, -\frac{\pi}{2}] \cup [\frac{\pi}{2}, \pi]$.

phase functions can describe forward and backward scattering simultaneously. Since most atmospheric scatterers are likely to have both forward and backward scattering components, NEMESIS uses instead the combined Henyey-Greenstein function:

$$p(\theta) = \frac{f}{4\pi}\frac{1-g_1^2}{(1+g_1^2-2g_1\cos\theta)^{3/2}} + \frac{1-f}{4\pi}\frac{1-g_2^2}{(1+g_2^2-2g_2\cos\theta)^{3/2}},$$

where $f$ is a fraction between 0 and 1, and $\{g_1, g_2\}$ are the asymmetry factors of the two contributing functions.

The Rayleigh and Mie phase functions are calculated for each small volume element within Saturn's atmosphere. RADTRANS first calculates the scattering properties for 5 zenith angles and 100 azimuth angles equally spaced in the ranges 0°-90° and 0°-180° respectively before integrating over all zenith and azimuth angles. A multiple scattering code is needed to compute the radiation emitted at the top of the atmosphere after being scattered by all small volume elements.

The numerical code uses a doubling or adding method which consists of calculating the reflection, transmission and source function for each individual layer. Adjacent layers are then combined to derive the reflection, transmission, and source functions for the two layers. This process can be iterated until all the layers are successively integrated into the numerical code.

Consider one homogeneous layer with bottom and top boundaries indexed by 1 and 2 respectively. For any incident, emission and azimuth angles ($\theta'$, $\theta$, $\phi$), the coefficients of reflection and transmission, and the source function due to thermal emission from each layer are given by $r_{\alpha\beta}$, $t_{\alpha\beta}$ and $J_{\alpha\beta}$ for $\{\alpha,\beta\} \in \{1,2\}$. The flux emitted at the top and bottom layers are given by:

$$I_2^+(\mu,\phi) = \int_0^{2\pi}\int_0^1 I_1^+(\mu',\phi')t_{12}(\mu,\mu',\phi'-\phi)\mu d\mu d\phi + \int_0^{2\pi}\int_0^1 I_2^-(\mu',\phi')r_{21}(\mu,\mu',\phi'-\phi)\mu d\mu d\phi + J_{12}(\mu,\phi)$$
$$I_1^-(\mu,\phi) = \int_0^{2\pi}\int_0^1 I_1^+(\mu',\phi')r_{12}(\mu,\mu',\phi'-\phi)\mu d\mu d\phi + \int_0^{2\pi}\int_0^1 I_2^-(\mu',\phi')t_{21}(\mu,\mu',\phi'-\phi)\mu d\mu d\phi + J_{21}(\mu,\phi)$$

where $\mu = \cos\theta$ and $\mu' = \cos\theta'$. In NEMESIS, the integral equations are replaced by the matrix equations:

$$I_2^+ = t_{12}I_1^+ + r_{21}I_1^- + J_{12}^+$$
$$I_2^- = r_{12}I_1^+ + t_{21}I_2^- + J_{21}^+$$

Similar equations as those shown above can also be written for the second layer boundered by the surfaces indexed by 2 and 3. Then the flux emitted by the combination of the layers is:

$$I_3^+ = t_{13} I_1^+ + r_{31} I_3^- + J_{13}^+$$
$$I_1^- = r_{13} I_1^+ + t_{31} I_3^- + J_{31}^+$$

where the coefficients of reflection and transmission, and the source function for the combined layer are

$$r_{13} = r_{32} + t_{23}(E - r_{21} r_{23})^{-1} r_{21} t_{32}$$
$$t_{13} = t_{23}(E - r_{21} r_{23})^{-1} t_{12}$$
$$J_{13}^+ = J_{23}^+ + t_{23}(E - r_{21} r_{23})^{-1}(J_{13}^+ + r_{21} J_{32}^-)$$

If there are $N$ pressure levels in the reference atmosphere, the adding method is used to generate the reflection $r_{1N}$, transmission $t_{1N}$ and source function $J_{1N}^+$ between the bottom and top layers.

Chapter 4

# Limb-darkening analysis of Saturn's near-infrared thermal emission

*The analysis and results described in this chapter are entirely my own. Referenced contributions from external works are also included in order to allow further discussions on the results.*

## 4.1 Saturn's thermal emission at 5 $\mu$m

Saturn's visible atmosphere is often reputed to be bland and colourless, especially when compared to Jupiter's noticeable system of bands and zones. This is mainly due to the scattering of sunlight by hazes located above the cloud layers at shorter wavelengths in the visible and near-infrared. By sounding deeper in the troposphere where clouds form, the Cassini/VIMS near-infrared instrument revealed a plethora of atmospheric activities, such as compact and dark spots, numerous vortices and storms with inferred lighting discharges (Choi et al., 2009). In this thesis, Saturn's thermal emission spectra and 5-$\mu$m window will be identically referred to as the planet's spectra at thermal wavelengths between 4.6 and 5.1 $\mu$m. At such wavelengths, collision-induced opacity due to $H_2$-He, as well as methane absorption are both negligible. Only nightside spectra of Saturn were considered so that the effects of reflected sunlight by aerosols can be ignored. Indeed, de Graauw *et al.* (1997) observed that reflected sunlight contributes to Saturn's spectra in the 5-$\mu$m window, with a ratio of dayside spectra over nightside spectra of approximately 2.5. Saturn's 5-$\mu$m window can probe at deeper pressure levels where tropospheric clouds are expected to form. Saturn's thermal emission spectra are formed

mainly by the warm thermal radiation emitted from the deepest layers of the planet's atmosphere and absorbed by the two main opacity sources, aerosols and gases. A typical VIMS image and several spectra of Saturn extracted from VIMS spectral cube CM1524383985 measured on 22 April 2006 at nighttime are shown in Fig. 4.1. Saturn's image at 5 $\mu$m shows significant latitudinal structure with a succession of bright and dark zonal lines, as well as the presence of spots. Regions of high opacity absorb more thermal radiation and so appear darker than regions of low opacity. Note that the northern hemisphere is significantly brighter than the southern hemisphere. This can be correlated to higher opacities in the summer southern hemisphere, either from gases or aerosols, at the time of observations. As a result, Saturn's spectrum measured at 30°N is brighter than the spectrum at 30°S, although both spectra are similar in shape. The equatorial region region is also dark in the 5-$\mu$m window, and so Saturn's spectrum at the equator is characterised by low radiances as in the spectrum at 30°S. However, a "kink" at 5.1 $\mu$m is observed only in the equatorial spectrum at all longitudes. Fletcher *et al.* (2011) suggested that this feature might be a signature of tropospheric ammonia. In chapter 6, the study of latitudinal variation of the ammonia volume mixing ratio in the deep troposphere shows that the ammonia abundance is indeed enhanced in the equatorial region. Finally, similar spatial variations of Saturn's radiances in the 4.6-5.1 $\mu$m wavelength range were found prior to Cassini's arrival at Saturn by Yanamandra-Fisher *et al.* (2001).

In the 5-$\mu$m window, the gaseous absorption is dominated by phosphine ($PH_3$) with smaller contributions from ammonia ($NH_3$), arsine ($AsH_3$), germane ($GeH_4$), deuterated methane ($CH_3D$), carbon monoxide (CO) and water ($H_2O$) (Fletcher *et al.*, 2011). These species were spectrally detected by earth-based and space observations. $PH_3$ and $CH_3D$ were first detected by the Kuiper Airborne Observatory (Fink and Larson, 1978; Larson, 1980). CO was detected by Noll *et al.* (1986) with the UK Infrared Telescope (UKIRT). $GeH_4$ was also first detected with UKIRT by Noll *et al.* (1986) followed later by de Graauw *et al.* (1997) in Infrared Space Observatory (ISO) measurements. $AsH_3$ was detected both with UKIRT (Noll *et al.*, 1989) and the Canada-France-Hawaii Telescope (Bézard *et al.*, 1989). The $2\nu_2$ and $\nu_4$ $NH_3$ bands were detected by the NASA Infrared Telescope Facility (Fink *et al.*, 1983), Voyager/IRIS (Courtin *et al.*, 1984) and ISO (de Graauw *et al.*, 1997). $H_2O$ was detected by de Graauw *et al.* (1997) in ISO measurements. Among the absorbing gases in the 5-$\mu$m window, $PH_3$, $GeH_4$ and CO are the only disequilibrium species, meaning that their presence in the upper troposphere and the stratosphere is due to upwelling of material from deeper atmospheric levels

(Lewis and Fegley, 1984; Fegley and Prinn, 1985). Despite a smaller spectral resolution than ground-based instruments, VIMS 5-$\mu$m window observations are particularly suited to map the distribution of these gases, as well as the aerosol opacities in Saturn's atmosphere.

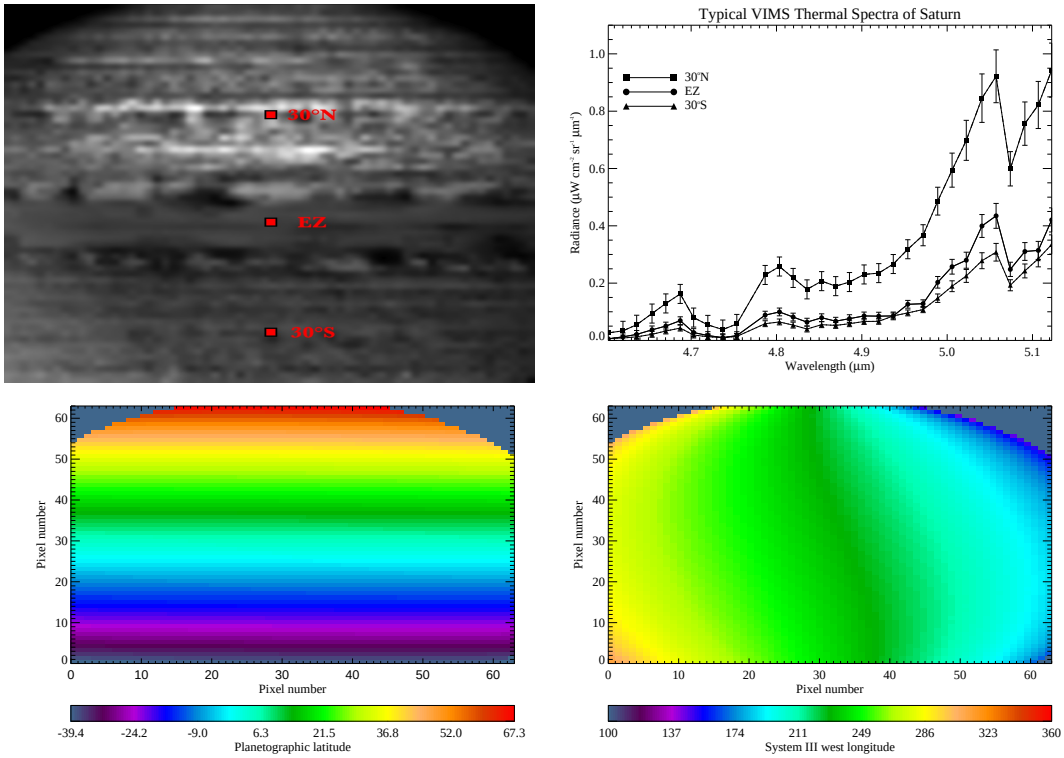



Figure 4.1: VIMS image and several spectra of Saturn in the 5-$\mu$m window. *Top-left:* VIMS night-side image at 5.06 $\mu$m extracted from the VIMS spectral cube CM1524383985 acquired on 22 April 2006 during Cassini's prime mission. The spectral cube was calibrated with the PDS pipeline. Planetographic latitudes and longitudes in the system III west are shown for each pixel in the bottom panels. Saturn's image at 5 $\mu$m shows significant latitudinal structure, as well as the presence of bright and dark spots. Here the dark pixels correspond to regions of high opacity where the internally generated heat radiation is absorbed by aerosols and gases. In contrast, bright pixels correspond to regions of relatively low opacity. *Top-right:* Typical VIMS thermal emission spectra measured at 30°S, in the equatorial zone and at 30°N. The three spectra were extracted from the same spectral cube CM1524383985 at the pixel positions shown by the red squares on the VIMS image. Absorption and scattering of thermal radiation by tropospheric gases and aerosols are mainly responsible for the shape of Saturn's spectrum between 4.6 and 5.1 $\mu$m. The northern hemisphere of Saturn is significantly brighter than the southern hemisphere in 2006, suggesting a strong asymmetry of opacity between the two hemispheres. Note that a representative pixel for each of the three plots was selected here, although radiances vary with longitude as well. However, at the observation time, the mean radiance in the northern hemisphere is larger than in the southern hemisphere. As a result, the selected pixels are also a representation of the mean radiances observed in the southern and northern hemispheres, and at the equator. A "kink" at 5.1 $\mu$m is present in Saturn's equatorial spectrum but was not observed at other latitudes. This feature is observed at all longitudes and is likely to be a signature of tropospheric ammonia (Fletcher *et al.*, 2011).

As mentioned earlier, Saturn's 5-$\mu$m window probes to upper tropospheric levels where thermochemical models predict the formation of clouds (Lewis, 1969; Weidenschilling and Lewis, 1973; Atreya *et al.*, 1999). The contribution weighting functions were evaluated for a cloud-free and three typical cloud models (see Fig. 4.2). The transmission weighting functions $K_\lambda(p)$ were calculated with RADTRANS at each wavelength $\lambda$ and pressure $p$ (see section 3.3.1). The contribution weighting functions, $C_\lambda(p)$, were then obtained by multiplying the transmission weighting functions with the Planck function at the atmospheric temperature $T(p)$. For a cloud-free atmosphere, only gases are responsible for the absorption of the warm thermal radiation. Most of the gaseous absorption at 5 $\mu$m occurs in the 1-5 bar pressure range. Note that the thermal emission spectrum of Saturn is still sensitive to pressure levels up to 500 mbar, especially at lower wavelengths. The contribution weighting functions were also calculated for an ammonia cloud located at 1 and 2 bar with an integrated optical depth equal to 5 at 5 $\mu$m. Indeed, thermochemical models predict the formation of ammonia ice between 1 and 2 bar. In these models, the contribution weighting functions for an ammonia cloud located at 1 and 2 bar are shifted higher up in the troposphere at the exact altitude of the cloud. The contribution weighting functions for an ammonia cloud at the 2-bar pressure level, but with a lower optical depth equal to 1 at 5 $\mu$m are also shown in Fig. 4.2. The shape of the contribution functions is halfway between the cloud model with a 5-optical depth and the cloud-free model. The balance between the aerosol and gas contributions to Saturn's thermal emission spectra depends on the cloud opacity. Although optically-thick clouds tend to mask gaseous absorption below the cloud base, both aerosol and gaseous opacities in the troposphere contribute most significantly to the shape of Saturn's spectrum between 4.6 and 5.1 $\mu$m. Therefore, Saturn's 5-$\mu$m window is particularly valuable for sounding the cloud structure and gas distribution in the troposphere of the planet. Fletcher *et al.* (2011) found that adding a thin haze layer above the cloud layer improved the fit to VIMS observations in the 4.6-5.1 $\mu$m wavelength range. If a haze layer is included in the atmospheric model, both gases and aerosols will contribute to Saturn's thermal emission spectra, with a relative strength depending on the haze opacity. In conclusion, any opacity source above the 5-bar level might potentially contribute to Saturn's 5-$\mu$m window. Below this level, the gas opacity is too high to allow the VIMS instrument to sound deeper in the troposphere. The key issue is thus to assess which opacity sources are actually responsible for Saturn's absorption of thermal emission at 5 $\mu$m.

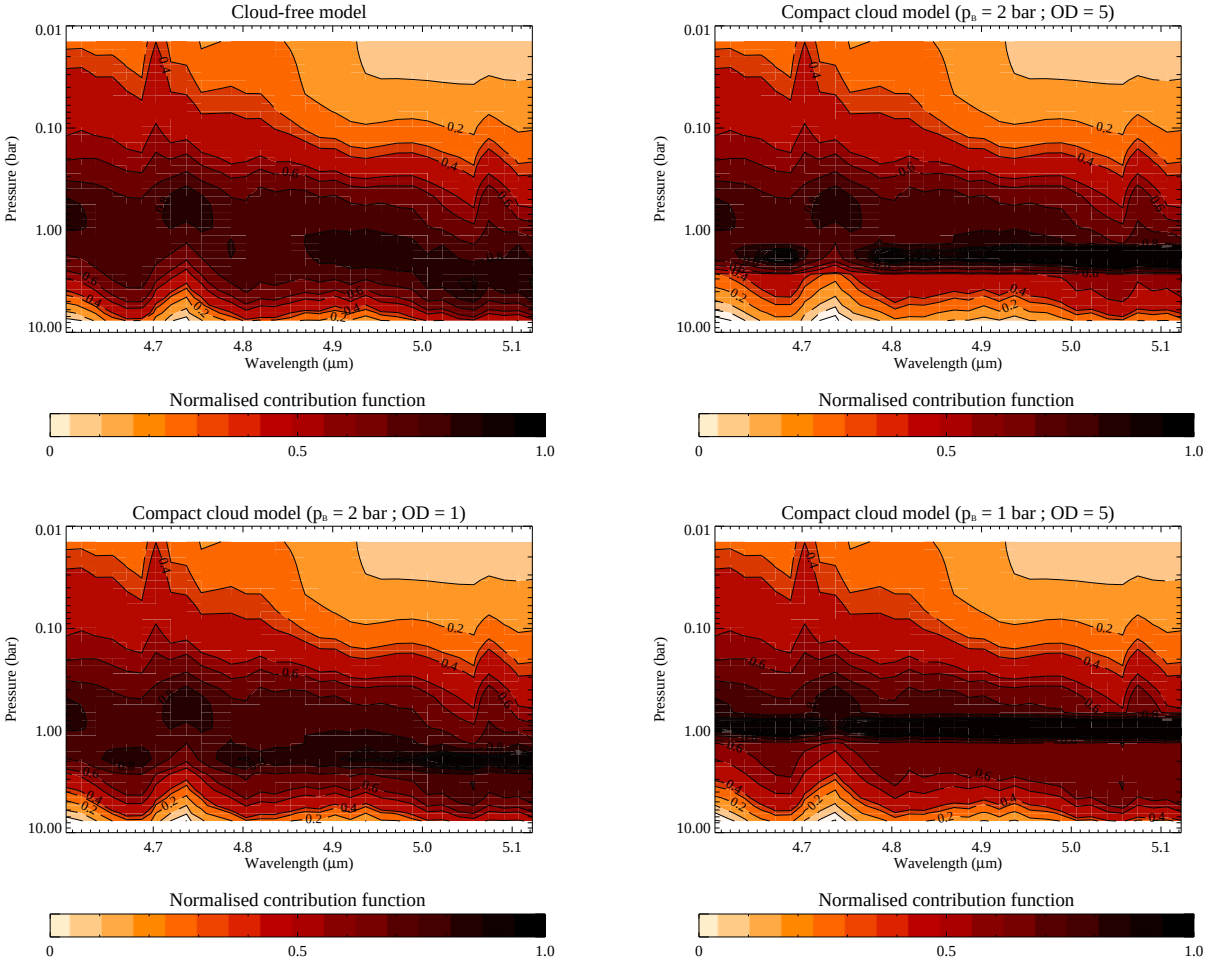



Figure 4.2: Altitude sensitivity of Saturn's thermal emission spectra. The contribution weighting functions were calculated for four atmospheric models with RADTRANS and normalised at each wavelength. *Top-left*: The contribution weighting functions for a cloud-free atmosphere. The dark colours show the pressure levels at which gaseous absorption is the most significant. At a given wavelength, the thermal emission spectrum is not sensitive to pressure levels below the peak of the contribution weighting function. *Top-right*: One compact ammonia cloud located at 2 bar and with an optical depth per bar of 5 at 5 $\mu$m is included in the reference atmosphere. The contribution weighting function is shifted to the altitude of the cloud layer. In this case, the tropospheric cloud contributes the most to the opacity sources, and any other aerosol or gas opacity below the 2 bar level would contribute very little to Saturn's thermal emission spectra. *Bottom-left*: the same as in the top-right pannel but for a lower value of the optical depth equal to 1. The peak of the contribution weighting function at 2 bar is less sharp than for an optically thicker cloud, and gaseous absorption below the cloud layer also contributes significantly to the shape of Saturn's thermal emission spectra. *Bottom-right*: Contribution weighting function for a cloud at 1 bar and of optical depth equal to 5. The peak of the function is here shifted at 1 bar at the location of the cloud.

## 4.2 Fitting strategy

### 4.2.1 Reference atmosphere

A reference atmosphere must be provided for NEMESIS, to allow first the radiative transfer code to evaluate Saturn's thermal emission in the 5-$\mu$m window, and then the retrieval algorithm to adjust selected atmospheric parameters so as to minimise any divergence between the synthetic and measured thermal emission spectra of Saturn. As mentioned in the previous section, gases absorb most of the thermal radiation in the 1-5 bar region. However, Saturn's window at 5 $\mu$m is also senstive to aerosols located in the troposphere and potentially in the lower part of the stratosphere. Therefore, pressures in the reference atmosphere range between 0.01 and 10 bar to include all possible opacity sources responsible for Saturn's thermal emission spectra. Indeed, models of the photochemical hazes suggest that they extend below the 0.01-bar level (West *et al.*, 2009), and gaseous absorption starts at approximately 5 bar. 39 pressure levels were included in the radiative transfer model, equally spaced in logarithm scale ($\Delta \log_{10} p \sim 0.076$)[1]. The main parameters in the reference atmosphere comprising the temperature, gaseous composition and aerosol distribution in the troposphere and stratosphere of the planet are reviewed in this section.

#### Temperature

The temperature distribution was obtained from CIRS far- and mid-infrared spectra of Saturn between 10 and 1400 cm$^{-1}$ at 15 cm$^{-1}$ spectral resolution and at a spatial resolution of 1-2° latitude. CIRS data at low emission angles were selected at observation times, latitudes and longitudes matching those of VIMS data. A two-step retrieval strategy as described by Fletcher *et al.* (2007) was adopted here to determine Saturn's thermal structure in the troposphere and stratosphere. Firstly, both the temperature structure and *para*-hydrogen distribution were retrieved from the FP1 detector covering the wavelength range 10-500 cm$^{-1}$ sensitive to pressure levels between 200 and 800 mbar. The thermal structure can be mapped over the planet's area with a longitudinal resolution ranging between 6° and 8°. The reference atmosphere was updated with the retrieved temperature profile and *para*-hydrogen distribution. Since the far-infrared spectra have a lower spatial resolution and are sensitive

[1] Atmospheric properties are not expected to undergo significant variations over the width of pressure levels chosen for the analysis of Saturn's near-infrared spectra

to the *para*-hydrogen distribution, they were used first to derive the thermal structure. The detectors FP3 and FP4 from 500-1400 $cm^{-1}$ were used to refine the temperature stucture at 60-200 mbar and 1-3 mbar. Because of the higher spatial resolution in FP3 and FP4, the second step implies that temperature profiles are finally obtained at a 1-2° latitudinal resolution. However, Saturn's spectra at near-infrared wavelengths covered by the VIMS instrument are sensitive to higher pressure levels up to a few bars. Below the radiative-convective boundary at 400-500 mbar, the heat is transferred upwards convectively and the variation of temperature with altitude for a dry atmosphere is given by

$$\frac{dT}{dz} = -\frac{g}{c_p} = -\Gamma_d$$

where $g$ is the gravitational acceleration, $c_p$ the specific heat capacity at constant pressure and $\Gamma_d$ the dry adiabatic lapse rate. The dry adiabatic lapse rate is approximately equal to 0.70K.$Km^{-1}$ on Saturn (Yung, 1998)[2]. If clouds are present in the troposphere, the temperature decreases more slowly with altitude due to the release of latent heat of vaporisation (or sublimation) by the condensing species. For a saturated atmosphere, the equation above is modified as follows:

$$\frac{dT}{dz} = -\frac{g}{c_p}\frac{\left[1+\frac{1}{RT}\sum L_i x_i\right]}{\left[1+\frac{1}{\bar{m}c_p T^2}\sum \frac{L_i^2 x_i}{R}\right]} = -\Gamma_s \text{ (Andrews, 2000; Atreya, 1986)}$$

where $L_i$ and $x_i$ are respectively the molar latent heat and the saturated volume mixing ratio of the $i^{th}$ condensing component, $T$ the temperature, $R$ the molar gas constant and $\bar{m}$ the mean molecular weight of the atmosphere (excluding condensates). On Saturn, differences between the dry and saturated adiabatic lapse rates are very small and so the variation of temperature with height can be assumed to be equal to $-\Gamma_d$. The saturated adabiatic lapse rates for an ammonia and ammonium hydrosulphide clouds are respectively equal to 0.68 and 0.67 K.$Km^{-1}$ (Sánchez-Lavega, 2010), and so they are indeed very similar to the dry adiabatic lapse rate. Therefore, the tropospheric temperature profile below the 800 mbar level was set to follow a dry adiabatic lapse rate. A specific heat mean value of 10.658 J·$Kg^{-1}$ (Irwin, 2009) was chosen for the extrapolation of Saturn's tropospheric temperature below the 800-mbar pressure level.

[2]In an atmosphere dominated by $H_2$ such as Saturn, the adiabatic lapse rate depends on the equilibrium between the ortho- and para- states. If they are in equilibrium at the local temperature, an equilibrium adiabat will be observed. On Saturn, it has been suggested that the ortho-para equilibration time is larger than the equilibration time of adiabatic parcel displacements, leading to a frozen equilibrium adiabat which (Bezard *et al.*, 1985). The lapse rate is given here for a frozen equilibrium adiabat which exceeds the value for an equilibrium adiabat

**Gaseous composition**

Gases in Saturn's troposphere attenuate the warm thermal radiation emitted at deeper atmospheric levels. The composition of gaseous components, their spatial distribution and absorption coefficients need to be integrated into the radiative transfer algorithm. The following 9 gases are expected to be radiatively active in Saturn's atmosphere and so are included in the reference atmospheric model of the planet: methane ($CH_4$), methane's first isotope ($^{13}CH_4$), methane's second isotope ($CH_3D$), water ($H_2O$), phosphine ($PH_3$), ammonia ($NH_3$), arsine ($AsH_3$), carbon monoxide (CO) and germane ($GeH_4$). Molecular hydrogen ($H_2$), hydrogen deuteride (HD), helium (He), ethane ($C_2H_6$) and acetylene ($C_2H_2$) were also included in the reference model for their relatively high abundances in Saturn's troposphere and stratosphere although they don't absorb thermal radiation in the 5-$\mu$m window. The helium-to-hydrogen ratio was set to 0.135 (Conrath and Gautier, 2000). Phosphine is the main tropospheric absorber in the 4.6-5.1 $\mu$m spectral range, and as a result models of Saturn's thermal emission are highly sensitive to the vertical distribution of phosphine. The phosphine volume mixing ratio was set to the constant value of $6.4\times10^{-6}$ up to the 0.55-bar pressure level (Fletcher *et al.*, 2009a). At lower pressures, phosphine is depleted due to photolysis with an estimated fractional scale height of 0.27 (Fletcher *et al.*, 2009a). A few other tropospheric gases including ammonia, arsine, germane, deuterated methane, carbon monoxyde, and water also contribute to Saturn's 5-$\mu$m window although less significantly than phosphine. A deep ammonia volume mixing ratio of $1\times10^{-4}$ was assumed in Saturn's reference atmosphere (Burgdorf *et al.*, 2004). Ammonia is expected to condense above the 2-bar pressure level and so the ammonia volume mixing ratio at lower pressures was set to follow a saturated vapour pressure profile. Photolysis decreases upper tropospheric ammonia abundances even further at pressures lower than 0.3 bar, and so the ammonia vertical profile was extrapolated linearly from the saturated vapour profile above the 0.3-bar level to represent this. Methane and its two isotopes are well-mixed at the pressure levels considered here, and so constant volume mixing ratios are assumed in Saturn's reference atmosphere. Methane, its first isotope $^{13}CH_4$ and second isotope $CH_3D$ volume mixing ratios were set respectively to $4.7\times10^{-3}$, $5.1\times10^{-5}$ and $3.0\times10^{-7}$ (Fletcher *et al.*, 2009b). The other minor gaseous absorbers are also expected to be well-mixed at the pressure levels considered here, and so they were included in the model with a constant volume mixing ratio at all altitudes. Minor constituents include water, arsine, carbon monoxide and germane

for which volume mixing ratios were set to $1.8\times10^{-7}$ (de Graauw *et al.*, 1997), $2.6\times10^{-9}$, $1.0\times10^{-9}$ and $3.5\times10^{-10}$ (Noll and Larson, 1990) respectively. Ethane and acetylene were also included in the reference atmosphere since they have the highest volume mixing ratios among hydrocarbons right after methane, although they are not expected to absorb thermal radiation. The gas vertical profiles between 0.01 and 10 bar as set up in Saturn's reference atmosphere are shown in Fig. 4.3 (Noll and Larson, 1990; de Graauw *et al.*, 1997; Conrath and Gautier, 2000; Burgdorf *et al.*, 2004; Fletcher *et al.*, 2009a).

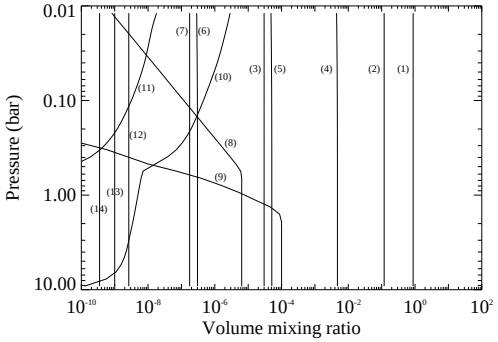



Figure 4.3: Reference gaseous composition in Saturn's troposphere and stratosphere between 10 mbar and 10 bar. The following gaseous components are included into the radiative transfer model: 1/ Hydrogen ($H_2$), 2/ Helium (He), 3/ hydrogen deuteride (HD), 4/ methane ($CH_4$), 5/ methane's first isotope ($^{13}CH_4$), 6/ methane's second isotope ($CH_3D$), 7/ water ($H_2O$), 8/ phosphine ($PH_3$), 9/ ammonia ($NH_3$), 10/ ethane ($C_2H_6$), 11/ acetylene ($C_2H_2$), 12/ arsine ($AsH_3$), 13/ carbon monoxide (CO) and 14/ germane ($GeH_4$).

In the radiative transfer equation, gas abundances are multiplied by their extinction coefficients $k_{\tilde{\nu}}(s)$ to determine the gaseous opacities in Saturn's troposphere and stratosphere (see section 3.1.1). Radiatively active gases absorb near-infrared radiation and so contribute to the shape of Saturn's thermal emission spectrum. Note that Rayleigh scattering can be ignored in the model since it is negligible at 5 $\mu$m (Del Genio *et al.*, 2009). The gas absorption coefficients between 4.6 and 5.1 $\mu$m were extracted from line databases in the 70-300 K temperature range for pressure levels between $3\times10^{-4}$ mbar and 20 bar equally spaced in logarithm scale ($\Delta\log_{10}p \sim 0.4$). The GEISA2003 (Jacquinet-Husson *et al.*, 2005) database was used for phosphine, ammonia and germane. Line data for carbon monoxide, water, methane and methane's first two isotopes were extracted from the HITRAN2008 database (Rothman *et al.*, 2009). Arsine line data were not available in the GEISA and HITRAN databases and so line data from Dana *et al.* (1993) and Mandin (1995) were used instead.

Gaseous opacities in Saturn's troposphere at the 3-bar pressure level, where most gaseous absorption occurs, are shown in Fig. 4.4 for radiatively active gases. The relative contribution of tropospheric gases to Saturn's 5-$\mu$m window discussed previously can be interpreted in terms of gas opacity variations. Phosphine dominates absorption of thermal radiation across the 4.6-5.1 $\mu$m wavelength range. Arsine, carbon dioxide and methane's second isotope ($CH_3D$) have typical opacities at shorter wavelengths around ten times smaller than the phosphine opacities. Their opacities above 4.9 $\mu$m, where most of thermal radiation is emitted, are completely negligible. Ammonia opacities have a similar order of magnitude as $CH_3D$, however ammonia absorbs throughout Saturn's 5-$\mu$m window. Water, germane, arsine, carbon monoxide, methane, $^{13}$CH4 have either only a few absorption lines or low opacities between 4.6 and 5.1 $\mu$m and so are likely to contribute very little to Saturn's thermal emission spectra.

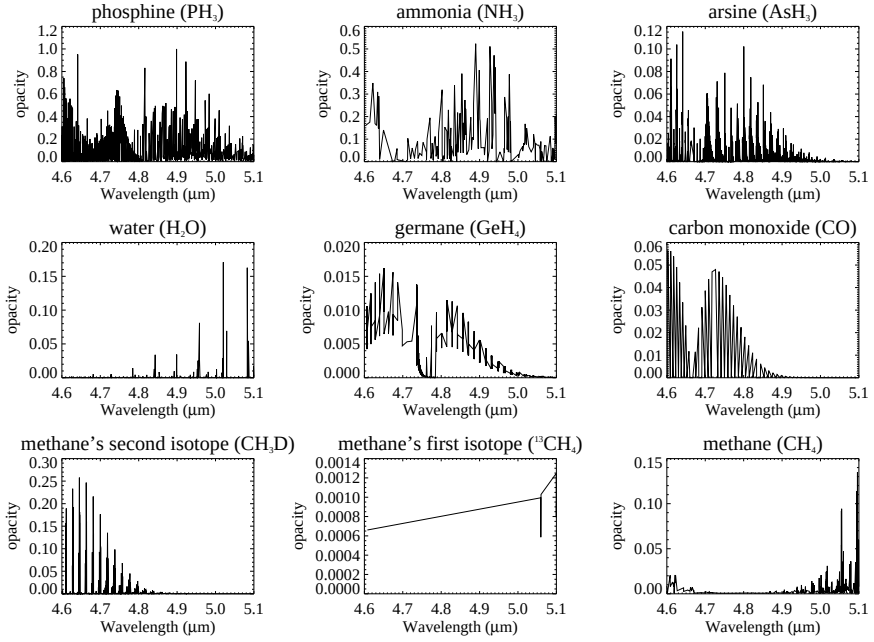



Figure 4.4: Absorption spectra between 4.6 and 5.1 $\mu$m of radiatively active gases in Saturn's troposphere at 3 bar. The spectra of phosphine, ammonia, arsine, water, germane, carbon monoxide, methane's second isotope, methane's first isotope and methane are plotted with a spectral resolution of $3.8\times10^{-4}$, $2.8\times10^{-3}$, $1.4\times10^{-4}$, $8.4\times10^{-4}$, $8.9\times10^{-4}$, $5.0\times10^{-3}$, $5.9\times10^{-4}$, $5.5\times10^{-2}$ and $1.1\times10^{-3}$ $\mu$m respectively. All spectra were normalised to the maximum gas opacity due to phosphine absorption at 4.9 $\mu$m. The contribution weighting functions for a cloud-free atmosphere peak in the troposphere between 1 and 5 bar, therefore the absorption spectra are calculated at the 3-bar pressure level for a 10 km path where most absorption occurs in Saturn's 5-$\mu$m window. Lina data are extracted from the GEISA2003 and HITRAN2008 databases except for arsine line data which are obtained from Dana *et al.* (1993) and Mandin (1995).

### Clouds

Aerosols are expected to form in Saturn's troposphere and stratosphere from thermochemical and photochemical models. Saturn's emitted radiance in the 4.6-5.1 $\mu$m wavelength range is particularly sensitive to clouds located in the troposphere of the planet (Baines *et al.*, 2006; Baines *et al.*, 2009; Choi *et al.*, 2009) although it was mentioned that Fletcher *et al.* (2011) obtained a better fit to VIMS observations by adding a thin haze layer on top of the tropospheric clouds. Cloud properties, as defined in Saturn's reference model, are reviewed below.

*i.:* Vertical structure: two models were tested in the analysis of Saturn's near-infrared spectra, one compact and one extended structures for the cloud. For the compact cloud model, the aerosol density is zero everywhere except at one pressure level of width $\Delta\log_{10}p \sim 0.076$. The retrieval code derives the cloud opacity at this specific pressure level that provides the best fit to VIMS observations. For the extended cloud model, there are two free parameters, the base pressure and the extension of the cloud. The extension above the pressure level at which condensation occurs is defined by the cloud scale height $H_c$, so that the vertical distribution of aerosols $\rho(z)$ in particles per gram varies as follows:

$$\begin{cases} \rho(z) = \rho_0 \exp\left[-\dfrac{(z-z_0)}{H_c}\right] & ; z \geq z_0 \\ \rho(z) = 0 & ; z < z_0 \end{cases}$$

where $z_0$ and $\rho_0$ are respectively the cloud base altitude and density. Either the actual value of the cloud scale height or its ratio to the bulk atmosphere's scale height (referred to as the fractional scale height) can be used to parametrise the cloud structure in NEMESIS. In the latter case, the cloud scale height is divided by the scale height of the Saturnian atmosphere $H_a$ given by

$$H_a = \frac{RT}{\bar{m}g},$$

where R is the molar gas constant constant, $T$ the temperature, $m$ the mean molecular weight of the atmosphere excluding condensates, and $g$ the gravitational acceleration. Note that NEMESIS can also retrieve a continuous aerosol density profile from an *a priori* profile where *a priori* values of

the cloud density must be given at each pressure level. There are 39 pressure levels in the reference atmosphere, leading to a significant increase of the free parameter number in the continuous cloud model in comparison with the compact and extended cloud models. In addition, the extended cloud model is consistent with thermochemical theories. The compact cloud model can be seen as a first approximation of the extended model where all the aerosol opacity would be concentrated at the cloud base. In conclusion, the compact and extended cloud models are preferred to the continuous cloud model for the study of Saturn's tropospheric clouds.

*ii.:* Composition: Retrievals were performed assuming that clouds are made of either ammonia or ammonium hydrosulphide aerosol particles since both molecules are expected to condense in thermodynamical models (see Fig. 1.4). The VIMS instrument cannot sound at pressure levels below which gases absorb the warm thermal emission. As seen in Fig. 4.2, the contribution weighting functions for a cloud-free atmosphere peak between 1 and 5 bar, and so Saturn's 5-$\mu$m window is not sensitive to the water ice cloud or water–ammonia solution cloud. The sensitivity of Saturn's thermal emission spectra to the haze layer was tested by assuming a third cloud composition consisting of grey particles, implying that the absorption and extinction coefficients are independent of wavelengths.

*iii.:* Interaction radiation-matter: In addition to absorption, scattering of infrared radiation by aerosol particles might also contribute to Saturn's thermal emission spectra. The effect of scattering was tested by assuming that cloud particles were either scattering or purely absorptive. A Mie scattering model was used to generate the cloud absorption coefficients, single scattering albedos and scattering phase functions at all wavelengths. The combined Henyey-Greenstein parameters were fitted to the Mie phase function. The complex refractive indexes and aerosol particle sizes for each cloud composition must be known in order to calculate the Mie phase function. The refractive indexes for ammonia (Martonchik *et al.*, 1984) and ammonium hydrosulphide (Howett *et al.*, 2007) are extracted from laboratory measurements. The Henyey-Greenstein parameters and complex refractive indexes were calculated at each wavelength $\lambda$ between 4.6 and 5.1 $\mu$m with $\Delta\lambda = 0.05$ $\mu$m, and for the following aerosol particle sizes: 100 nm, 200 nm, 300 nm, 400 nm, 500 nm, 600 nm, 700 nm, 800 nm, 900 nm, 1 $\mu$m, 2 $\mu$m, 3 $\mu$m, 4 $\mu$m, 5 $\mu$m, 6 $\mu$m, 7 $\mu$m, 8 $\mu$m, 9 $\mu$m and 10 $\mu$m. A variance of 0.05 (Fletcher *et al.*, 2011) is adopted in the standard gamma size distribution (see section 3.3 for the mathematical equation of the distribution). A single scattering albedo equal to 0.95 and an isotropic phase function, as suggested by Fletcher *et al.* (2011), was assumed for the grey aerosol model.

### 4.2.2 Sensitivity analysis

Sensitivity tests of Saturn's 5-$\mu$m window to atmospheric parameters were carried out to determine which parameters to retrieve with NEMESIS. The retrieval algorithm can retrieve simultaneously the aerosol opacity and gas abundances from Saturn's thermal emission spectra. A typical nightside spectrum was extracted from VIMS cube CM1524383985 measured on 22 April 2006 at the equator and low emission angle (see Fig. 4.5). Four different retrieval strategies, referred to as models (a), (b), (c) and (d), are considered here. In the spectral range considered for this analysis, Saturn's spectrum is sensitive to tropospheric gases in the 1-5 bar pressure range. At such pressure levels, the absorbing gases have homogeneous distribution, therefore scaling factors to their *a priori* values in the deep troposphere were retrieved from the VIMS thermal emission spectrum. Phosphine is the main gaseous absorber in the 4.6-5.1 $\mu$m wavelength, even though other minor components might contribute to Saturn's 5-$\mu$m window. In addition to tropospheric gases, aerosols also absorb and scatter the warm thermal emission, and so a cloud layer is included in models (b), (c) and (d). The cloud-free assumption is finally considered in model (a). For each of the four models, both non-scattering and scattering conditions were tested where Rayleigh and Mie scattering were assumed for gases and aerosols respectively.

In model (a), no aerosols are included in the reference atmosphere and so only gases are assumed to absorb and scatter thermal radiation. Since phosphine is the main source of gaseous opacity, a scaled factor of its vertical profile is retrieved with NEMESIS. A deep volume mixing ratio for phosphine equal to 193 $\pm$ 67 ppm is retrieved in the non-scattering case whereas a value of 212 $\pm$ 67 ppm is retrieved in the scattering case. Previous studies of phosphine distribution in Saturn's troposphere concluded on a volume mixing ratio of a few parts-per-millions (Fletcher *et al.*, 2009a, 2011), in contradiction with the values retrieved in model (a). Furthermore, this model fails at matching VIMS measurements and so a model based only on gaseous absoption by phosphine cannot account for Saturn's thermal emission at 5 $\mu$m. A different version of the cloud-free model (a) was tested by including ammonia as a second gaseous absorber. Unrealistic volume mixing ratios of both phosphine and ammonia were retrieved with NEMESIS in that case, and the synthetic spectrum also could not match the obsevations. If the other minor gases are added to the cloud-free model, that is to say arsine, carbon monoxide and methane's second isotope, the conclusions are similar to model

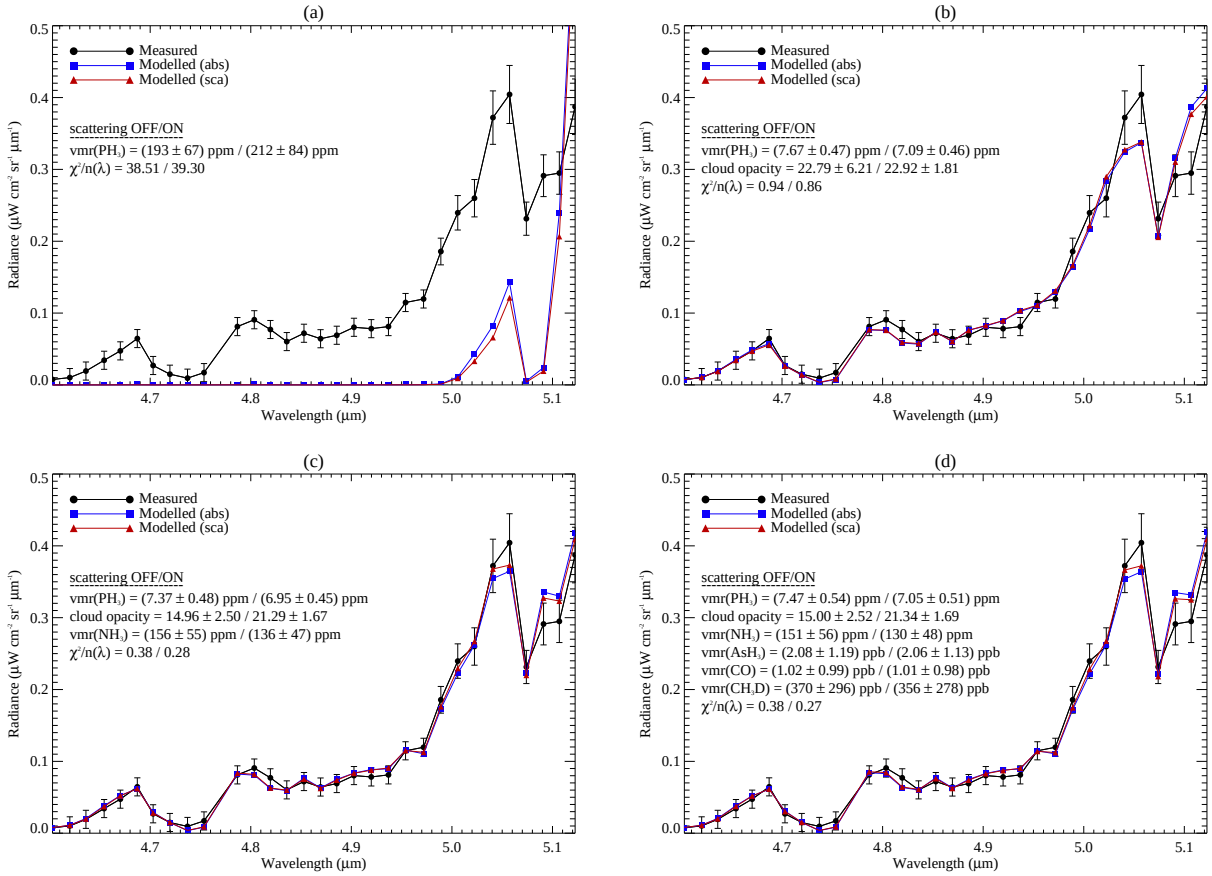



Figure 4.5: Sensitivity analysis of Saturn's 5-$\mu$m window to retrieved atmospheric parameters in NEMESIS. Saturn's nightside spectrum, extracted from VIMS spectral cube CM1524383985, was measured on 22 April 2006 at equator and at 10° emission angle. NEMESIS was used here to retrieve: (a) phosphine, (b): phosphine and cloud opacity, (c): phosphine, cloud opacity and ammonia, (d): phosphine, cloud opacity, ammonia, arsine, carbon monoxide and $CH_3D$. The retrieved parameters, that is to say the deep volume mixing ratios of absorbing gases and the cloud optical depth at 5 $\mu$m, as well as the $\chi^2/N_\lambda$ values are also shown here. These tests were carried out for both purely absorptive and scattering opacity sources. The retrieval of aerosol opacity and abundances of phosphine and ammonia in model (c) provided the best fit to VIMS thermal emission spectrum. The model (d) did not lead to any improvement of the former model and so model (c) was finally adopted as a retrieval strategy.

(a). In conclusion, aerosols must be included in the atmospheric model in order to fit VIMS thermal emission spectra.

In model (b), a very simple cloud model was set-up consisting of a compact ammonia cloud with a particle size of 1 $\mu$m and with a variable pressure base. The scaling factor of phosphine volume mixing ratio and cloud opacity were retrieved simultaneously, varying the ammonia cloud pressure base between 0.01 and 10 bar. The best fit to VIMS data was obtained for a cloud base at 2.7 bar, and a phosphine volume mixing ratio of 7.67 $\pm$ 0.47 ppm and 7.09 $\pm$ 0.46 ppm respectively in the non-scattering case and in the scattering case. As can be seen in Fig. 4.5, adding a thin cloud layer

greatly improved the agreement to VIMS observations confirming that aerosols must be included in the model as expected. By comparison with model (a), the The goodness-of-fit ($\chi^2/N_\lambda$ with $N_\lambda$ the number of wavelengths) values decreases from 38.51 to 0.94 in the non-scattering case, and from 39.30 to 0.86 in the scattering case.

The next step in the sensitivity analysis is to estimate the effects of gaseous components other than phosphine. As discussed in section 4.2.1, ammonia is the second gaseous absorber after phosphine most likely to contribute to Saturn's thermal emission spectrum. Therefore, ammonia, phosphine and cloud opacity were simultaneously retrieved in model (c). The inclusion of ammonia in the model led to a closer fit to the measured spectrum especially at longer wavelengths. The $\chi^2/N_\lambda$ value drops to 0.38 in the non-scattering case and 0.28 in the scattering case. As shown in Fig. 4.3, the phosphine volume mixing ratio in the reference atmosphere is constant in the troposphere up to a "knee" at 0.55 bar, and decreases above this pressure level with a fractional scale height of 0.27. Tropospheric gases absorb in the 1-5 bar pressure range, and so Saturn' s 5-$\mu$m window is unlikely to be sensitive to the gas distibution above the pressure level of the knee. However, phosphine is the main gaseous absorber and so the effect on Saturn's thermal emission spectra of both the pressure knee and the vertical distribution above the knee was tested by retrieving a parametrised abundance profile. In the "parametrised" model, the deep phosphine volume mixing ratio, the pressure knee and the fractional scale height, as well as the deep ammonia volume mixing ratio and cloud opacity were retrieved for both a purely absorptive and scattering clouds. The retrieved parameters in the parametrised model are compared to model (c), or "scaled" model, in Table 4.1. The $\chi^2/N_\lambda$ values obtained for the parametrised model are nearly identical to the scaled model, therefore retrieving the pressure knee and the fractional scale height in addition to the other parameters does not improve the fit to VIMS data. Also the retrieved values of phosphine and ammonia volume mixing ratios, and the cloud opacity are similar within the retrieval errors for both models. Finally, the pressure knee and fractional scale height have large retrieval errors ranging between 83 and 97%. This is due to the lower sensitivity of Saturn's 5-$\mu$m window to gaseous absorption above the 1-bar pressure level. The retrieved value of the fractional scale height is very similar to the 0.27 value assumed in the reference model. However, there are significant variations in the retrieved values of the pressure knee, between 0.37 in the non-scattering case and 0.77 in the scattering case. Note that Fletcher *et al.* (2011) retrieved from VIMS spectra in the 4.6-5.1 $\mu$m spectral range a pressure knee even

deeper at approximately 1.3 bar. In addition to the large retrieval errors of the pressure knee and the fractional scale height, the retrieval errors on the deep phosphine volume mixing ratio are also larger than in the scaled model, especially in the scattering case. Therefore increasing the number of free parameters in the phosphine profile raises the uncertainities on the only parameter which can be accurately determined in the 5-$\mu$m window, the deep volume mixing ratio. On the other hand, the pressure knee and fractional scale height assumed in the scaled model are retrieved from CIRS mid- and far-infrared spectra, which are sensitive to pressure levels above 0.8 bar (Fletcher *et al.*, 2009a). In conclusion, the pressure knee and fractional scale height are set up to their values derived from CIRS measurements equal to 0.55 bar and 0.27 respectively, and a scale factor of the phosphine vertical profile is retrieved with NEMESIS in the analysis of Saturn's 5-$\mu$m window.

| | | NON-SCATTERING | | SCATTERING | |
|---|---|---|---|---|---|
| | | Parametrised | Scaled | Parametrised | Scaled |
| | $\chi^2/N_\lambda$ | 0.38 | 0.38 | 0.27 | 0.28 |
| Phosphine | vmr (ppm) | 7.13±0.58 | 7.37±0.48 | 7.53±1.41 | 6.95±0.45 |
| | pressure knee (bar) | 0.37±0.36 | 0.55 | 0.77±0.64 | 0.55 |
| | fractional scale height | 0.23±0.22 | 0.27 | 0.22±0.21 | 0.27 |
| Ammonia | vmr (ppm) | 160±58 | 156±55 | 132±46 | 136±47 |
| Cloud | OD at 5 $\mu$m | 14.78±2.44 | 14.96±2.50 | 21.39±1.69 | 21.29±1.67 |

Table 4.1: Effects of the parametrisation of phosphine vertical profile on Saturn's 5-$\mu$m window. In the "parametrised" model, the deep volume mixing ratio, pressure knee and fractional scale height of phosphine, as well as the deep ammonia volume mixing ratio and the ammonia cloud optical depth at 5 $\mu$m, are retrieved with NEMESIS in the non-scattering and scattering cases. The retrieved parameters are compared to the "scaled" model where a scale factor of the phosphine vertical profile as defined in section 4.2.1 is derived from Saturn's thermal spectrum.

In model (d), arsine, carbon monoxide and methane's second isotope were added to the list of retrieved parameters. The retrieved quantity for phosphine, ammonia and aerosols are similar to model (c) within the retrieval errors and model (d) did not improve the fit to VIMS observations. Water, germane, methane and methane's first isotope have even smaller opacities than phosphine and ammonia. Furthermore, their abundances can only be retrieved from Saturn's thermal emission spectra with high relative errors between 55 and 97%. This applies to both purely absorptive and scattering gases and aerosols.

All spectra between 39.4°S and 67.3°N at the lowest emission angles were extracted from the

VIMS spectral cube CM1524383985, and a similar sensitivity analysis carried out for each spectrum. Although the retrieved values of cloud opacity and gaseous volume mixing ratios vary with latitude, similar conclusions on the validity of model (c) can be drawn. In conclusion, the model (c) was therefore adopted for all viewing geometries as a retrieval strategy in order to study the cloud properties and distribution of phosphine and ammonia in Saturn's troposphere and stratosphere.

## 4.3 Degeneracies of Saturn's 5-$\mu$m window

NEMESIS is capable of retrieving atmospheric properties from one or many spectra[3]. Therefore, the same atmospheric parameter can be derived from a set of different measurements. In particular, the cloud opacity and gas abundance can be retrieved from VIMS spectra measured for various observation geometries. In this section, the analysis of individual Saturnian thermal emission spectra is carried out with NEMESIS for various physical and optical properties of tropospheric and stratospheric aerosols. The atmospheric properties are thus retrieved for one specific geometry of observation. Nightside spectra were extracted from the VIMS cube CM1524383985 measured on 22 April 2006 and covering most southern and northern latitudes (VIMS image CM1524383985 at 5.06 $\mu$m is shown in Fig. 4.1).

Ten spectra measured at low emission angles and along the same meridian were selected at the latitudes of 30°S, 20°S, 10°S, 0°, 10°N, 20°N, 30°N, 40°N, 50°N and 60°N. Initially, one compact ammonia cloud, made of purely absorptive particles, with variable base pressure and aerosol particle size, was chosen as the cloud model. The goodness-of-fit was found to be slightly better in the scattering case, however synthetic spectra calculated for non-scattering conditions still match VIMS spectra quite well within the measurement errors (see Fig. 4.5). Therefore both scattering and non-scattering conditions are tested in this section. The base pressure and aerosol particle size were allowed to vary respectively between 0.01 and 10 bar, and 0.1 and 10 $\mu$m. The cloud opacity and the volume mixing ratios of phosphine and ammonia were retrieved with NEMESIS from each thermal emission spectrum at a given latitude. The goodness-of-fit was calculated by the retrieval algorithm after the last iteration for all cloud properties. Values of $\chi^2/N_\lambda$ above 5.0 can be omitted since the

[3]The retrieval algorithm is built-up so that the number of spectral points is limited to an upper value, which can be modified in the code. As a result, what matters in NEMESIS is the total number of spectral points instead of the number of spectra.

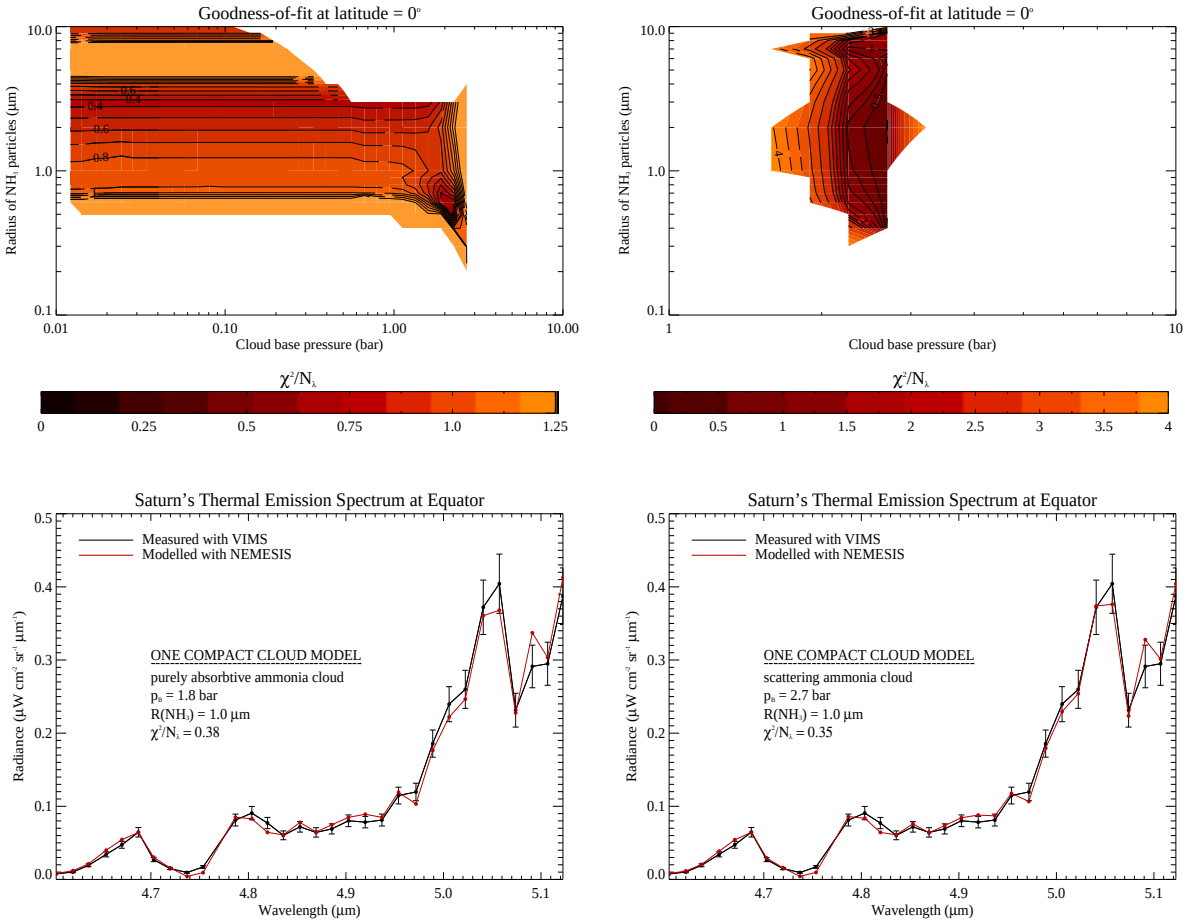
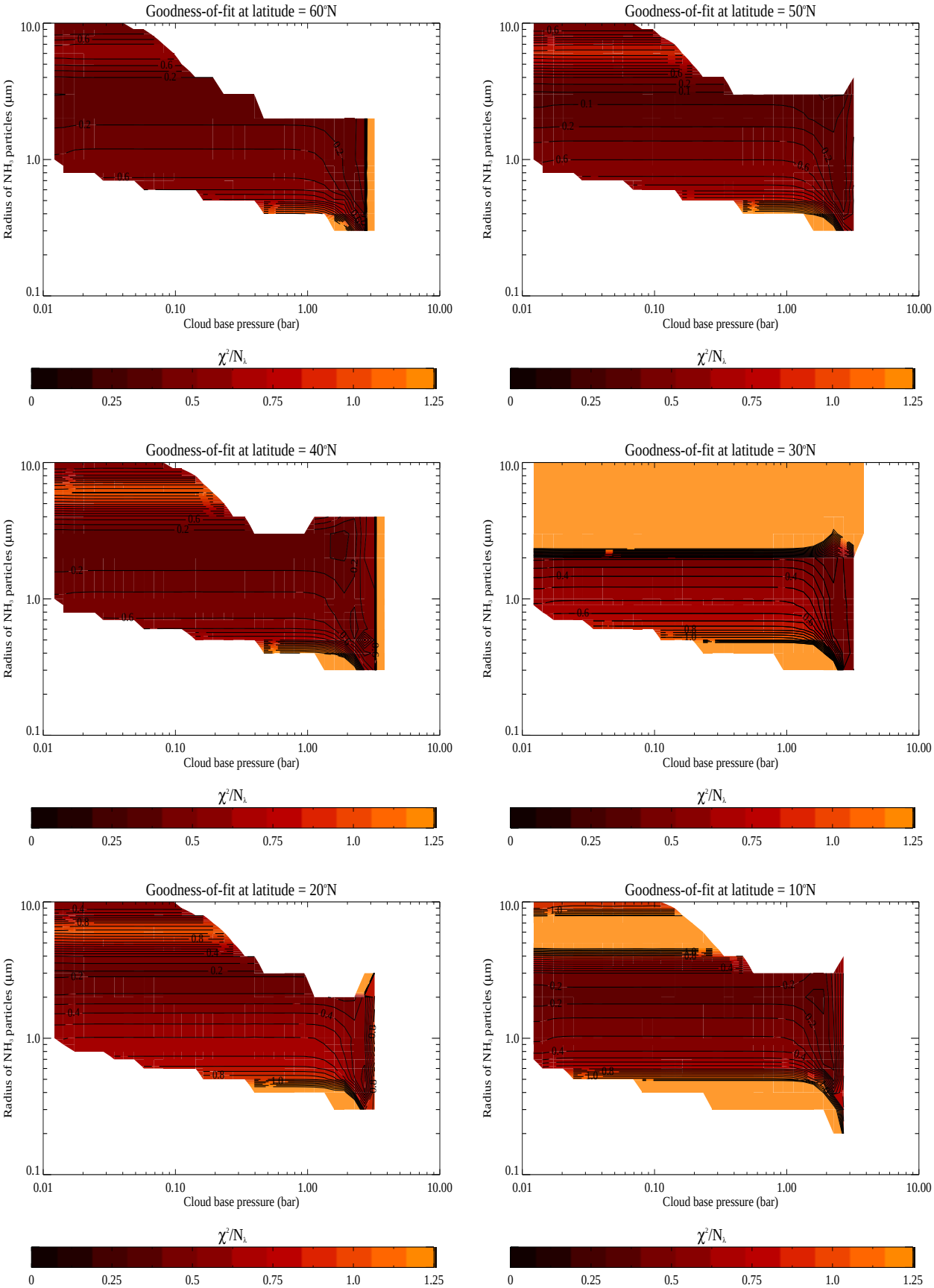



Figure 4.6: Retrieval of cloud base pressure and aerosol particle size for a purely absorptive (*left*) and scattering (*right*) ammonia cloud. The spectrum used here was extracted from the VIMS cube CM1524383985 (see Fig. 4.1), and measured at a latitude of $0.23° \pm 1.31°$, longitude of $235.94° \pm 1.62°$ and emission angle of $0.93° \pm 1.78°$. The results are shown for one compact cloud made of ammonia ice. The two figures at the top correspond to the goodness-of-fit [$\chi^2$/(number of wavelengths)] as a function of the cloud base pressure and aerosol particle size. Optimum fits to the observations are obtained for typical $\chi^2/N_\lambda$ values $\lesssim 1.0$, so values above 5.0 are omitted here. The synthetic and observed spectra are shown in the lower panels for optimum values of the cloud pressure level ($P_b = 1.8$ bar in the non-scattering case and $P_b = 2.7$ bar in the scattering case) and particle size (radius = 1 $\mu$m).

corresponding synthetic spectra fail at matching VIMS near-infrared observations. The goodness-of-fit as a function of the cloud base pressure and aerosol particle size is shown in Fig. 4.6 for this purely absoptive cloud at the equator. Many cloud properties are found to provide synthetic spectra in good agreement with VIMS data within the measurement errors. The synthetic spectrum for an ammonia cloud at 1.8 bar in the non-scattering case and 2.7 bar in the scattering case, and for an aerosol particle size of 1 $\mu$m is compared to VIMS spectrum in Fig. 4.6. The modelled radiances match the measured radiances at most spectral points within the error bars. The same conclusion holds for all the cloud

properties associated to low $\chi^2/N_\lambda$ shown in the goodness-of-fit map. In particular, the cloud base pressure is not constrained and any aerosol layer located at a pressure higher than 3 bar provides a good fit to the observations. The aerosol particle size is also poorly constrained and any particle size of about a few micrometers is associated to low $\chi^2/N_\lambda$ values. Smaller particles with sizes down to 300 nm in deeper tropospheric clouds are also found to provide a good match to the observations, while larger particles are associated with aerosol layers at higher altitudes. Although the retrieved values of the cloud opacity and volume mixing ratios of phosphine and ammonia vary with latitude, similar goodness-of-fit maps are obtained for the thermal emission spectra at other latitudes between 30°S and 60°N as it can be seen in Fig. 4.7.

A similar analysis as above was carried out for a scattering compact ammonia cloud. The goodness-of-fit and a typical modelled spectrum for low $\chi^2/N_\lambda$ values at the equator are also compared to the non-scattering cloud case in Fig. 4.6. The cloud base pressure is much more constrained in the scattering case and optimum fits to VIMS data are obtained for a tropospheric cloud based between 2 and 3 bar. The aerosol particle size is however less constrained, and any radius ranging from 400 nm to 10 $\mu$m is associated to low $\chi^2/N_\lambda$ values. The modelled spectra are shown for a cloud base pressure at 1.8 bar and aerosol particle size of 1 $\mu$m in the scattering case, to allow direct comparison with the non-scattering case. The fit to the observations is slightly better at longer wavelengths for a scattering cloud. However the modelled spectrum for a purely absorptive cloud still matches the VIMS spectrum quite well within the measurement errors, and so a non-scattering cloud model cannot be ruled out. The optical depth, phosphine and ammonia volume mixing ratios retrieved with NEMESIS depends on whether the cloud is scattering or not. The optical depths at 5 $\mu$m integrated over the optical path, and the deep volume mixing ratios of phosphine and ammonia are respectively estimated to be $7.7 \pm 0.5$, $(5.59 \pm 0.36)\times10^{-6}$, $(2.17 \pm 0.83)\times10^{-4}$ for a purely absorptive cloud at 1.8 bar with 1-$\mu$m aerosol particles. The same cloud model, but with scattering aerosol particles, leads to an optical depth of $11.3 \pm 0.4$, a phosphine volume mixing ratio of $(4.16 \pm 0.23)\times10^{-6}$ and an ammonia volume mixing ratio of $(1.63 \pm 0.21)\times10^{-4}$.


Goodness-of-fit at latitude = 60°N
Goodness-of-fit at latitude = 50°N
Goodness-of-fit at latitude = 40°N
Goodness-of-fit at latitude = 30°N
Goodness-of-fit at latitude = 20°N
Goodness-of-fit at latitude = 10°N
Radius of NH3 particles (μm)
Cloud base pressure (bar)
χ²/Nλ
10.0
1.0
0.1
0.01
0.10
1.00
10.00
0
0.25
0.5
0.75
1.0
1.25

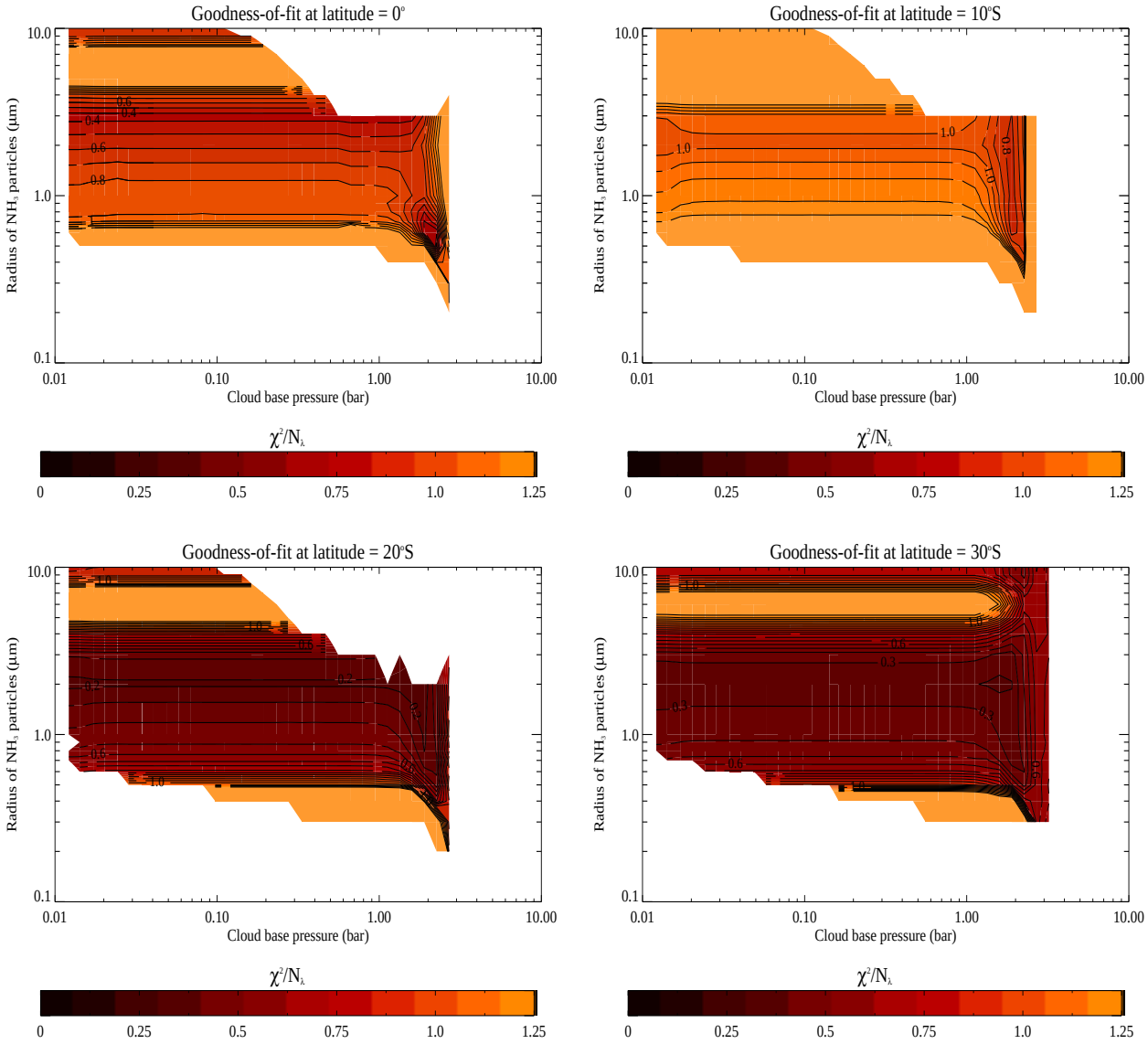



Figure 4.7: Retrieval of cloud base pressure and aerosol particle size for a purely absorptive ammonia cloud at various latitudes between 30°S and 60°N. All spectra used were extracted from the VIMS spectral cube CM1524383985. The goodness-of-fit maps are shown for $\chi^2/N_\lambda$ values below 5.0 as a function of the cloud base pressure and aerosol particle size. The 60°N-spectrum was measured at a latitude of 59.04° ± 2.63°, a longitude of 183.96° ± 3.43° and an emission angle of 68.55° ± 4.39°. The 50°N-spectrum was measured at a latitude of 49.93° ± 2.05°, a longitude of 227.03° ± 3.21° and an emission angle of 50.82° ± 4.12°. The 40°N-spectrum was measured at a latitude of 39.05° ± 1.89°, a longitude of 228.38° ± 2.64° and an emission angle of 39.80° ± 3.31°. The 30°N-spectrum was measured at a latitude of 30.20° ± 1.71°, a longitude of 229.93° ± 2.43° and an emission angle of 30.80° ± 3.01°. The 20°N-spectrum was measured at a latitude of 19.54° ± 1.67°, a longitude of 231.93° ± 2.32° and an emission angle of 19.94° ± 2.86°. The 10°N-spectrum was measured at a latitude of 9.96° ± 1.48°, a longitude of 233.81° ± 1.97° and an emission angle of 10.17° ± 1.98°. The latitudinal spectrum was measured at a latitude of 0.23° ± 1.31°, a longitude of 235.94° ± 1.62° and emission angle of 0.93° ± 1.78°. The 10°S-spectrum was measured at a latitude of -10.84° ± 1.53°, a longitude of 238.56° ± 2.01°, and an emission angle of 11.08° ± 2.13°. The 20°S-spectrum was measured at a latitude of -20.52° ± 1.76°, a longitude of 240.43° ± 2.54° and an emission angle of 20.96° ± 3.02°. The 30°S-spectrum was measured at a latitude of -29.71° ± 1.98°, a longitude of 242.27° ± 2.65° and an emission angle of 30.33° ± 3.43°.

In the radiative transfer equation, the optical depth is calculated at each pressure level by multiplying the gas abundances and absorption coefficients with the optical path. In the scattering case, the optical path is slightly longer than if only absorption is assumed in the model. As a result, lower gas abundances are necessary in the scattering case in order to fit the observations, leading to lower volume mixing ratios than in the non-scattering case. Note that the retrieved values depend also on the cloud base pressure and aerosol particle size. Both a purely absorptive and scattering clouds were found to fit the observations for a wide range of cloud properties, resulting in different retrieved values of the cloud optical depth, and volume mixing ratios of phosphine and ammonia. It is thus necessary to constrain much more the cloud properties in order to accurately determine the aerosol opacity, as well as the gaseous abundances.

Ammonia is expected to condense at pressure levels where VIMS probes, although no ammonia ice spectral features have yet been detected. A wide range of cloud base pressures and aerosol particle sizes have been found to fit the observations quite well both for purely absorptive and scattering ammonia clouds. This does not rule out ammonia ice as a potential candidate for Saturn's tropospheric cloud, although other materials might condense in Saturn's troposphere. Furthermore, Saturn's 5-$\mu$m window might also be sensitive to the tropospheric and stratospheric hazes located above the cloud layers. The cloud properties and gas abundances were thus retrieved with NEMESIS for two other aerosol compositions. First, an ammonium hydrosulphide ($NH_4SH$) cloud was assumed since thermochemical equilibrium models predict its condensation in the troposphere although at deeper atmospheric levels than ammonia. The cloud opacity, and volume mixing ratios of phosphine and ammonia are retrieved for a wide range of cloud base pressures and aerosol particle sizes. Then a similar grey aerosol model as described by Fletcher *et al.* (2011) was also tested. In this model, a grey cross-section and single scattering albedo ($\omega_0 = 0.95$), and an isotropic phase function are assumed so that the retrieval is performed only for various base pressures of the grey cloud. The cloud properties are retrieved assuming both purely absoptive and scattering aerosol particles for each of the cloud compositions.

The goodness-of-fit maps for a compact ammonium hydrosulphide cloud has a similar pattern as for an ammonia cloud (see Fig. 4.8). The cloud base pressure is not constrained for a purely absorptive cloud and the cloud can be placed anywhere between 10 mbar and 3 bar. Any aerosol particle size ranging from 500 nm to 3 $\mu$m provides a possible solution to the retrieval problem for

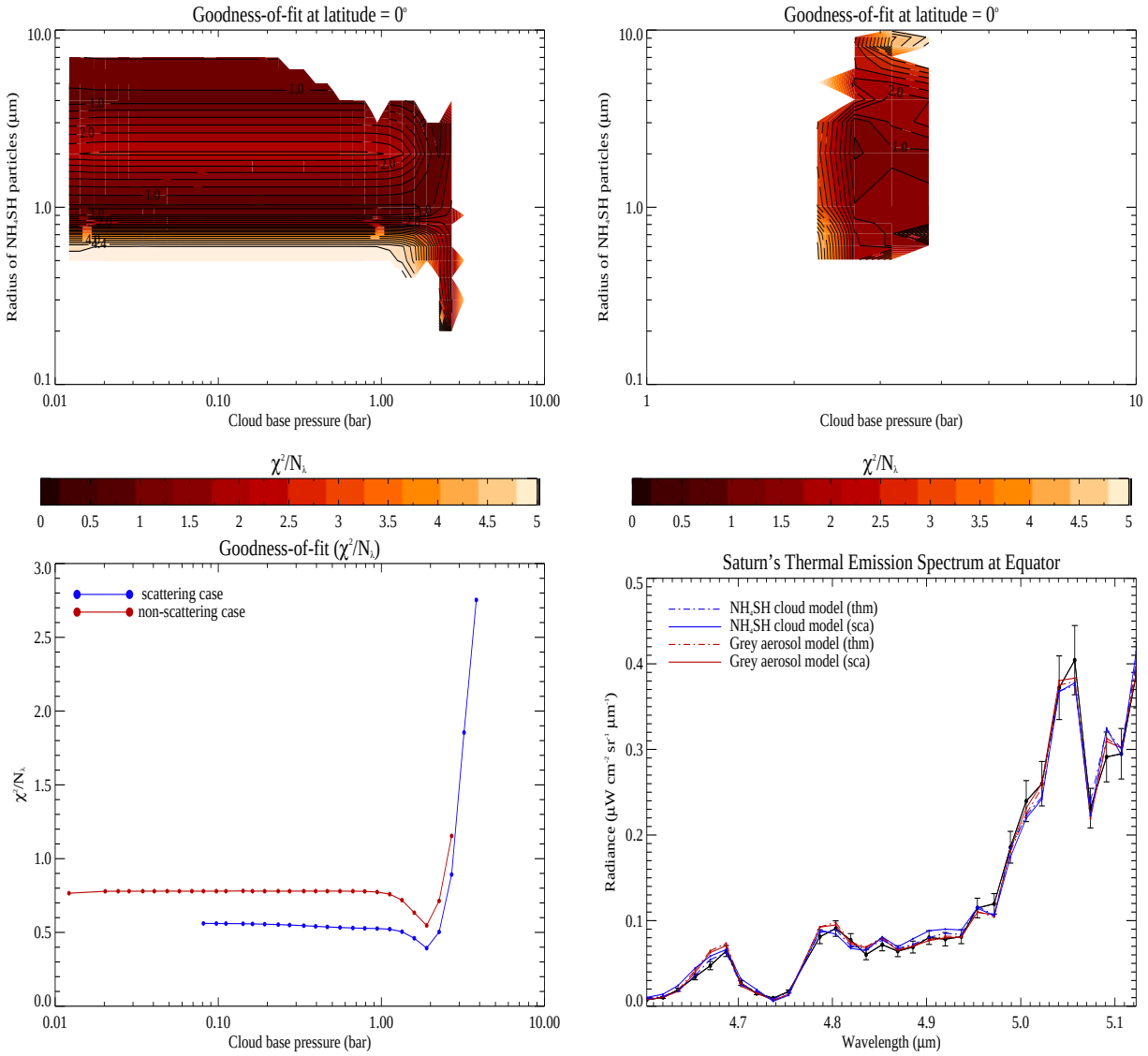



Figure 4.8: Retrieval of aerosol properties for a compact ammonium hydrosulphide ($NH_4SH$) cloud and a grey aerosol layer made of purely absorptive and scattering aerosol particles. Aerosol properties are retrieved here from one thermal emission spectrum (CM1524383985) measured at nighttime at a latitude of $0.23° \pm 1.31°$, longitude of $235.94° \pm 1.62°$ and emission angle of $0.93° \pm 1.78°$. The cloud base pressure and aerosol particle size are retrieved with NEMESIS for the $NH_4SH$ cloud model in the non-scattering case (*top-left*) and scattering case (*top-right*). A grey cross-section and single scattering albedo ($\omega_0 = 0.95$), and an isotropic phase function were chosen for the grey aerosol model following Fletcher *et al.* (2011). Therefore, only the base pressure of the grey layer is retrieved (*bottom-left*). The goodness-of-fit for the ammonium hydrosulphide and grey aerosol layer models are shown for $\chi^2/N_\lambda$ values below the 5.0 threshold value. The synthetic spectra for each aerosol model are compared to VIMS thermal emission spectrum (*bottom-right*). The synthetic spectra are calculated for a purely absorptive and scattering grey aerosol layers at 1.8 bar. For an ammonium hydrosulphide cloud, a cloud pressure base of 1.8 bar and an aerosol particle size of 1 $\mu$m are assumed in the non-scattering case. The synthetic spectra for a scattering ammonium hydrosulphide cloud are shown for a cloud base pressure at 2.7 bar and a 2-$\mu$m aerosol particle size.

each pressure level above 3 bar. Larger particles within aerosol layers above 500 mbar are also compatible with VIMS observations. As for the ammonia cloud model, aerosol properties are most constrained for a scattering ammonium hydrosulphide cloud, and optimum $\chi^2/N_\lambda$ values are found for a cloud base pressure between 2 and 4 bar, and for an aerosol particle size between 500 nm and 10 $\mu$m. Therefore, the ammonium hydrosulphide cloud can be placed around 1 bar deeper than the ammonia cloud in the scattering case. The grey aerosol model is tested here to account for the hazes expected to form above the cloud layers. The aerosol layer can be placed between 10 mbar and 3 bar in the non-scattering case, and between 80 mbar and 3 bar in the scattering case, leading to more new sets of potential solutions to the retrieval problem. $\chi^2/N_\lambda$ values are slightly smaller for a scattering grey aerosol layer, however synthetic spectra in the non-scattering case also match VIMS data quite well within the measurement errors, and so the purely absorptive grey model cannot be ruled out.

The analysis of individual thermal emission spectra has not singled out any of the aerosol models tested in this section. For each cloud composition, both purely absorptive and scattering aerosol particles provided synthetic spectra consistent with VIMS near-infrared observations, leading to more degeneracies in the model. The aerosol opacity, and volume mixing ratios of phosphine and ammonia retrieved with NEMESIS depend on the cloud composition and the presence of scattering in the model. As a result, it is necessary to constrain further the cloud model to allow a quantitative analysis of the aerosol and gas distribution in Saturn's troposphere and stratosphere. For the same reason, analysis of VIMS near-infrared thermal emission must also focus on determining whether Saturn's clouds are purely absorptive or if scattering effects are predominant in the 5-$\mu$m window. In the next section, spectra in the 4.6-5.1 $\mu$m spectral range at a similar area onto the planet but observed with different viewing geometries will be combined to break the degeneracies inherent to the retrieval problem.

## 4.4 Limb-darkening analysis

### 4.4.1 Methodology

Many cloud models are found to fit individual VIMS spectra perfectly well resulting in a wide range of possible solutions to the retrieval problem. This is mainly due to the large number of free atmo-

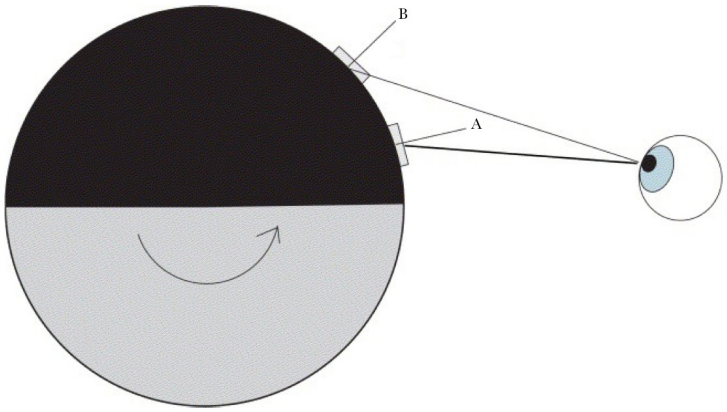



Figure 4.9: Limb-darkening observation scheme. A specific area (latitude, longitude) is seen first by the observer at a low emission angle (A). At the next observation time, the same area will be seen at a higher emission angle (B) due to the rotation of the planet. The motion of the observer relative to the planet is negligible. This limb-darkening observation scheme can be applied to the strategy adopted for the analysis of VIMS near-infrared data. Indeed, only VIMS limb-darkening data measured over a few hours are considered in this thesis, and so the spacecraft motion can be neglected with respect to the planet rotation over such a period of time. Source: Roos-Serote and Irwin (2006).

spheric parameters in the model in comparison with a lower number of measurements. In theory, if there are as many unknown variables as measurements, the retrieval algorithm would ideally retrieve one unique set of solutions. This is obviously never the case, and so one way to better constrain the atmospheric properties retrieved with NEMESIS is to increase the number of measurements of the same physical quantity. This can be done for example by considering limb-darkening observations of Saturn. In this section, the analysis of thermal emission spectra emitted from the same region (longitude, latitude) of Saturn but viewed at different emission angles is carried out with NEMESIS. This can be done by using limb-darkening observations of Saturn performed with the VIMS instrument. As the planet rotates, VIMS keeps taking measurements and so the same area onto the planet can be observed with different emission angles and at different times not far apart (see Fig. 4.9). VIMS measures limb-darkening thermal emission spectra over a short time period of typically a few hours. The aerosol opacity and volume mixing ratios of tropospheric gases are unlikely to undergo large variations over such a short time. Over larger time scales, the atmospheric structure in belts and perhaps zones might vary and so the limb-darkening analysis of such data has been avoided. The variations of aerosol vertical structure and composition are also expected to be negligible over a few hours, and so limb-darkening spectra can be considered as measurements of the same physical quantity and therefore analysed simultaneously to constrain the aerosol and gas properties in Saturn's

troposphere and stratosphere.

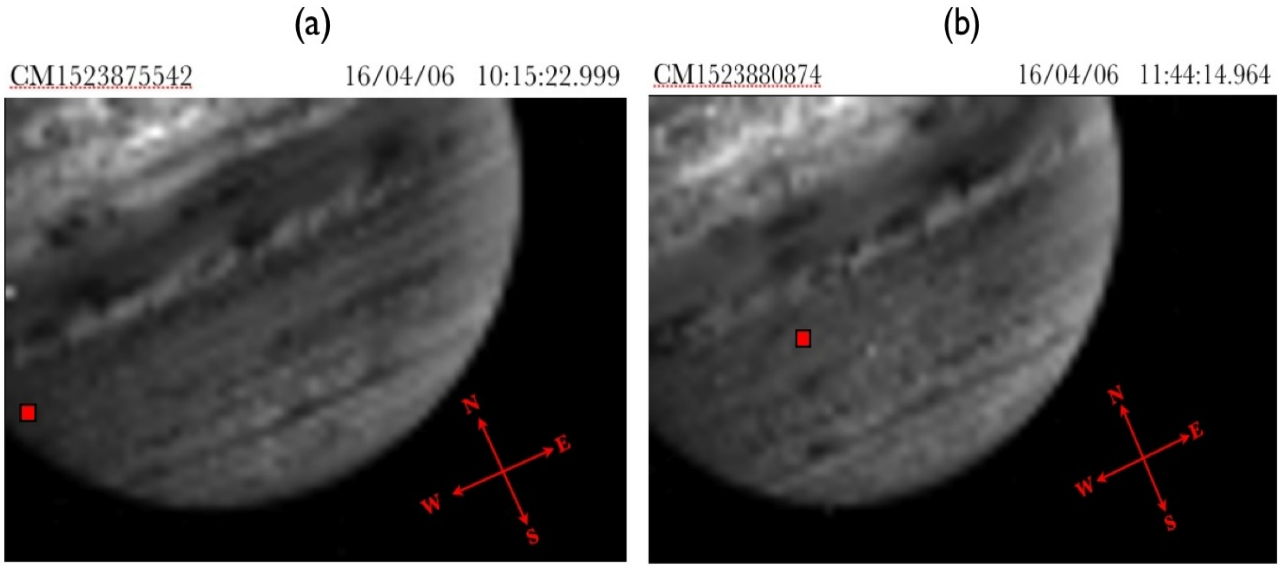
| spectral cube | observation date | observation time | Δt from first observation |
|---|---|---|---|
| CM1523875542 | 16 April 2006 | $10^h15^m14.964^s$ | $0^h0^m0.000^s$ |
| CM1523877318 | 16 April 2006 | $10^h44^m58.987^s$ | $0^h29^m35.988^s$ |
| CM1523879088 | 16 April 2006 | $11^h14^m28.976^s$ | $0^h59^m5.977^s$ |
| CM1523880874 | 16 April 2006 | $11^h44^m14.964^s$ | $1^h28^m51.965^s$ |
| spectral cube | latitude | longitude | emission angle |
| CM1523875542 | -20.92°±1.63° | 249.81°±5.20° | 72.04°±5.07° |
| CM1523877318 | -20.05°±1.54° | 251.53°±2.35° | 54.72°±2.39° |
| CM1523879088 | -20.11°±1.53° | 249.09°±1.82° | 41.97°±1.90° |
| CM1523880874 | -20.62°±1.55° | 250.35°±1.52° | 28.00°±1.62° |

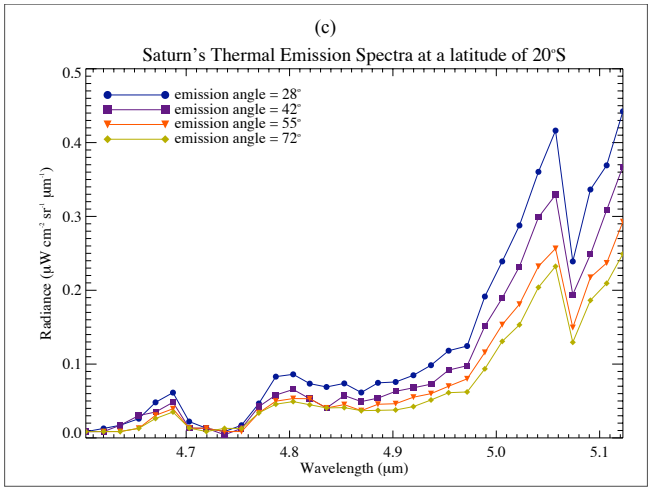
Table 4.2: VIMS spectral cubes selected for the limb-darkening analysis of Saturn's thermal emission spectra. The data are extracted from the Planetary Data System database (see Chapter 2 Section 3)

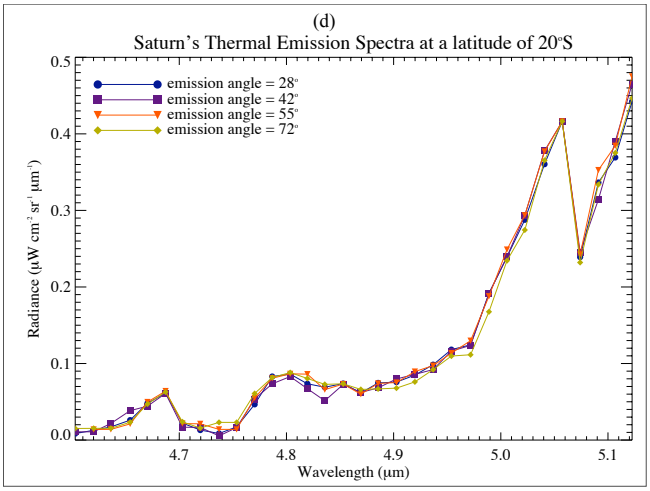
Four thermal emission spectra of the same region of the planet (latitude $\simeq$ 20°S, longitude $\simeq$ 250°) but viewed at different emission angles between about 28° and 72° were extracted from VIMS spectral cubes CM1523875542, CM1523877318, CM1523879088 and CM1523880874 measured the same day on 16 April 2006 at $10^h15^m22.999^s$, $10^h44^m58.987^s$, $11^h14^m28.976^s$ and $11^h44^m14.964^s$ (UTC) respectively (see Fig. 4.10). The first and last observations are thus $1^h28^m51.965^s$ apart, and two consecutive onservations are about 30 minutes apart (see Table 4.2). The aerosol structure, as well as the phosphine and ammonia vertical distributions are not expected to vary significantly over such a short period of time. The spectrum selected in the spectral cube CM1523875542 were measured at a latitude of -20.92° ± 1.63°, longitude of 249.81° ± 5.20° and high emission angle of 72.04° ± 5.07°. Saturn's thermal emission spectrum at the lowest emission angle was extracted from VIMS cube CM1523880874. The latitude, longitude and emission angle for this spectrum are respectively -20.62° ± 1.55°, 250.35° ± 1.52° and 28.00° ± 1.62°. Nightside spectra at a similar area on the planet but observed at intermediate emission angles are also extracted from VIMS spectral cubes CM1523877318 and CM1523879088. The two spectra are measured at a latitude, longitude and emission angle of -20.05° ± 1.54°, 251.53° ± 2.35° and 54.72° ± 2.39° (CM1523877318), and -20.11° ± 1.53°, 249.09° ± 1.82° and 41.97° ± 1.90° (CM1523879088). The cloud opacity, and deep volume mixing ratios of phosphine and ammonia were retrieved with NEMESIS from VIMS spectrum at lower emission angle in CM1523880874 cube. This was done for an ammonia, ammonium

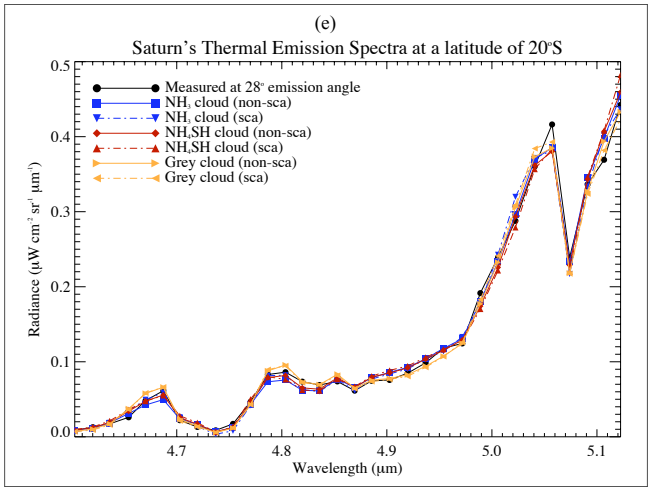
hydrosulphide and grey clouds made of purely absorptive and scattering aerosol particles. A 1-$\mu$m aerosol particle size was assumed for the ammonia and ammonium hydrosulphide cloud models. The ammonia and grey clouds were placed at 1.8 bar both in the non-scattering and scattering cases. The purely absorptive and scattering ammonium hydrosulphide clouds were placed at respectively 1.9 and 2.7 bar. The cloud base pressures were chosen for each of the six cloud models so that the modelled spectra are in good agreement with the VIMS spectrum measured at the lower emission angle (see Fig. 4.10: panel *e*) .The cloud opacity, and volume mixing ratios of phosphine and ammonia were set to the retrieved valued from the lower emission angle spectrum, and then synthetic spectra were calculated with the forward radiative transfer code at 42°, 55° and 72° emission angles (Fig. 4.10: panels *f*, *g* and *h*). The synthetic spectra at higher emission angles can be seen to match quite poorly the observations for non-scattering cloud cases. However, the synthetic spectra associated with scattering cloud models are in much better agreement with the observations than in the non-scattering case.

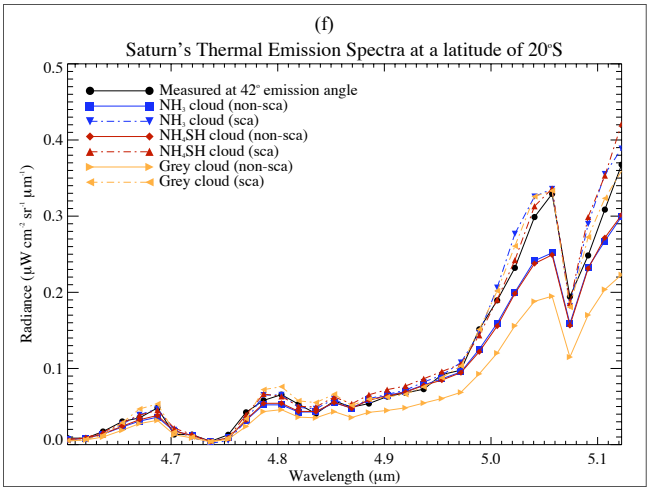
Saturn's spectra measured at higher emission angles were scaled to the lower emission angle spectrum in Fig. 4.10 (panel *d*). Although radiances decrease as the emission angle increases (see panels *i* and *j* in Fig. 4.10), the four spectra have a very similar shape suggesting a homogeneous atmosphere with scattering clouds. This is because in non-scattering compact stratified cloud models, data at higher emission angles are sensitive to lower pressures. Vertical variations of aerosol properties and gas volume mixing ratios are responsible for varying the shape of Saturn's spectra at higher emission angles in the non-scattering case. For a perfectly scattering cloud in a homogeneous atmosphere, the thermal emission should be approximated to the hemispherically integrated radiance, and so is expected to be very similar at all emission angles (Roos-Serote and Irwin, 2006). If all spectra were not independent measurements of the same physical quantity, the solution found at lower emission angle should also be a solution at higher emission angles. As seen in Fig. 4.10, this is clearly not the case, and so the analysis of each spectrum individually provides different sets of solutions to the retrieval problem. By retrieving Saturn's cloud opacity and gas volume mixing ratios from all spectra simultaneously, only the common solutions can provide a good fit to the observations at both low and high emission angles. Limb-darkening analysis of VIMS thermal emission spectra is carried out in the next section in order to narrow the solutions to the retrieval problem, and so better constrain the aerosol and gas properties in Saturn's troposphere and stratosphere.


(a)
CM1523875542 16/04/06 10:15:22.999
N
E
W
S
(b)
CM1523880874 16/04/06 11:44:14.964
N
E
W
S


(c)
Saturn's Thermal Emission Spectra at a latitude of 20°S
emission angle = 28°
emission angle = 42°
emission angle = 55°
emission angle = 72°
Radiance (μW cm⁻² sr⁻¹ μm⁻¹)
Wavelength (μm)


(d)
Saturn's Thermal Emission Spectra at a latitude of 20°S
emission angle = 28°
emission angle = 42°
emission angle = 55°
emission angle = 72°
Radiance (μW cm⁻² sr⁻¹ μm⁻¹)
Wavelength (μm)


(e)
Saturn's Thermal Emission Spectra at a latitude of 20°S
Measured at 28° emission angle
NH₃ cloud (non-sca)
NH₃ cloud (sca)
NH₄SH cloud (non-sca)
NH₄SH cloud (sca)
Grey cloud (non-sca)
Grey cloud (sca)
Radiance (μW cm⁻² sr⁻¹ μm⁻¹)
Wavelength (μm)


(f)
Saturn's Thermal Emission Spectra at a latitude of 20°S
Measured at 42° emission angle
NH₃ cloud (non-sca)
NH₃ cloud (sca)
NH₄SH cloud (non-sca)
NH₄SH cloud (sca)
Grey cloud (non-sca)
Grey cloud (sca)
Radiance (μW cm⁻² sr⁻¹ μm⁻¹)
Wavelength (μm)

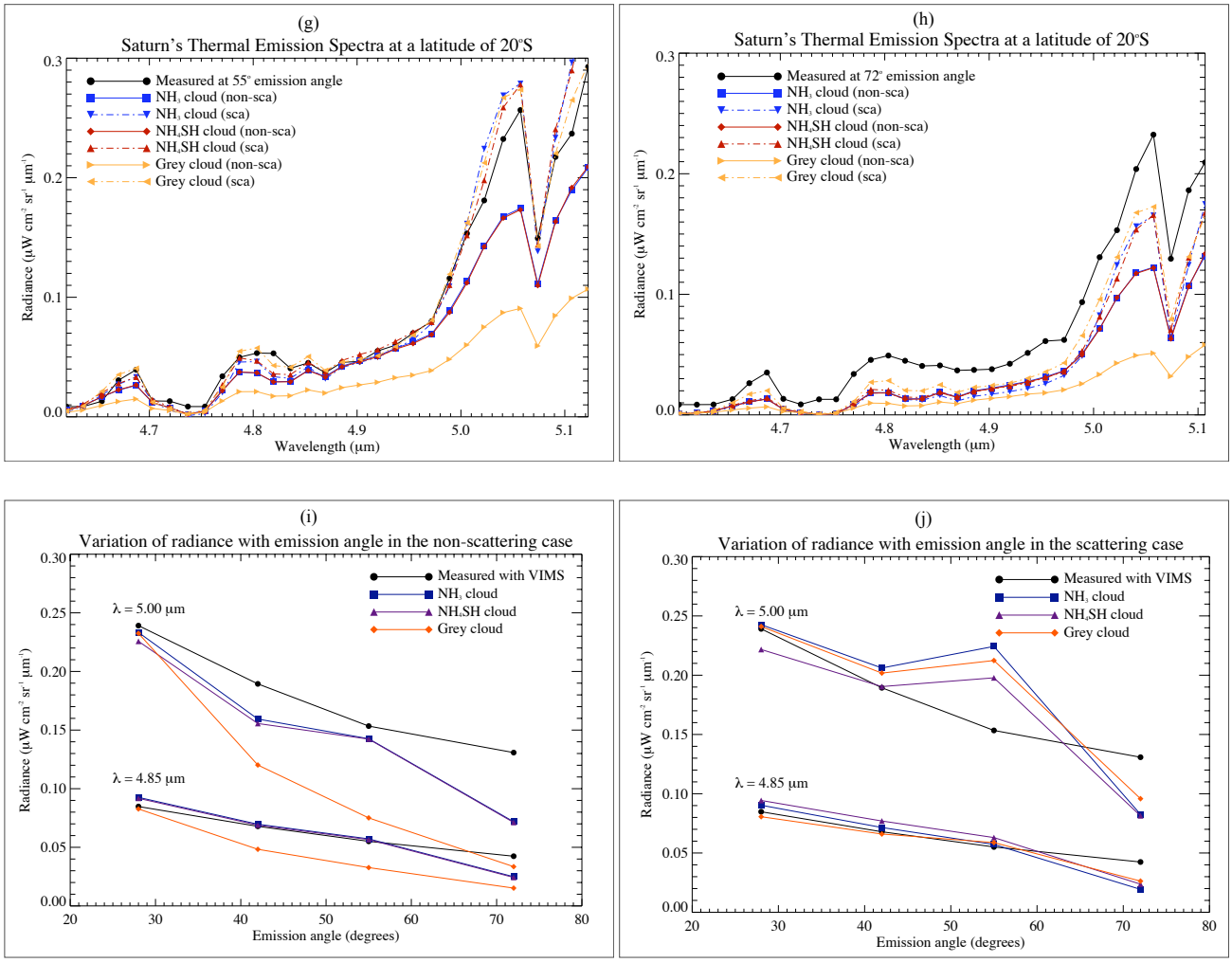



Figure 4.10: Limb-darkening observation of Saturn. VIMS images CM1523875542 (*a*) and CM1523880874 (*b*) at 5.06 $\mu$m were acquired on 16 April 2006 at 10:15:22.999 and 11:44:14.964 (UTC) respectively. Nightside thermal emission spectra were extracted at latitude and longitude coordinates shown by the red squares. The spectra in CM1523880874 and CM1523875542 are measured at low (28°) and high (72°) emission angles respectively. Two other spectra are measured at the intermediate emission angles of 42° (CM1523879088) and 55° (CM1523877318). The four spectra (*c*) are observed at times not far apart and at the same latitude and longitude locations, but viewed at different emission angles ranging from 28° to 72°. In panel *d*, the three spectra in the CM1523875542, CM1523877318 and CM1523879088 cubes have been scaled to match the smaller emission angle spectrum. The four spectra have very similar shapes, suggesting that scattering of the warm thermal radiation by aerosols is important in the 5-$\mu$m window. The cloud opacity as well as the phosphine and ammonia deep volume mixing ratios are retrieved from Saturn's spectrum at 28° emission angle for a compact ammonia, ammonium hydrosulphide and grey clouds. An aerosol particle size of 1 $\mu$m was assumed for all cloud models. The cloud base pressure is set to 1.8 bar for the grey and ammonia cloud models. The ammonium hydrosulphide cloud is placed at 1.8 and 2.7 bar, respectively in the non-scattering and scattering cases. Both purely absorptive and scattering aerosol particles are considered for each of the three cloud compositions. The synthetic spectra calculated with NEMESIS for each of the six cloud models are shown in panel *e*. The reference atmosphere is updated with the cloud opacity and gas abundances retrieved at the lower emission angle, and the synthetic spectra are calculated with the forward radiative transfer code at the emission angles of 42°, 55° and 72° (panels *f*, *g* and *h*). The measured and model radiances at 4.85 and 5.00 $\mu$m are plotted as a function of the emission angle in non-scattering (panel *i*) and scattering (panel *j*) cases for an ammonia, ammonium hydrosulphide and grey clouds.

### 4.4.2 Limb-darkening retrievals

In this section, two thermal emission spectra at low and high emission angles were extracted respectively from the VIMS spectral cubes CM1523880874 and CM1523875542. The low emission angle spectrum is measured at a latitude of -19.14° ± 1.53°, a longitude of 252.82° ± 1.48° and an emission angle of 24.35° ± 1.58°. The high emission angle spectrum is measured at similar latitude and longitude of respectively -19.24° ± 1.54° and 257.42° ± 3.31°, but at a higher emission angle of 71.76° ± 3.24°. Note that different spectra from the previous section are used here because of the smaller dispersion on the latitude, longitude and emission angle both for the low and high emission angle spectra. A simple cloud model consisting of one compact aerosol layer is first assumed for ammonia, ammonium hydrosulphide and grey aerosol particles. The effect of scattering of the warm thermal radiation by aerosols was tested by assuming non-scattering and scattering conditions. Then, a similar limb-darkening analysis was carried out, but for the extended cloud models. Such models are in better agreement to the vertical structure predicted by thermochemical theories. As for the compact cloud models, various aerosol properties were tested for the extended cloud models. Finally, the sensitivity of Saturn's 5-$\mu$m window to the tropospheric and stratospheric hazes was also assessed in this section by considering a grey aerosol model.

#### One compact cloud model

The cloud opacity and volume mixing ratios of ammonia and phosphine were retrieved with NEMESIS from the low and high emission angle observations simultaneously for one compact cloud with variable base pressures and aerosol particle sizes. Three cloud compositions were assumed: an ammonia, ammonium hydrosulphide and grey clouds. Both a scattering and non-scattering cloud models were tested. The goodness-of-fits are shown in Fig. 4.11 for the compact ammonia and ammonium hydrosulphide cloud models. In the non-scattering case, the lowest $\chi^2/N_\lambda$ values are obtained for a cloud base pressure between approximately 2 and 3 bar and an aerosol particle size between 200 nm and 10 $\mu m$. However, the $\chi^2/N_\lambda$ values are all above the 5 threshold value, and so none of the cloud base pressure and aerosol particle size could provide a synthetic spectrum in agreement with the VIMS data. In particular, the modelled spectra fit very poorly the observations at longer wavelengths both at low and high emission angles. Therefore, a single ammonia non-scattering cloud fails

at modelling VIMS limb-darkening observations in the 5-$\mu m$ window. This was not the case when atmospheric parameters were retrieved from one single thermal emission spectrum at a given emission angle. Limb-darkening analysis shows that Saturn's tropospheric cloud model cannot be represented by one compact ammonia cloud made of purely absorptive particles. The same analysis is also carried out for a scattering ammonia cloud. The best fits are obtained for a cloud base pressure either below the 2-bar level or above the1.5-bar level. As for the non-scattering case, the lowest $\chi^2/N_\lambda$ values are approximately equal to 5. As a result, including scattering in the compact ammonia cloud model does not improve the fit to Saturn's limb-darkening spectra in the 4.6-5.1 $\mu$m spectral range. In conclusion, a simple cloud model with ammonia ice as the main aerosol constituent can be ruled out, and new assumptions must be made in the cloud model in order to match VIMS limb-darkening data. The first revision of the cloud model consists in varying the cloud composition. Ammonium hydrosulphide particles are expected to condense in Saturn's troposphere although at deeper pressure levels than ammonia ice. The cloud opacity and deep volume mixing ratios of phosphine and ammonia are thus retrieved for one compact ammonium hydrosulphide cloud, both for scattering and non-scattering conditions (see Fig. 4.11). For a purely absorptive cloud, the best fits to VIMS near-infared data are obtained for a cloud base pressure between 2 and 3 bar and an aerosol particle size between 200 nm and 1 $\mu$m. The minimum $\chi/N_\lambda$ values, around 4, are slightly smaller than for a compact ammonia cloud. However there are still significant discrepancies between the model and the observations, and so new modifiactions must be brought to the cloud model. The same ammonium hydrosulphide cloud model consisting of one compact aerosol layer at a variable pressure level but with scattering aerosol particles is also tested. The lowest $\chi^2/N_\lambda$ values are obtained for a cloud base pressure between 2 and 3 bar and an aerosol particle size between 200 nm and 8 $\mu$m in the scattering case. A scattering cloud matches more closely VIMS spectra at low and high emission angles than a purely absorptive cloud. However, modelled spectra for a scattering ammonium hydrosulphide cloud also provide poor fits to the VIMS data within the measurement errors, with associated $\chi/N_\lambda$ values above 5.0. Therefore a compact ammonium hydrosulphide cloud made of either purely absorptive or scattering aerosol particles is also not a good representation of Saturn's tropospheric clouds. Although thermochemical models predict the condensation of ammonia and ammonium hydosulphide clouds at tropospheric pressure levels sounded by the VIMS instrument, none of the compact cloud models detailed above has managed to provide synthetic spectra in good agreement with limb-darkening observations in the

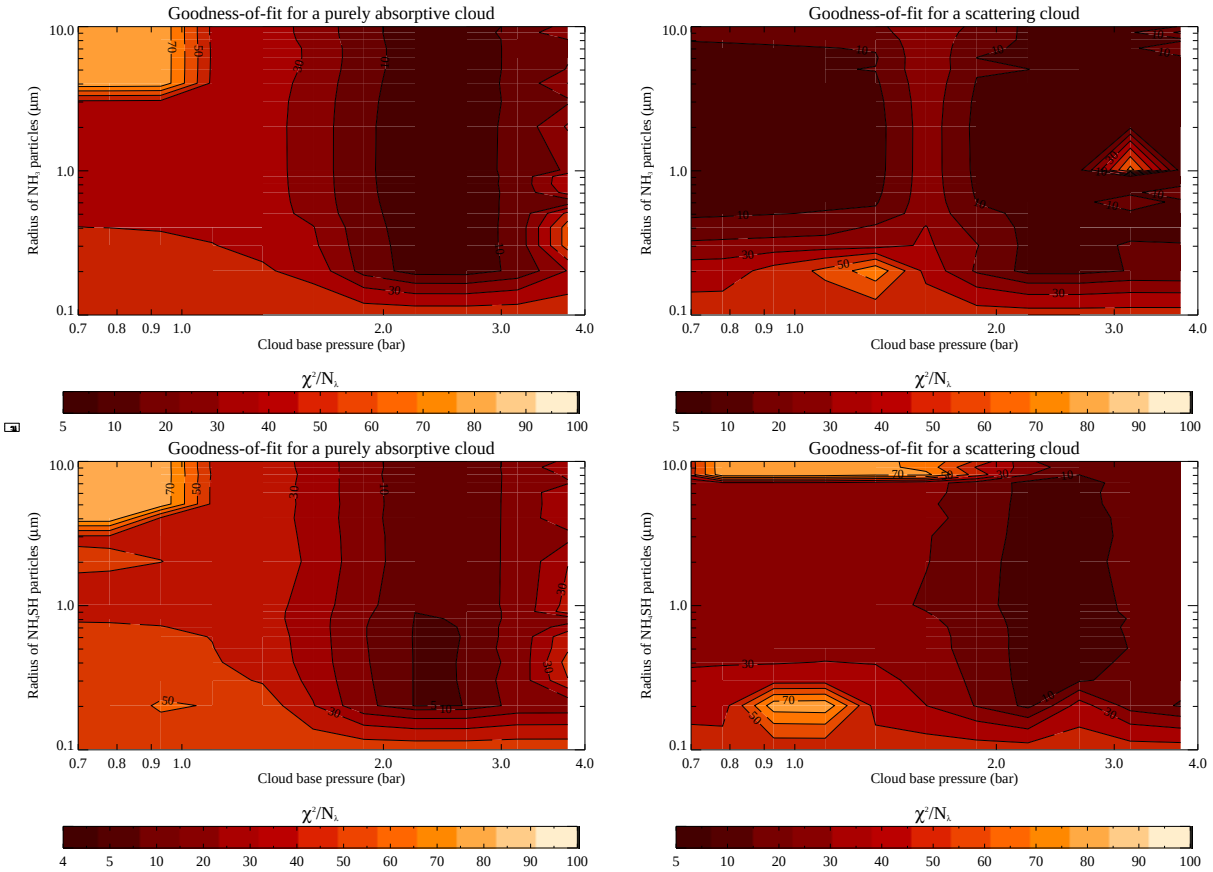



Figure 4.11: Limb-darkening analysis for one compact ammonia and ammonium hydrosulphide cloud models. The cloud opacity, as well as the deep volume mixing ratios of phosphine and ammonia are retrieved with NEMESIS from limb-darkening data acquired on 16 April 2006 at a latitude of 20°S. The low (24°) and high (72°) emission angle spectra are extracted from VIMS spectral cubes CM1523880874 and CM1523875542 respectively and fitted simultaneously. The goodness-of-fits ($\chi^2/N_\lambda$) as a function of the cloud base pressure and aerosol particle size are shown for one ammonia cloud (*top*) and one ammonium hydrosulphide cloud (*bottom*) in the non-scattering (*left*) and scattering (*right*) cases.

5-$\mu$m window. This could be explained by many factors including the sensitivity of Saturn's thermal emission to the tropospheric and stratospheric hazes, the extension and number of tropospheric clouds, as well as a different cloud composition than expected from thermochemical models.

The effect of absorption and scattering by the hazes is tested by considering one compact grey aerosol layer at variable pressure levels. As in the previous section, a grey cross-section, single scattering albedo ($\omega_0 = 0.95$) and isotropic phase function are assumed for the grey model following Fletcher *et al* (2011). The goodness-of-fit as a function of the cloud base pressure is shown in Fig. 4.12 for both a purely absorptive and scattering grey clouds. There is a clear $\chi^2/N_\lambda$ minumum of around 5 for a cloud base pressure between 2 and 3 bar in the non-scattering case. However, the

synthetic spectra associated to these pressure levels do not match VIMS limb-darkening data within the measurement errors, and so the aerosol model consisting of one single grey cloud in the non-scattering case can be ruled out. Lower $\chi^2/N_\lambda$ are obtained if scattering is included in the grey cloud model. In that case, the best fits are obtained for any aerosol layer between 0.01 and 1.0 bar, and the corresponding $\chi^2/N_\lambda$ values are approximately equal to 2. The synthetic spectrum for a cloud base pressure at 0.11 bar is compared with VIMS spectra at low and high emission angles in Fig. 4.12. The modelled radiances match the measured radiances within the measurement errors at almost all the spectral points. This is observed for all scattering grey clouds at higher altitudes above the 1-bar pressure level.

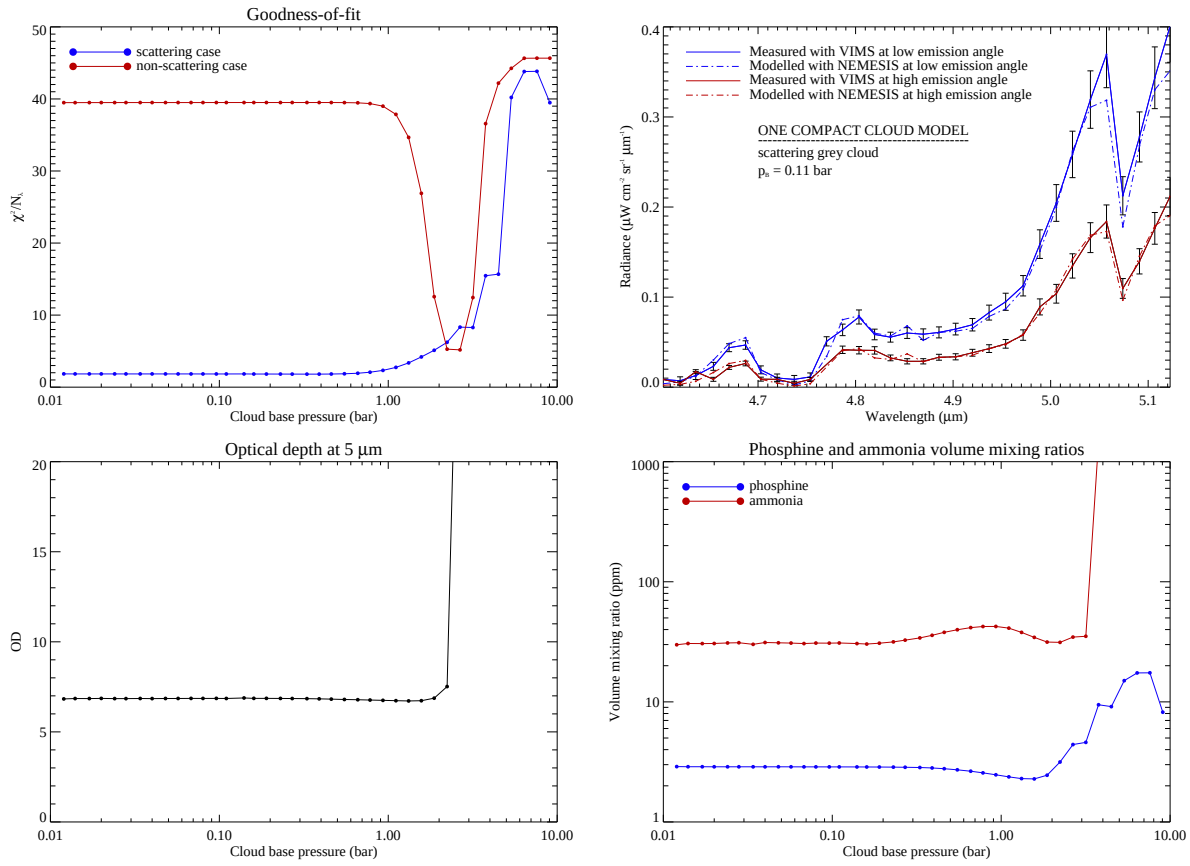



Figure 4.12: Limb-darkening analysis for one compact grey cloud model. A grey cross-section and single scattering albedo ($\omega_0 = 0.95$), and isotropic phase function are chosen here. Goodness-of-fit as a function of the cloud base pressure and aerosol particle size for a purely absorptive and scattering cloud (*top-left*). The modelled spectra at low and high emission angles are compared to the VIMS data for a scattering grey cloud at 0.11 bar (*top-right*). The optical depth at 5 $\mu$m (*bottom-left*) and the deep volume mixing ratios of phosphine and ammonia (*bottom-right*) retrieved with NEMESIS for a scattering grey cloud are plotted as a function of the cloud base pressure.

The cloud opacity, and volume mixing ratios of phosphine and ammonia retrieved with NEMESIS in the scattering case are also shown for all values of the base pressure in Fig. 4.12. A constant optical depth at 5 $\mu$m of around 6.0 is retrieved with NEMESIS at all base pressures less than 1.0 bar. The retrieval algorithm retrieved a volume mixing ratio between 2 and $3\times10^{-6}$ for phosphine, and between 3 and $4\times10^{-5}$ for ammonia. Bézard *et al.* (1989) and Larson and Noll (1991) found a deep phosphine volume mixing ratio in the range (4-10)$\times10^{-6}$. This value was confirmed by Graauw *et al.* (1997) who found a volume mixing ratio of $4.4\times10^{-6}$ from ISO measurements. More recently, Fletcher *et al.* (2011) retrieved a deep phosphine mixing ratio ranging between 2 and 4 $\times10^{-6}$. The ratios retrieved here with NEMESIS for a scattering grey cloud are then consistent with previous studies of the phosphine distribution. However the deep ammonia volume mixing ratios are smaller than the published values.

A list of previous determinations of the ammonia volume mixing ratios at pressure levels sounded by the VIMS instrument is shown in Table 4.3. Briggs and Sackett (1989) found a volume mixing ratio of (4.8 $\pm$ 1)$\times10^{-4}$ at deep tropospheric levels around 25 bar from centimetre observations. Around condensation level, ammonia is expected to combine with hydrogen sulphide to form an ammonium hydrosulphide cloud, leading to a lower ammonia volume mixing ratio. As seen in Table 4.3, previous determinations of the ammonia volume mixing ratios concluded on values in the range 0.7-5 $\times10^{-4}$. In particular, a recent analysis of Saturn's 5-$\mu$m window by Fletcher *et al.* (2011) led to a volume mixing ratio in the range (1-5)$\times10^{-4}$. A scattering albedo of 0.95 is assumed in the grey model. A similar model is tested for each value of the scattering albedo $\omega_0$ ranging between 0 and 1, with a step $\Delta\omega_0$ equal to 0.05.

The model better matches VIMS limb-darkening data for higher values of the scattering albedo, and any value below approximately 0.9 provides a poor fit to the near-infrared observations. Even by varying the scattering albedo, the ammonia volume mixing ratios retrieved with NEMESIS are still in the range 2-5$\times10^{-5}$, and so are not consistent with the values already published. Although the scattering grey cloud model provides a possible solution to the retrieval problem, it is very likely that the low values of the deep ammonia volume mixing ratio are due to an attempt of the retrieval algorithm to fit VIMS limb-darkening observations more closely.

| Reference | Ammonia VMR (ppm) | Method |
|---|---|---|
| de Pater and Massie (1985) | 500 | Very Large Array (VLA) ; radio |
| Briggs and Sackett (1989) | 70-100 | VLA and Arecibo ; radio |
| Grossman *et al.* (1989) | 120 | VLA ; radio |
| Noll and Larson (1990) | 300 | 5 $\mu$m analysis |
| de Graauw *et al.* (1997) | 110 | ISO/SWS |
| Orton *et al.* (2000) | 100 | Sub-mm $PH_3$ analysis |
| Burgdorf *et al.* (2004) | 100 | ISO/LWS 96-101 $cm^{-1}$ |
| Fletcher *et al.* (2011) | 100-500 | 5 $\mu$m analysis |
| Merlet | 30-40 | limb-darkening analysis at 4.6-5.1 $\mu$m for a scattering grey cloud. |

Table 4.3: Comparison of the ammonia VMR retrieved for a scattering grey cloud with tropospheric ammonia abundances from previous studies. The ammonia volume mixing ratios correspond to pressure levels sounded by the VIMS instrument where clouds are expected to form. Below the condensation levels, Briggs and Sackett (1989) obtained a volume mixing ratio of 480 ppm from centimetre observations. The ammonia volume mixing abundances, derived from the limb-darkening analysis in the 4.6-5.1 $\mu$m wavelength range, correspond to a scattering grey cloud above the 1-bar pressure level. The ammonia abundances retrieved for an ammonia and ammonium hydrosulphide clouds are not included since they did not match VIMS limb-darkening data.

Limb-darkening analysis of Saturn in the 4.6-5.1 $\mu$m wavelength range have shown that one compact cloud made of ammonia, ammonium hydrosulphide or grey aerosol particles fails at modelling VIMS limb-darkening data properly both in the non-scattering and scattering cases. In the next section, a similar approach as for the compact cloud models is adopted but for an extended cloud above the cloud base.

**One extended cloud model**

Since none of the compact cloud models detailed in the previous section could fit VIMS limb-darkening observations in the 5-$\mu$m window, Saturn's tropospheric cloud models are revised by considering an extended cloud with variable base pressure, scale height and aerosol particle size. Indeed, Weidenschilling and Lewis (1973), followed later by Atreya and Romani and Atreya (1986), predict from thermochemical theory that tropospheric clouds should extend above the pressure level at which condensation starts. Although most of the cloud opacity is found at the cloud base pressure, the other layers might contribute significantly to the absorption and scattering of thermal emission.

The extended cloud model is parametrised by the cloud base pressure, the cloud scale height in kilometres and the aerosol particle size. As for the compact cloud model, the cloud base pressure and aerosol particle size were allowed to vary respectively between 0.01 and 10 bar, and between 100 nm and 10 $\mu$m. The cloud scale height was chosen to be between 1 and 60 kilometres, with a step of one kilometre. The *a priori* vertical distribution of aerosols was set up so that the cloud density drops exponentially with altitude above the cloud base at a rate equal to the cloud scale height (see section 4.2.1). NEMESIS retrieved a scale factor of the *a priori* aerosol profile, as well as the volume mixing ratios of phosphine and ammonia. As for the compact cloud models, the analysis of VIMS limb-darkening observations was carried out for ammonia, ammonium hydrosulphide and grey clouds made of either purely absorptive or scattering aerosol particles. The cloud opacity, as well as the VMRs of gaseous ammonia and phosphine were retrieved with NEMESIS for a wide range of particle size, cloud base pressure and cloud extension.

The goodness-of-fit for a non-scattering ammonia cloud with a scale height of 5, 10, 15, 20, 25 and 30 kilometres above the cloud base are shown in Fig. 4.13. The minimum $\chi^2/N_\lambda$ values are obtained for lower values of the cloud scale height. It can be seen in the goodness-of-fit map for a 5-kilometre scale height that optimum fits are obtained for a cloud base pressure below the 2-bar level and for aerosol particle size ranging between 300 nm and 10 $\mu$m. However, the corresponding $\chi^2/N_\lambda$ values are all above the 5.0 threshold value, and so none of the synthetic spectra manage to match VIMS limb-darkening observations within the measurement errors. The minimum $\chi^2/N_\lambda$ values increase with the cloud extension and so none of the extended ammonia cloud models can fit VIMS limb-darkening data in the 4.6-5.1 $\mu$m wavelength range. For a scattering ammonia cloud, minimum $\chi^2/N_\lambda$ values are found for higher values of the cloud scale height (see Fig. 4.14). A cloud extension in the range 20-60 kilometres provides synthetic spectra in good agreement with the observations. For example, a cloud extension of 25 kilometres, a cloud base pressure between 2.5 and 4 bar and an aerosol particle size between 1 and 3 $\mu$m manage to fit VIMS data quite well. As the cloud scale height increases, the range of cloud base pressures and aerosol particle sizes, which provides possible solutions to the retrieval problem, also increases. In Fig. 4.15, the deep ammonia volume mixing ratios and cloud density profile are shown for a cloud scale height of 25 kilometres.

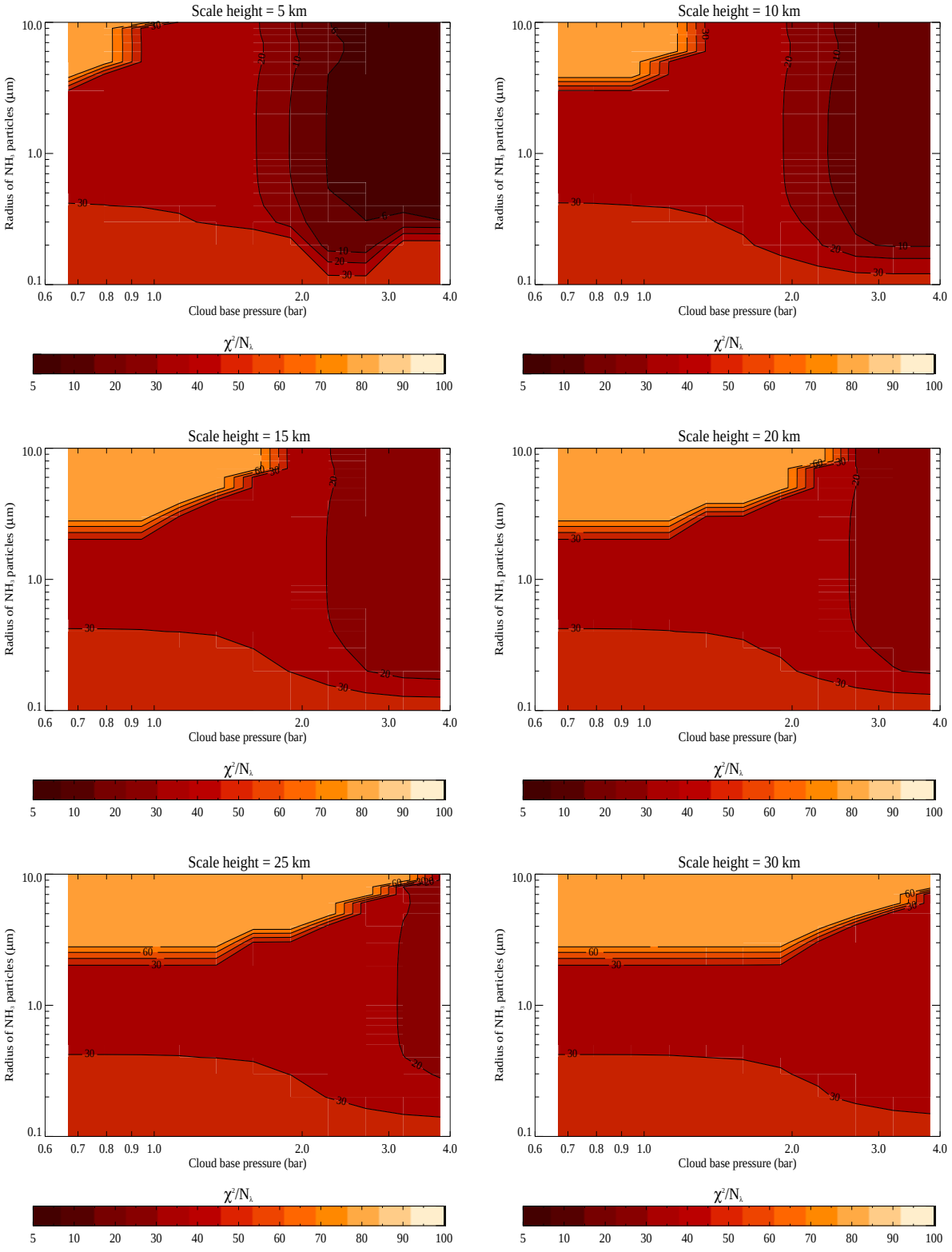



Figure 4.13: Limb-darkening analysis for an extended ammonia cloud made of purely absorptive aerosol particles. The cloud extension is parametrised by the scale height in kilometres. Results are shown for a scale height of 5, 10, 15, 20, 25 and 30 kilometres.

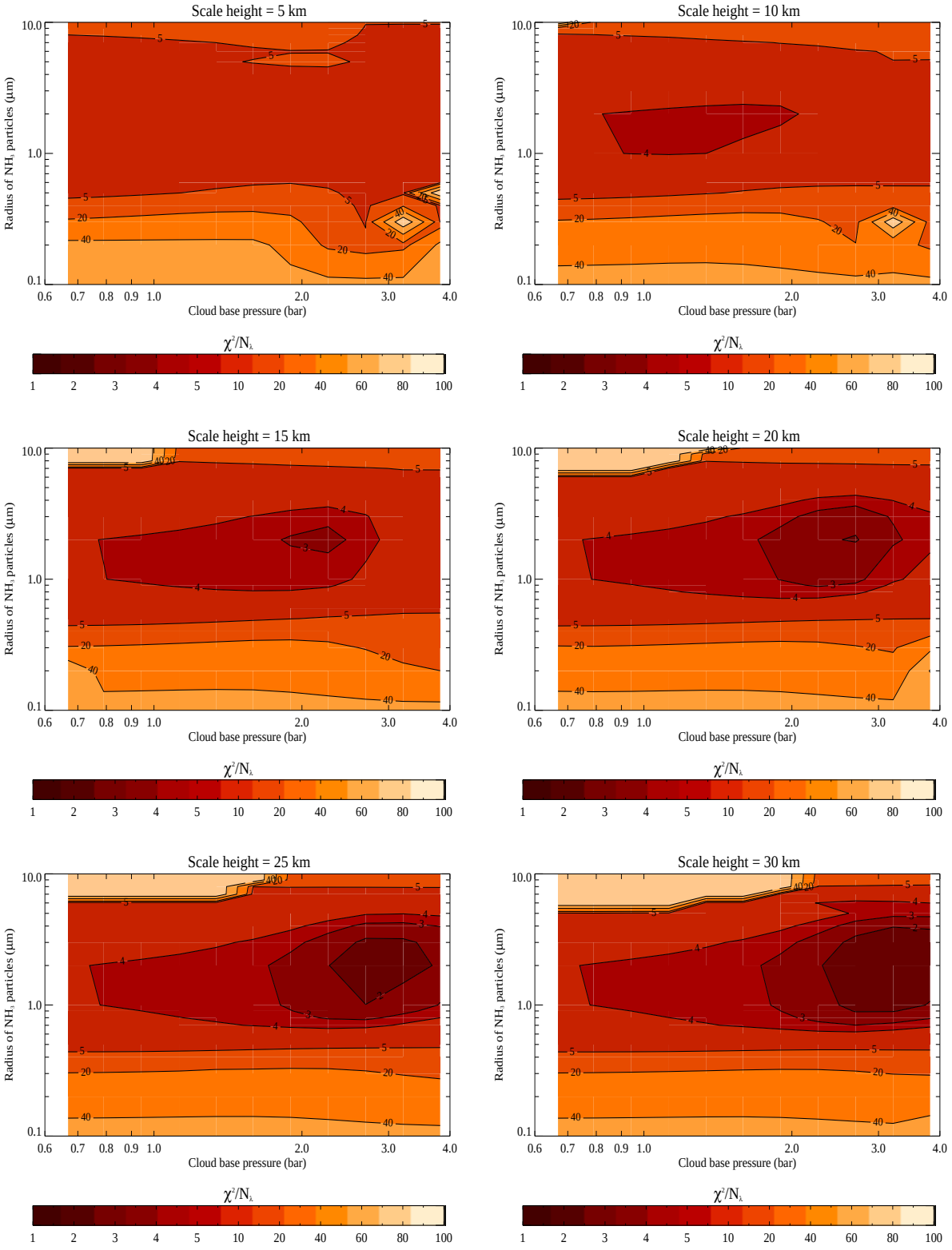



Figure 4.14: Limb-darkening analysis for an extended ammonia cloud made of scattering aerosol particles. The cloud extension is parametrised by the scale height in kilometres. Results are shown for a scale height of 5, 10, 15, 20, 25 and 30 kilometres.

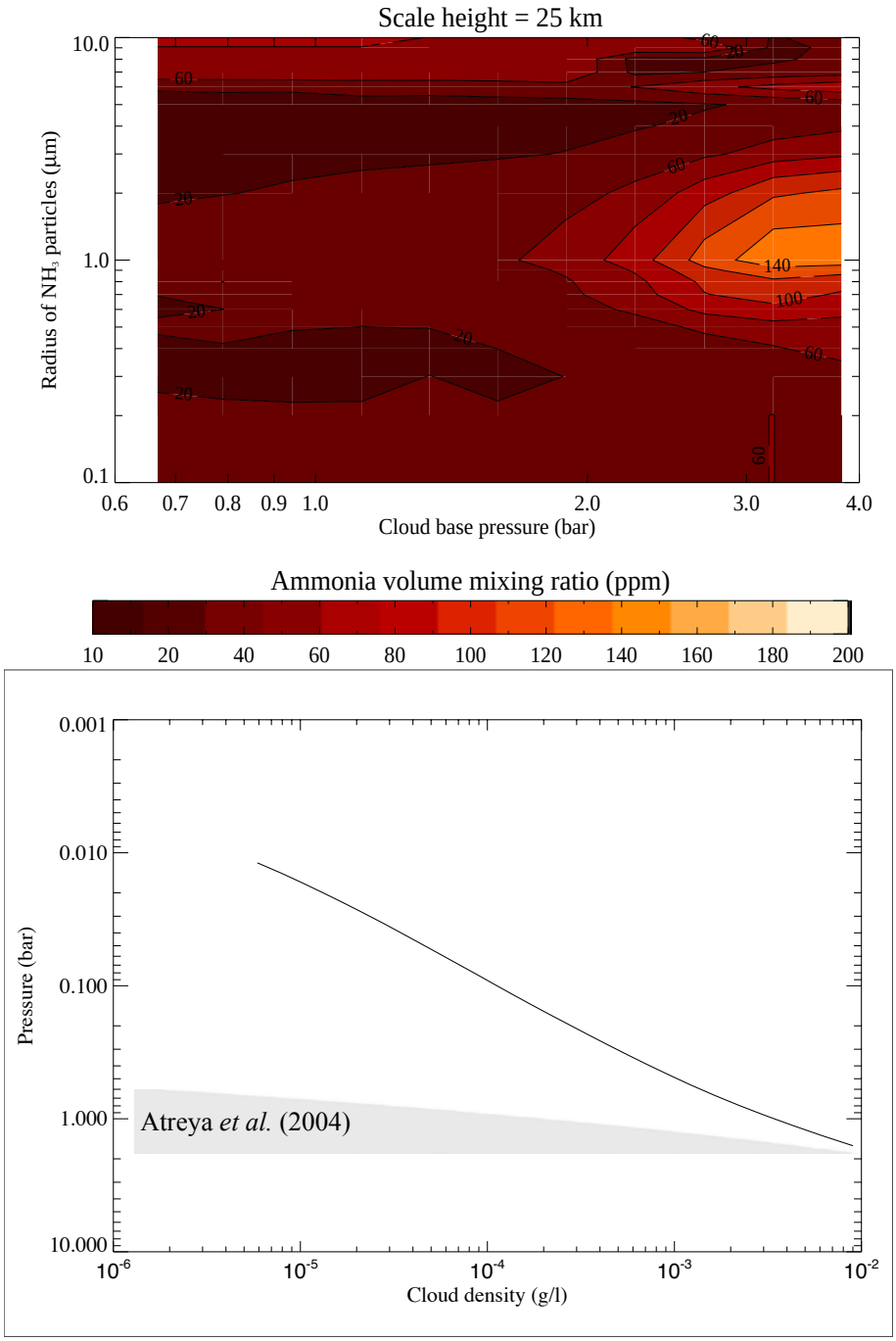



Figure 4.15: Ammonia volume mixing ratio and aerosol vertical profile for an extended ammonia cloud made of scattering aerosol particles retrieved from limb-darkening observations. The deep ammonia abundance in parts-per-million retrieved with NEMESIS is shown in the top panel. The cloud density profile in particle number per gramme of atmosphere generated by the retrieval algorithm is shown in the bottom pannel for a cloud base pressure at 1.8 bar and an aerosol particle size of 1 $\mu$m. The cloud profile for an extended ammonia cloud was multiplied by the atmospheric density in gramme per litre, so as to obtain the cloud density in particle number per litre of atmosphere. The cloud density retrieved with NEMESIS (solid line) is compared with the ammonia cloud density profile generated by Atreya *et al.* (2004) in their equilibrium cloud condensation model (grey shade). The cloud density profile obtained from limb-darkening observations was multiplied by a mass scale factor so as to match the aerosol abundance in gramme per litre at the cloud base pressure as described in text.

The deep ammonia abundances for a cloud base pressure between 2.5 and 4 bar and an aerosol particle size between 1 and 3 $\mu$m range between 0.8 and $1.5\times10^{-4}$ for an ammonia cloud with an extension of 25 kilometres (see Fig. 4.15). The compact grey cloud model in the scattering case was ruled out because of the unrealistic deep ammonia abundances retrieved with NEMESIS. For an extended ammonia cloud in the scattering case, the deep ammonia volume mixing ratios are in good agreement with the published values. The cloud density profile retrieved with NEMESIS for a cloud base pressure of 2.8 bar and an a gamma size distribution, with main parameter 1 $\mu$m and variance 0.05, is compared in Fig. 4.15 to theoretical predictions based on the equilibrium cloud condensation model (ECCM) developed by Atreya *at al.* (2004). In Saturn's troposphere, only ammonia, hydrogen sulphide and water are expected to condense. However, hydrogen sulphide in gas phase does not condense by itself at the temperatures found in Saturn's atmosphere but instead combines with ammonia to form ammonium hydrosulphide clouds if the temperature is low enough. The ammonia cloud density profile in the ECCM are calculated in gramme per litre. The aerosol density profile in NEMESIS is calculated in particle number per gramme of atmosphere, and so the density is first converted into particle number per litre by multiplying the cloud profile with the density of the atmosphere in gramme per litre at each pressure level. The resulting density profile must then be multiplied by the mass of aerosol particles so that to be converted into gramme per litre. The mass is obtained my multiplying the mean volume calculated from the gamma size distribution with the particle density since the same particle density is assumed for all particle sizes. The particle density was chosen so that the aerosol opacity at the cloud base in the retrieval model matches the cloud base opacity in the ECCM to allow direct comparison between the two models. The aerosol density profile for a cloud scale height of 25 kilometres retrieved with NEMESIS from limb-darkening observations drops above the cloud base pressure at a rate significantly smaller than in the ECCM aerosol density profile. As mentioned earlier, only clouds extended above the 25-kilometre threshold value are associated with synthetic thermal emission spectra in good agreement with VIMS observations. However, the formation of a tropospheric ammonia cloud with a scale height of at least 25 kilometres is in contradiction with thermochemical equilibrium models. Although a high cloud extension is unrealistic, it shows that Saturn's thermal emission spectra are probably also affected by another scattering source located at higher altitude above the tropospheric clouds. Hazes are expected to form above the cloud layers in the troposphere and stratosphere of Saturn (Karkoschka and Tomasko, 1992, 1993, 2005; Baines

*et al.*, 2006; West *et al.*, 2009), and so the large cloud extension obtained here is likely to be due to the 5-$\mu$m window sensitivity to Saturn's hazes.

The conclusions for an extended ammonium hydrosulphide cloud are very similar to those for an ammonia cloud. In the non-scattering case, none of the cloud scale height, cloud base pressure and aerosol particle size values provide a solution to the retrieval problem. The minimum $\chi^2/N_\lambda$ values around 5.0 are found for low extension of the ammonium hydrosulphide cloud, and for a cloud pressure base and aerosol particle size ranging respectively between 2 and 4 bar, and between 200 nm and 10 $\mu$m. As for an extended ammonia cloud, better fits to limb-darkening observations are obtained in the scattering case and the goodness-of-fit improves for higher values of the cloud scale height above the 20-kilometre threshold value. The vertical extension above the base pressure of the ammonium hydrosulphide cloud expected from thermochemical equilibrium models is very similar to the ammonia cloud extension (see Fig. 1.4). As a result, a cloud extension in the 20-60 kilometre range is significantly larger than the extension predicted by thermochemical theories, and so a cloud model consisting of only ammonium hydrosulphide particles must also be ruled out. Therefore, none of the extended ammonium hydrosulphide cloud models with a realistic cloud scale height manage to fit VIMS limb-darkening observations, both in the non-scattering and scattering cases. As for the ammonia cloud model, it is very likely that hazes located at higher altitude also contribute to the absorption and scattering of Saturn's thermal emission at 5 $\mu$m, and so hazes should be considered in the atmospheric model so as to fit VIMS limb-darkening data.

The extended cloud was finally assumed to be made of grey particles. As for an ammonia and ammonium hydrosulphide cloud model, a purely absorptive grey cloud model also fails at matching VIMS spectra both at low and high emission angles. The minimum $\chi^2/N_\lambda$ values around 9.0 are observed for a grey cloud located at a pressure above 2 bar and with a small extension above the cloud base. In the scattering case, a grey cloud at a pressure below 1 bar manages to fit quite well the limb-darkening data. This is observed for all values of the grey cloud scale height. Contrary to the ammonia and ammonium hydrosulphine extended cloud models, no minimum cloud extension is derived from the limb-darkening analysis. The grey aerosol model is assumed to account for the hazes formed above the tropospheric clouds. As a result, the grey aerosol density profiles can not be compared to theoretical predictions from by thermochemical equilibrium models. However, the deep ammonia volume mixing ratios retrieved with NEMESIS are all around $5\times10^{-5}$ for an aerosol

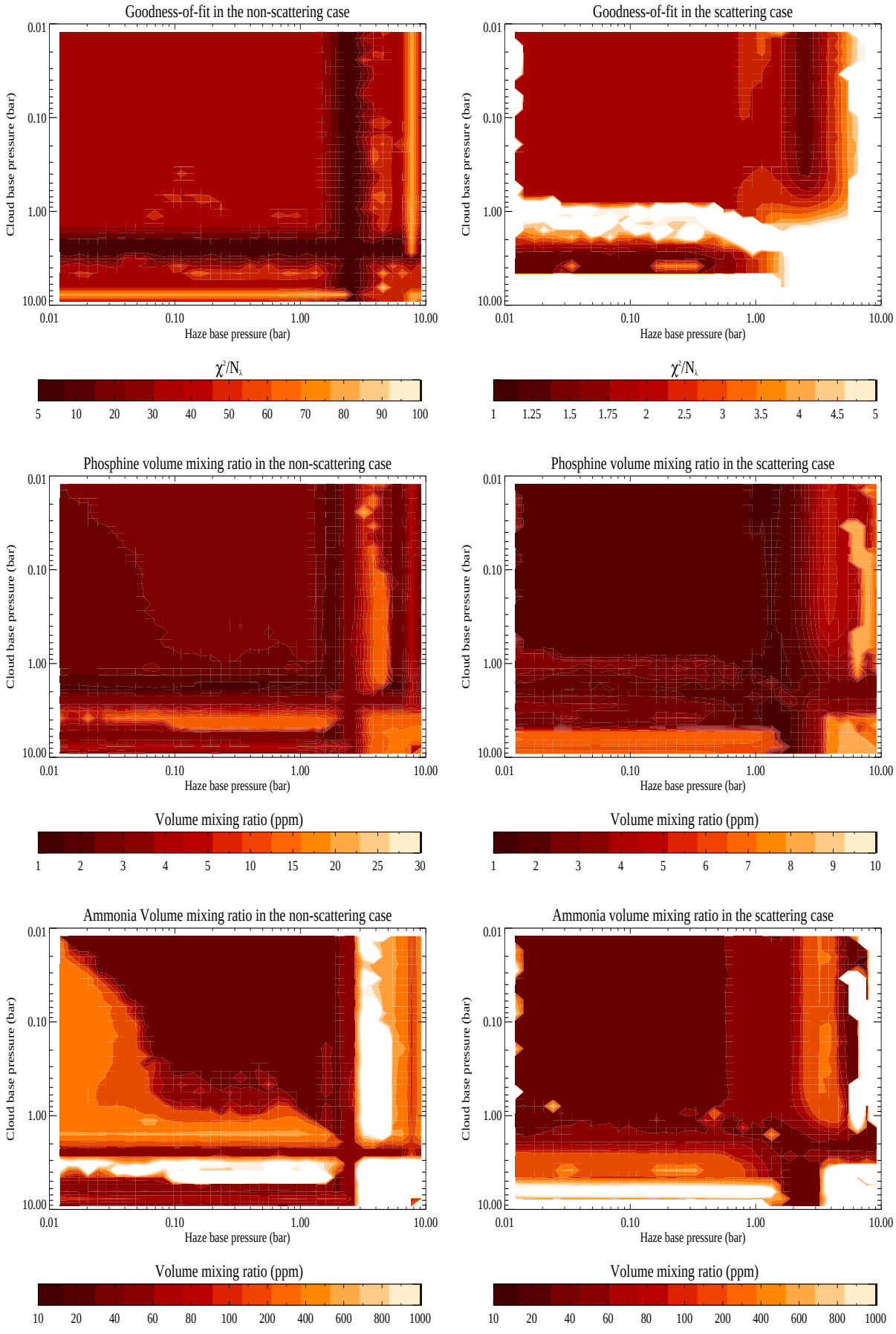
layer base at a pressure below 1 bar and for all scale height values. As for the compact grey aerosol model, the deep ammonia abundances are unrealistically low. Therefore an aerosol model based on only one extended grey cloud is probably a poor representation of Saturn's aerosol opacity sources in the 5-$\mu$m window.

The extended cloud model does not improve the fit to limb-darkening data in the non-scattering case. Results for a scattering extended cloud made of either ammonia or ammonium hydrosulphide particles show that an additional aerosol layer may be necessary to match VIMS thermal emission spectra both at low and high emission angles. This hypothesis is tested by considering two new cloud models: a two compact aerosol layer and continuous aerosol opacity models.

**Two compact aerosol layer and continuous aerosol opacity models**

The sensitivity of Saturn's 5-$\mu$m window to the haze located above the deeper clouds is tested by assuming that two aerosol layers are present in the troposphere or stratosphere of the planet. The haze is modelled as the grey aerosol layer described in the previous sections. As for the second aerosol layer, both an ammonia and ammonium hydrosulphide clouds are considered in the limb-darkening analysis. Both the haze and cloud models consist of one compact aerosol layer at a variable pressure level. The haze and cloud pressure levels are allowed to vary each between 0.01 and 10 bar in the model. Results are shown for an ammonia cloud made of purely absorptive and scattering aerosol particles in Fig. 4.16. Minimum $\chi^2/N_\lambda$ values around 5.0 are obtained for one aerosol layer at a pressure level between 2 and 3 bar while the other aerosol layer can placed anywhere between 0.01 and 10 bar. There is a perfect symmetry between the roles of the grey aerosol layer and the cloud, and as a result any of the two can be placed between 2 and 3 bar. However, synthetic spectra in the non-scattering case are in poor agreement with limb-darkening measurements, even for the lowest $\chi^2/N_\lambda$ values.

If scattering is included in the model, a good fit to limb-darkening observations is obtained for a cloud base pressure between 3 and 4 bar and a haze located above the 500-mbar pressure level. The maximum altitude of the haze is not constrained from limb-darkening analysis in the 5-$\mu$m window, and consequently the haze can placed anywhere up to the 10 mbar level. No conclusions can be drawn on the composition of the deep cloud by simply looking at the goodness-of-fit maps. Indeed the roles of the grey aerosol layer and ammonia cloud can be exchanged, and so the grey aerosol


Goodness-of-fit in the non-scattering case
Goodness-of-fit in the scattering case
Cloud base pressure (bar)
Haze base pressure (bar)
0.01
0.10
1.00
10.00
χ²/Nλ
5 10 20 30 40 50 60 70 80 90 100
1 1.25 1.5 1.75 2 2.5 3 3.5 4 4.5 5
Phosphine volume mixing ratio in the non-scattering case
Phosphine volume mixing ratio in the scattering case
Volume mixing ratio (ppm)
1 2 3 4 5 10 15 20 25 30
1 2 3 4 5 6 7 8 9 10
Ammonia Volume mixing ratio in the non-scattering case
Ammonia volume mixing ratio in the scattering case
10 20 40 60 80 100 200 400 600 800 1000

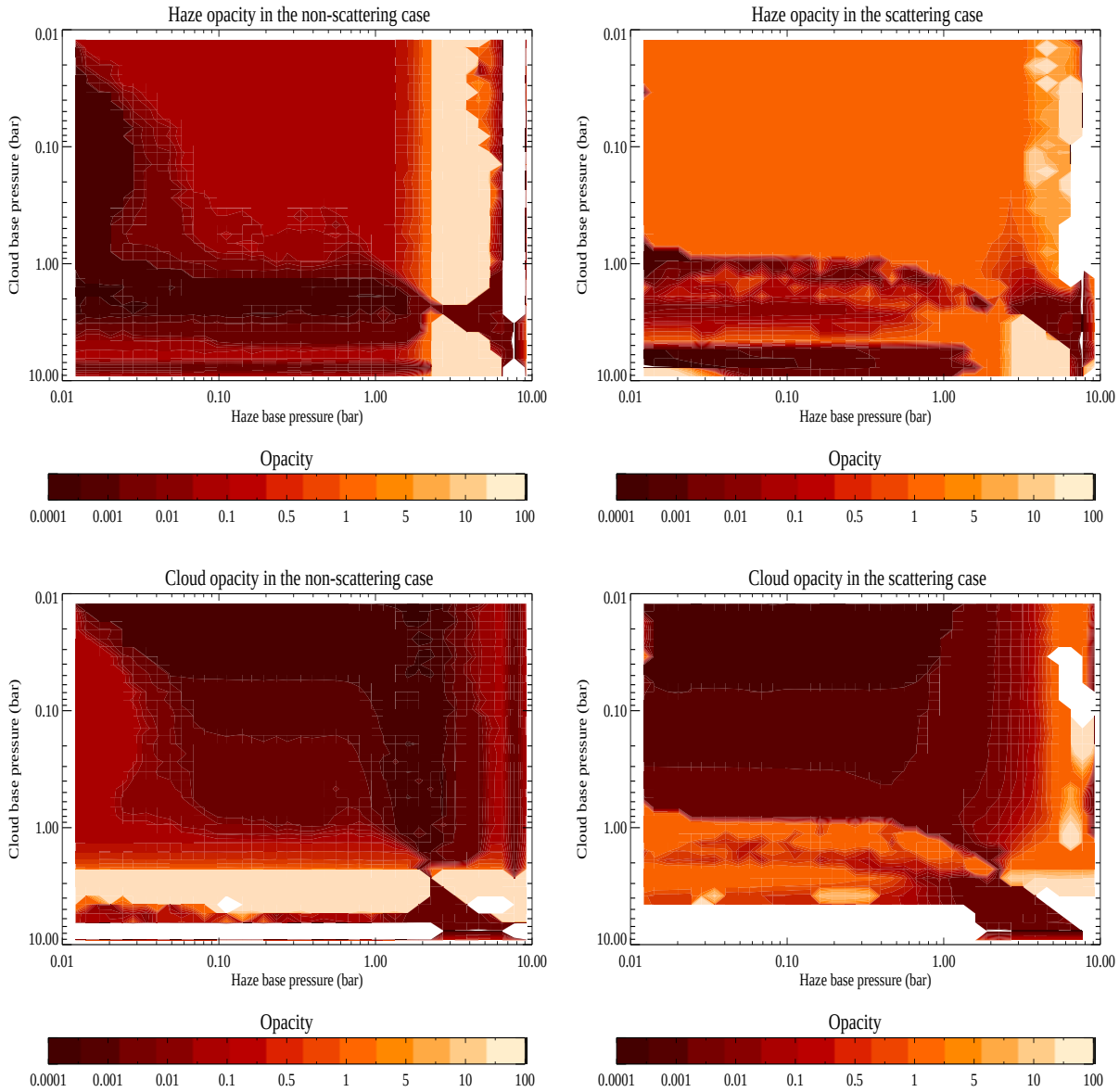



Figure 4.16: Limb-darkening analysis for a two compact aerosol layer model in the non-scattering and scattering cases. The two layers are assumed to represent the haze and cloud formed in Saturn's troposphere and stratosphere. The haze is modelled by the grey aerosol layer while the cloud is assumed to be made of ammonia particles with a one micrometre size. The aerosol opacities, and deep volume mixing ratios of phosphine and ammonia were retrieved with NEMESIS for a haze and cloud pressure ranges between 0.01 and 10.0 bar in the non-scattering and scattering cases. only $\chi^2/N_\lambda$ values below the 5.0 threshold are shown here in the scattering case. Better fits are obtained in the scattering case. The retrieved parameters are also presented here for both purely absorptive and scattering aerosol particles. Only realistic values of the phosphine volume mixing ratios between 1 and 100 ppm, ammonia volume mixing ratios between 10 and 1000, and aerosol opacities below 100 are shown here.

model can also represent the tropospheric cloud.

The retrieved values of the ammonia volume mixing ratio are also shown in Fig. 4.16 for each ammonia cloud and haze base pressures. In the scattering case, the best fits to VIMS limb-darkening observations are associated with deep volume mixing ratios in the range 1.5-4$\times 10^{-4}$, in good agreement with previous determinations of the ammonia abundance around the condensation level. The best-fitting values for the deep phosphine abundance, haze opacity and cloud opacity are in the range 2-7$\times 10^{-6}$, 0.01-5 and 0.1-10 respectively.

A similar two compact cloud model was considered but with an ammonium hydrosulphide cloud instead of the ammonia cloud. Similar conclusions as for an ammonia cloud were drawn from the goodness-of-fit maps both in the non-scattering and scattering cases. Also the ammonia volume mixing ratios retrieved were again consistent with the values already published. Therefore, a two cloud model with ammonia ice can not be distinguished from a similar model but with ammonia hydrosulphide aerosol particles. These results show, however, that both scattering and a haze layer need to be included in Saturn's atmospheric model, in order to match the limb-darkening observations of the planet in the 5-$\mu$m window and also obtain plausible ammonia abundances.

The same conclusion as above can be drawn by assuming a continuous aerosol density profile throughout the 0.01-10 bar pressure range. NEMESIS can adjust the aerosol opacity at each pressure level from an *a priori* profile, while retrieving the deep volume mixing ratios of phosphine and ammonia. The results are shown in Fig. 4.17 for an aerosol model made of ammonia, ammonium hydrosulphide and grey particles in the scattering case (as for the two compact cloud model, a non-scattering continuous profile fails at modelling VIMS limb-darkening observations) . The modelled spectra match the measured spectra at low and high emission angles for each of the three compositions. The optical depth values vary between the three models, however the retrieved vertical profile presents two distinct peaks at around 150 mbar and 3 bar for each case. In particular, the haze opacity is significantly larger than the cloud opacity for a grey cloud. This is consistent with the "one compact grey cloud" model, where the best fits were obtained for a grey cloud above the 1-bar level (see Fig. 4.12). However, the cloud opacity is larger for an ammonium hydrosulphide cloud, consistent with the retrieval of a tropospheric cloud at around 3 bar in the "one compact ammonium hydrosulphide" model (see Fig. 4.11). The cloud and haze opacities have similar values for an ammonia cloud, therefore the $\chi^2/N_\lambda$ values are also very similar in the upper troposphere and the lower stratosphere for a compact cloud as seen in Fig. 4.11.

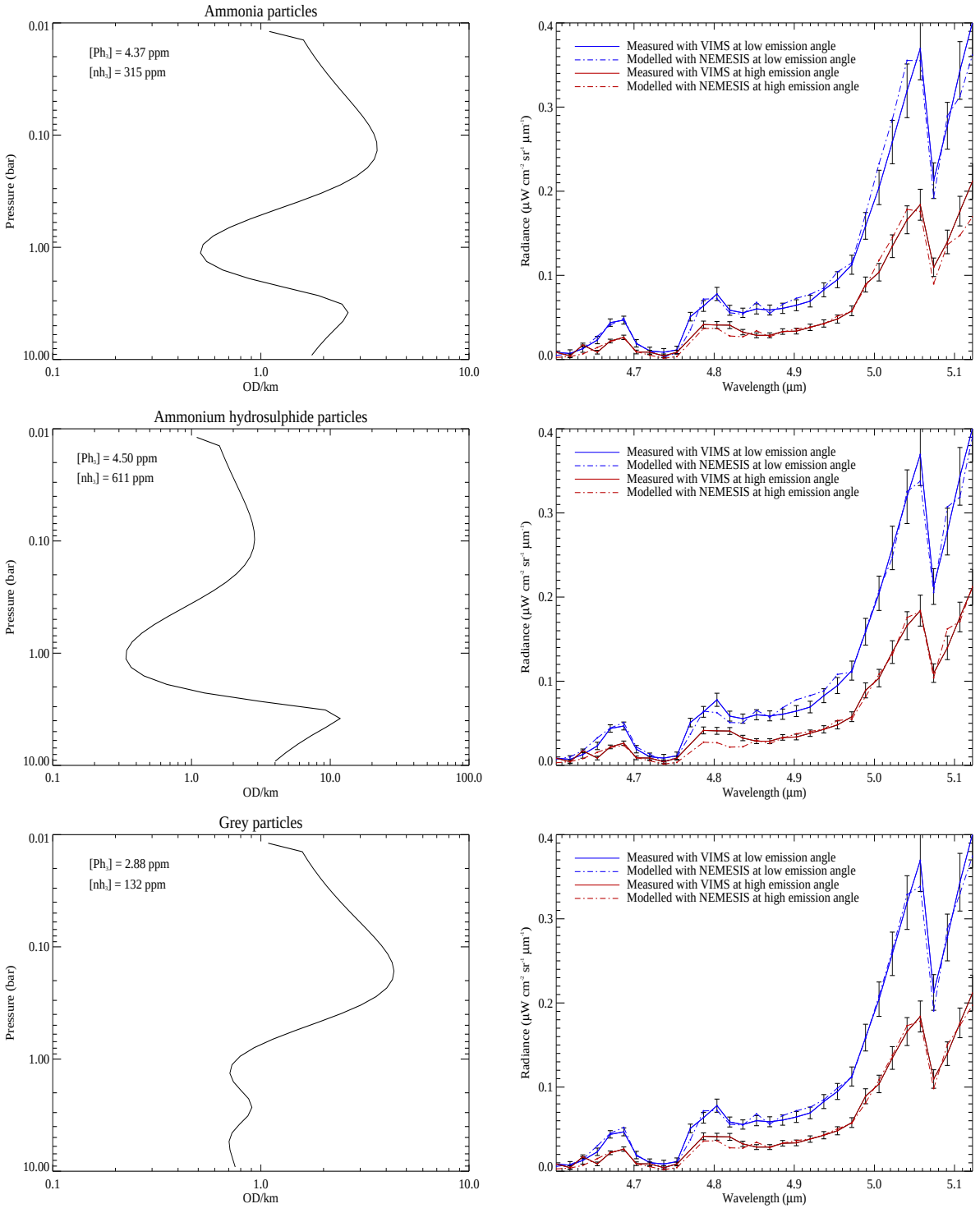



Figure 4.17: Limb-darkening analysis for a continuous aerosol opacity model in the scattering case. Three composition are assumed over the pressure range 0.01-10 bar: ammonia, ammonium hydrosulphide and grey aerosol particles. NEMESIS retrieved a continuous opacity profile from an *a priori* profile, as well as the deep volume mixing ratios of phosphine and ammonia. The optical depths per bar at 5 $\mu$m are shown at each pressure level in the left panels. For all three particle types, NEMESIS returned two clouds, one at 2-4 bar and the other near 100 mbar. The modelled and measured thermal emission spectra at low and high emission angles are shown in the right panels for each cloud composition.

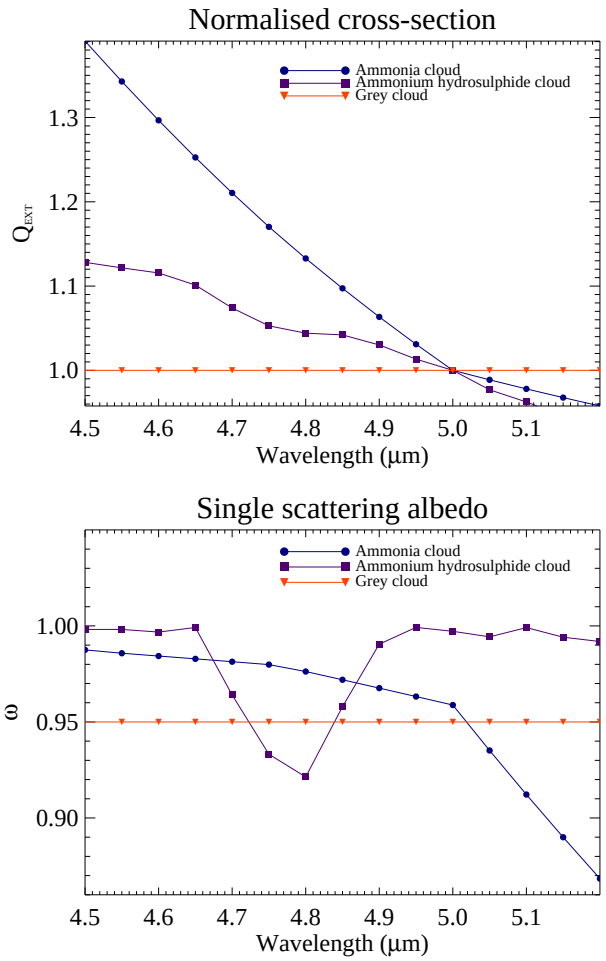



Figure 4.18: Extinction coefficients and single scattering albedos of ammonia, ammonium hydrosulphide and grey particles in the 4.6-5.1 $\mu$m wavelength range (Martonchik *et al.*, 1984; Howett *et al.*, 2007; )

The variation of aerosol opacities between the three cloud compositions are likely to be due to spectral differences of the optical properties of these molecules. The extinction coefficients and single scattering albedos vary significantly between the cloud models as seen in Fig. 4.18. These variations lead to different retrieved values of phosphine and ammonia abundances. The cloud and haze are not expected to have the same composition, and so the continuous aerosol opacity model can only confirm that Saturn's 5-$\mu$m window is sensitive to two scattering opacity sources: at least one tropospheric cloud, and the haze located above the cloud layers. The haze altitude cannot be precisely determined from the limb-darkening analysis. Also, adding another opacity source increases the number of free parameters in the retrieval algorithm leading to more uncertainties on the cloud and haze composition. In the next chapter, dayside reflection spectra of Saturn are analysed in order to better constrain the haze composition and vertical structure.

### 4.4.3 North-south limb-darkening analysis

In the previous section, the limb-darkening analysis was carried out at a specific latitude of approximately 20° in the southern atmosphere. The retrieval strategy has shown the necessity of including both scattering and a secondary aerosol layer above the tropospheric cloud. In this section, the "1 layer" and "2 layers" cloud models are compared in the non-scattering and scattering cases at various latitudes in the southern and northern hemispheres. The low and high emission angle spectra are extracted from respectively the VIMS spectral cube CM1517773991 measured respectively on 6 February 2006 at $07^h20^m42.267^s$ and the VIMS spectral cube CM1517945348 measured on 7 February 2006 at $07^h02^m39.375^s$. The latitude, longitude and emission angle of each spectrum considered in the limb-darkening analysis are shown in Table 4.4. Since the VIMS spectral cubes were acquired at different days, the pixels at low and high emission angles were selected so that the same cloud structure was sounded. Three aerosol models are considered for the deep tropospheric model: one compact ammonia cloud, one compact ammonium hydrosulphide cloud and one grey cloud. The aerosol particle size is assumed to be equal to 1 $\mu$m. The haze layer is placed at a fixed 0.11-bar pressure level. The deep cloud base is set at a variable pressure in the range 0.01-10 bar. In the "1 layer" cloud model, only the deep cloud is included in the reference atmosphere, whereas both the haze and cloud are considered in the "2 layers" cloud model. The aerosol opacity and deep volume mixing ratios of phosphine and ammonia are retrieved with the numerical code NEMESIS simultaneously from low and high emission angle spectra. The modelled radiances at 5.05 $\mu$m are compared to the observations in Fig. 4.19 for all cloud models in the non-scattering and scattering cases. The modelled radiances calculated for purely absorptive aerosol particles fail at maching VIMS limb-darkening data. This is observed for all latitudes in the southern and northern hemispheres. However, VIMS limb-darkening data are in good agreement with the model at all latitudes if scattering is implemented in the radiative transfer algorithm. Therefore, the same conclusion drawn for the analysis of VIMS data at 20°N holds for other latitudes: only scattering aerosol particles can match VIMS limb-darkening data quite well. Also, the fit to the observations is improved if a secondary layer is included on top of the cloud layer, especially in the southern hemisphere. Finally, this section only focuses on North-South variations, however meridional variations will be addressed more extensively in the following chapters.

| | LATITUDE | LONGITUDE | EMISSION ANGLE |
|---|---|---|---|
| 50°N | 50.25° ± 2.63° | 180.32° ± 4.11° | 44.87° ± 3.76° |
| | 50.73° ± 2.97° | 182.35° ± 4.65° | 76.34° ± 5.01° |
| 40°N | 39.87° ± 2.41° | 184.02° ± 3.77° | 32.65° ± 2.89° |
| | 40.21° ± 2.65° | 182.98° ± 3.83° | 69.02° ± 3.26° |
| 30°N | 30.65° ± 2.32° | 179.76° ± 3.21° | 30.54° ± 2.69° |
| | 31.06° ± 2.45° | 181.18° ± 3.76° | 65.98° ± 3.00° |
| 20°N | 20.22° ± 2.27° | 178.98° ± 3.16° | 21.98° ± 2.22° |
| | 19.78° ± 2.33° | 180.11° ± 3.23° | 62.76° ± 2.99° |
| 10°N | 10.05° ± 1.98° | 179.09° ± 2.05° | 17.54° ± 2.00° |
| | 9.98° ± 2.02° | 180.01° ± 2.17° | 60.99° ± 2.34° |
| 0° | 0.15° ± 1.32° | 183.90° ± 1.79° | 15.62° ± 1.53° |
| | 0.11° ± 0.15° | 179.54° ± 2.21° | 60.12° ± 2.27° |
| 10°S | -10.13° ± 1.87° | 178.87° ± 2.03° | 18.12° ± 2.13° |
| | -10.02° ± 2.21° | 179.13° ± 2.23° | 62.02° ± 2.47° |
| 20°S | -20.76° ± 2.81° | 180.09° ± 2.95° | 20.32° ± 1.97° |
| | -20.43° ± 2.52∘ | 180.45° ± 3.54° | 64.75° ± 3.05° |
| 30°S | -29.85° ± 2.98° | 178.97° ± 3.33° | 32.37° ± 2.71° |
| | -30.00° ± 2.91° | 181.01° ± 3.97° | 70.11° ± 3.12° |
| 40°S | -40.05° ± 2.34° | 183.34° ± 3.32° | 39.04° ± 3.03° |
| | -39.23° ± 3.02° | 184.56° ± 4.05° | 74.21° ± 4.20° |
| 50°S | -51.09° ± 3.54° | 180.34° ± 3.98° | 46.98° ± 3.65° |
| | -52.13° ± 3.98° | 178.45° ± 4.20° | 77.43° ± 4.43° |

Table 4.4: Viewing geometries of VIMS limb-darkening data at various latitudes between 50°S and 50°N. VIMS spectra at low and high emission angles are extracted from VIMS spectral cubes CM1517773991 and CM1517945348 measured respectively on 6 February 2006 at $07^h20^m42.267^s$, and on 7 February 2006 at $07^h02^m39.375^s$. For each latitude, the latitude, longitude and emission angles are presented for the low and high emission angle spectra.

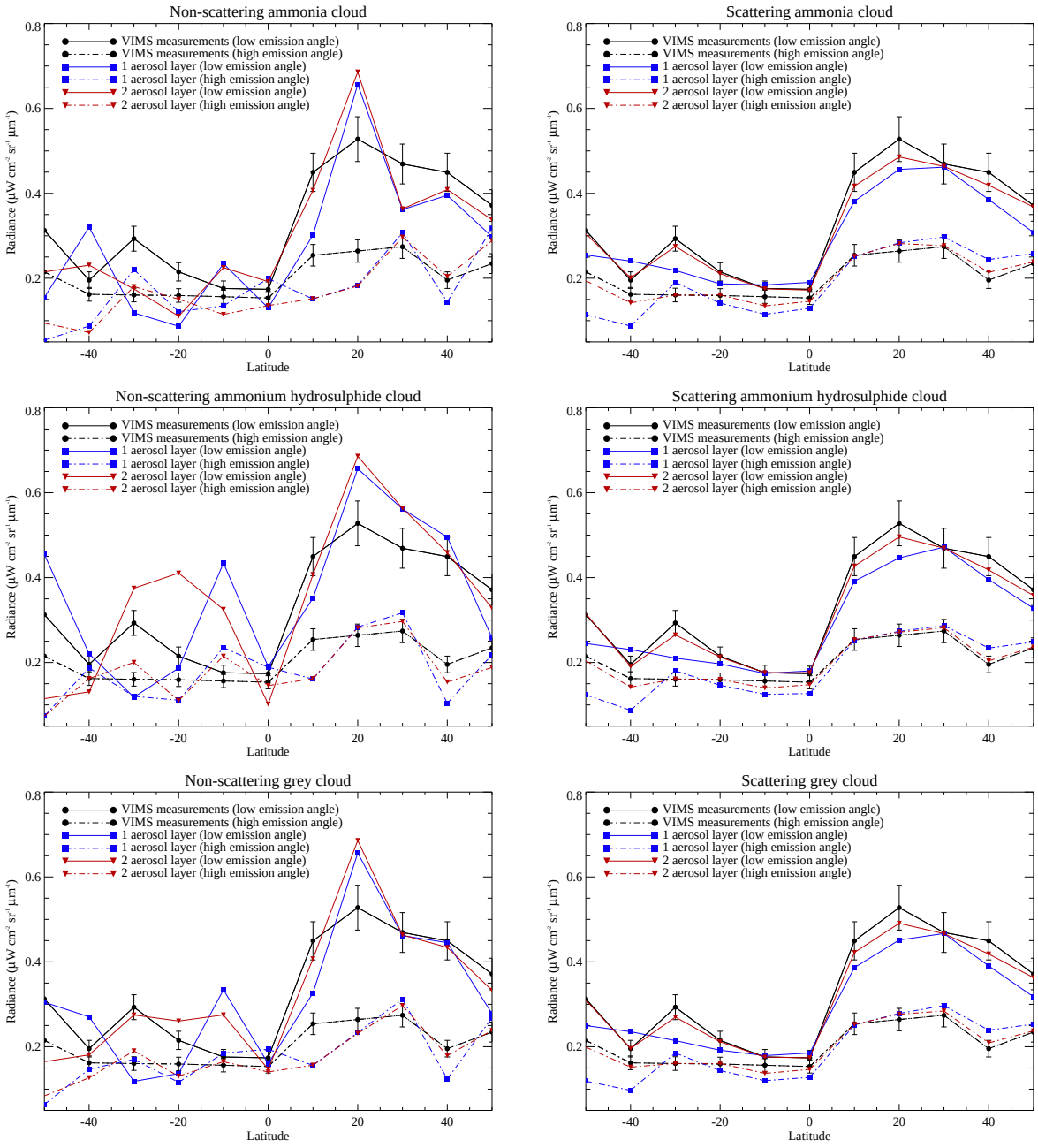



Figure 4.19: Limb-darkening analysis at various latitudes for one and two compact aerosol layers. 5.05-$\mu$m radiances at low (dot-dashed line) and high (solid line) emission angles are plotted as a function of the latitude in both panels. VIMS data are extracted from the spectral cubes CM1517773991 and CM1517945348 acquired respectively on 6 February 2006 at $07^h20^m42.267^s$, and on 7 February 2006 at $07^h02^m39.375^s$. The deep tropospheric cloud is assumed to be made of aerosol particles with a radius of 1 $\mu$m in the non-scattering (*top panel*) and scattering (*bottom panel*) cases. Three cloud compositions are assumed here, consisting of ammonia ice, ammonium hydrosulphice and grey aerosol particles. A single scattering albedo of 0.95 and an isotropic phase functions are assumed for the grey cloud and haze layer. The cloud layer is included in both the "1 aerosol layer" (blue line) and "2 aerosol layers" (red line) models. The haze layer above the cloud is included only in the "2 aerosol layers" model. The haze layer is placed below the tropopause at the 0.11-bar pressure level. The modelled radiances are shown for the best-fitting value of the cloud base pressure which ranges between 2.3 and 2.7 bar.

## 4.5 Summary

In Chapter 4, Saturn's near-infared thermal emission spectra between 4.6 and 5.1 $\mu$m measured with VIMS are analysed in order to retrieve the tropospheric cloud properties and the deep abundances of phosphine and ammonia. Indeed, gas and aerosol opacities in the stratosphere and upper troposphere of the planet become less important at longer near-infrared wavelengths. As a result, the infrared channel of the VIMS instrument on board the spacecraft Cassini can sound at deeper tropospheric levels where clouds are expected to condense from thermochemical equilibrium theories. The contribution weighting functions for a cloud-free atmosphere have demonstrated that most of the gaseous absorption in the 5-$\mu$m window occurs between 1 and 5 bar. Phosphine is the main gaseous absorber in the 4.6-5.1 $\mu$m, with a minor contribution from ammonia. Thermochemical equilibrium models predict the formation of ammonia and ammonium hydrosulphide clouds in the 2-6 bar pressure range. The contribution weighting functions for an atmospheric model including tropospheric clouds have shown that both aerosols and gases contribute to the absorption at 5 $\mu$m.

At first, single spectra measured for a specific viewing geometry are analysed. The aerosol opacities and deep volume mixing ratios of phosphine are retrieved with the numerical code NEMESIS for various cloud models. The cloud model consists of one compact cloud located at a variable pressure level. Three cloud compositions are assumed in this chapter: an ammonia cloud, an ammonium hydrosulphide cloud and a grey cloud, for scattering and non-scattering conditions. The aerosol opacities and gas abundances are retrieved for a variable cloud base pressure and aerosol particle radius in the ranges 0.01-10 bar and 0.1-10 $\mu$m respectively. None of the cloud composition could be ruled out, and a good agreement between the model and the data was generally found for various values of the cloud base pressure and aerosol particle size. Also, both purely absorptive and scattering aerosol particles manage to fit the observations quite well within the measurement errors.

The aerosol opacities and gase abundances retrieved with NEMESIS are largely dependent on the atmospheric model assumed in the numerical code. Therefore, the next step was to constrain the cloud model much more by considering VIMS limb-darkening data. Spectra measured at similar latitude and longitude onto the planet but at different emission angles are also analysed in this chapter. Such data can be considered as independent measurements of the same physical quantity, and as a result they can be used in order to constrain the cloud properties.

A similar "one compact cloud model" as in the first part of this chapter is first considered in the limb-darkening analysis. The cloud opacities, and deep volume mixing ratios of phosphine and ammonia are retrieved with NEMESIS simultaneously from low and high emission angle spectra. None of the cloud model managed to match the observations in the non-scattering and scattering cases. This shows that limb-darkening analysis is expectedly a more efficient strategy for rulling out aerosol models than the analysis of single spectra. An "extended cloud model" consisting of a variable cloud base pressure and vertical extension is assumed instead. This model fails at modelling VIMS limb-darkening data in the non-scattering case. However, synthetic spectra for a scattering cloud with a large extension are similar to the measured data both at low and high emission angles within the measurement errors. Very large extensions of the tropopsheric cloud are in contradiction with the aerosol vertical structure expected from thermochemical equilibrium theories. However, this result suggests that Saturn's 5-$\mu$m window is very likely to be sensitive to hazes above the cloud layers. The sensitivity of Saturn's 5-$\mu$m window was tested by considering two different cloud models consisting of two compact aerosol layers and one continuous aerosol profile. Both models have shown than a secondary aerosol layer must be implemented in the atmospheric model at higher altitudes above the tropospheric cloud. This confirms the results obtained by Fletcher *et al.* (2011) who showed that the fit to VIMS infared data was improved by adding a thin tropospheric haze layer. However, they also managed to fit the observations quite well within the measurement errors with only one deeper tropospheric cloud. The limb-darkening analysis developed in this thesis has shown that a one-cloud scheme could not match the observations, therefore validating the use of a haze layer on top of the deep cloud. Besides, the limb-darkening analysis has shown that both the haze and cloud must be scattering in order to fit limb-darkening data. However, the haze composition and vertical distribution are very poorly constrained at 5 $\mu$m. The limb-darkening analysis has been carried out first at approximately 20°S, and then extended to all north-south latitudes between 50°S and 50°N. Closer fits to the limb-darkening data are obtained for two aerosol layers in the scattering case. This is observed at all latitudes, especially in the southern hemisphere. The discrepancies between the "one aerosol layer" and "two aerosol layer" models are smaller in the northern hemisphere, although lower $\chi/N_\lambda$ values are obtained for the "one aerosol layer" model. In the next chapter, near-infrared reflection spectra in the 0.8-3.5 $\mu$m wavelength range are analysed in order to study the optical and physical properties, as well as the vertical structure of the upper tropospheric and stratospheric haze.

Chapter 5

# Saturn's hazes from VIMS near-infrared reflection spectra

*The analysis and results described in this chapter are entirely my own. Referenced contributions from external works are also included in order to allow further discussions on the results.*

## 5.1 Saturn's spectrum at 0.8-3.5 $\mu$m

The dayside near-infrared spectra of Saturn in the 0.8-3.5 $\mu$m wavelength range are made of six distinctive peaks (see Fig. 5.1). These features are the result of strong gaseous absorption of the continuum at 0.90, 1.01, 1.17, 1.40, 1.75, and 2.25 $\mu$m (Clark *et al.*, 1979). Methane is the main gaseous absorber with many absorption bands between 0.8 and 3.5 $\mu$m. Ammonia, hydrogen, and phosphine also contribute to the absorption of the continuum at these wavelengths (Baines *et al.*, 2005; Butler *et al.*, 2005) as seen in Fig.5.1. In particular, the 1-0 band pressure-induced absorption due to molecular hydrogen dominates the 2.0-2.5 $\mu$m spectral region. The continuum is made by the scattering of sunlight in Saturn's atmosphere by the tropospheric and stratospheric hazes[1], so spectral features at 0.8-3.5 $\mu$m are only present in dayside spectra (Baines *et al.*, 2005). The sunlight is continuously scattered back into the direction of the spacecraft, except at specific wavelengths corresponding to gaseous absorption bands. Therefore, the 0.8-3.5 $\mu$m spectra and the individual peaks can be equally referred to as the reflection spectra and the reflection peaks.

[1] Tropospheric hazes accounts for most of Saturn's near-infrared spectra in the 0.8-3.5 $\mu$m spectral range, with perhaps a contribution from hazes in the lower stratosphere. The sunlight is still scattered back from hazes at higher altitude in the stratosphere, but such a signal is not detected in the 0.8-3.5 $\mu$m spectra except in the absorption bands.

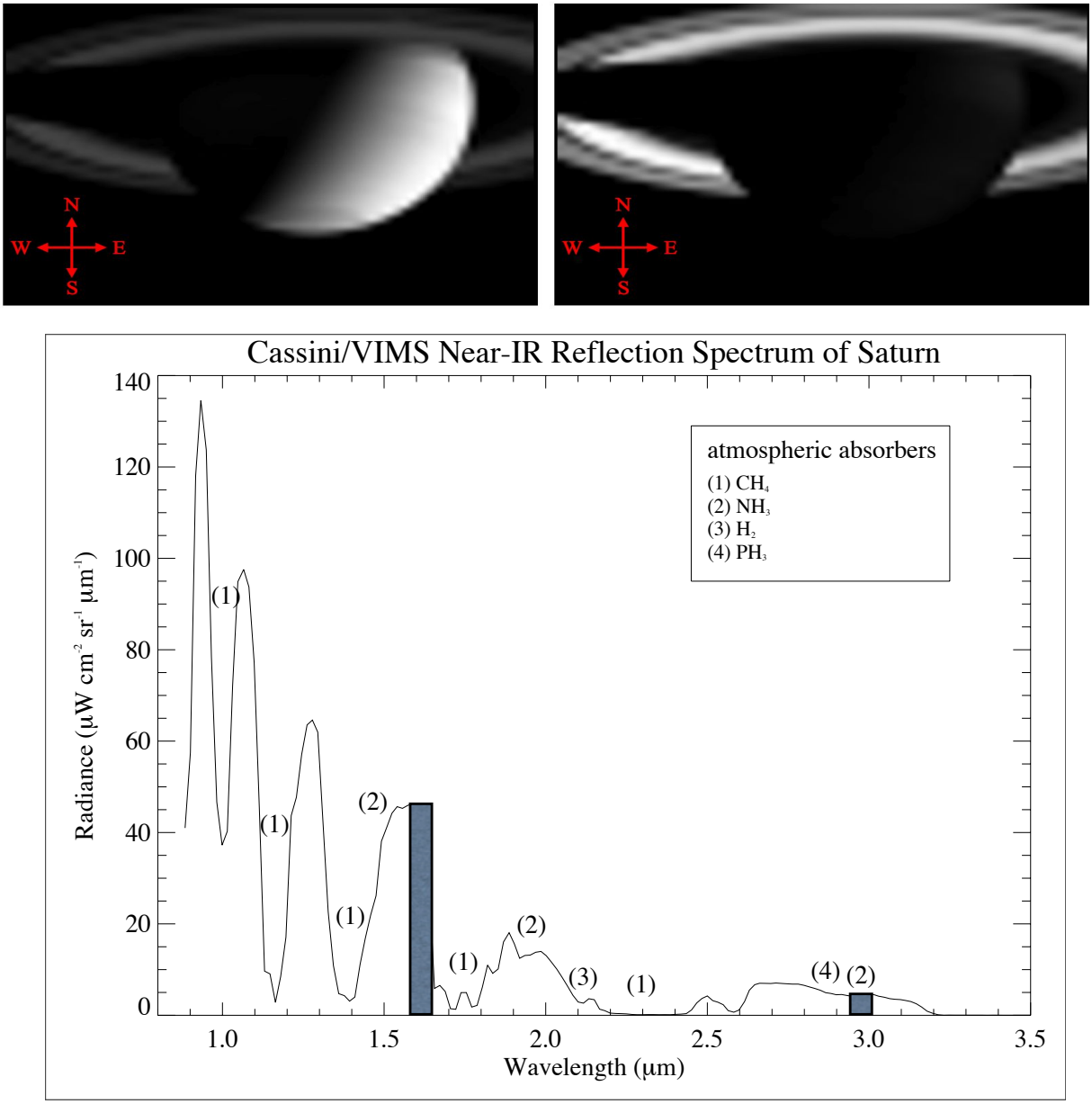



Figure 5.1: VIMS near-infrared reflection images and spectrum of Saturn. *Top:* VIMS images of Saturn at 1.07 $\mu$m (*left*) and 1.40 $\mu$m (*right*). These images are extracted from the VIMS cube CM1469004529 acquired on 20 July 2004 at $08^h24^m23.889^s$. The bright pixels in the 1.07 $\mu$m image correspond to the reflection of sunlight by the planet's hazes and rings. In contrast to Saturn's image at 5.06 $\mu$m, radiation at 1.07 $\mu$m is homogeneously distributed over the whole dayside area of the planet (here, on the right side of VIMS image). The sunlight scattered by tropospheric aerosols is absorbed at 1.40 $\mu$m by gaseous methane located at higher altitude levels. Therefore the planet is dark at this wavelength, while scattering of sunlight by Saturn's rings is still measured. *Bottom:* Dayside near-infrared reflection spectrum of Saturn at 0.8-3.5 $\mu$m. The spectrum is also extracted from the spectral cube CM1469004529. The selected spectrum is measured at a latitude of 4° ± 1.72°, a longitude of 185° ± 1.93° an emission angle of 61° ± 2.05°, a solar angle of 51° ± 1.87° and an azimuthal angle of 58° ± 1.90°. The regions shown in blue have low signal quality and so are ignored in the analysis of VIMS reflection data (Sromovsky *et al.*, 2010).

Two typical VIMS images at 1.07 and 1.40 $\mu$m are shown in Fig. 5.1. At the 1.07-$\mu$m reflection peak, tropospheric and stratospheric aerosols as well as Saturn's rings reflect the sunlight, and so VIMS image appears bright at daytime. The dark pixels on the planet's surface are measured at solar angles above 90°, and so there is no signal at nighttime in the 0.8-3.5 $\mu$m wavelength range. Gaseous absorption at 1.40 $\mu$m, mainly from methane, prevents the detection of scattered sunlight from the deeper clouds. As a result, the whole area of Saturn is dark at 1.40 $\mu$m, and in all absorption bands, leading to the presence of troughs in Saturn's reflection spectra.

Note that the signal between 1.60 and 1.65 $\mu$m, where two filters overlap, has a very low quality, and so this spectral range is ignored in the analysis of VIMS data. There is also another joint at 2.98 $\mu$m where response corrections are poor. Sromovsky *et al.* (2010) noticed yet another VIMS artefact in the reflection spectra of Jupiter. They observed an enhancement of radiance at 2.3 $\mu$m probably due to light scattered by the grating of the infrared channel. This feature is not present in the VIMS spectra of Saturn. Indeed, no significant signal in the gaseous absorption bands is measured by the VIMS instrument except in the methane absorption band at 1.01 $\mu$m. In Fig. 5.2, a typical VIMS dayside spectrum is compared with Saturn's reflection spectrum as measured by the SpeX instrument mounted on the NASA Infrared Telescope Facility (IRTF) in Mauna Kea (Rayner *et al.*, 2009). A similar feature is observed in the SpeX spectrum, and so the high reflectance at 1.01 $\mu$m is unlikely to be an artefact correlated to VIMS instrumentation.

A limit on the vertical location of the near-infrared scatterers can be inferred by mapping the two-way transmision weighting functions for an aerosol-free atmosphere (see Fig. 5.3). Assuming no aerosols are present in Saturn's atmosphere, gaseous absorption only contributes to the total opacity of the planet's atmosphere in the 0.8-3.5 $\mu$m wavelength range. The two-way transmission weighting functions are derived from the transmission functions to and from the reflective layers at each pressure level. They show the pressure levels at which gases absorb the reflected sunlight. At the first four reflection peaks, absorption is significant at pressures higher than 1 bar, and so only scatterers located above this level can contribute to the reflection spectrum. At the fifth and sixth reflection peaks, the near-infared signal is absorbed at lower pressures, respectively at 300 and 600 mbar. In between the reflection peaks, absorption starts above the tropopause at $\sim$100 mbar and extends throughout the lower stratosphere up to $\sim$10 mbar. Therefore, the scatterers detected in the 0.8-3.5 $\mu$m spectral range must be located deeper than the 10 mbar level, or else they would contribute significantly to

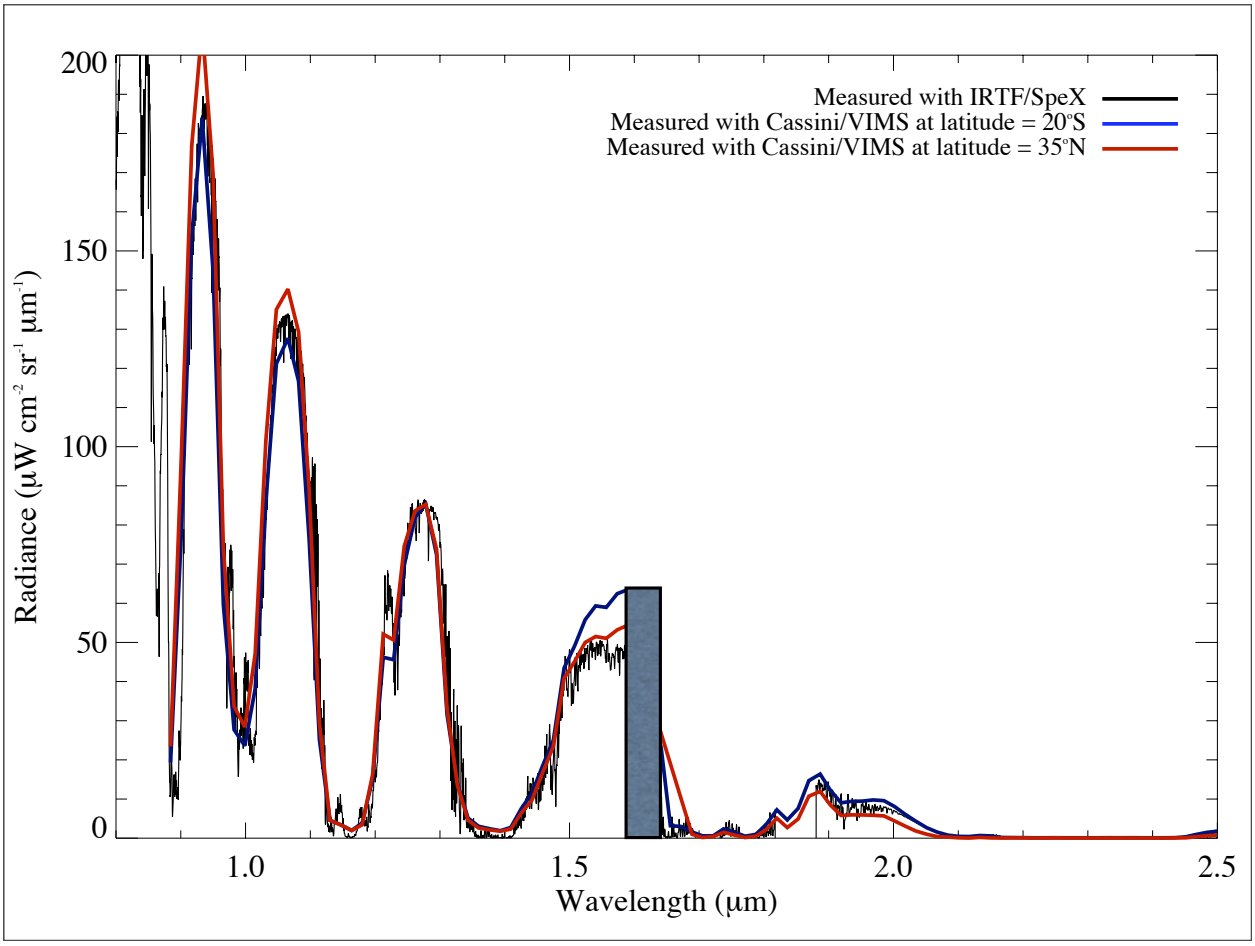



Figure 5.2: Comparison of VIMS and SpeX near-infrared reflection spectra of Saturn.Two VIMS spectra are extracted from the spectral cube CM1564373826 acquired on 29 July 2007 at a latitude of 20°S and 35°N. SpeX spectra are measured on May 2007 and co-added along the central meridian (Rayner *et al.*, 2009). All spectra are scaled to the VIMS spectrum measured at a latitude of 20°S. The change in reflectance at 1.50 $\mu$m is due to latitudinal variations of aerosol opacity. The high reflectance in the first absorption band at 1.01 $\mu$m is observed in all VIMS measurements and also in the SpeX spectrum. Therefore, this feature is unlikely to be a VIMS artefact and is probably formed by scattering of sunlight by hazes located at upper stratospheric levels.

the spectrum in the absorption bands. Note that aerosols present higher in the stratosphere can only be detected in the absorption bands. However, the signal at such wavelengths is very low as can be seen in Fig. 5.1 and Fig. 5.2. This is because the optical depth of such hazes is low and the particles are very small leading to a rapid decrease of opacity with wavelength. Stratospheric hazes have typical sizes in the range 0.1-0.2 $\mu$m (Karkoschka and Tomasko, 1993, 2005; Muñoz *et al.*, 1994; Pérez-Hoyos *et al.*, 2005) smaller than wavelengths ($\lambda$) in the near-infrared. The interaction of small stratospheric aerosols with near-infrared radiation, described by Rayleigh theory, is proportional to $\lambda^{-4}$. Therefore the opacities of such hazes may be important at visible wavelengths but are very low in the 0.8-3.5 $\mu$m spectral range.

Saturn's near-infrared reflection spectra are then particularly valuable for surveying the composition and vertical distribution of aerosols located at pressures lower than 1 bar. In conclusion, this chapter focuses on the determination of the optical and physical properties, as well as the vertical distribution of tropospheric and stratospheric hazes by analysing Saturn's near-infrared reflection spectra measured with the VIMS instrument.

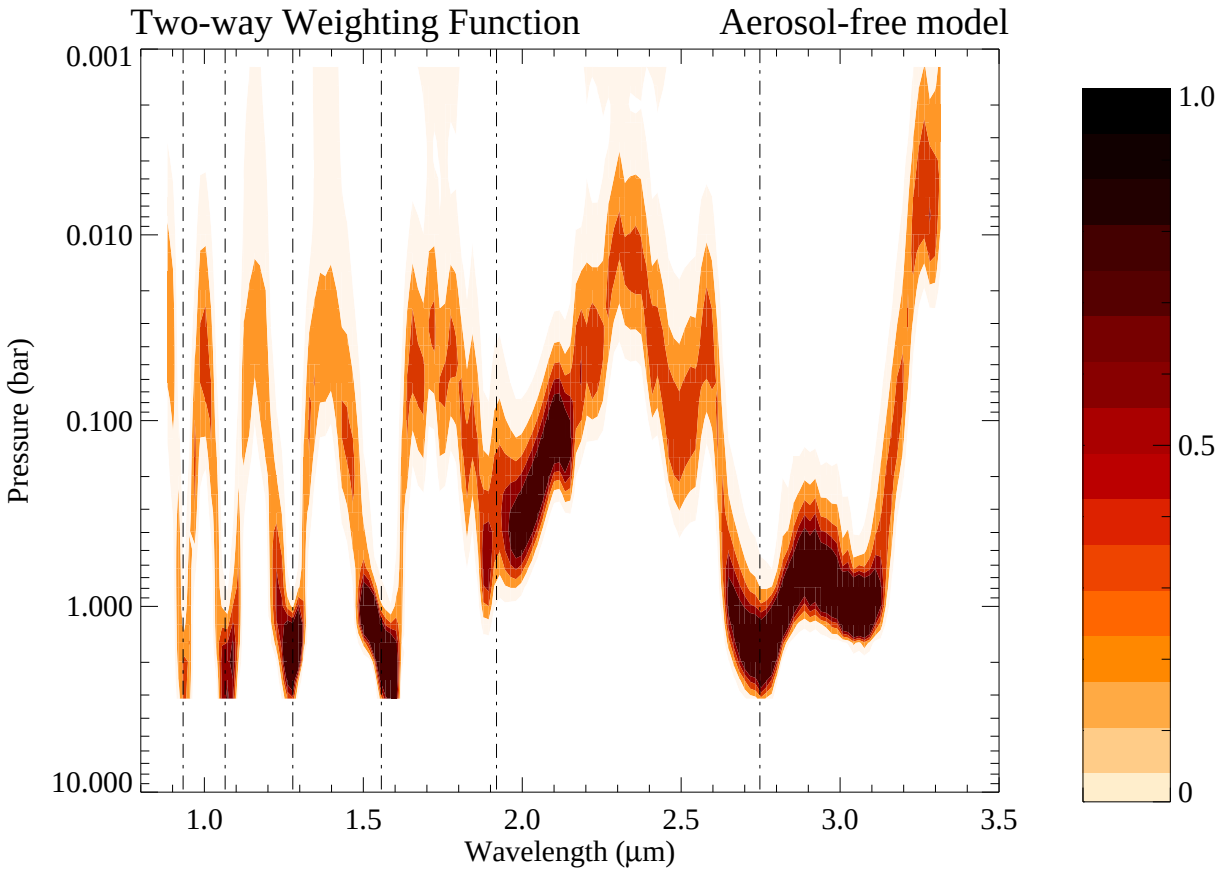



Figure 5.3: Normalised two-way transmission weighting functions for an aerosol-free atmosphere. The weighting functions at each wavelength are derived from the two-way transmission function calculated to and from each atmospheric level. The calculation is made assuming that no aerosols are present in Saturn's troposphere and stratosphere. As a result, the only source of near-infared opacity is gaseous absorption. Rayleigh scattering by atmospheric gases is also included in the calculation of the transmission functions. The dot-dashed lines show the position of the six reflection peaks. The two-way contribution weighting functions were normalised to 1.

## 5.2 Modelling VIMS near-infrared reflection spectra

### 5.2.1 Reference atmosphere

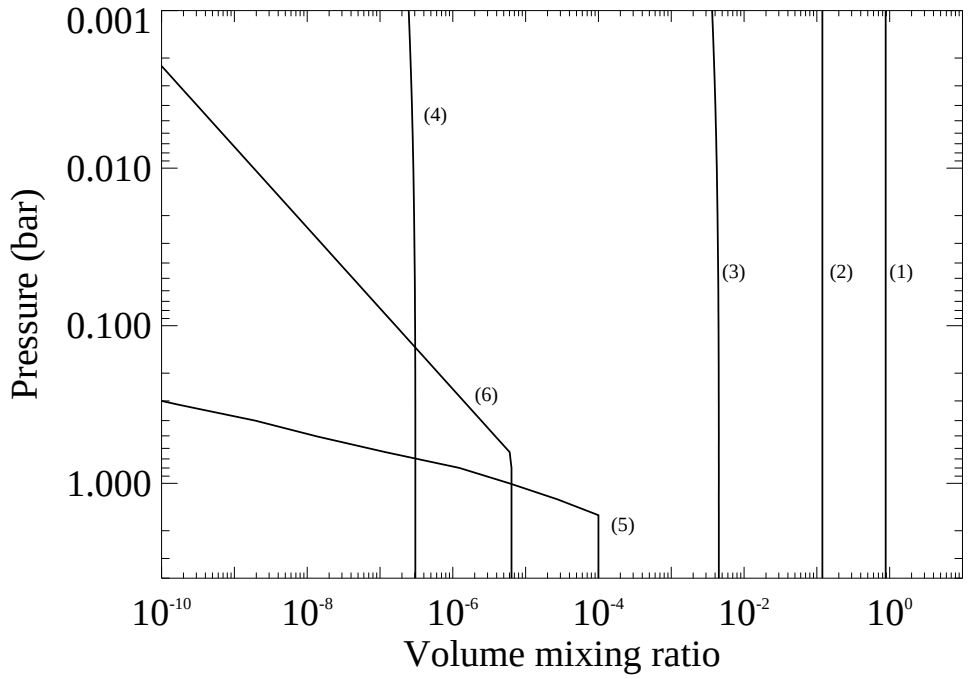



Figure 5.4: Vertical distribution of gases in Saturn's reference atmosphere for the analysis of VIMS reflection spectra. The volume mixing ratios of $H_2$ (1), He (2) (Conrath *et al.*, 2000), $CH_4$ (3), $CH_3D$ (4), $NH_3$ (5) and $PH_3$ (6) (Fletcher *et al.*, 2009) between 1 mbar and 4 bar are integrated into the radiative transfer algorithm. Methane is the main gaseous absorber at 0.8-3.5 $\mu$m, with minor contribution from ammonia, hydrogen and phosphine.

As for the analysis of Saturn's thermal emission at 5 $\mu$m, a reference atmosphere must be integrated into the radiative transfer numerical code in order to generate Saturn's synthetic spectra at 0.8-3.5 $\mu$m. This includes the temperature profile, as well as the gas abundance profiles and absorption coefficients. The VIMS instrument in the near-infrared sounds higher altitudes at lower wavelengths. Thus, the reference atmosphere is defined for 37 pressure levels between 1 mbar and 4 bar, equally spaced in logarithm scale with $\Delta \log_{10} p \sim 0.1$. For each selected VIMS near-infrared data set, the temperature profiles are calculated from CIRS mid- and far-infrared spectra at similar observation time, latitude and longitude, using the method described by Fletcher *et al.* (2007). The vertical profiles of methane ($CH_4$), ammonia ($NH_3$), hydrogen ($H_2$) and phosphine ($PH_3$) are included into the reference atmosphere, since they absorb the near-infrared continuum spectrum in the 0.8-3.5 $\mu$m

wavelength range. Helium (He) and the second isotope of methane ($CH_3D$) are also added to the model, because of their relatively high abundance in Saturn's troposphere and stratosphere. In the end, Saturn's reference atmosphere comprises a total of 6 different gases whose vertical distributions are shown in Fig. 5.4. For each gas except $CH_4$ and $CH_3D$, the absorption coefficients at 0.8-3.5 $\mu$m are generated over the 0.001-4 bar pressure range from the GEISA2003 (Jacquinet-Husson *et al.*, 2005) and HITRAN2008 (Rothman *et al.*, 2009) line databases. The k-distributions of $CH_4$ and $CH_3D$ are calculated by Irwin *et al.* (2005) from laboratory measurements of methane transmission spectra in the near-infrared (Strong*et al.*, 1993; Sihra, 1998).

### 5.2.2 Aerosol-free atmosphere

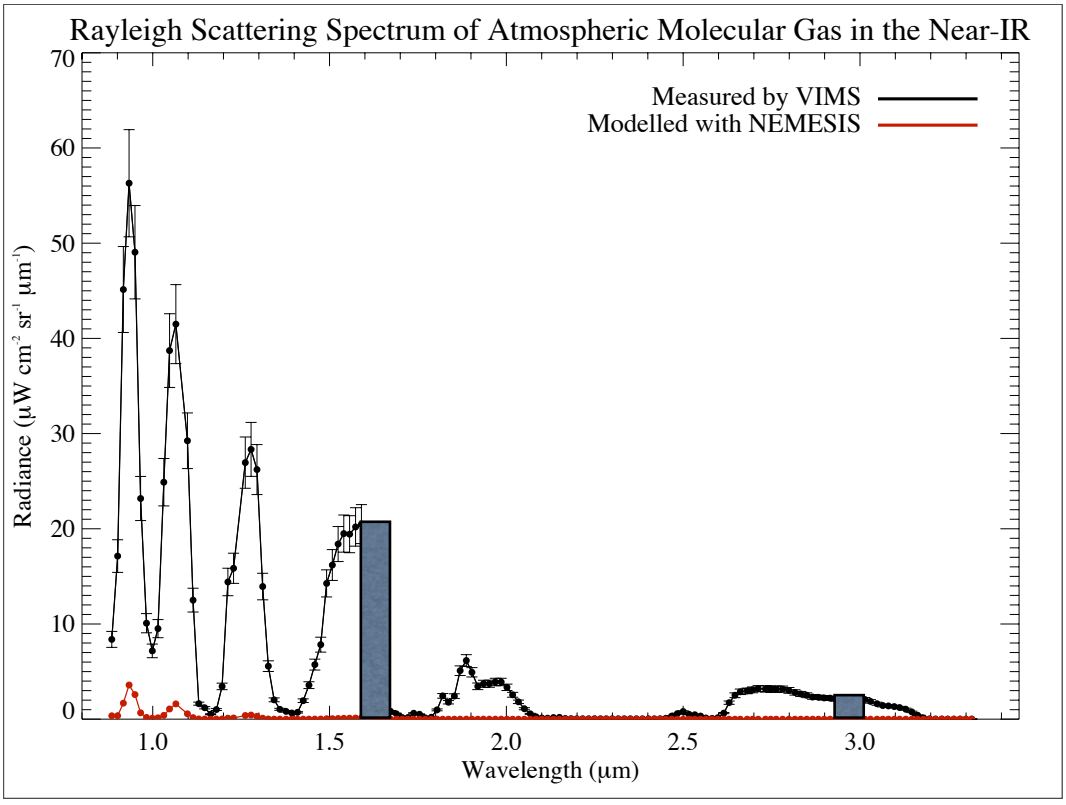



Figure 5.5: Effects of Rayleigh scattering by tropospheric and stratospheric gases on Saturn's near-infared reflection spectrum. The VIMS spectral cube CM1524386400 was measured on 26 April 2006 at $08^h09^m37.759^s$. The dayside spectrum was extracted a latitude of - 19.93° ± 1.67° and a longitude of 108.06° ± 2.34° at daytime. The solar, emission and azimuth angles are respectively 76.48° ± 2.26°, 38.49° ± 2.39° and 7.59° ± 2.17°. The modelled spectrum is generated with NEMESIS assuming that no aerosols are present in Saturn's atmosphere. Therefore only tropospheric and stratospheric gases scatter the near-infrared sunlight radiation. Comparison between the observed and synthetic spectra of Saturn shows that Rayleigh scattering contributes very little to the planet's reflection spectra. Therefore, Mie scattering from aerosol particles is expected to account for the shape of Saturn's spectra at 0.8-3.5 $\mu$m.

Molecular gases and aerosol particles are the two main opacity sources in Saturn's troposphere and stratosphere by absorbing and scattering near-infrared radiation. These effects must be taken into account in the radiative transfer model in order to generate Saturn's synthetic spectra at the same spectral range as VIMS instrument. In the radiative transfer model, scattering of sunlight by gases and aerosol particles are respectively described by Rayleigh and Mie scattering theories. The synthetic reflection spectrum generated by NEMESIS for an atmosphere free of aerosols is shown in Fig. 5.5. The only scatterers present in this atmospheric model are then molecular gases, which can deviate the sunlight through Rayleigh scattering. Rayleigh theory states that the ratio between emitted and incident radiation decreases with wavelength. Therefore, Rayleigh scattering by gases should dominate Saturn's reflection spectra at lower wavelengths.

The synthetic spectrum shows two distinctive signals at the spectral position of the first two peaks. The radiances of these peaks are respectively $\sim 4$ and $\sim 2$ $\mu$W cm$^{-2}$sr$^{-1}\mu$m$^{-1}$. Comparison with VIMS spectra measured at the same latitude and longitude, and for identical solar and emission angles shows that Rayleigh emission from molecular gases is very small compared to measurements. Therefore, this effect cannot account for the 0.8-3.5 $\mu$m spectrum and so aerosols are the main scatterers at these wavelengths.

## 5.3 Optical and physical properties of Saturn's hazes

### 5.3.1 Strategy

Hazes in Saturn's troposphere and stratosphere are expected to extend over a few scale heights (Karkoschka and Tomasko, 1993). Therefore, a compact layer model as assumed for tropospheric clouds is unlikely to be a good representation of the haze vertical distribution in Saturn's atmosphere. Instead, the haze vertical distribution is retrieved from a continuous *a priori* vertical profile with NEMESIS. In this way, no particular vertical distribution is assumed in the haze model. This also means that the number of retrieved paramaters is higher than for a compact model. Indeed, the retrieval algorithm estimates the aerosol specific density in number of particles per gram at each of the 37 pressure levels in the reference atmosphere.

The aerosol concentration in number of particles per cubic centimetre can be estimated by multi-

plying the specific density with the atmospheric density at each pressure level. The *a priori* value of the specific density is fixed to a constant value at all pressure levels. Different *a priori* values were tested and a value of $10^4$ was finally adopted since it provided a better fit to the data. The *a priori* errors were chosen so that to balance the measurements with the *a priori* constaints (Irwin *et al.*, 2007).

Note that this section focuses on the particle properties in Saturn's haze. However, the vertical profile of the aerosol concentration, as well as its sensitivity to the *a priori* profile are discussed in the next section. Unlike the fitting strategy applied to Saturn's 5-$\mu$m window, no gas abundance is retrieved from near-infrared reflection spectra, and so there are no additional retrieved parameters in the model. Finally, a correlation length between the different pressure levels equal to 1.5 is assumed in the model.

In addition to the vertical distribution, the input parameters characterising the physical and optical haze properties in the numerical code are: the extinction coefficient, the scattering albedo, and the three Henyey-Greenstein coefficients $f$, $g_1$, and $g_2$. Each parameter is expected to vary with wavelength and so should be defined properly at each spectral point. Assuming that there are $N_\lambda$ wavelengths in the spectrum, the retrieval problem has then $5N_\lambda$ free parameters. Although it is very unlikely that all sets of parameters would fit the VIMS near-infrared reflection spectra, it is practically impossible to try all of them. Indeed, each of the five parameters can take an infinite number of values. Then, the 0.8-3.5 $\mu$m VIMS spectrum contains 146 wavelengths, which gives more than 730 degrees of freedom to the retrieval problem. Furthermore, the retrieval problem might be highly degenerate and so many combinations of the five parameters could potentially fit VIMS data. This is especially true for large spectra spread over many wavelengths, such as Saturn's near-infrared reflection spectra. On one hand, a high number of measurements further constrains solutions to the retrieval problem, but on the other hand it also increases the number of wavelength-dependent free parameters in the model. Finally, very little is known about the actual values of the extinction coefficient, scattering albedo, and Henyey-Greenstein coefficients, as well as their dependency with wavelength, and so it is very likely that no distinction could be made amongst all possible solutions.

Another approach is adopted here for the analysis of Saturn's near-infrared spectra, in order to break the degeneracies inherent to the retrieval problem. The extinction coefficient, the scattering albedo, and the three Henyey-Greenstein coefficients can be pre-calculated in Mie theory assuming

a particular size distribution and complex refractive index. The number of degrees of freedom then reduces to $2 \times (1 + N_\lambda)$ instead of $5N_\lambda$. The size distribution of aerosol particles is defined by a mean size value plus a variance, leading to two degrees of freedom. The complex refractive index consists of an imaginary part and a real part, which both vary independently with wavelength. There are then $2N_\lambda$ degrees of freedom associated with the complex refractive index. For a spectrum made of 146 wavelengths, the new parametrisation of aerosol physical and optical properties decreases the number of free parameters from 730 to 294. This is still a large number especially if a full spectral range is retrieved with NEMESIS. However, contrary to parameters in the first parametrisation, a few assumptions can be made on the aerosol distribution and complex refractive index as follows:

*i.* Haze particles have typical sizes ranging from a few hunded nanometers (Karkoschka and Tomasko, 1993, 2005 ; Pérez-Hoyos *et al.*, 2005) to a few microns (Pope *et al.*, 1992). The aerosol particle size is then allowed to vary in the range 0.1-10 $\mu$m. A variance of 0.05 was chosen in the distribution for each particle size (Fletcher *et al.*, 2011).

*ii.* The complex refractive index of typical particles found in Saturn's troposphere and stratosphere are presented in Fig. 5.24. This shows that imaginary refractive indexes have typical values below 0.1. The real refractive index of most materials ranges between 1 and 2, including molecules present in Saturn's atmosphere.

### 5.3.2 Results at a latitude of 20°S

One near-infrared spectrum at 0.8-3.5 $\mu$m was selected from the VIMS spectral cube CM1524386400 measured on 26 April 2006 at $08^h09^m37.759^s$. The dayside spectrum was measured at a latitude of -19.93° ± 1.67°, a longitude of 108.06° ± 2.34°, an emission angle of 38.49° ± 2.39°, a solar angle of 76.48° ± 2.26° and an azimuth angle of 7.59° ± 2.17°. A vertical aerosol profile was retrieved with the numerical code NEMESIS for various values of the aerosol particle size and complex refractive index. The particle radius $\phi$ can take values in the interval: [100 nm, 200 nm, 300 nm, 400 nm, 500 nm, 600 nm, 700 nm, 800 nm, 900 nm, 1 $\mu$m, 2 $\mu$m, 3 $\mu$m, 4 $\mu$m, 5 $\mu$m, 6 $\mu$m, 7 $\mu$m, 8 $\mu$m, 9 $\mu$m, 10 $\mu$m]. On the other hand, the real $n_r$ and imaginary $n_i$ parts of the complex refractive index take values respectively in the intervals [1.0, 1.1, 1.2, 1.3, 1.4, 1.5, 1.6, 1.7, 1.8, 1.9, 2.0] and [0, $10^{-7}$, $10^{-6}$, $10^{-5}$, $10^{-4}$, $10^{-3}$, $10^{-2}$, $10^{-1}$, 1]. The three parameters are tested simultaneously, that is to say the

retrieval algorithm is run 19×11×9 times for all combinations of $\phi$, $n_r$ and $n_i$. The $\chi^2/N_\lambda$ values are evaluated for each of the haze models defined by the particle size and the refractive index. Retrievals with $\chi^2/N_\lambda$ values above 5.0 fail to provide a solution to the retrieval problem in good agreement with VIMS observations. Synthetic spectra for $\chi^2/N_\lambda$ values below 1.0 generally match quite well the measured reflection spectra.

The best fits to the observations are obtained for a real refractive index between 1.1 and 1.8, and for low values of the imaginary refractive index below 0.001. Optimum fits to VIMS near-infrared measurements are obtained for an aerosol particle size in the range 0.5-5 $\mu$m. The goodness-of-fit maps are shown in Fig. 5.6 for real and imaginary refractive indices equal to 1.4 and $10^{-5}$ respectively. The lowest $\chi^2/N_\lambda$ values are obtained for a real refractive index between 1.1 and 1.5, although values in the range 1.5-1.8 lead to synthetic spectra similar to VIMS spectra within the measurement errors. The best-fitting values of the aerosol particle size are in the range 0.8-5 $\mu$m. If all values of the imaginary refractive index are taken into account, smaller particles with size down to 500 nm are also found to fit VIMS observations quite well. However, only imaginary refractive indexes below the 0.001 threshold values have low $\chi^2/N_\lambda$ values. This is observed for $n_r = 1.4$ but also for all the other values of the real refractive index.

By plotting all the synthetic spectra against the VIMS near-infared reflection spectrum, it can be shown that any set of parameters with $\chi^2/N_\lambda$ values above 5.0 cannot properly fit the observations within the measurement errors. Therefore, the analysis of Saturn's near-infrared reflection data has concluded that aerosols with a particle size $\phi$, real $n_r$ and imaginary $n_i$ complex refractive indexes in the range:

$$\begin{aligned} \phi(\mu m) &\in [0.5, 5] \\ n_r &\in [1.1, 1.8] \\ n_i &\in [0, 0.001] \end{aligned}$$

best represent the optical and physical properties of hazes in Saturn's troposphere and stratosphere.

The low values for the imaginary refractive index correspond to high single scattering albedos. Indeed, the imaginary index represents the absorption power of scatterers at 0.8-3.5 $\mu$m, and so weak

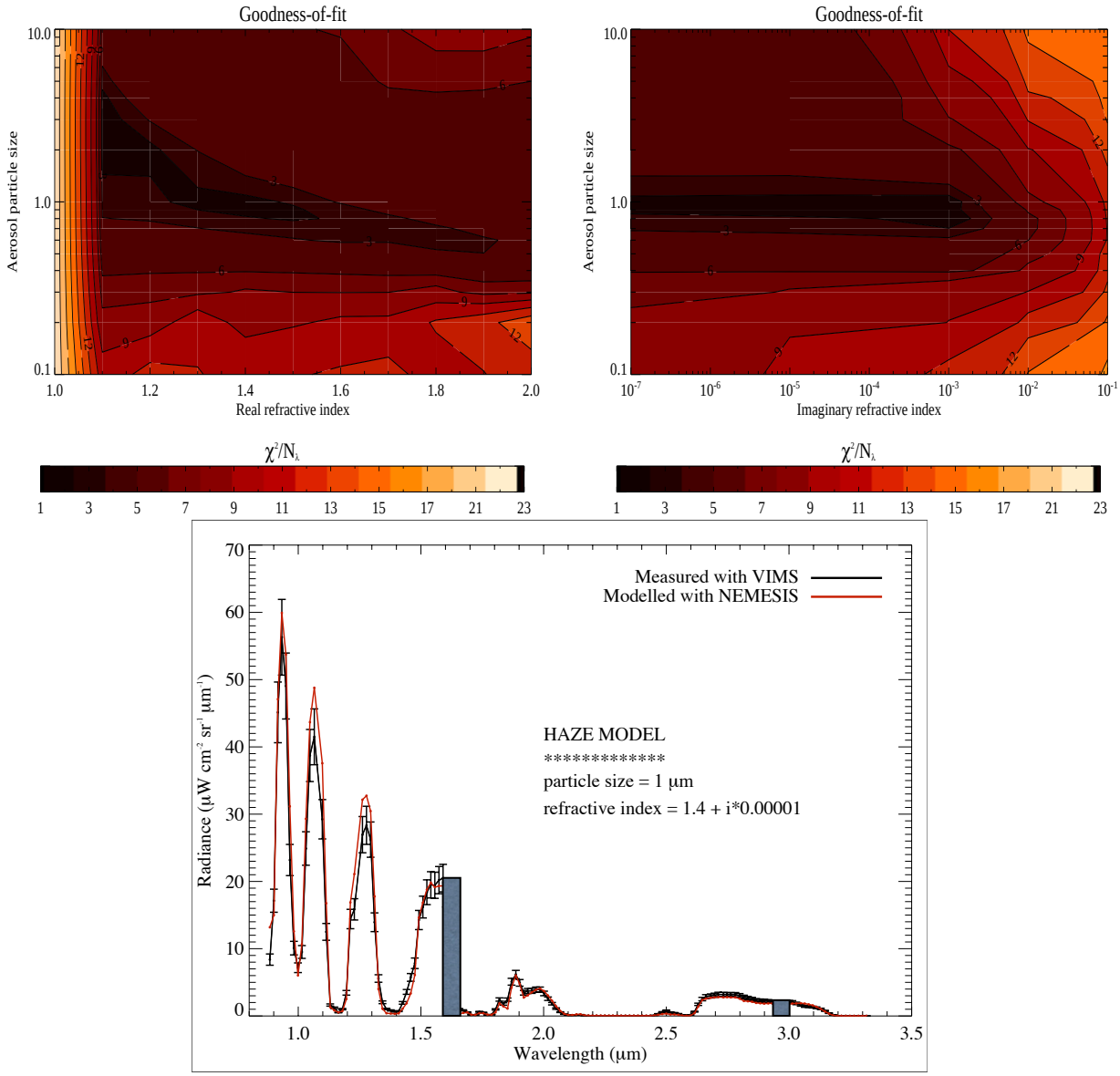



Figure 5.6: Optical and physical parameters of Saturn's hazes determined from the analysis of VIMS near-infrared reflection spectrum. The dayside spectrum is extracted from VIMS spectral cube CM1524386400 measured at $08^h09^m37.759^s$ on 26 April 2006. A continuous aerosol profile is retrieved with NEMESIS for various values of the aerosol particle size and complex refractive index. The aerosol opacity is retrieved at each of the pressure levels considered in the reference atmosphere. In the top-left figure, the imaginary refractive index is set to $10^{-5}$, and the goodness-of-fit is shown as a function of the particle size and the real refractive index. Optimum fits to the observations are found for a real refractive index between 1.1 and 1.8 and for an aerosol particle size in the range 0.8-5 $\mu$m. In the top-right figure, the goodness-of-fit is given as a function of the particle size and the imaginary refractive index for a real refractive index equal to 1.4. Only low values of the imaginary refractive index, below 0.01, provide possible solutions to the retrieval problem, suggesting that aerosol particles in Saturn's hazes are likely to have high scattering albedos. The synthetic reflection spectrum for an aerosol particle size of 1 $\mu$m and a complex refractive index of $1.4 + i\times10^{-5}$ is compared to the measured spectrum in the bottom figure. The modelled radiances match the observed radiances at most spectral points within the error bars.

absorption is correlated to high scattering efficiency for a given extinction coefficient[2]. The single scattering albedo varies with wavelengths over 0.8-3.5 $\mu$m, although most values are higher than 0.9. Variation of the single scattering albedo with wavelength shows the difficulty of choosing this parameter as a free variable in the haze model. However, the representation of haze properties by the aerosol particle size and the complex refractive index has led to a range of coherent haze models in good agreement with VIMS measurements of reflected sunlight in the near-infrared. The fitting strategy used here in this analysis of VIMS reflection spectrum has also proved to be efficient in reducing the range of possible solutions to the retrieval problem by constraining the aerosol particle size and complex refractive index.

For each set of parameters $\{\phi, n_r, n_i\}$, the single scattering albedo ($\omega$), and the three double Henyey-Greenstein phase function parameters ($f$, $g_1$, $g_2$) are calculated by Mie theory at each wavelength in the 0.8-3.5 $\mu$m spectral range. In Table 5.1, the physical and optical parameters have been averaged over the ranges of aerosol particle size and complex refractive index which are consistent with VIMS near-infrared reflection spectra. Therefore, the dispersions of $\omega$, $f$, $g_1$ and $g_2$ are also evaluated, in addition to their mean values. At 2.15 $\mu$m, the single scattering albedo has a large value of $0.995 \pm 0.009$, suggesting that aerosol particles in Saturn's hazes are highly scattering. Comparison with the scattering albedo in the visible at "blue" and "red" wavelengths (Tomasko and Doose, 1984) shows that $\omega$ probably increases with wavelength. The phase parameters $f$, $g_1$ and $g_2$ take respectively the values $0.960 \pm 0.051$, $0.658 \pm 0.160$ and $-0.241 \pm 0.341$ at 2.15 $\mu$m.

The parameter $f$ represents the ratio of forward over backward scattering, thus such a high value for this parameter is consistent with little back-scattering. The high value of $g_1$ and the low value of $g_2$ also support the idea that aerosol particles have a low back-scattering component. Note that the large dispersion of $g_2$ is due to significant variations of this parameter with the aerosol particle size and the complex refractive index. However, since back-scattering is negligible, large variations of $g_2$ have small effects on the phase function. Results are very similar if the scattering albedo and Henyey-Greenstein phase function parameters are averaged over the 0.8-3.5 $\mu$m wavelength range, as it can be seen in Table5.1.

[2]The extinction represents the sum of absorption and scattering. For a given value of the extinction cross-section, the absorption coefficient can only drop by increasing the scattering albedo.

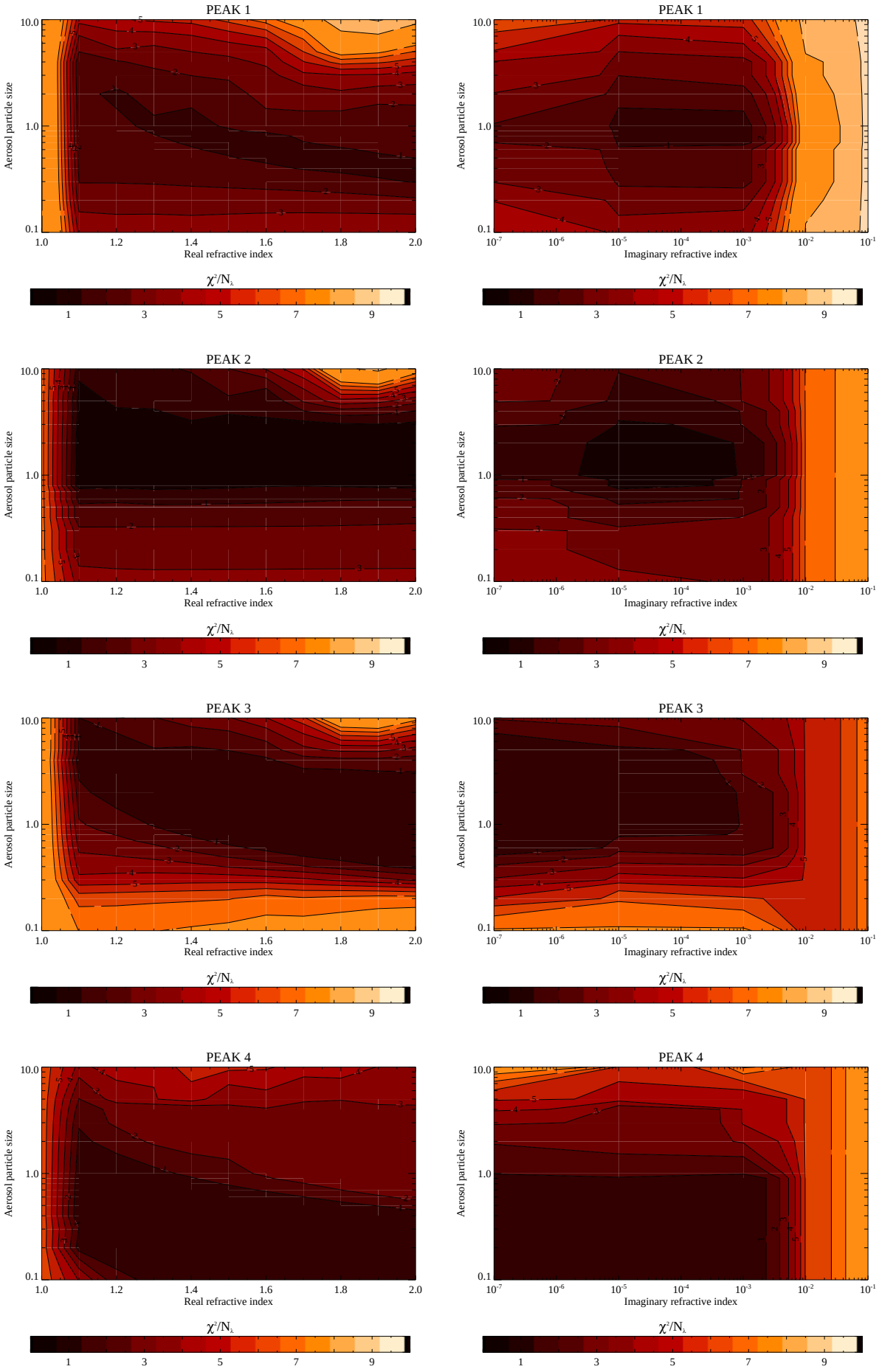
| | Wavelength ($\mu$m) | | | |
|---|---|---|---|---|
| Parameter | 0.44 | 0.64 | 2.15 | 0.8-3.5 |
| $\omega$ | 0.920 | 0.986 | $0.995 \pm 0.009$ | $0.995 \pm 0.011$ |
| $f$ | 0.764 | 0.768 | $0.960 \pm 0.051$ | $0.953 \pm 0.053$ |
| $g_1$ | 0.870 | 0.603 | $0.658 \pm 0.160$ | $0.670 \pm 0.176$ |
| $g_2$ | -0.116 | -0.302 | $-0.241 \pm 0.341$ | $-0.300 \pm 0.349$ |

Table 5.1: Best-fitting scattering albedo and phase function parameters. The single scattering albedo ($\omega$) and the double Henyey-Greenstein phase function parameters ($f$, $g_1$ and $g_2$) are given at 0.44, 0.64 and 2.15 $\mu$m, as well as their average value over the wavelength range 0.8-3.5 $\mu$m. The optical parameters at 0.44 and 0.64 $\mu$m are obtained from Tomasko and Doose (1984) at 15-17°S. At 2.15 $\mu$m, the mean value and dispersion are calculated for a particle size ($\phi$) between 500 nm and 5 $\mu$m, a real refractive index ($n_r$) between 1.1 and 1.8, and an imaginary refractive index ($n_i$) below the 0.001 threshold value. Similar ranges for $\phi$, $n_r$ and $n_i$ are considered for the estimation of the optical parameters at 0.8-3.5 $\mu$m. The large values for $\omega$ and $f$ show that aerosol particles in Saturn's hazes are highly scattering and have little back-scattering.

### 5.3.3 Retrieval of aerosol properties from individual reflection speaks

In the previous section, Saturn's tropospheric and stratospheric hazes are characterised by the complex refractive index and the aerosol particle size. A constant value with wavelength was assumed for both the real and imaginary parts of the complex refractive index. This is the first natural approximation that can be made in the atmospheric model since very little is known about the value and variation of the complex refractive index with wavelength. As shown in Fig. 5.6, there exists a range of values for the complex refractive index for which the synthetic spectra calculated with NEMESIS are in good agreement with VIMS spectra within the measurement errors. If none of the constant values of the complex refractive index had matched the observations, the next step would have been to model this parameter as a variable function with wavelength. Therefore, the complex refractive index can be assumed to be constant with wavelength at first aproximation, if the full near-infrared refraction spectrum from 0.8 until 3.5 $\mu$m is analysed.

In this section, the variation of the complex refractive index with wavelength is investigated by retrieving the aerosol properties from each of the six individual peaks. The continuous aerosol density profile is retrieved from each peak for all the combinations of the aerosol particle radius, real refractive index and imaginary refractive index. The results are shown here for the same spectrum in Fig. 5.6 extracted from VIMS spectral cube CM1524386400 measured on 26 April 2006 in order to


PEAK 1
Aerosol particle size
Real refractive index
Imaginary refractive index
χ²/Nλ
PEAK 2
PEAK 3
PEAK 4

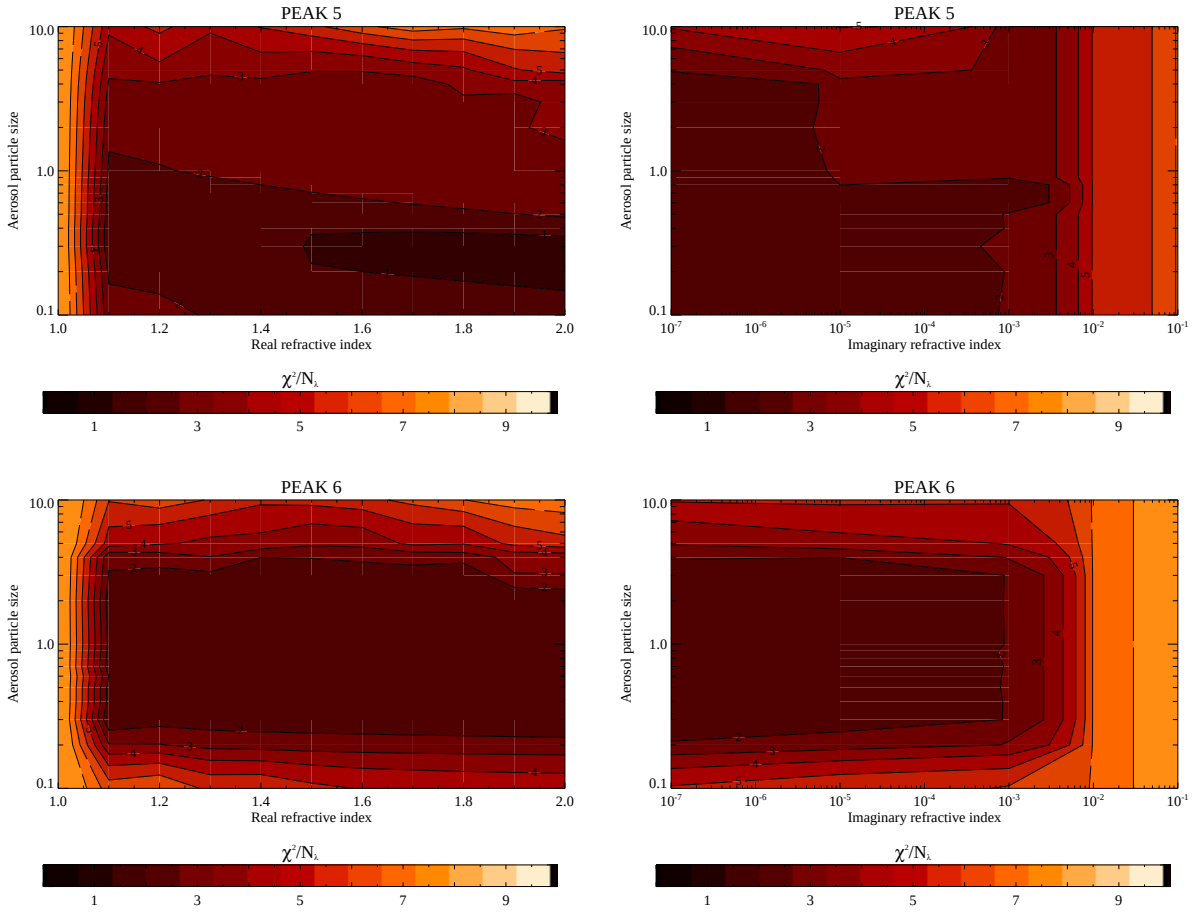



Figure 5.7: Retrieval of the complex refractive index and aerosol particle size from the individual reflection peaks. The goodness-of-fit maps are shown as a function of the real refractive index and aerosol particle size for an imaginary refractive index equal to $10^{-5}$. The goodness-of-fit maps are shown as a function of the imaginary reftactive index and aerosol particle size for a real refractive index equal to 1.4.

direct comparison between the two methods. The goodness-of-fit maps are presented in Fig.5.7 for a real and imaginet parts of the refractive index equal to 1.4 and $10^{-5}$ respectively. The results for the first reflection peak in Saturn's spectrum show that any value of the aerosol particle size below 6 $\mu$m and any value above 1.1 of the real refractive index are associated with $\chi^2/N_\lambda$ values below the 5.0-threshold value, if the imaginary refractive index is fixed to $10^{-5}$. Note that for lower values of the real refractive index below 1.6, higher particle sizes up to 10 $\mu$m also manage fit VIMS data within the error bars.The goodness-of-fit map as a function of the particle size and imaginary reafractive index, for a real refractive index of 1.4 shows that all aerosol models for an imaginary refractive index below 0.001 match the observations quite well within the measurement errors. This is observed for all sizes of the aerosol particles. For all combinations of the three parameters characterising Saturn's hazes,

the optimum values of the aerosol particle size, real refractive index and imaginary refractive index fall respectively in the ranges [100 nm-6$\mu$m], [1.1-2.0] and [0-0.001].

The previous sections has shown that if a full 0.8-3.5 $\mu$m is retrieved, the the optimum values are in the ranges [500 nm-5 $\mu$m], [1.1-1.8] and [0-0.001] for the particle size, real refractive index and imaginary refractive index respectively. Therefore, the optical and physical parameters of Saturn's hazes are less constrained if they are retrieved from one individual peak instead of from the full near-infrared reflection spectrum of the planet. The same conclusion can be drawn for the five other relection peaks at larger wavelengths. Fig.5.7 shows that the ranges of best-fitting parameters retrieved from each individual peak are significantly larger than if retrieved from the full near-infrared spectrum. This can be explained as follows: by considering the full spectrum instead of one individual peak, the number of measurements increases and so the retrieval problem is more constrained by the observations leading to a decrease of optimum input parameters in the atmospheric model. Ideally, the retrieval of the complex refractive index from each individual peak would provide one unique value for this parameter. Knowing the optimum complex refractive index at each peak would give the variation of this parameters with wavelength. The results in Fig.5.7 show that such a method cannot be applied due to the high level of degeneracies in the retrieval model if the parameters are retrieved from only one peak. Besides, the physical and optimal parameters of the haze are less constrained in comparison with the analysis of the full 0.8-3.5 $\mu$m spectrum. In conclusion, the stategy consisting in retrieving the haze's parameters from the full near-infrared reflection spectrum assuming a constant value of the complex refractive index with wavelength is adopted mostly in this thesis.

### 5.3.4 Testing the viewing geometry

In the previous section, the best-fitting values of the aerosol particle radius and complex refractive index were derived from Saturn's near-infrared reflection spectrum at a latitude of 20°S measured at a specific solar angle and emission angle. The effect of the viewing geometry on the haze optical and physical properties is determined by analysing Saturn's spectra measured at the same latitude and longitude but with different solar and emission angles.

The five VIMS spectral cubes considered in this section are shown in Fig 5.8. The pixel locations of the five spectra are shown by the red squares. The viewing geometries of each spectrum are listed

in Table 5.2. The five reflection spectra at 0.8-3.5 are measured on 16 and 17 February 2006 at a similar latitude and longitude of approximately 20°S and 195° respectively. The emisson angle varies between 30° and 65°, and the solar angle takes values between 34° and 88°.

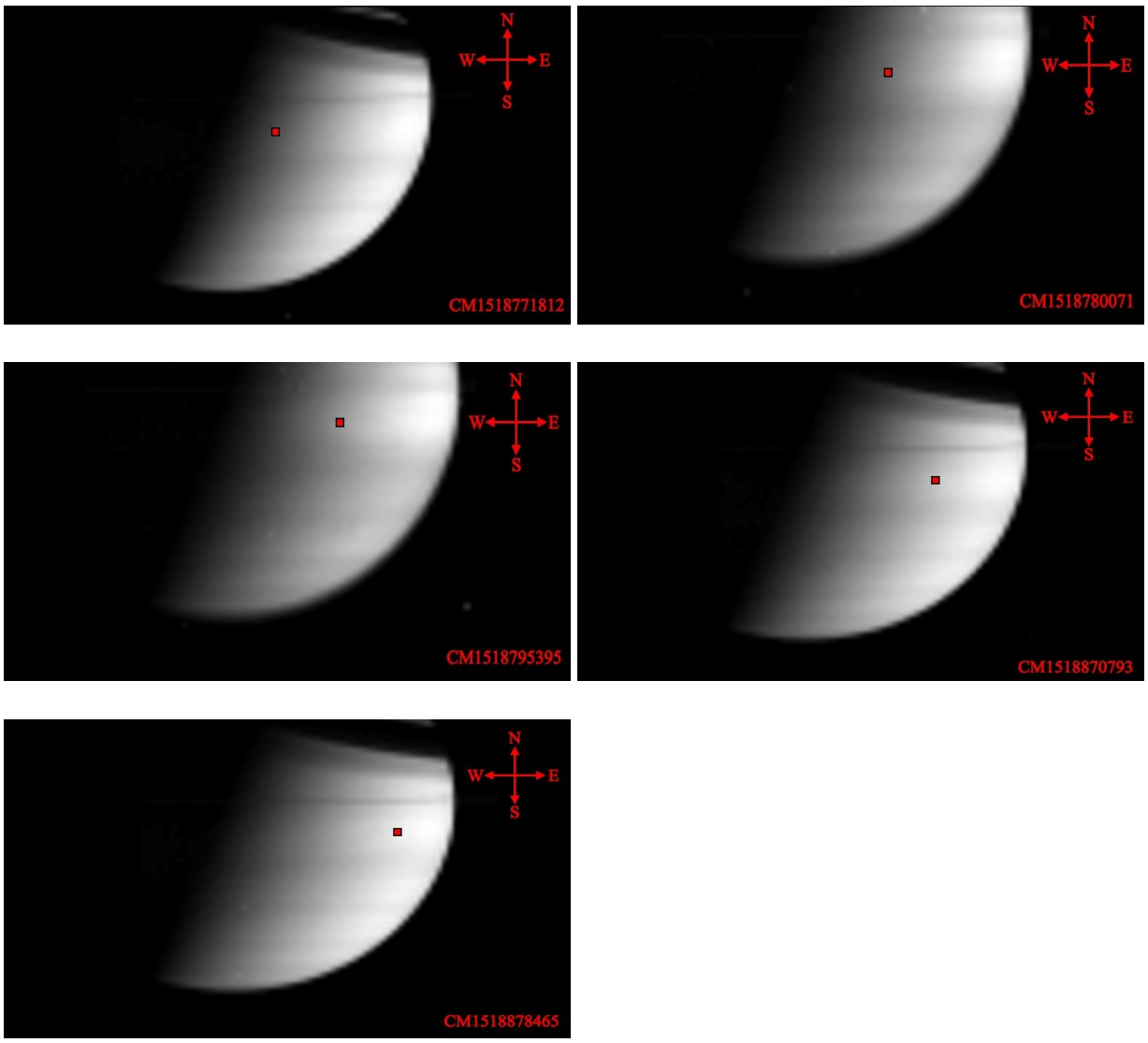



Figure 5.8: VIMS cubes used for the sensitivity analysis of the haze optical and physical parameters to the viewing geometry. The red squares show the extracted pixel for each spectral cube.

The same retrieval strategy as described in the previous section is applied to each reflection spectrum. The vertical profile of aerosol concentration is retrieved with NEMESIS from VIMS near-infrared data for different values of the aerosol particle radius and complex refractive index. The particle radius takes values between 100 nm and 10 $\mu$m. The real and imaginary parts of the refractive index take values in the range 1-2 and 0-1 respectively. The aerosol concentration is retrieved for all combinations of these three parameters. The goodness-of-fit maps are shown in Fig. 5.9 for

| | CM1518771812 | CM1518780071 | CM1518795395 |
|---|---|---|---|
| Date | 16 February 2006 | 16 February 2006 | 16 February 2006 |
| Time | $08^h33^m45.475^s$ | $10^h51^m24.422^s$ | $15^h06^m48.323^s$ |
| Latitude | -20.14° ± 1.12° | -19.93° ± 1.20° | -20.11° ± 1.45° |
| Longitude | 195.41° ± 1.88° | 195.75° ± 1.96° | 194.53° ± 2.25° |
| Emission angle | 30.18° ± 1.90° | 35.21° ± 2.01° | 42.69° ± 2.29° |
| Solar angle | 87.63° ± 1.76° | 68.42° ± 1.93° | 49.13° ± 2.14° |

| | CM1518870793 | CM1518878465 |
|---|---|---|
| Date | 17 February 2006 | 17 February 2006 |
| Time | $12^h03^m25.844^s$ | $14^h11^m17.795^s$ |
| Latitude | -20.41° ± 1.69° | -20.07° ± 1.98° |
| Longitude | 195.21° ± 2.41° | 196.98° ± 2.68° |
| Emission angle | 51.18° ± 2.53° | 65.92° ± 2.74° |
| Solar angle | 35.59° ± 2.47° | 23.74° ± 2.70° |

Table 5.2: List of VIMS observations used for testing the sensitivity of retrievals to the viewing geometry. Five spectra measured at the same latitude and longitude but for different emission and solar angles are extracted from five different spectral cubes.

each spectrum. The $\chi^2/N_\lambda$ values as a function of the real refractive index and particle radius are shown for an imaginary refractive index of $10^{-5}$. The $\chi^2/N_\lambda$ values are also presented in Fig. 5.9 as a function of the imaginary refractive index and particle radius for a real refractive index equal to 1.4.

The first goodness-of-fit map in Fig. 5.9 as a function of the particle size and real refractive index for the VIMS spectrum measured at an emission of 66° and a solar angle of 24° shows that the lowest $\chi^2/N_\lambda$ values are obtained for a real refractive index between 1.1 and 1.8 and an aerosol particle size between 500 nm and 5 $\mu$m. Larger particule sizes between 7 $\mu$m and 10 $\mu$m are associated with $\chi^2/N_\lambda$ values of around 2, however smaller particules provide a better fit to the obervations. The goodness-of-fit map as a function of the aerosol particle size and imaginary refractive index shows that only low values of the imaginary refractive index, below 0.001, manage to fit the observations quite well within the measurement errors. Aerosol particle sizes around one micrometre have smaller $\chi^2/N_\lambda$ values, although larger particles also have $\chi^2/N_\lambda$ values below the 5.0-threshold value.

The goodness-of-fit maps at an emission angle of 51° and a solar angle of 36° have a similar pattern as observed in the two first maps. The best-fitting values of the aerosol particule size, real

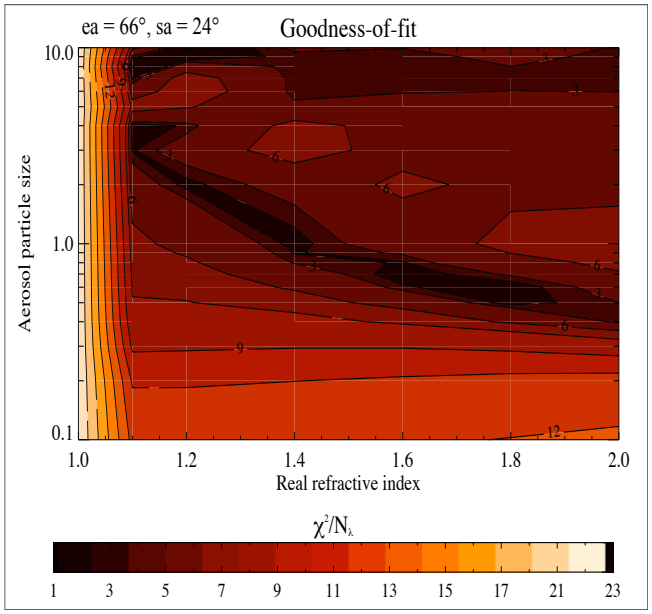
refractive index and imaginary refractive index are obtained in the range 0.5-5 $\mu$m, 1.1-1.8 and 0-0.001 respectively. A similar conclusion can be drawn from the VIMS spectrum measured at an emission angle of 43° and a solar angle of 49°. It was mentioned before that larger particule sizes above 7 $\mu$m also have small $\chi^2/N_\lambda$ values around 2. However, such aerosol particules are associated with higher $\chi^2/N_\lambda$ values if higher solar angles are considered. In particular, large aerosol particles cannot model the VIMS reflection spectrum at an emission angle of 35° and a solar angle of 68°.

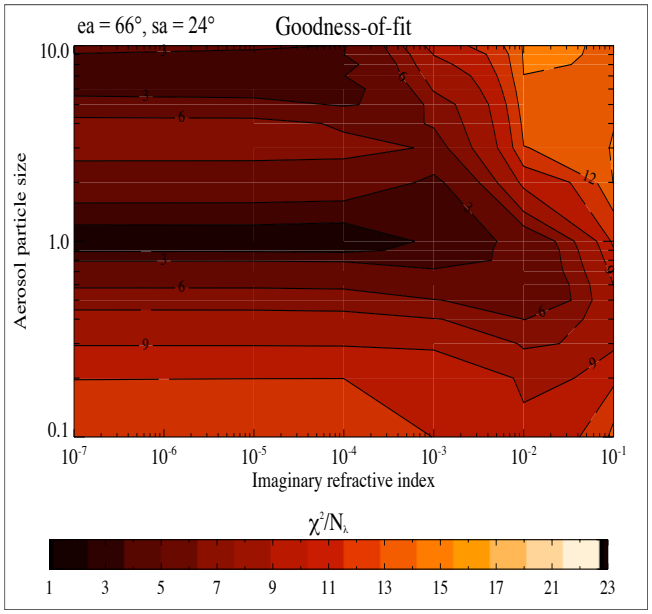
Since Saturn's spectrum in the 0.8-3.5 $\mu$m wavelength range consists of the reflection of sunlight by the tropospheric and stratospheric haze, only dayside data are extracted from VIMS spectral cubes. Typically, NEMESIS can retrieve the aerosol concentration profile from spectra measured at a solar angle between 0° and 85°. Between 85° and 90°, the signal becomes to low and the numerical algorithm cannot properly model VIMS data for any combination of the aerosol particle size and complex refractive index in a plane parallel atmosphere.

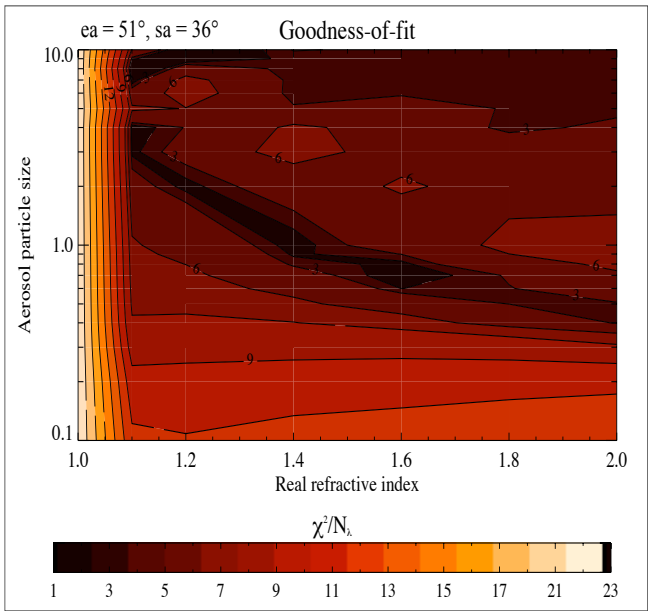
The results of the retrievals are shown in Fig. 5.9 for an emission angle of 30° and a solar angle of 88°. The lowest $\chi^2/N_\lambda$ values are approximately equal to 6, so above the 5-threshold value. Therefore, none of the particule size and complex refractive index values provide a good fit to VIMS data. Note that 5 zenith angles are used in the scatter model (see section 3.3). For such a large value of the solar angle, the retrievals were also performed for 21 zenith angles. In the two cases, the synthetic spectra could not fit VIMS data. The goodness-of-fit maps for an emission angle of 30° and a solar angle of 88° in Fig. 5.9 are shown for a scatter model assuming 21 zenith angles.

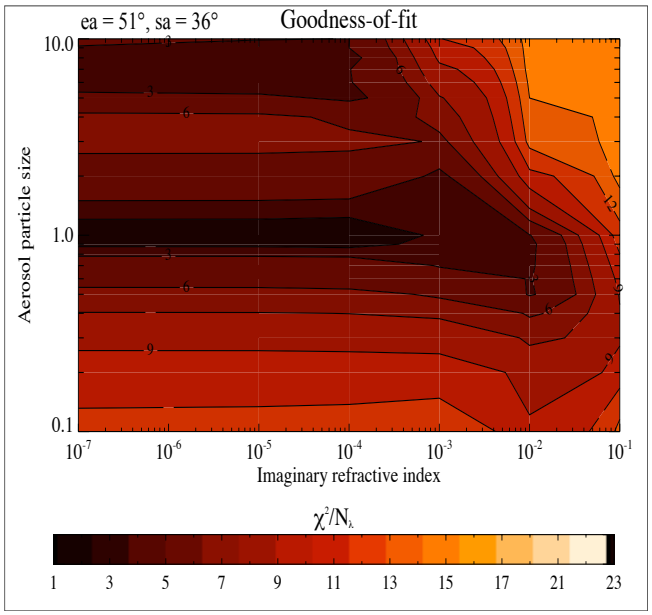
In the previous section, the aerosol optical and physical properties were derived from one 20° latitude spectrum measured at an emission and solar angles of 38° and 76° respectively. The best-fitting values of the aerosol particle size, real refractive index and complex refractive index for that particular spectrum were obtained in the same range as for the 20°S latitude spectra measured with VIMS at other emission and solar angles, assuming that the solar angle is below 85°. $\chi^2/N_\lambda$ values below the 5.0-threshold value are obtained for larger aerosol particles, above 7 $\mu$m, from low solar angle spectra. However, such particles have higher $\chi^2/N_\lambda$ values than for smaller particles. Besides, large aerosol particules cannot model VIMS spectra measured at higher solar angles.

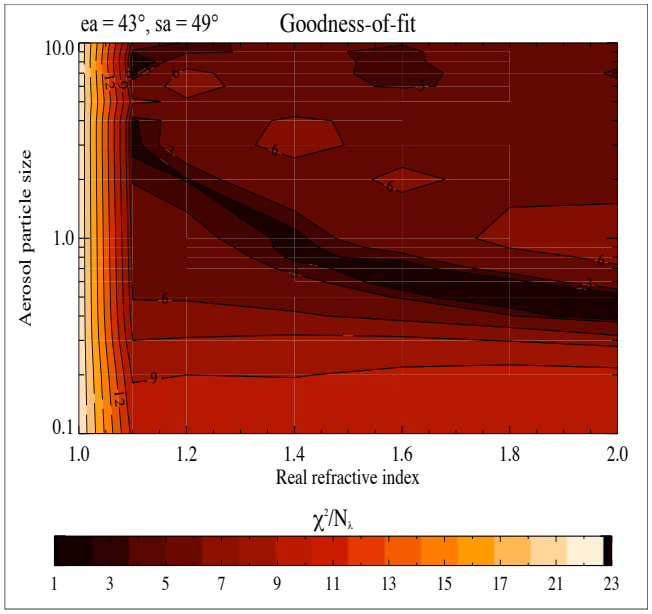
In conclusion, similar properties of the aerosol particles at a latitude of 20°S are obtained in this section: a particle size between 500 nm and 5 $\mu$m values, a real refractive index between 1.1 and 1.8 and an imaginary refractive index between 0 and 0.001 are in good agreement with VIMS data.

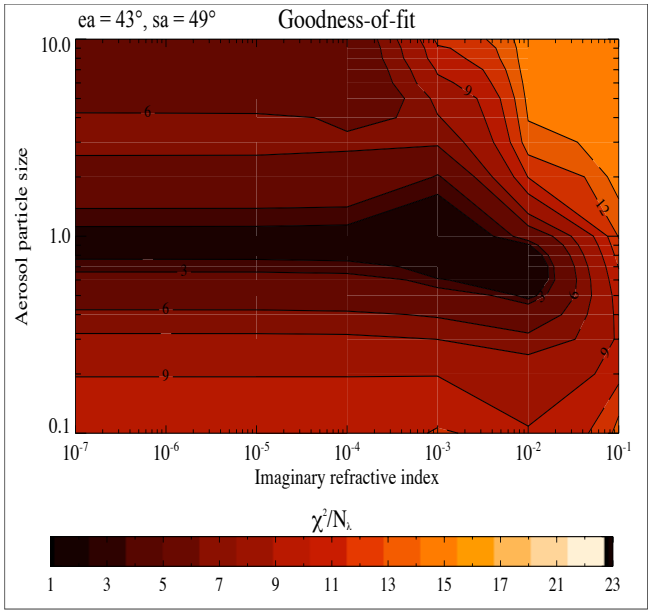

ea = 66°, sa = 24°
Goodness-of-fit
Aerosol particle size
Real refractive index
$\chi^2/N_\lambda$


ea = 66°, sa = 24°
Goodness-of-fit
Aerosol particle size
Imaginary refractive index
$\chi^2/N_\lambda$


ea = 51°, sa = 36°
Goodness-of-fit
Aerosol particle size
Real refractive index
$\chi^2/N_\lambda$


ea = 51°, sa = 36°
Goodness-of-fit
Aerosol particle size
Imaginary refractive index
$\chi^2/N_\lambda$


ea = 43°, sa = 49°
Goodness-of-fit
Aerosol particle size
Real refractive index
$\chi^2/N_\lambda$


ea = 43°, sa = 49°
Goodness-of-fit
Aerosol particle size
Imaginary refractive index
$\chi^2/N_\lambda$

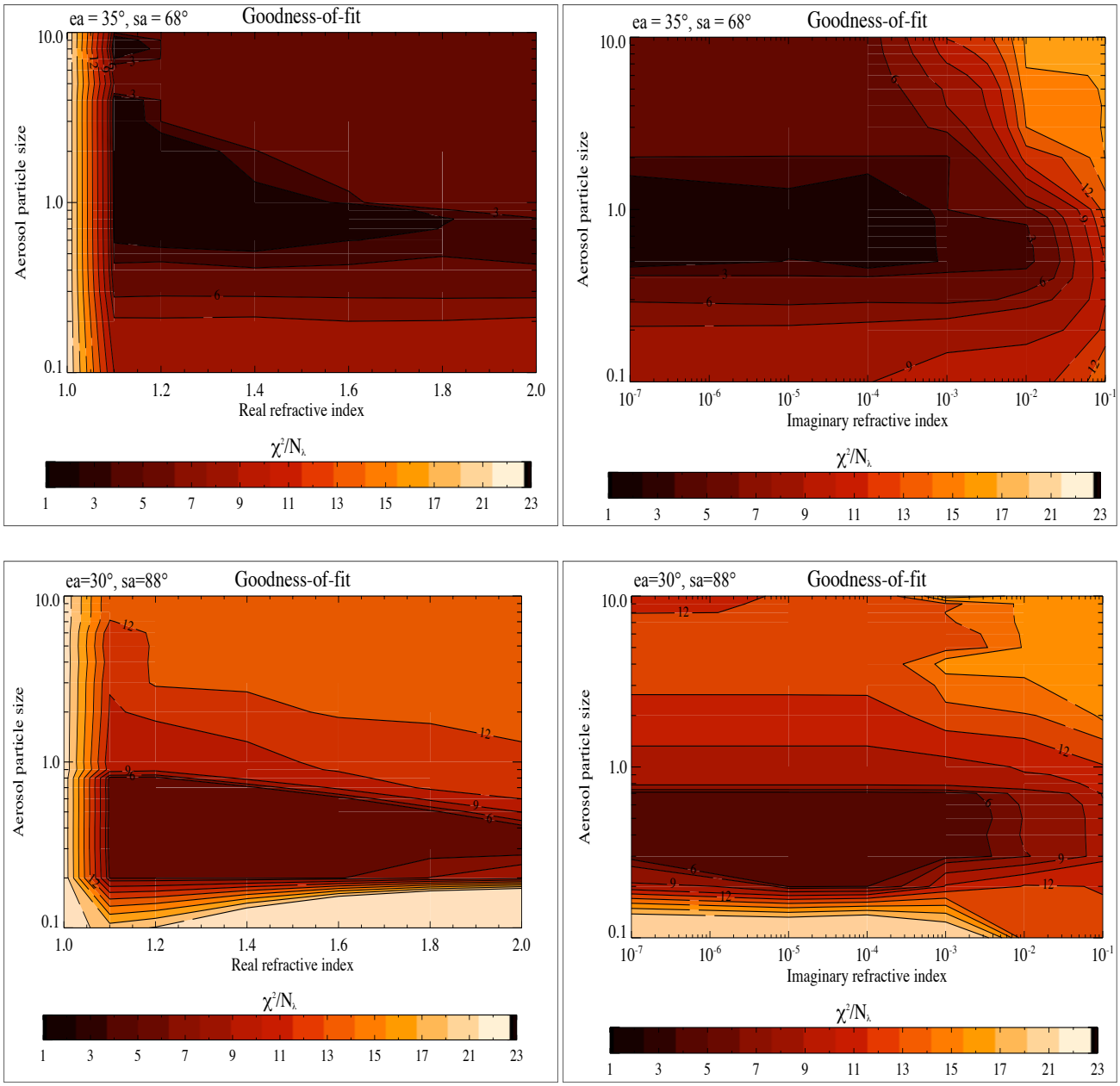



Figure 5.9: Retrieval of the haze optical and physical properties at a latitude of 20°S for different values of the solar and emission angles. The near-infrared reflection spectra are extracted from five VIMS spectral cubes acquired on 16 and 17 February 2006. The goodness-of-fit maps are shown for each of the five reflection spectra as a function of the particle radius and real refractive index for an imaginary refractive index of $10^{-5}$. The goodness-of-fit maps are also plotted as a function of the particle size and imaginary refractive index for a real refractive index equal to 1.4. Note that for an emission angle 30° of and a solar angle of 88°, 21 zenith angles instead of 5 are included in the scatter model.

### 5.3.5 Results at all latitudes

In this section, the optical and physical parameters of aerosols are retrieved at various latitudes in Saturn's southern and nothern hemispheres. As for the analysis of Saturn's reflection spectrum at 20°S, the haze is characterised by three parameters including the particle radius, and the real and imaginary parts of the complex refractive index. The same retrieval strategy is adopted here: the aerosol vertical profile is retrieved with NEMESIS from the near-infrared reflection spectra for all combinations of the three parameters.

The results are shown here for Saturn's spectra extracted from VIMS spectral cube CM1518982598 measured on 18 february 2006 at $19^h06^m48.130^s$. The latitude, longitude, emission angle and solar angle of each spectrum analysed in this section are shown in Table 5.3. The twelve dayside spectra are measured at similar longitudes but at various latitudes between 60°N and 60°S. Note that the shadow of the rings at low latitudes in the northern hemisphere prevents the analysis of Saturn's spectrum between 10°N and 20°N.

| | LATITUDE | LONGITUDE | EMISSION ANGLE | SOLAR ANGLE |
|---|---|---|---|---|
| 60°N | 60.39° ± 3.12° | 109.12° ± 4.98° | 49.34° ± 4.87° | 37.11° ± 3.54° |
| 50°N | 50.02° ± 2.69° | 110.08° ± 4.20° | 43.76° ± 3.18° | 36.20° ± 2.83° |
| 40°N | 40.87° ± 2.43° | 109.65° ± 3.11° | 30.34° ± 2.76° | 36.05° ± 2.53° |
| 30°N | 30.12° ± 2.07° | 109.32° ± 3.09° | 27.56° ± 2.34° | 35.98° ± 2.29° |
| 0° | 0.09° ± 0.87° | 109.98° ± 1.88° | 18.06° ± 1.85° | 35.56° ± 1.76° |
| 10°S | -10.34° ± 1.89° | 109.54° ± 2.05° | 20.45° ± 1.99° | 35.59° ± 2.05° |
| 20°S | -20.34° ± 2.21° | 109.21° ± 2.38° | 23.32° ± 2.27° | 35.63° ± 2.19° |
| 30°S | -30.33° ± 2.43° | 110.37° ± 2.86° | 25.99° ± 2.37° | 35.84° ± 2.27° |
| 40°S | -40.12° ± 2.47° | 109.09° ± 3.33° | 30.65° ± 2.65° | 36.01° ± 2.39° |
| 50°S | -50.76° ± 2.54° | 109.21° ± 4.01° | 42.67° ± 3.51° | 36.23° ± 2.59° |
| 60°S | -60.40° ± 3.76° | 109.45° ± 4.65° | 49.41° ± 3.99° | 36.69° ± 2.96° |

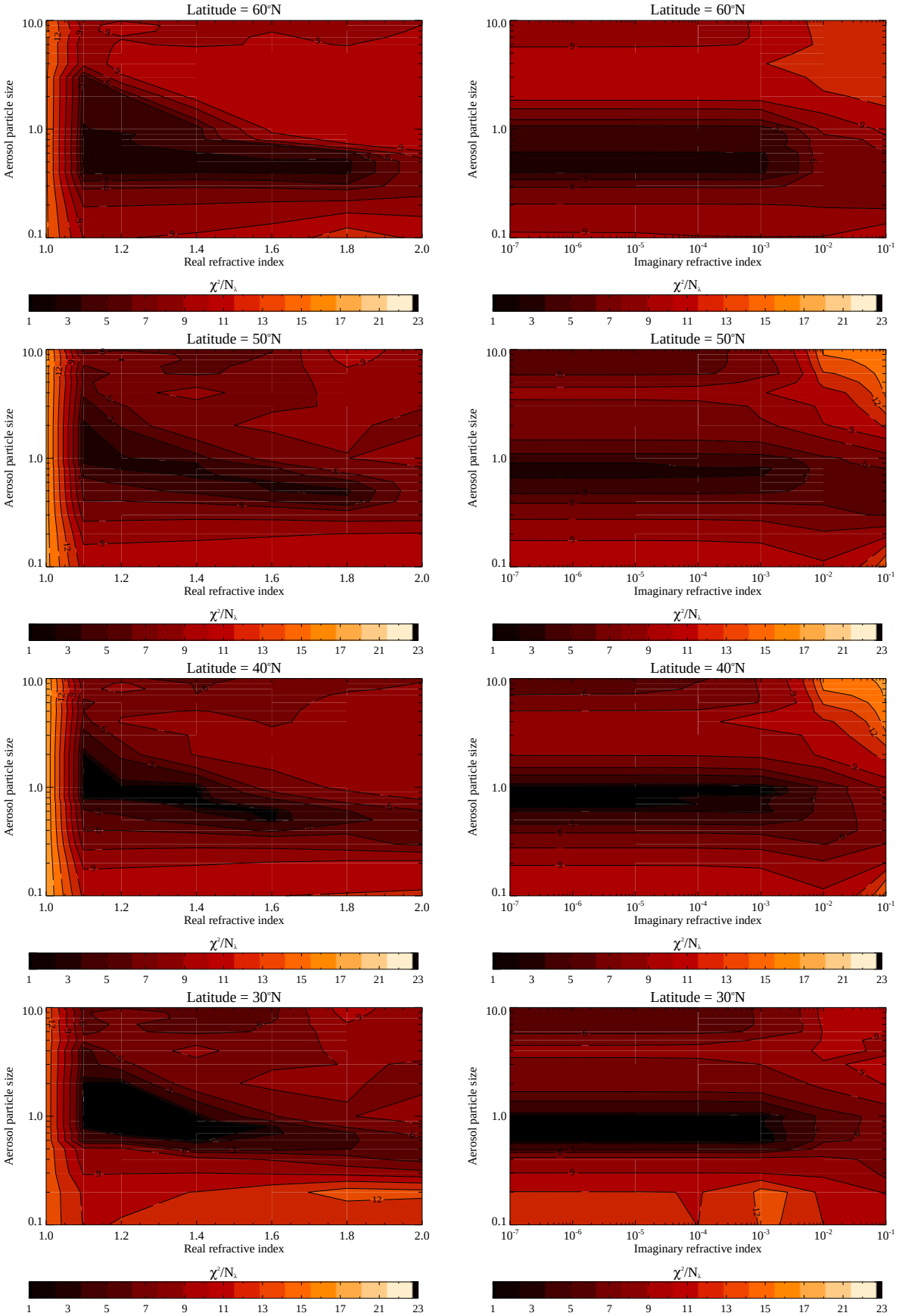
Table 5.3: Viewing geometries of VIMS data at various latitudes between 60°S and 60°N used for the analysis of Saturn's near-infrared reflection spectra. The 12 spectra are extracted from VIMS spectral cube CM1518982598 measured on 18 february 2006 at $19^h06^m48.130^s$.

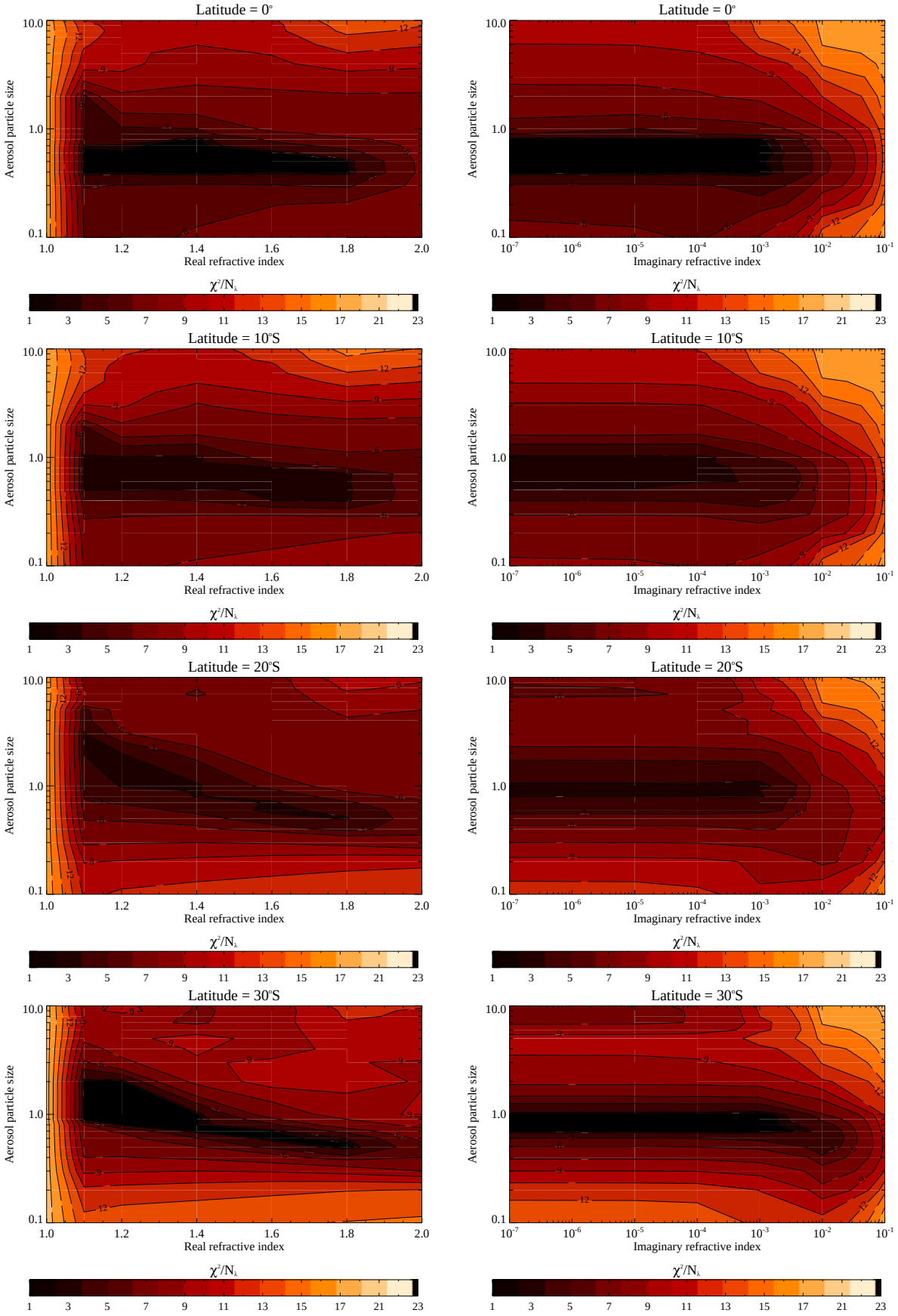
In Fig. 5.10, the goodness-of-fit maps are shown as a function of the aerosol particle size and real refractive index for an imaginary refractive index equal to $10^{-5}$. The goodness-of-fit maps are also plotted as a function of the aerosol particle size and imaginary refractive index assuming a real refractive index of 1.4. The best-fitting values of the aerosol particle size, real imaginary index and imaginary refractive index are listed in Table 5.4.

| Latitude | radius ($\mu$m) | real refractive index | imaginary |
|---|---|---|---|
| 60°N | 0.4-4 | 1.1-1.8 | 0-0.001 |
| 50°N | 0.4-4 | 1.1-1.8 | 0-0.001 |
| 40°N | 0.4-4 | 1.1-1.8 | 0-0.001 |
| 30°N | 0.5-5 | 1.1-1.8 | 0-0.001 |
| 0 | 0.3-2 | 1.1-1.8 | 0-0.001 |
| 10°S | 0.4-2 | 1.1-1.8 | 0-0.001 |
| 20°S | 0.5-5 | 1.1-1.8 | 0-0.001 |
| 30°S | 0.4-3 | 1.1-1.8 | 0-0.01 |
| 40°S | 0.4-3 | 1.1-1.8 | 0-0.01 |
| 50°S | 0.4-3 | 1.1-1.8 | 0-0.01 |
| 60°S | 0.4-3 | 1.1-1.8 | 0-0.01 |

Table 5.4: Best-fitting values of aerosol properties at all latitudes from VIMS near-infrared reflection spectra

A real refractive index in the range 1.1-1.8 is found to provide the best fits to VIMS observations at all latitudes. Low imaginary refractive indices are also derived from the analysis of Saturn's reflection spectra. Optimum values of the imaginary refractive index are obtained between 0 and 0.001 at nearly all latitudes except at higher latitudes in the southern hemisphere. Indeed, values in the range 0-0.01 manage to fit VIMS spectra measured at 30°S, 20°S, 30°S, 40°S, 50°S and 60°S. The best-fitting values of the aerosol particle size are found around one micrometre with slight variations of the lower and upper boundary values as can be seen in Table 5.4. In conclusion, the optical and physical parameters of aerosol particles derived from the planet's near-infrared reflection spectra at 0.8-3.5 $\mu$m are nearly uniform at all latitudes in the southern and nothern hemispheres.


Latitude = 60°N
Latitude = 50°N
Latitude = 40°N
Latitude = 30°N
Aerosol particle size
Real refractive index
Imaginary refractive index
χ²/Nλ


Latitude = 0°
Aerosol particle size
Real refractive index
Imaginary refractive index
χ²/Nλ
Latitude = 10°S
Latitude = 20°S
Latitude = 30°S

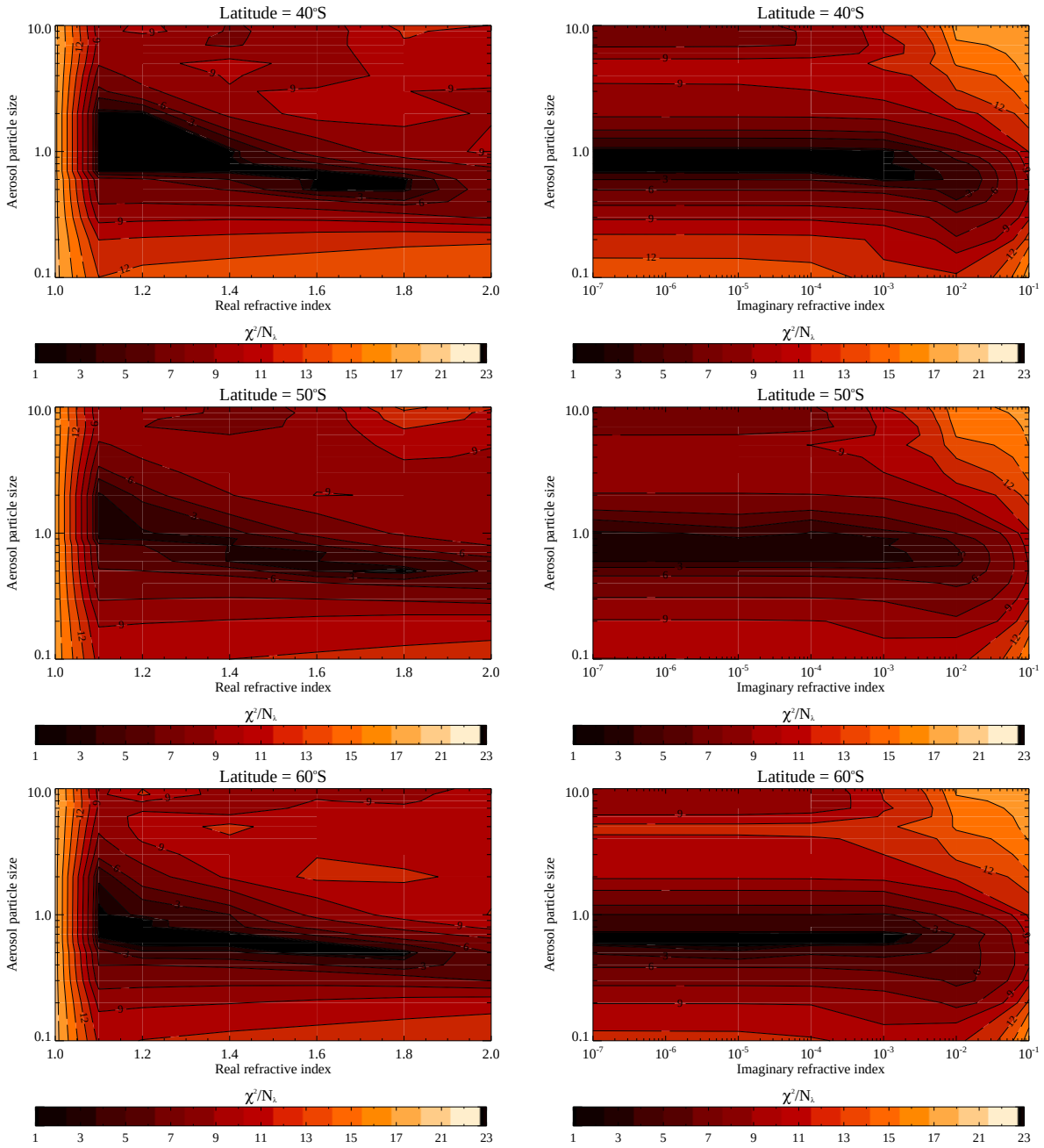



Figure 5.10: Goodness-of-fit as a function of the aerosol particle size, real refractive index and imaginary refractive index.

## 5.4 Haze vertical structure

### 5.4.1 Variations with optical and physical parameters

The haze density profile retrieved from the VIMS spectrum at 20°S presented in section 5.3.2, assuming that the aerosol particles have a radius of 1 $\mu$m with a variance of 0.05, and a complex refractive index equal to $1.4 + i\times10^{-5}$, is shown in Fig. 5.11. NEMESIS retrieves the specific density in number of particles per gramme of atmosphere. This was multiplied by the atmospheric density in gramme per cubic centimetre, in order to obtain the haze profile in particles per cubic centimetre. The haze vertical profile is characterised by a sharp peak of concentration below the tropopause at around 200 mbar, where the density is approximately equal to 150 $cm^{-3}$. The aerosol concentration decreases below the peak until it relaxes to the *a priori* profile at deeper tropospheric levels. The aerosol density clears above the peak and reaches a minimum at 10 mbar where the concentration drops to $7\times 10^{-4}$ $cm^{-3}$. The concentration increases at higher altitudes until it reaches a value of $7\times 10^{-2}$ $cm^{-3}$ at the 1-mbar pressure level.

The vertical profiles of tropospheric and stratospheric hazes for other values of the aerosol particle size and complex refractive index all have a very similar shape, with a peak at 200 mbar and a drop of aerosol concentration below and above the peak. In Fig. 5.11, the haze density profiles are compared for various particle sizes in the range 0.5-5 $\mu$m. For all particle sizes, the complex refractive index is set to $1.4 + i\times10^{-5}$. The aerosol concentration at the peak increases when the particle size decreases. At the end, the radiative transfer algorithm multiplies the aerosol concentration with the cross-section, which is proportional to the square of the particle size, in order to calculate the optical depth. Therefore, a smaller particle size implies higher aerosol concentrations for the same optical depth. Note that the aerosol profiles for a particle size of 3, 4 and 5 $\mu$m are characterised by a local increase of aerosol concentration around the 7-mbar level. This features is not present for other values of the aerosol particle size, and is probably due to the relaxation of the retrieved density profile to the *a priori* profile. There are no significant variations of the haze vertical profile with the real refractive index for values in the range 1.4-1.8. However, the aerosol concentration at the peak increases for smaller values of the real refractive index. As expected, the peak concentration increases with the imaginary refractive index. For high values of the imaginary refractive index, the single scattering albedo is smaller and so more aerosol particles are needed to reflect the sunlight radiation.

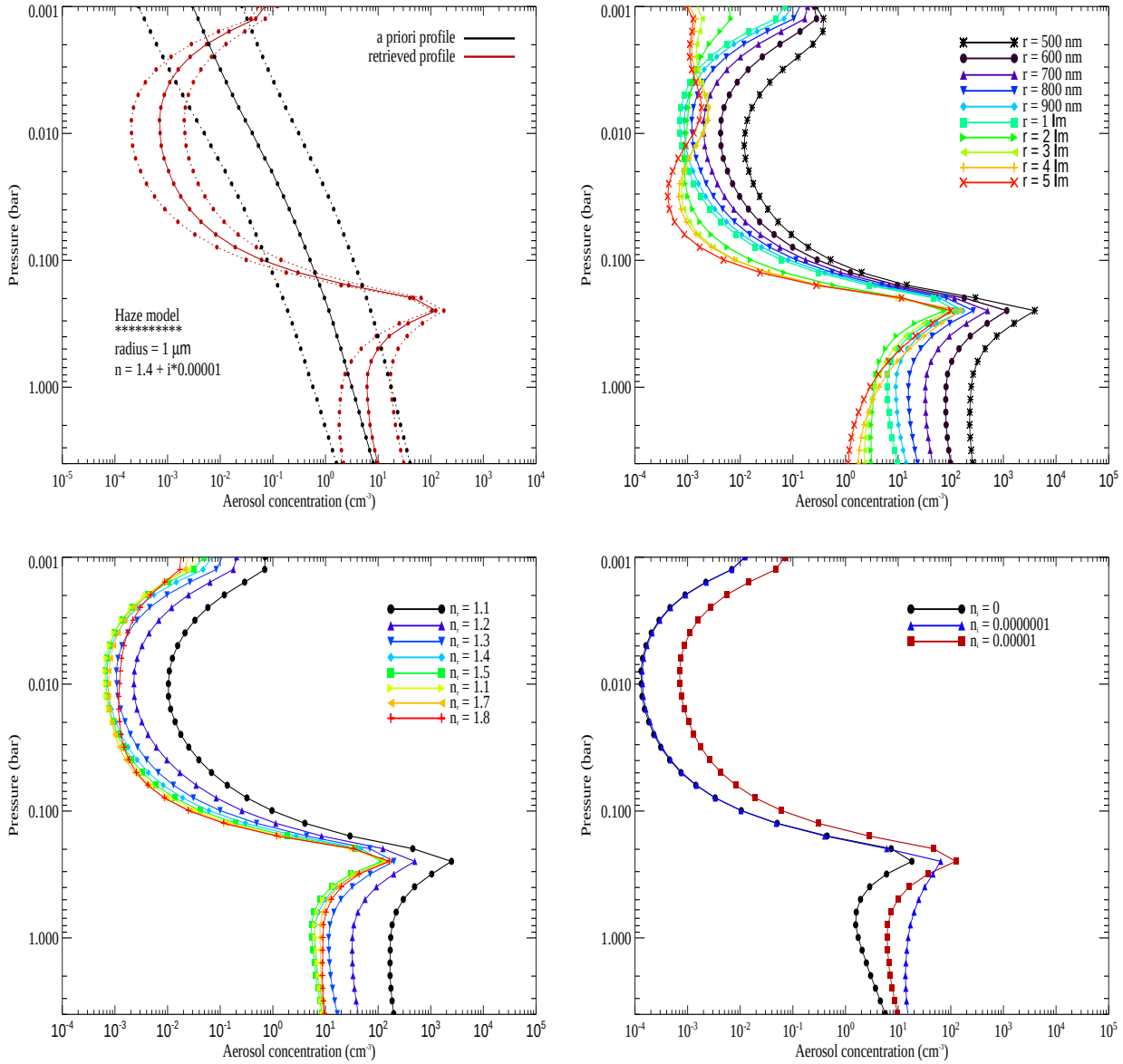



Figure 5.11: Haze vertical structure derived from the VIMS near-infrared reflection spectrum at 20° S measured on 26 April 2006 at an emission angle of 38° and a solar angle of 76°. The *a priori* (black solid line) and retrieved (red solid line) aerosol density profiles for a particle size of 1 $\mu$m and a complex refractive index equal to 1.4 + i$\times 10^{-5}$ are plotted in the top-left figure. Errors on the *a priori* and retrieved profiles are shown respectively in black and red dot-dashed lines. The effect of the particle size and complex refractive index on the retrieved density profiles is presented in the three other figures. *Top-right*: The complex refractive index is set to the value 1.4 + i$\times 10^{-5}$ while the particle size is allowed to vary between 500 nm and 5 $\mu$m. Larger aerosol particles have smaller retrieved concentrations. *Bottom-left*: the imaginary refractive index and the particle size are fixed to respectively $10^{-5}$ and 1 $\mu$m. The aerosol density profiles are plotted for a real refractive index in the range 1.1-1.8. The haze profiles are very similar for all values of the real refractive index above 1.4. Below 1.4, the aerosol concentration at the peak increases as the real refractive index decreases. *Bottom-right*: The density profiles are retrieved for three values of the imaginary refractive index below the 0.001 threshold value, and for a real refractive index of 1.4 and a particle size of 1 $\mu$m. Aerosol particles with a higher imaginary refractive index have a smaller single scattering albedo, and thus have higher concentrations.

### 5.4.2 Testing the *a priori* profile

The aerosol concentration is retrieved from a first guess vertical profile, or *a priori* profile. In NEMESIS, both the *a priori* value and error must be specified at each pressure level considered in the atmospheric model. As mentioned in the previous section, the *a priori* value of the specific density in number of particles per gram is fixed to $10^4$. The *a priori* errors are set so that to balance the measurements with the *a priori* constraints. The sensitivity of the retrieved vertical distribution to the *a priori* profile is tested here by assuming different values for the *a priori* value and error. The vertical profiles retrieved with NEMESIS for an *a priori* value of $10^2$, $10^4$ and $10^6$ are shown in Fig. 5.12. The results of the retrievals are shown for the 20° S latitude spectrum measured at an emission angle of 38° and a solar angle of 76°. The modelled spectra for each of the *a priori* values are also compared to VIMS observations in Fig. 5.12. The lowest $\chi^2/N_\lambda$ value, equal to 1.3, is obtained for an *a priori* value of $10^4$. In that case, the *a priori* value is very close to the median value of the retrieved aerosol concentrations. As a result, the numerical code retrieves the concentration profile with better accuracy. The *a priori* profiles for an *a priori* value of $10^2$ and $10^6$ are further way from the retrieved solution, and so the retrieval errors are larger than for an *a priori* value of $10^4$.The three retrieved profiles share common features. They all show a peak of concentration below the tropopause at around 200 mbar. The concentration decreases significantly at lower pressures above the peak up to the 10-mbar level, and then increases above that level. Below the peak, the aerosol concentration decreases until it relaxes to its *a priori* profile. The concentration profile is retrieved for an *a priori* value of $10^4$ and different *a priori* constraints in Fig. 5.13. Lower *a priori* constraints have smaller $\chi^2/N_\lambda$ values, since the retrieved profile is allowed to deviate further away from the *a priori* profile. However, the $\chi^2/N_\lambda$ values for the three *a priori* constraints are still very close, and so the three modelled spectra are in good agreement with VIMS data. The three retrieved profiles are very similar especially above the concentration peak. Below the peak, the aerosol profile relaxes more closely to the *a priori* profile if higher *a priori* constraints are applied. The retrieval strategy adopted in the previous section provides the best fits to the observations: the *a priori* value is chosen so that to minimise the $\chi^2/N_\lambda$ value and the *a priori* constraints are chosen so that to balance the measurements.

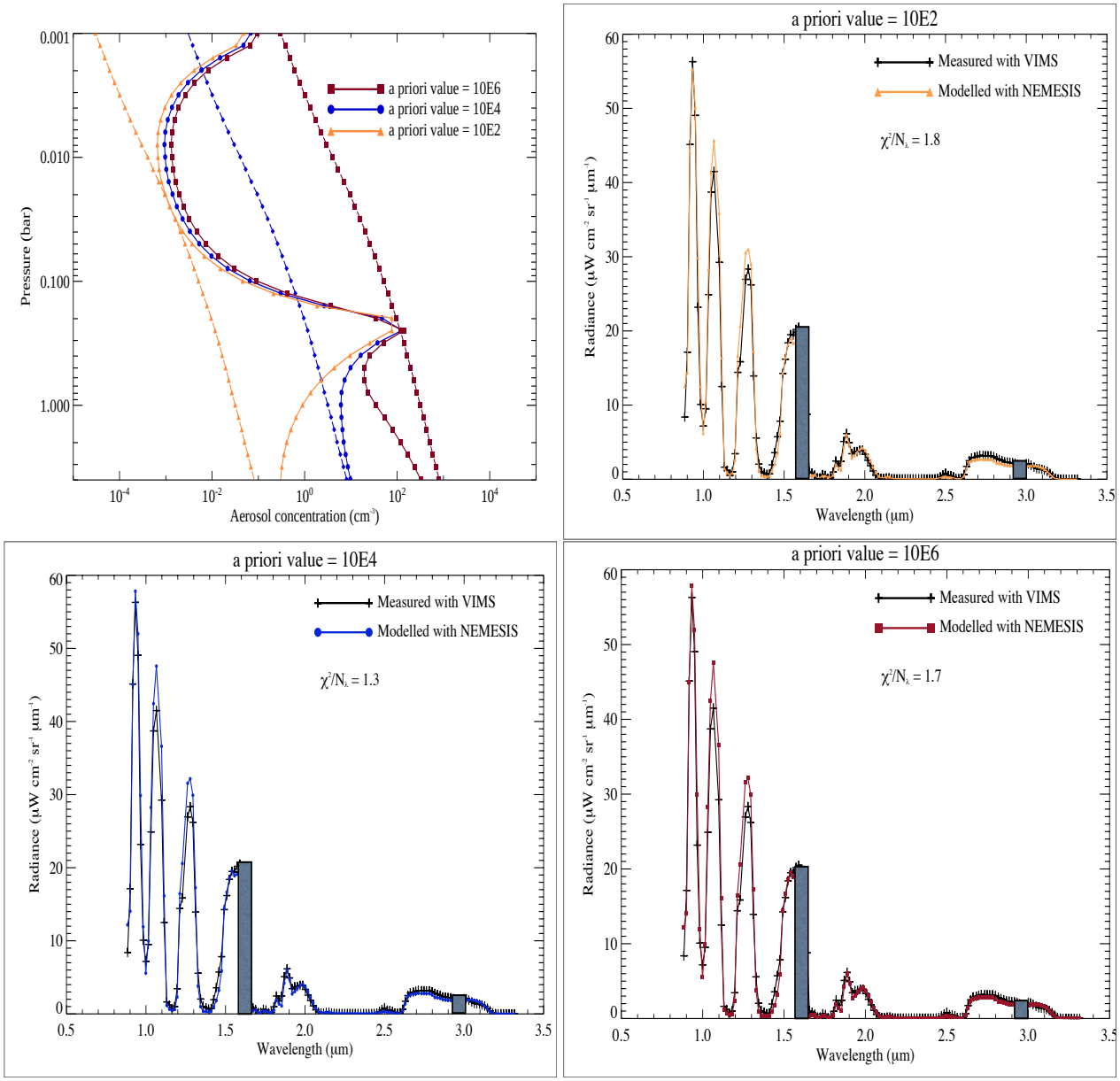



Figure 5.12: Sensitivity of the retrieved haze vertical profile to the *a priori* value. A particule size of one micrometre and a complex refractive index of $1.4 + i \times 10^{-5}$ are assumed in the model. NEMESIS retrieves the specific density in number of particles per gram. The specific density is multiplied here by the atmospheric density in order to obtain the aerosol concentration in number of particles per cubic centimetre. The aerosol concentration is retrieved for three different *a priori* value equal to $10^2$, $10^4$ and $10^6$. Both the *a priori* and retrieved vertical profiles are shown in the top-left panel. The *a priori* errors are chosen so that to balance the measurements. The measured and modelled spectra are compared with each other for *a priori* value of $10^2$, $10^4$ and $10^6$ in the top-right, bottom-left and bottom-right panels respectively.

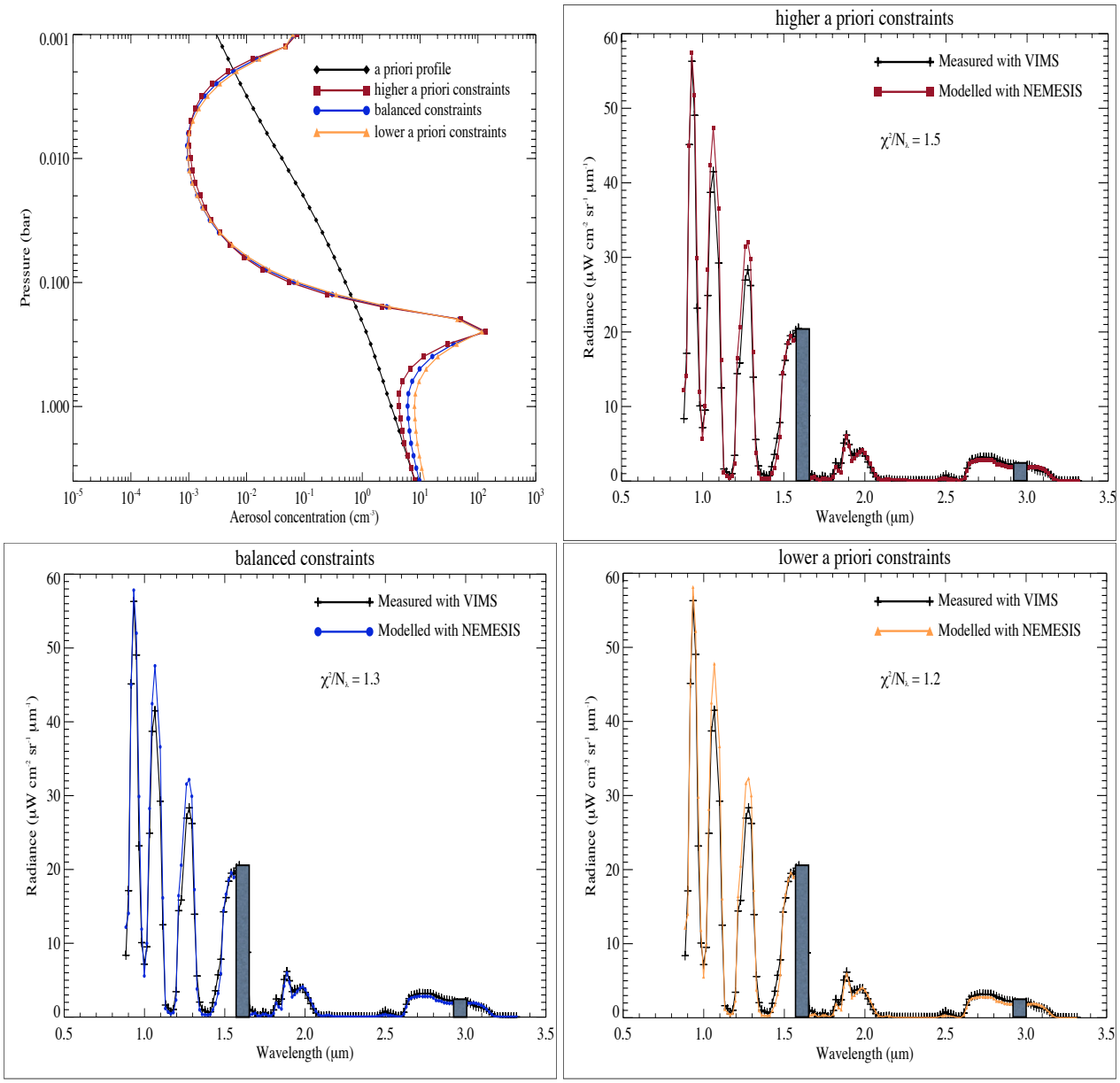


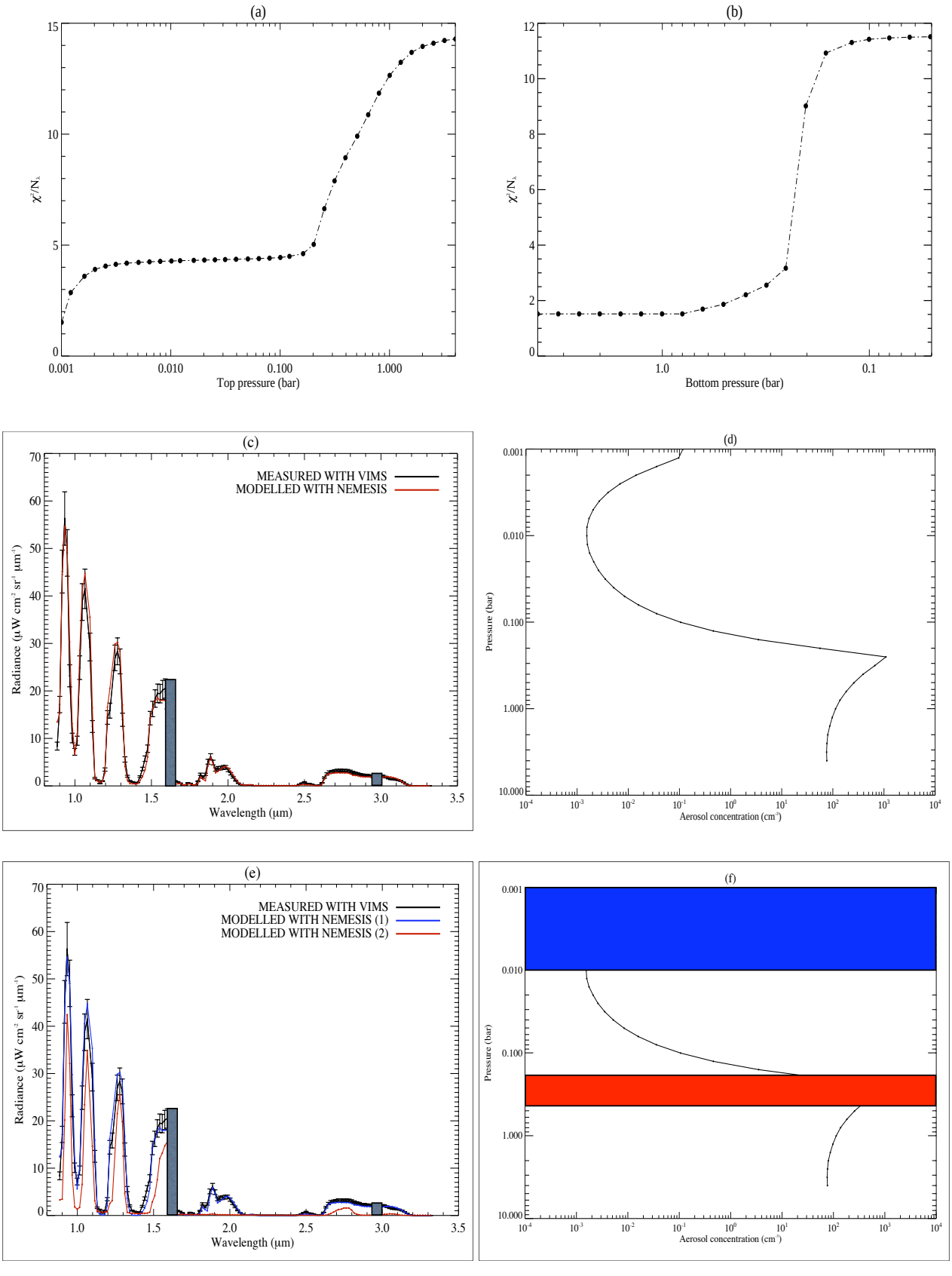

Figure 5.13: Sensitivity of the retrieved haze vertical profile to the *a priori* error. The aerosol concentration at each pressure level is retrieved from Saturn's reflection spectrum for a particle size of 1 $\mu$m and a complex refractive index of $1.4+i\times10^{-5}$. The *a priori* value of the specific density is fixed to a constant value at all pressure levels equal to $10^4$. The *a priori* profile of the aerosol concentration is shown in black line in the top-left panel The retrieved profile for an *a priori* error of $10^3$ is shown in blue line. The retrieved profiles for lower and higher *a priori* constraints are shown respectively in orange and red lines. The spectrum measured with VIMS is compared with the modelled spectrum for each of the three *a priori* constraints in the top-right and bottom panels.

### 5.4.3 Sensitivity to pressure levels

NEMESIS retrieves the haze vertical distribution from a continuous *a priori* profile between the 1-mbar and 4-bar pressure levels. The contribution weighting functions at the reflection peaks have shown that any aerosols present above 1 bar might be detected by the VIMS instrument. In between the reflection peaks, the absorption of solar radiation prevents the detection of aerosol particles approximately below the 10-mbar pressure level. However, any aerosol particle above that level could potentially reflect the sunlight in the absorption bands. Indeed, the stratospheric haze is responsible for the very low radiances in the absorption bands. As a result, the aerosol concentration retrieved with NEMESIS increases above the 10-bar level until at least 1 mbar (see Fig. 5.11).

The effect of stratospheric aerosols at higher altitudes on Saturn's near-infrared reflection spectra is assessed by running sensitivity tests for various physical and optical haze properties. For all values of the aerosol particle size and complex refractive index, the haze concentration is retrieved at each of the 37 pressure levels between 1 mbar and 4 bar. The first pressure level at the top of the atmosphere is removed from the retrieved profile and the reference atmosphere, and then the synthetic near-infrared spectrum is recalculated and the new $\chi^2/N_\lambda$ values evaluated. Therefore, the effect of the first pressure level on the reflection spectrum can be assessed. The same calculation is made after removing all levels from the top atmosphere until the second pressure level. This process is iterated 37 times by removing the first through to the $N^{th}$ levels until the bottom pressure is reached ( N = 37). At each iteration, the reference atmosphere is thus redefined between a new top pressure level (corresponding to the $N^{th}$ level) and the 4-bar pressure level.

The $\chi^2/N_\lambda$ values as a function of the new top pressure level for an aerosol particle size of 700 nm and a complex refractive index of $1.4 + i\times10^{-7}$ are shown in Fig. 5.14. By lowering the top pressure level from the 1-mbar level to the 3-mbar level, the $\chi^2/N_\lambda$ value increases from 1.5 to 3. As expected this mainly affects VIMS near-infrared reflection spectrum in the absorption bands, but not at all at the reflection peaks. Therefore, aerosols must be present at higher altitudes in the stratosphere in order to fit the low radiances in the absorption bands. The effect of stratospheric aerosols above the 10-mbar pressure level was also assessed by removing the 1-10 mbar region in the reference atmosphere. As can be seen in 5.14, the low radiances in the first four absoption bands could not be modelled anymore.


(a)
χ²/N_ε
Top pressure (bar)
(b)
χ²/N_ε
Bottom pressure (bar)
(c)
MEASURED WITH VIMS
MODELLED WITH NEMESIS
Radiance (μW cm⁻² sr⁻¹ μm⁻¹)
Wavelength (μm)
(d)
Pressure (bar)
Aerosol concentration (cm⁻³)
(e)
MEASURED WITH VIMS
MODELLED WITH NEMESIS (1)
MODELLED WITH NEMESIS (2)
Radiance (μW cm⁻² sr⁻¹ μm⁻¹)
Wavelength (μm)
(f)
Pressure (bar)
Aerosol concentration (cm⁻³)

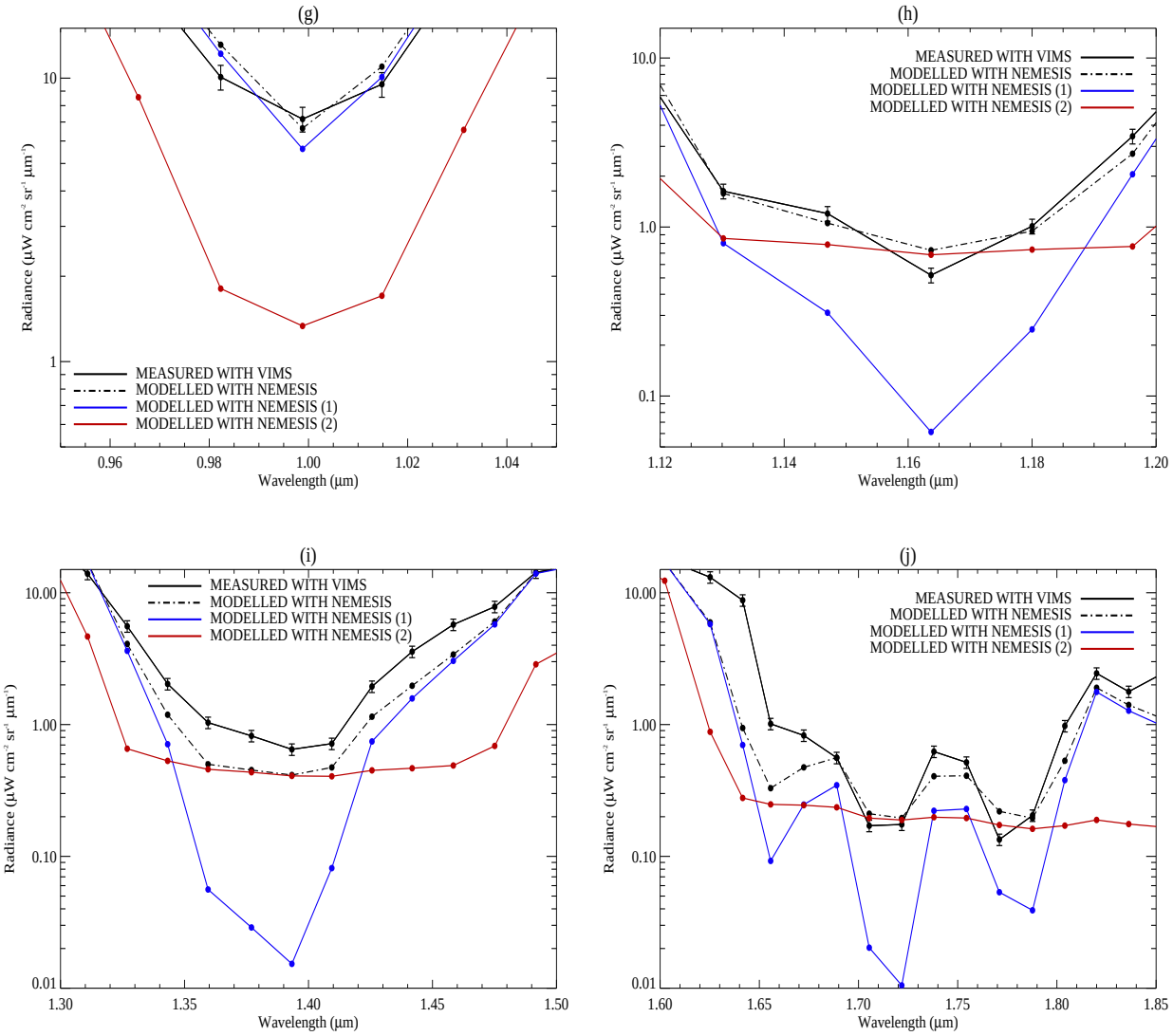



Figure 5.14: Sensitivity of Saturn's near-infrared reflection spectrum to the haze pressure levels. *(a)*: The sensitivity to the haze's top pressure level is tested by removing all levels between 1 mbar and a new top pressure level defined as the x-coordinate. For example, the $\chi^2/N_\lambda$ value at 10 mbar corresponds to the goodness-of-fit after all pressure levels beween 1 mbar and 10 mbar are removed. *(b)*: A similar method is applied to test the sensitivity of Saturn's reflection spectrum to the haze concentration at lower altitudes. This time, the pressure levels between 4 bar and a new bottom pressure are removed, and the $\chi^2/N_\lambda$ value recalculated. The goodness-of-fit is plotted as a function of the new bottom pressure. *(c)*: Modelled and measured reflection spectra for aerosols with a radius of 700 nm and a refractive index of $1.4 + i\times10^{-7}$. The retrieved haze profile is shown in panel *(d)*. *(e)*: The synthetic spectra are recalculated after either the 1-10 mbar region (1) or the concentration peak (2) are removed from the haze profile. The two regions are shown in panel *(f)* in blue and red respectively. The panels *(g)*, *(h)*, *(i)* and *(j)* show the fit to the observations in the first four different absorption bands after the red and blue regions have been removed from the temperature profile. The modelled spectrum for an atmospheric model including all pressure levels is shown in black dot-dashed line. The stratospheric haze is mainly necessary to model the low radiances in the first four absorption bands. Note that trospospheric aerosols also contribute to the first absorption band at 1.1 $\mu$m since the two-way weighting function peaks slightly deeper at this wavelength (see Fig. 5.3).

The $\chi^2/N_\lambda$ value is constant for a top pressure between 3 and 100 mbar. As mentioned earlier, there is a sharp drop of aerosol concentration above the peak up to 10 mbar, which is further on referred to as the "opacity clearing". The low concentration at the opacity clearing has barely any effect on Saturn's near-infrared reflection spectrum. the goodness-of-fit worsens for a top pressure higher than 200 mbar. As expected, aerosols at the concentration peak and below contribute the most to the reflection of sunlight at 0.8-3.5 $\mu$m. The concentration peak was removed in the reference atmosphere and the new synthetic spectrum recalculated. As expected, the intensity at the reflectance peaks and in the first absorption band at 1.1 $\mu$m dropped quite significantly. A similar sensitivity analysis is carried out for the haze bottom pressure. Also this time, the goodness-of-fit is evaluated for haze particles between 1 mbar and a new bottom pressure (see Fig. 5.14). The $\chi^2/N_\lambda$ value is constant for a bottom pressure between 4 bar and 600 mbar, and then increases for bottom pressures lower than 600 mbar. This confirms that aerosols present in the vicinity of peak at 200 mbar contribute the most to Saturn's near-infrared spectrum.

The main features of the the haze profile and their contribution to Saturn's near-infrared reflection spectrum can be summed up as follows:

*i.* A peak of aerosol concentration at 200 mbar contributing to most of the sunlight reflection.

*ii.* A sharp decrease of aerosol concentration above the peak until 10 mbar, referred to as the "opacity clearing". Aerosol concentrations at those pressure levels are not large enough to affect the 0.8-3.5 $\mu$m spectrum.

*iii.* An increase of aerosol concentration above the 10-mbar level which reflect the sunlight radiation in the absorption bands.

*iv.* A decrease of aerosol concentration below the peak down to the 600-mbar pressure level. The opacity at deeper tropospheric levels becomes too high to allow sounding by the VIMS instrument, and so the retrieved profile relaxes ultimately to the *a priori* profile. Because near-infrared VIMS data can sound as deep as 600 mbar, these data are sensistive to the region right below the peak. If opacity sources are added in the region between 300 and 600 mbar, the model differs significantly from the measured spectra. Only opacity sources at pressures higher than 600 mbar would have no effect on the model. Therefore, the analysis of VIM near-infrared reflection spectra has shown that only a detached peak is in good agreement with the data observations.

### 5.4.4 Opacity clearing

The haze vertical distribution is characterised by the opacity clearing above the concentration peak. The existence of this feature is tested by considering two new parametrisations of the haze vertical profile. A simple compact model similar to the compact cloud model in chapter 4 is first considered. In this model, the aerosol concentration is equal to zero everywhere except at one pressure level. The aerosol concentration is retrieved with NEMESIS for each base pressure of the aerosol layer varying between 1 mbar and 4 bar.

The goodness-of-fit as a function of the base pressure is shown in Fig. 5.15 for an aerosol particle size of one micrometre and a complex refractive index of 1.4 + i$\times$0.00001. The best fit to the observations is obtained for a compact aerosol layer at 0.16 bar. Despite the large $\chi^2/N_\lambda$ value of around 10, this result shows that the solution to the retrieval problem tends towards an opacity source right below the tropopause.

Note that haze particles formed in gas giants may have migrated from the location where they were originated as suggested by Friedson *et al.* (2010). Although his model originally applies to Jupiter's atmosphere, it is suggested that Saturn might undergo similar microphysical processes. Photochemical reactions are responsible for the formation of haze particles. However, microphysical reactions leading to the growth of haze particles, such as nucleation, can lead to a vertical displacement of haze particules which then undergo sedimentation at deeper atmospheric levels.

The synthetic spectrum for a haze layer at 0.16 bar calculated with the radiative transfer algoritm is compared with the measured VIMS spectrum. Radiances modelled at the six reflection peaks have lower values than the measurements. This suggests that reflection from adjacent layers also contributes to Saturn's near-infrared spectra at 0.8-3.5 $\mu$m. However, placing the haze layer further away from the 0.16-bar pressure level significantly worsens the discrepancies between the compact model and the observations. In particular, an aerosol layer at any pressure level in the opacity clearing region leads to $\chi^2/N_\lambda$ values around twice the value at 0.16 bar. This result also supports the idea of an opacity clearing above the tropopause.

The haze model was modified to an extended vertical profile since a simple compact model can only match very approximately the observations. Saturn's haze is now represented by an extended "block" model where aerosols have a constant density in particle number per gram between a top

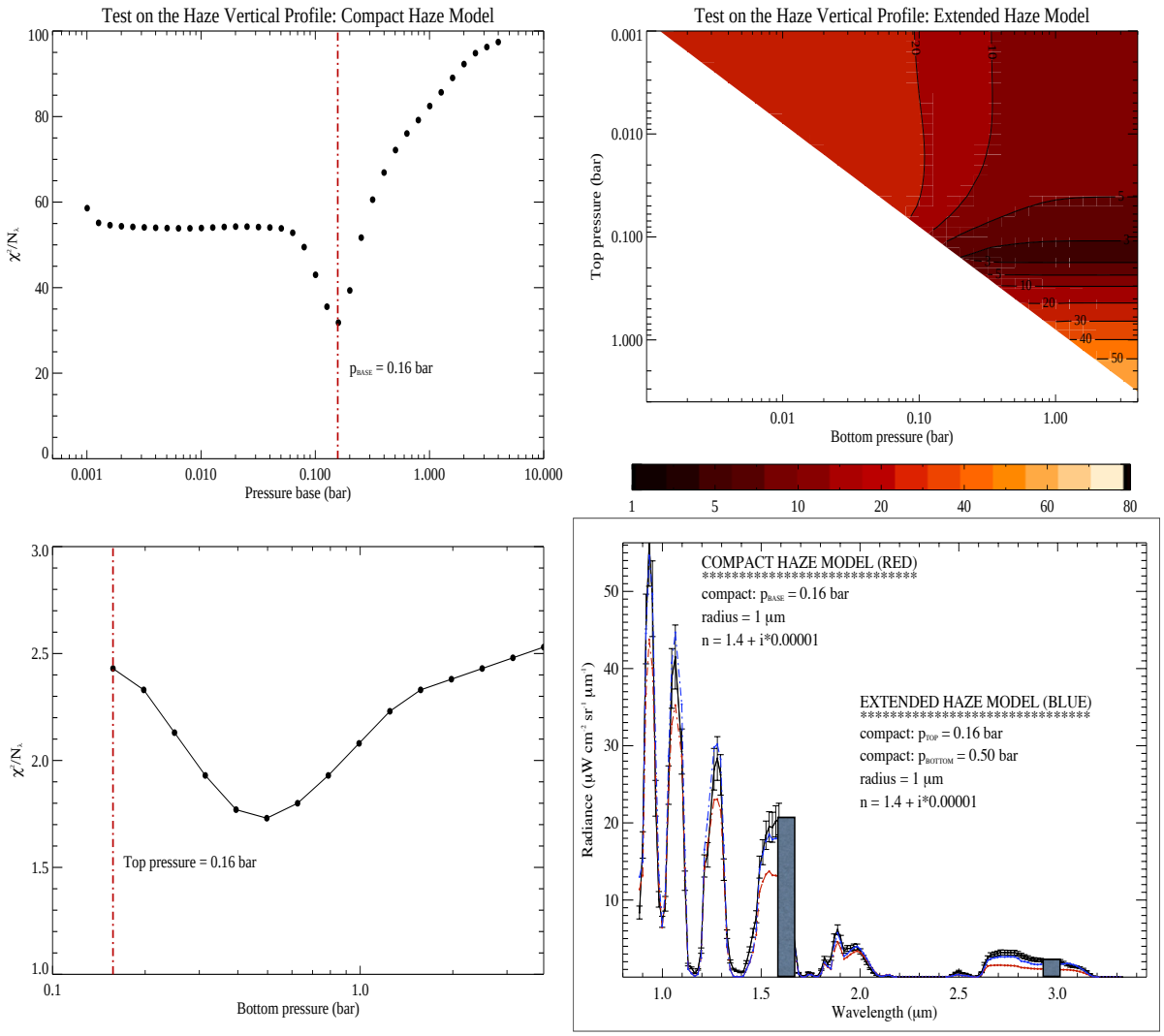



Figure 5.15: Validity of the opacity clearing. An aerosol particle size of one micrometre and a complex refractive index of 1.4 + i×0.00001 are assumed here for both the compact and block models. *Top-left:* Goodness-of-fit as a function of the pressure base for a compact aerosol layer. The lowest $\chi^2/N_\lambda$ value is obtained for an aerosol layer at 0.16 bar. *Top-right:* The goodness-of-fit for an extended aerosol layer as a function of the bottom and top pressures of the haze. In the extended "block" model, the aerosol concentration is constant between a bottom and top pressures which are allowed to vary simultaneously in the range 0.001-4 bar. The best fits to the data are obtained for a top pressure of 0.16 bar. *Bottom-left:* Goodness-of-fit as a function of the bottom pressure for an extended cloud with a top pressure at 0.16 bar. *Bottom-right:* The synthetic spectra for a compact haze layer at 0.16 bar and an extended layer between 0.16 and 0.50 bar are plotted against the near-infrared reflection spectrum measured with VIMS.

and bottom pressures, and are absent everywhere else. The top and bottom pressures are allowed to vary simultaneously between 1 mbar and 4 bar, with the only condition that the bottom pressure must always have a higher value than the top pressure.

The scale factor of the aerosol density profile is retrieved, and the $\chi^2/N_\lambda$ value calculated for each case. The goodness-of-fit map for the block model shows that there is a tight constraint on the

top pressure level (see Fig. 5.15). Only top pressure levels between 100 and 200 mbar have $\chi^2/N_\lambda$ values sufficiently low, below the 5-threshold value, to match VIMS observations. The constaint on the bottom pressure is not as strong as for the top pressure, and the haze layer can potentially extend from the top pressure level down to the 4-bar level. However, the minimum $\chi^2/N_\lambda$ value is obtained for a bottom pressure at 0.50 bar as it can be seen in the bottom-left pannel in Fig. 5.15. This is consistent with the aerosol concentration peak and the decrease of concentration below the peak observed in the continuous model.

The synthetic spectrum for a haze layer extending between 0.16 and 0.50 bar is compared to VIMS data in Fig. 5.15. The model matches the observations quite well within the measurement errors, contrary to the compact model. For any value of the top pressure in the opacity clearing region, there are no bottom pressure values for which the model can match the observations. That is to say, a block distribution with the top pressure level located anywhere in the opacity clearing region cannot match the observations.

Similar conclusions are drawn for all combinations of the aerosol particle size, real refractive index and imaginary refractive index respectively in the ranges 0.5-5 $\mu$m, 1.1-1.8, and 0-0.001. In conclusion, the compact and extended models, as well as the continous model all support the idea of an opacity clearing above the concentration peak.

Furthermore, the compact and extended models have shown that the aerosol concentration should peak between 100 and 200 mbar, which is coherent with the results obtained from a continuous model. Note that the lowest $\chi^2/N_\lambda$ values for the continuous model are around 1.5, whereas optimal $\chi^2/N_\lambda$ values for the extended model are in the range 1.8-2.5. Therefore, the continuous model provides synthetic spectra in better agreement with VIMS reflection data, and is widely used in this thesis. However, the extended model is particularly useful to test the validity of the opacity clearing.

## 5.5 Latitudinal variations

The analysis of Saturn's reflection spectra from 0.8 to 3.1 $\mu$m has focused on one specific latitudinal band so far. Although such an analysis has constrained the haze optical and physical properties, the vertical aerosol structure is very likely to have spatial variations (Karkoschka and Tomasko, 2005; Pérez-Hoyos *et al.*, 2005; West *et al.*, 2009). The variation of haze distribution with latitude is

investigated in this section. The VIMS spectral cube CM1564373826 measured on 29 July 2007 at $03^h42^m29.596^s$ was extracted from the PDS pipeline. The calibrated image at the 0.93-$\mu$m reflection peak as well as the relevant backplane information are presented in Fig. 5.16. Only dayside near-infrared reflection spectra were considered in the retrieval of haze vertical structure. In addition, the VIMS image covers all latitudes between 80°S and 50°N, and so this spectral cube is particularly appropriate to study the spatial distribution of Saturn's hazes.

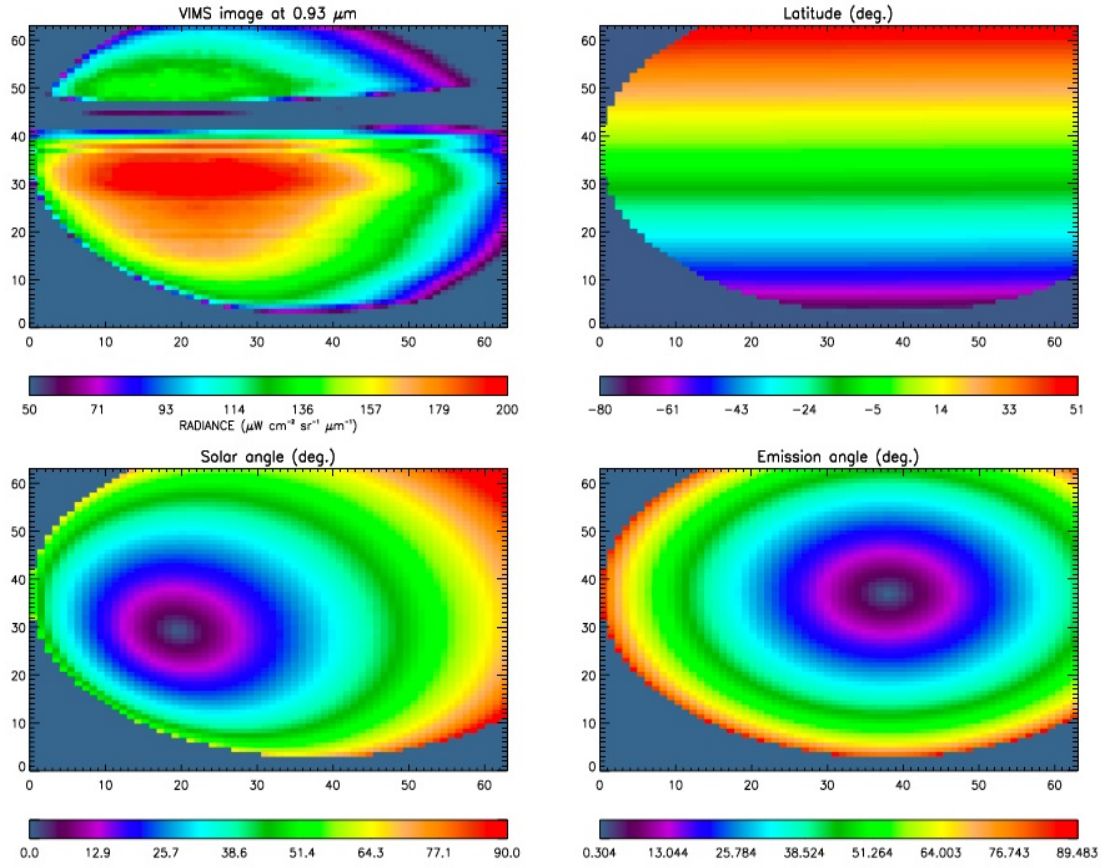



Figure 5.16: VIMS image at 0.93 $\mu$m and viewing geometry for the study of latitudinal variations of the haze structure in Saturn's troposphere and stratosphere . The spectral cube CM1564373826 was measured on 29 July 2007 at $03^h42^m29.596^s$. The VIMS image at the first reflection peak ($\lambda$ = 0.93 $\mu$m) is shown in the top-left panel. The shadows of the rings between around 10°N and 20°N mask the reflection of sunlight by hazes at these latitudes. The backplane data including the latitude (*top-right*), the solar angle (*bottom-left*) and the emission angle (*bottom-right*) are given for all pixels.

Fig. 5.16 shows that radiances measured at the first reflection peak range between 50 and 200 $\mu$W·cm$^{-2}$·sr$^{-1}$·$\mu$m$^{-1}$. There is no signal detected between approximately 10°N and 20°N because of Saturn's ring shadows over the area of the planet at those latitudes. The rings are aligned with the Saturnian equator, however VIMS cube CM1564373826 was measured on July 2007 between the

southern summer solstice in 2002 and the vernal equinox in 2009 (Saturn's sidereal orbital period is 29.42 years as it can be seen in Table 1.1). The southern hemisphere was thence tilted toward the Sun at the time of observation. As a result, the rings casted shadows on the northern hemisphere of Saturn in 2007. As the planet approached the vernal equinox, the ring shadows became thinner and moved closer to the equator. From 2009 until the northern summer solstice in 2017, the ring shadows will grow wider and wider and move from equator to south. The radiance effectively measured at 0.93 $\mu$m depends on the solar and emission angles. The hazes reflect more sunlight when the Sun is near the zenith, and so lower solar angles are associated with higher radiances, all other viewing angles being equal. Spatial variations of haze properties will also affect Saturn's near-infrared reflection spectra. As a result, radiances measured with VIMS instrument vary with the location on the planet.

The changes of solar and emission angles are responsible for the ringed pattern in Saturn's image at 0.93 $\mu$m. Radiances generally decrease from the centre until the sides of the image where data have higher solar and emission angles. However, regions of similar radiances are stretched in the horizontal direction, especially at lower values of the solar and emission angles. This suggests that the haze opacity varies with latitude. In particular, radiances reach their maximum value at the equator and decrease at higher latitudes where the zenith angle is higher. More aerosols present in the troposphere will reflect more solar radiation, and so higher radiance values in the equatorial region might be caused by the enhancement of haze opacity.

There is also an asymmetry between the southern and northern hemispheres of the planet, with the south being significantly brighter than the north. This can also be interpreted in terms of haze opacity gradient with latitude: larger aerosol concentrations in the southern hemisphere would indeed reflect more sunlight. This is particularly true for observations made at the same solar and emission angles. As described before, the range of viewing angles can also potentially affect Saturn's reflection spectra and so only preliminary conclusions can be drawn from simply looking at VIMS images. Note that similar features are observed at the five other reflection peaks, and so the next step is to consider the full 0.8-3.5 $\mu$m spectra in order to test the north-south variations of haze opacity.

All spectra are selected from single pixels between 80°S and 50°N along the central meridian were selected in the VIMS spectral cube CM1564373826. The aerosol particle size and complex refractive index were fixed to 1 $\mu$m and $1.4 + i\times10^{-7}$ respectively. The best-fitting aerosol density at each of the 37 pressure levels was retrieved with NEMESIS as before. The goodness-of-fit slightly

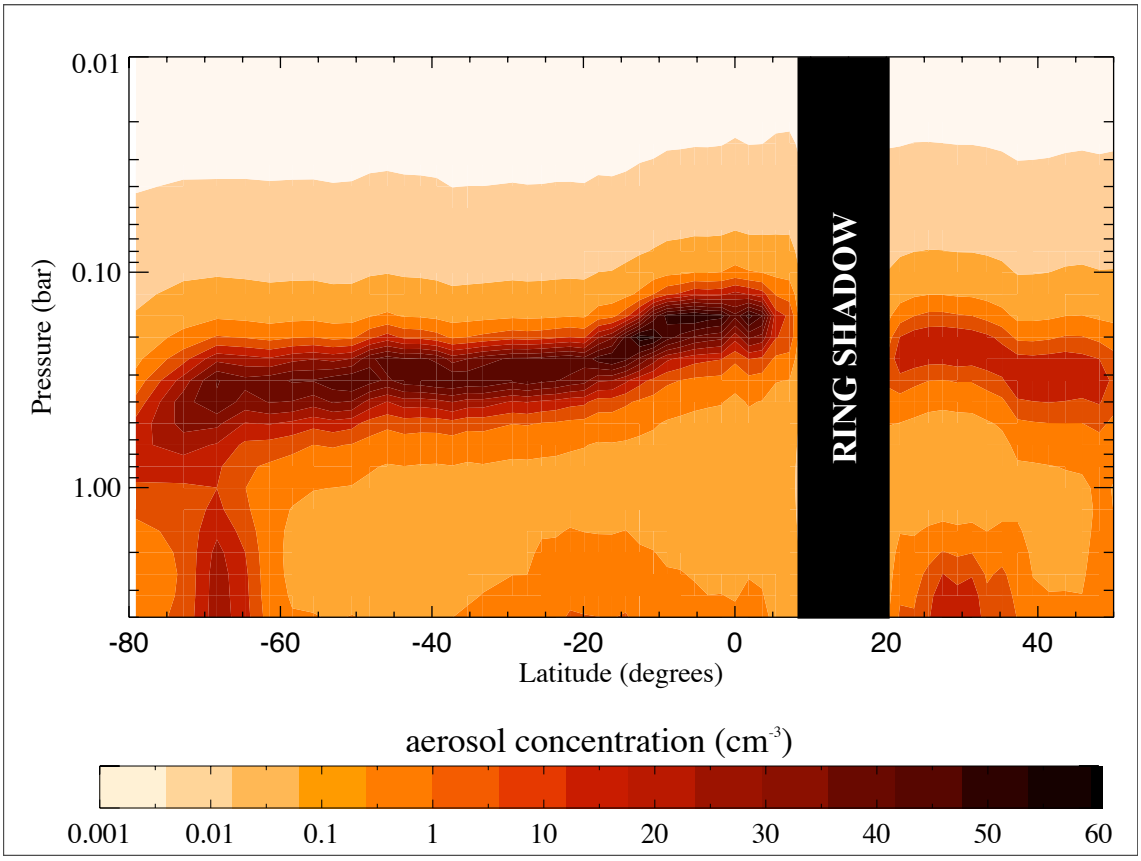



Figure 5.17: North-south variations of haze vertical distribution in 2007. VIMS near-infrared reflection spectra are extracted from VIMS cube CM1564373826. The spectra are measured at several latitude bands between 80°S and 50°N along the central meridian. A continuous density profile between 4 bar and 1 mbar is retrieved from each spectrum with NEMESIS for an aerosol particle size of 1 $\mu$m and a complex refractive index equal to $1.4 + i\times10^{-7}$. The aerosol concentrations in cm$^{-3}$ are mapped over all latitudes except between 10°N and 20°N where the shadows of Saturn's rings obscure the planet's area.

improves at lower latitudes where spectra are observed at lower emission angles, however $\chi^2/N_\lambda$ values at all latitudes are low enough to provide synthetic spectra similar to VIMS data within the measurement errors. The derived map of aerosol concentration in cm$^{-3}$ as a function of latitude and pressure is presented in Fig. 5.17.

The shadows of Saturn's rings between approximately 10°N and 20°N prevent the retrieval of haze concentration at these latitudes. The aerosol vertical profiles at other latitudes have a similar shape as described in Fig. 5.11. They are characterised by a peak of concentration at a pressure level varying with latitude, an opacity clearing above the peak and a relaxation of aerosol concentrations to their *a priori* values below the peak. The peak of density is located at higher altitudes at the equator, at about the 150-mbar pressure level. Vertical motions, abundance variation of photochemical parents and different solar penetrations are likely to explain the location of the peak higher up at the equator.

This is addressed in section 5.8 after haze candidates are identified. The variation of the peak location. As the latitude increases, the peak is retrieved at deeper pressure levels down to 600 mbar at 80°S. Furthermore, larger concentrations are retrieved at the equator than at higher latitudes in the southern hemisphere. Finally, the haze is less dense at the concentration peak in the northern hemisphere, as suggested from VIMS image at 0.93 $\mu$m in Fig. 5.16.

## 5.6 Temporal variations

| | CM1475290432 | CM1486552182 | CM1519321223 |
|---|---|---|---|
| Date | 6 October 2004 | 9 February 2005 | 23 February 2006 |
| Time | $02^h28^m45.678^s$ | $20^h09^m26.389^s$ | $17^h10^m32.970^s$ |
| | CM1564397814 | CM1585479555 | CM1635624405 |
| Date | 30 July 2007 | 29 March 2008 | 26 October 2009 |
| Time | $10^h22^m17.444^s$ | $03^h28^m52.244^s$ | $20^h43^m51.698^s$ |
| | CM1662581972 | CM1678106223 | CM1705877050 |
| Date | 20 September 2010 | 5 March 2011 | 21 January 2012 |
| Time | $19^h33^m22.496^s$ | $11^h49^m11.298^s$ | $21^h53^m22.493^s$ |

Table 5.5: List of VIMS observations used for the study of the haze temporal variations

The seasonal variation of the haze vertical structure is assessed in this section by considering nine VIMS spectral cubes measured in 2004, 2005, 2006, 2007, 2008, 2009, 2010, 2011 and 2012. The spectral cubes were selected so that the dayside images cover most of the northern and southern hemispheres. The nine cubes selected in this section are presented in Table 5.5. VIMS images at 1.07 $\mu$m corresponding to the second reflection peak are shown in Fig. 5.18 for each year. The ring shadows are systematically observed at dayside. The shadow due to the ring thickness is stronger at low solar angles. The shadow due to the largest and most massive of the rings, the B ring, is the most visible and is found closer to the equator. The A ring is located further away from the B ring so its shadow is found at higher latitudes.

The gap between the shadows of the A ring and B ring corresponds to the Cassini division. VIMS data in 2004-2008 are measured after the start of summer in the southern hemisphere in 2003 and before the Equinox in 2009. As a result, the ring shadows are observed in the norther hemisphere,

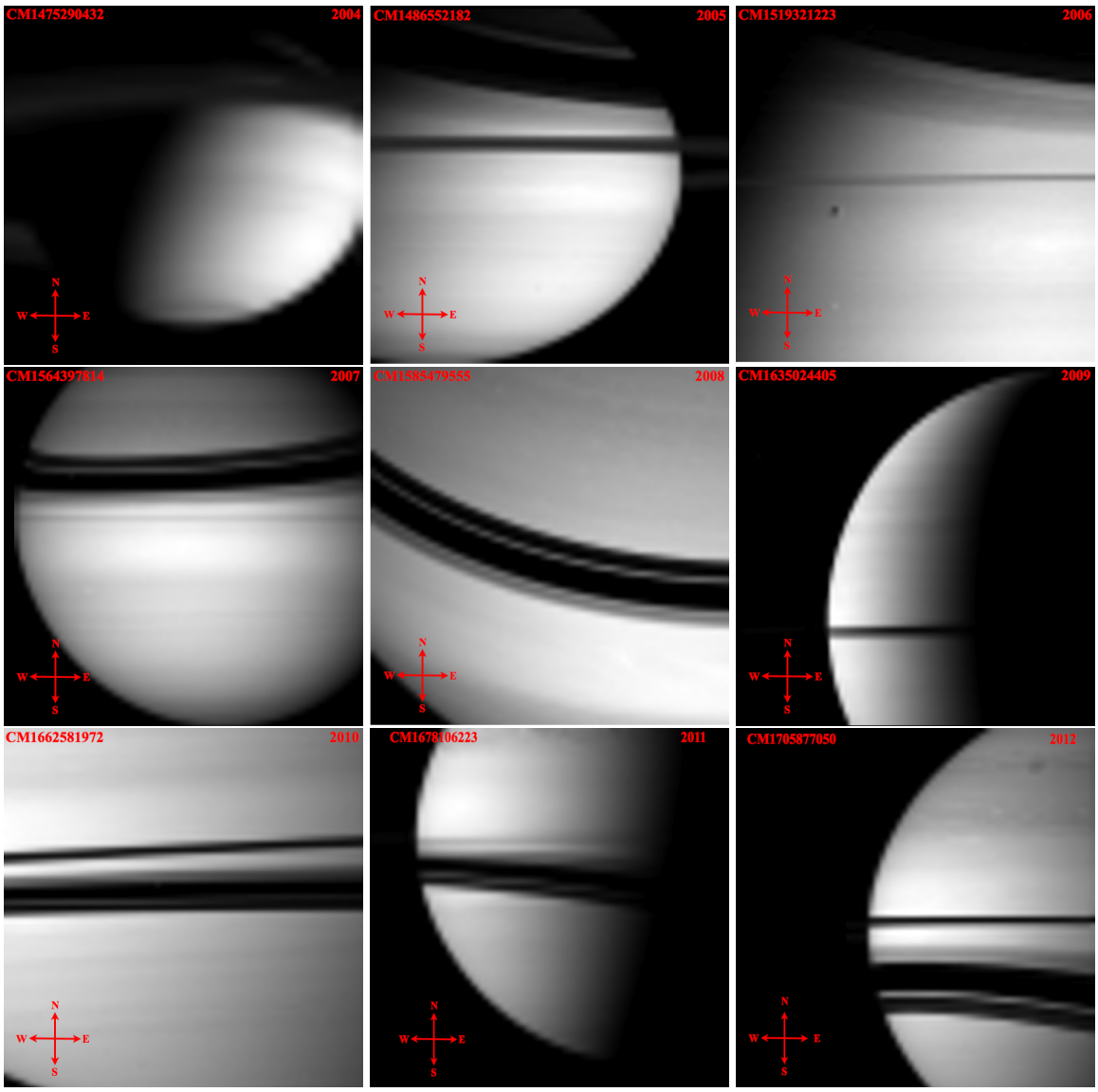



Figure 5.18: VIMS images at 1.07 $\mu$m used for the retrieval of haze properties in 2004-2012.

before they disappear in 2009 when the sun is facing the equator. After 2009, the Sun is moving towards the north pole of Saturn until 2017 when the northern hemisphere enters summer conditions. Therefore, the ring shadows in 2010-2012 are visible in the southern hemisphere of the planet.

For each data set, the $\chi^2/N_\lambda$ value is evaluated for all possible values of the aerosol particle size and complex refractive index. The results obtained for each year are very similar to those obtained in section 5.3. Very little variation of the optical and physical parameters with latitude is observed for each year and the best-fitting parameter values are uniform in 2004-2012. The optimum particle sizes in 2004-2012 are retrieved around one micrometre with lower or upper boundary values of about 500 nm and 5 $\mu$m. The real and complex parts of the refractive index are found mainly in the ranges 1.1-1.8 and 0-0.001 respectively.

The haze vertical structure is retrieved with NEMESIS for an aerosol particle size of 1 $\mu$m and a complex refractive index of $1.4 + \mathrm{i}\times10^{-7}$ from each of the nine spectral cubes. The meridians of observation are chosen so that similar longitudes are selected between the nine spectral cubes. The results of the retrievals are presented in Fig. 5.19. The ring shadows are shown in black on the maps. The vertical shape of haze opacity does not vary significantly in 2004-2012. The vertical profile is characterised by a peak of concentration below the tropopause, and the opacity drops below and above the peak. The concentration peak is retrieved at higher altitudes near the equator in all data sets.

The haze concentration shows significant variations between 2004 and 2012. Especially, the haze concentration in the southern hemisphere decreases with time whereas the concentration is stable in the northern hemisphere until 2012 when it starts increasing. The tropsopheric haze is made from the condensation of photochemical products, and so higher aerosol concentrations in the southern hemisphere are expected in 2002.

The haze concentration in the southern hemisphere drops between 2004 and 2012 as the south pole is moving further away from the Sun of the planet. In 2009-2011, the haze concentration is symmetric between the southern and northern hemispheres.

The haze becomes denser in the northern hemisphere only in 2012. Long photochemical times or lower volume mixing ratios of the photochemical parents in the northern hemisphere are very likely to explain the variation of response to the Sun exposure. This question is addressed at the end of section 5.8 where haze candidates are identified.

A similar analysis was carried out for all combinations of the best-fitting values of the aerosol particle radius and complex refractive. As seen in Fig. 5.11, the haze concentration varies with these parameters but the vertical structure stays the same. Similar qualitative results as for an aerosol particle size of 1 $\mu$m and a complex refractive index of $1.4 + \mathrm{i}\times10^{-7}$ are obtained for other parameter values. Therefore, the conclusions drawn from Fig. 5.19 can be extended to all particle size and complex refractive index.

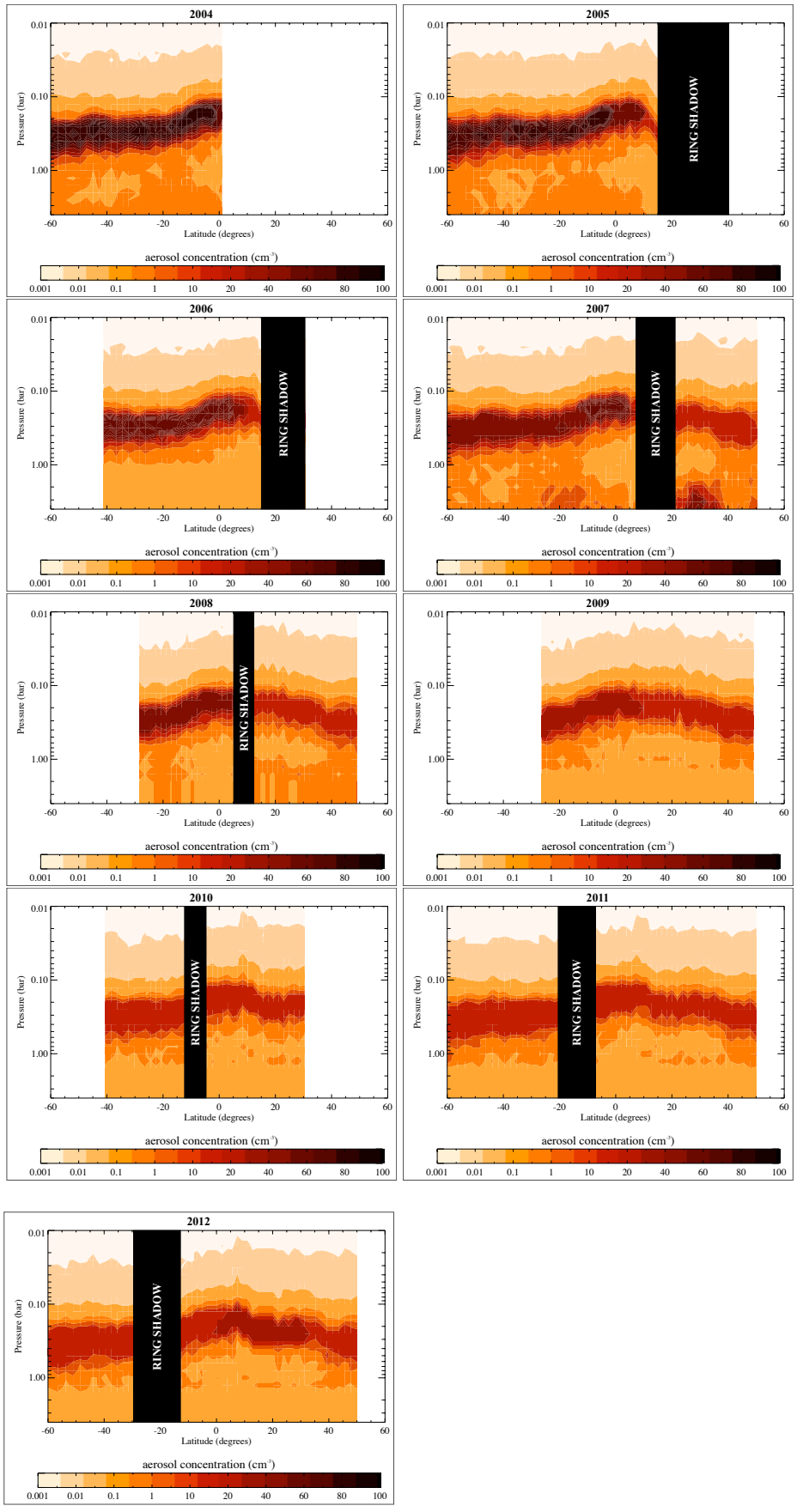



Figure 5.19: Latitudinal variation of haze concentration in 2004-2012.

## 5.7 The temperature knee: a correlation with the tropospheric haze ?

### 5.7.1 Overview

The "temperature knee" refers to a local increase of temperature below the tropopause and above the radiative-convective boundary, observed in the thermal structure of Saturn. A temperature knee was first derived from infrared spectra at 180-2500 $cm^{-1}$ measured with the IRIS instrument on board the Voyager 1 spacecraft by Hanel *et al.* (1981). They observed a local increase of temperature below the tropopause and above the radiative-convective boundary, at low northern latitudes and over much of the southern hemisphere. The IRIS infrared spectra were acquired in 1979, thus a year before the northern spring equinox. Note that such a feature has never been observed on Jupiter. A similar feature was observed by Fletcher *et al.* (2007) from the inversion of Cassini/CIRS mid- and far-infrared spectra measured during the 2004-2008 prime mission, just after the southern summer solstice in 2002 (see Fig. 1.3). They also observed variations of the temperature knee with latitude, with the knee being larger in the southern hemisphere, and smaller and higher over the equatorial zone. The asymmetry between the northern and southern hemispheres suggests that the temperature knee is dominated by radiative effects. Indeed, the knee has been observed at pressure levels above the radiative-convective boundary where the thermal structure of the troposphere is mainly determined by radiative cooling and heating of aerosols. Gravity waves propagating vertically might potentially also transfer energy at the altitude where they break. However such a process should occur at various altitudes rather than at specific altitude as observed for the temperature knee. Also, gravity waves are more likely to break at higher altitudes in the stratosphere. The conversion between ortho- and para-hydrogen has been suggested as the cause of the temperature knee, however there are no local features in the vertical profile of the para-hydrogen ratio that might explain the location of the temperature knee (Fletcher *et al.*, 2007). Finally, the absorption of visible and near-infrared sunlight might lead to a localised heating of the troposphere and so be responsible for the presence of a knee in Saturn's temperature profile (Pérez-Hoyos and Sánchez-Lavega, 2006). A local heating by Saturn's haze would be sensitive to seasonal variations and as a result would affect differently the northern and southern hemispheres. The insolation rate is larger in the summer hemisphere although

the thermal response in Saturn's atmosphere is expected to lag behind the solar forcing by one Saturnian season. This implies that the temperature knee should be larger just after the summer solstice which is coherent with the temperature structure retrieved from IRIS and CIRS spectra.

### 5.7.2 Temperature structure from CIRS infrared spectra

The FIRMAP spectra measured with the Cassini/CIRS instrument were used to study Saturn's thermal structure in the troposphere and stratosphere. In this observation mode, interferograms are obtained at a low spectral resolution of 15 $cm^{-1}$ from a close proximity within 17-37 Saturnian radii. As a result, the FIRMAP data are acquired at a high spatial resolution of 6-8° in the far-infrared and 1-2° in the mid-infrared. The FP1, FP3 and FP4 detectors scan all latitudes along the central meridian as the planet spins around its own axis. Typically, the equatorial zone is observed at lower emission angles and the emission angle increases at higher latitudes. FP1 far-infrared spectra at 30-550 $cm^{-1}$ are sensitive to the upper troposphere down to the 800-mbar pressure level (Fletcher *et al.*, 2007), covering the vertical region where the temperature knee has been observed so far. Only the far-infrared spectra are considered at first for the retrieval of Saturn's tropospheric temperature. A typical FP1 far-infrared spectrum at mid-latitude in the southern hemisphere is presented in Fig. 5.20. The rotational absorption lines of phosphine, ammonia and methane are expected to form in Saturn's spectra at 30-550 $cm^{-1}$, although there are not resolved at such the spectral resolution of 15 $cm^{-1}$. Instead the continuous spectrum is dominated by collision induced absorption (CIA) processes (Frommhold, 2006). This absorption arises from molecular collisions which lead to the formation of transient electric dipoles capable of interacting with the electromagnetic field. Saturn's atmosphere is mainly dominated by moelecular hydrogen ($H_2$) and helium (He). Therefore the $H_2$-$H_2$ and $H_2$-He collision pairs are responsible for most of the CIA opacity. There is also a smaller contribution to FP1 spectra from $H_2$-$CH_4$ and $CH_4$-$CH_4$ pairs. The CIA coeffients of the four collision pairs were included in the model from the tabulations of Borysow (1991, 1993) and Borysow *et al.* (1986, 1987, 1988). Fletcher *et al.* (2007) showed that Saturn's FP1 spectra are mainly sensitive to the temperature structure and the para-hydrogen distribution and so the vertical profiles of these two parameters were retrieved with NEMESIS. Saturn's far-infared spectra at 30-550 $cm^{-1}$ are not sensitive to the aerosol opacity and as a result an aerosol-free atmosphere was assumed for the analysis of CIRS

data. The reference atmosphere is defined for 120 pressure levels between 0.001 mbar and 10 bar, equally spaced in logarithm scale with $\Delta \log_{10} p \sim 0.06$. The six following gases are included in the model: $H_2$, HD, He, $PH_3$, $NH_3$ and $CH_4$. The vertical distribution of these gases as described by Fletcher *et al.* (2007) was set up in the reference atmosphere. The other gases present in Saturn's troposphere and stratosphere have either a negligible effect on the planet's spectra at 30-550 $cm^{-1}$ or a low volume mixing ratio.

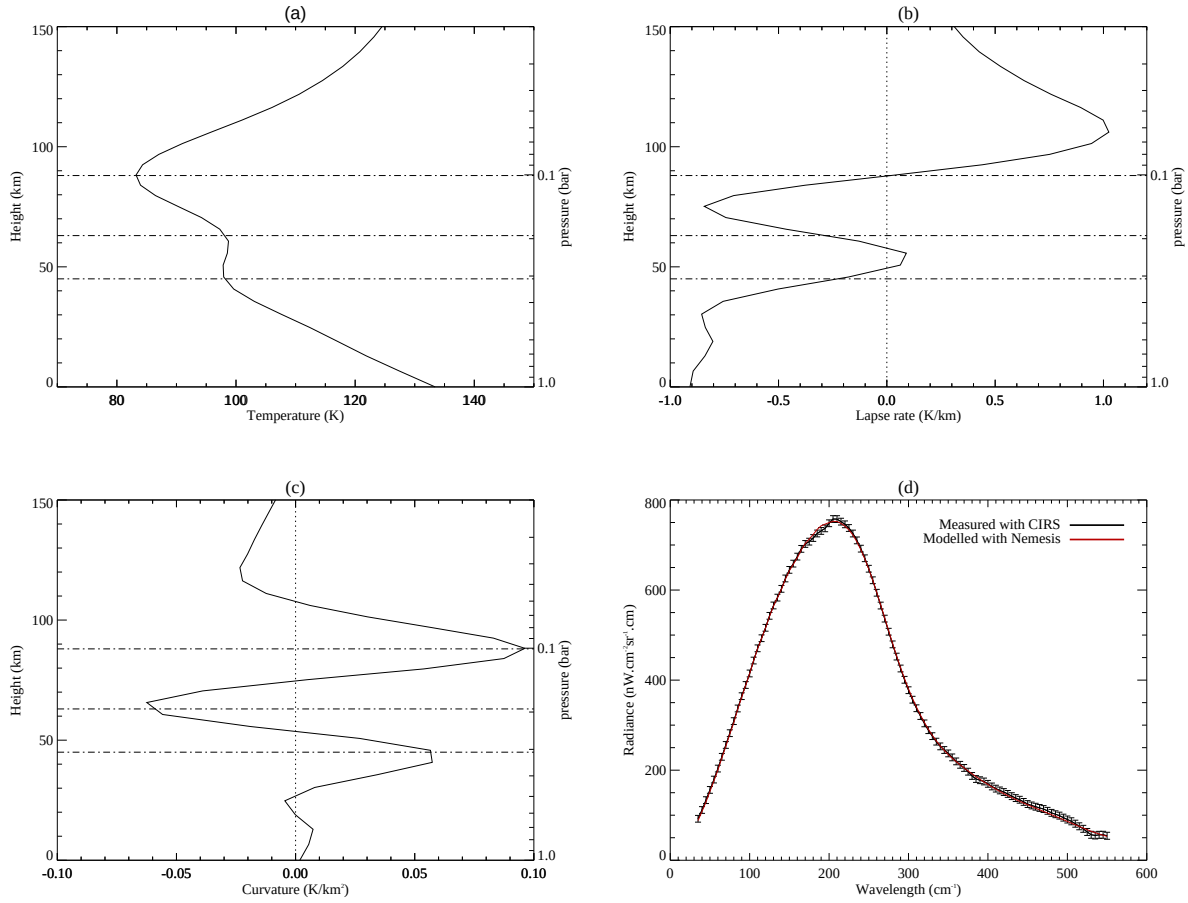



Figure 5.20: Temperature, lapse rate and curvature profiles in Saturn's troposphere and stratosphere at 30°S. Both the thermal structure (a) and the para-hydrogen distribution are retrieved with NEMESIS from CIRS far-infrared data in the 30-550 $cm^{-1}$ wavenumber range. 147 spectra measured on 26 January 2009 between $14^h06^m00^s$ and $18^h05^m22^s$ were averaged over a latitude, longitude and emission angle of respectively -30.03° ± 0.58°, 200.55° ± 34.16° and 12.08° ± 0.98°.The temperature knee, as well as the local minima of temperature below and above the knee are shown in dot-dashed lines. The measured and modelled spectra are presented in panel (d). The lapse rate (b) and curvature (c) are calculated at each pressure level from the temperature profile.

The temperature and para-hydrogen vertical profiles were retrieved from a co-added 30-550 $cm^{-1}$ spectrum at 30°S averaged over 147 spectra measured on 26 January 2009 between $14^h06^m00^s$ and $18^h05^m22^s$. As seen in Fig. 5.20, the modelled spectrum matches CIRS observations very well within

the measurement errors. The temperature knee is clearly present at approximately 200 mbar, and so the temperature profile presents two local minima below and above the knee. The temperature knee can also be characterised by the lapse rate and more importantly by the curvature, defined respectively by the first and second derivatives of the temperature with respect to the height. At the location of the knee, the curvature reaches its minimum value of approximately -0.06 K/km$^2$. The deformation of the temperature profile due to the presence of the knee leads to the formation of two local maxima for the curvature above and below the knee at about 0.1 and 0.3 bar. If the temperature knee were absent in the vertical profile, there would be only one maximum value for the curvature corresponding to the minimum temperature below the tropopause. The presence of three peaks in the curvature profile is then characteristic of a thermal structure with a temperature knee.

### 5.7.3 Sensitivity of the temperature knee to the retrieval strategy

In this section, the robustness of the temperature knee is tested by assuming various retrieval strategies in NEMESIS which may have a significant impact on the modelled temperature structure. The numerical algorithm retrieves a continuous temperature profile from an existing *a priori* vertical profile. The *a priori* temperatures as well as the *a priori* errors must then be defined in the reference atmosphere at each of the 120 pressure levels between 0.001 mbar and 10 bar. The *a priori* errors must be set up in NEMESIS so that the retrieval solution is equally constrained by CIRS data and by the *a priori* profile (Irwin *et al.*, 2007). Test retrievals were performed so that intermediate conditions would be found between underconstrained and overconstrained *a priori* errors. If the temperature profile is retrieved from FP1 spectra from 30 to 350 cm$^{-1}$, the optimal a priori errors was found to be approximately 10 K above the 1-bar pressure level. The *a priori* errors converge to zero as the pressure gets bigger than 1 bar in order to keep the lower troposphere barotropic. Further away from the optimum *a priori* error, the retrieval solutions start being underconstrained or overconstrained. *A priori* errors below 5 K are associated with synthetic spectra in poor agreement with CIRS data, and so they can be ruled out. Large a priori errors above the 20-K threshold value lead to unrealistic oscillations in the retrieved temperature profile.

The retrieved temperature profile for lower values of the *a priori* error differ less from the *a priori* profile. However, the temperature knee is apparent for all tested values of the *a priori* errors. The

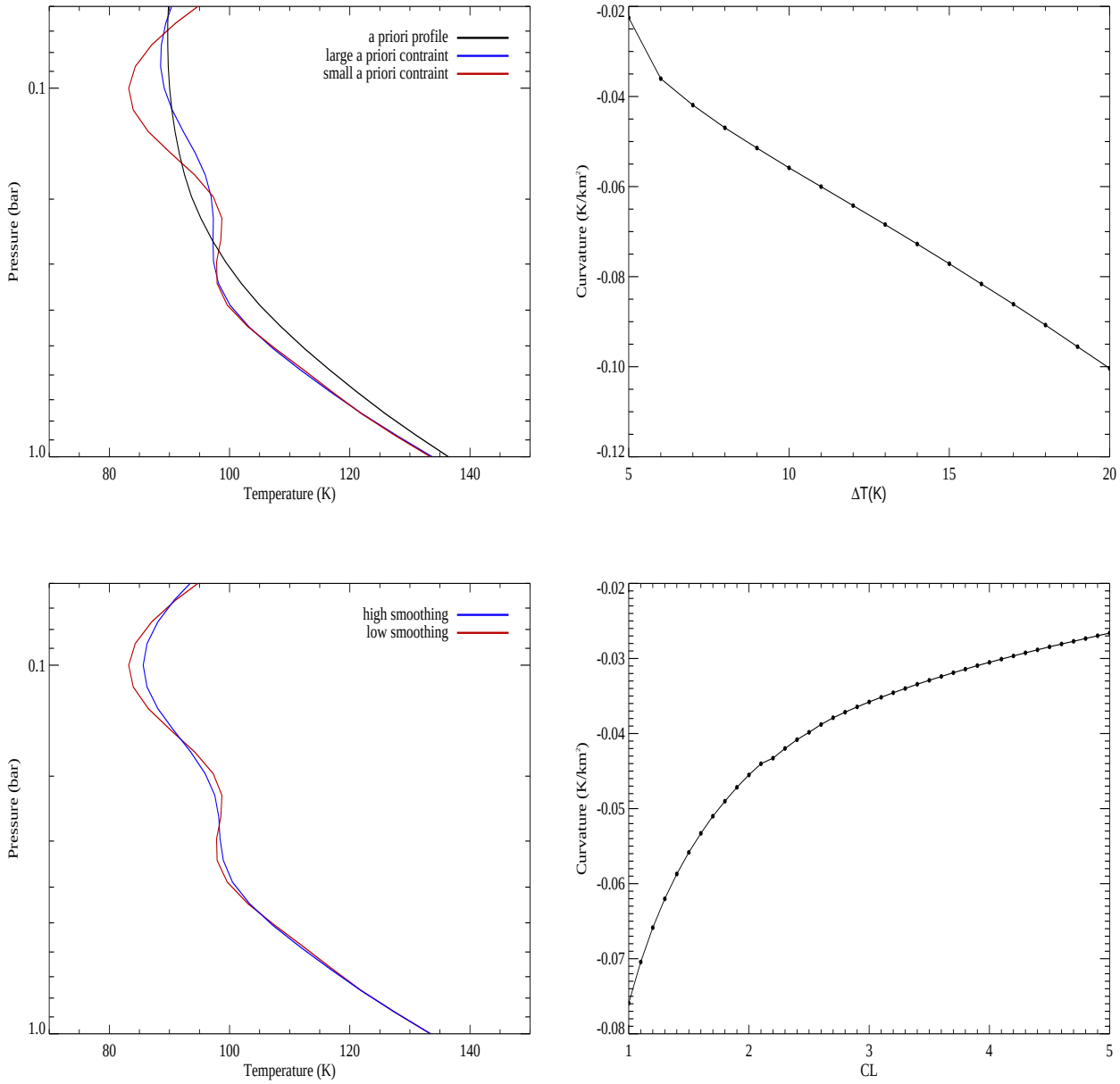



Figure 5.21: Sensitivity of the temperature knee to the retrieval strategy. *Top-left*: The temperature profile is retrieved for small ($\Delta T = 7$ K) and large ($\Delta T = 17$ K) values of the *a priori* errors. The temperature knee is stronger for smaller *a priori* constraints although the knee is present for all tested values of the *a priori* errors. *Top-right*: Curvature of the retrieved temperature profile at the pressure level of the temperature knee as a function of the *a priori* errors. The strength of the temperature knee can be estimated by calculating the curvature defined as the second derivative of the temperature as a function of height. A stronger knee typically has a larger absolute curvature. Therefore, the knee is stronger for higher *a priori* errors. *Bottom-left*: The retrieved temperature profiles for a correlation length of 1.5 (low smoothing) and 4 (high smoothing). *Bottom-right*: Curvature of the temperature knee as a function of the correlation length. As expected, a smoother temperature profile leads to a weaker temperature knee. However the knee is observed even for very large values of the correlation length, suggesting that the knee is indeed a physical feature of Saturn's thermal structure in the troposphere.

retrieved temperature profiles for low and high *a priori* constraints are show in Fig. 5.21. If small constraints are set up in the model, the retrieved profile is allowed to depart further away from the *a priori* profile, and as a result a stronger temperature knee is retrieved. This can be seen by calculating the curvature of the temperature knee as a function on the *a priori* error. The absolute value of the curvature increases with the *a priori* error, or identically the temperature knee is stronger for smaller *a priori* constraints. Although the *a priori* error has an effect on the curvature of temperature knee, none of the tested values has managed to remove the knee from the thermal structure. Smaller variations of the thermal structure with the correlation length are also observed. The correlation length characterises the vertical smoothing of the temperature profile (Rodgers, 2000 ; Conrath *et al.*, 1998). This parameter is defined as the length scale in units of $\log_{10} p$ over which the interlevel correlation of temperature decreases by a ratio equal to $e^{-1}$. Therefore, low values of the correlation length are associated with low vertical smoothing. The optimum value for the correlation length in Saturn's troposphere and stratosphere is approximately equal to 1.5 although values in the range 1-5 are still physically acceptable (Irwin *et al.*, 2007; Fletcher *et al.*, 2008). In Fig. 5.21, the curvature of the tempearture knee is plotted as a function of the correlation length. The knee is slightly weaker for high smoothing, although this feature is still present for all values of the correlation length. In conclusion, the set-up of the *a priori* profile in the model has a non negligible effect on the retrieved thermal structure, yet the temperature knee has been observed for all the retrieval strategies tested here. The *a priori* error has the biggest impact on the curvature of the temperature knee while varying the correlation length only has a minor effect on the retrieved thermal structure.

### 5.7.4 Comparison of haze distribution with the thermal structure

FIRMAPS data at 30-550 $cm^{-1}$ measured on 03 August 2005 and 22 May 2005 were combined to retrieve Saturn's thermal structure respectively in the southern and northern hemispheres. The curvature was calculated from the temperature profile at each pressure level and latitude. The curvature map is presented in Fig. 5.22. Negative values of the curvature in the upper troposphere below the 100-mbar pressure level correspond to the temperature knee. The curvature map shows that the temperature knee is present throughout the southern hemisphere at higher latitudes but is globally absent in the equatorial zone between $\pm$ 10°. Note that the curvature is negative at the equator just above

the tropopause, however FP1 data are not sensitive to such lower pressures (the peak of the FP1 weighting function is found at approximately 500 mbar (Fletcher *et al.*, 2007)) and so this feature is very likely to be a discontinuity between the retrieved profile in the upper troposphere and the *a priori* profile in the lower stratosphere. Fletcher *et al.* (2007) found that a weaker knee was present at higher altitudes around the equator. They used FP3 low-resolution spectra at higher wavenumbers in the range 600-680 $cm^{-1}$ to update the thermal structure initially derived from FPI data. FP3 data are sensitive to lower pressures between approximately 56 and 228 mbar, therefore mid-infared spectra may be used to search for a temperature knee at higher altitudes.

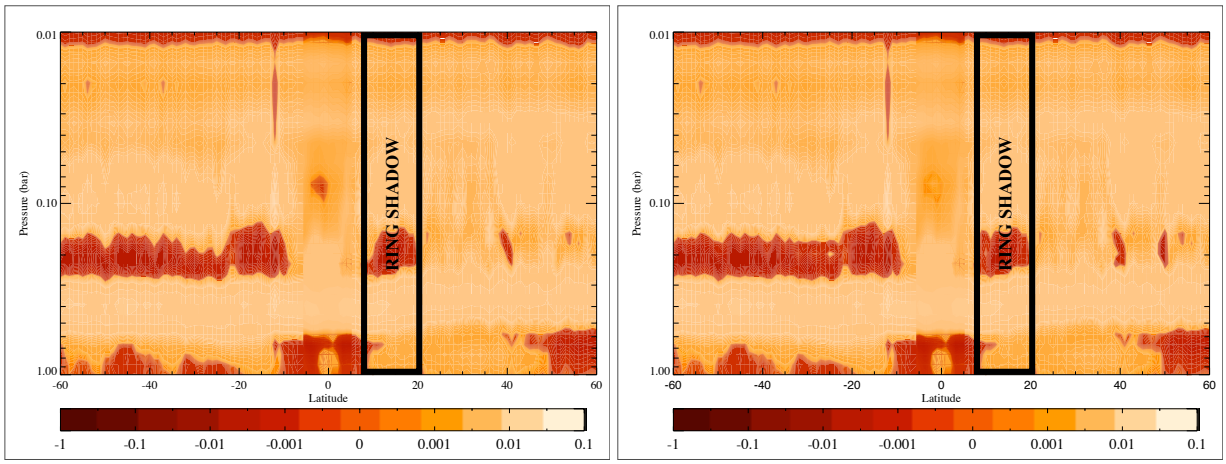



Figure 5.22: The 2005 curvature maps retrieved from FP1 (*left*) and FP1+FP3 (*right*) spectra.

The thermal structure was updated with FP3 data as follows. The temperature and para-hydrogen vertical profiles retrieved from FP1 far-infrared spectra were included in the reference atmosphere of Saturn. The *a priori* temperature profile was set to follow the retrieved profile. The *a priori* errors which best balance the measurement and modelling errors were also included in the model. FP3 data at 15-$cm^{-1}$ spectral resolution are only sensitive to the thermal structure and so the temperature was the unique atmospheric parameter retrieved with NEMESIS. The negative curvature at the equator above the tropopause is absent in the updated thermal structure (see Fig. 5.22), suggesting that this feature is non physical but only due to the low sensibility of FP1 data above the 100-mbar level. However, the temperature knee is still not observed in the equatorial zone between $\pm$ 10°, when FP1 and FP3 data are combined together although Fletcher *et al.* (2007) retrieved a weak temperature knee at the equator.

The 2005 haze distribution in the southern and northern hemispheres was retrieved from the

VIMS spectral cubes CM1493938233, CM1493939345 and CM1493940444 measured on 4 May 2005 at $22^h23^m26.137^s$, $22^h41^m58.137^s$ and $23^h00^m16.362^s$ respectively. These spectral cubes were extracted from the PDS database in order to cover all latitudes between 60°S and 60°N. The haze distribution is compared with the thermal structure observed in the same year in Fig. 5.23. The contour lines for aerosol concentrations above 10 $cm^{-3}$ are plotted over the curvature map. Aerosol concentrations below the 10-$cm^{-3}$ threshold value correspond mostly to the opacity clearing in the lower stratosphere and so have negligible impact on the tropospheric thermal structure. Larger concentrations at the peak below the tropopause are found in the southern hemisphere with values around 20 $cm^{-3}$, whereas concentrations in the northern hemisphere have maximum values around 10 $cm^{-3}$. As seen in Fig. 5.23, the knee is stronger in the southern hemisphere where haze concentrations are larger. If absorption of sunlight by aerosols is responsible for the temperature knee, larger concentration at the peak and higher daily insolation should result in a stronger temperature knee in the summer hemisphere as observed in the curvature map.

A correlation between the vertical location of the haze and the temperature knee would be also expected. The temperature knee is found at 200 mbar at all southern latitudes below 30°S. The aerosol peak is retrieved at variable pressure levels between 150 mbar and 300 mbar, with the peak being higher up at lower latitudes. As a result, the peak of aerosol concentration is observed slightly below the temperature knee. At such pressure levels, the thermal structure is dominated by radiative cooling and so the convective transport of tropospheric aerosols up to the 200-mbar level is unlikely to account for the vertical location of the temperature knee. Pérez-Hoyos and Sánchez-Lavega (2006) showed that the sunlight radiation at visible wavelengths would not penetrate deeper than 200 mbar. Although infrared sunlight may reach deeper atmospheric levels, visible solar radiation accounts for most of the heating source. The aerosol concentration starts increasing below the tropopause until it reaches a maximum value at around 200 mbar. If the aerosol opacity at 200 mbar is enough to block the penetration of solar radiation at deeper pressure levels, then the temperature knee may be located above the concentration peak. Such a scenario would be consistent with both the thermal structure and the haze distribution in Saturn's troposphere.

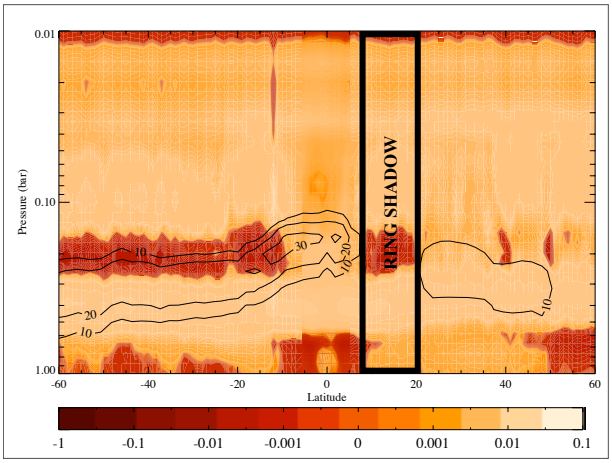



Figure 5.23: The curvature map compared with the haze contour profile. The curvature in K/km$^2$ (red tones) is presented for most southern and northern latitudes. The haze contour profile retrieved from VIMS cube is plotted over the 2005 curvature map for aerosol concentrations above 10 cm$^{-3}$. The haze distribution is retrieved from VIMS spectral cubes CM1493938233, CM1493939345 and CM1493940444 measured on 4 May 2005 at $22^h23^m26.137^s$, $22^h41^m58.137^s$ and $23^h00^m16.362^s$ respectively. Both CIRS and VIMS data are acquired between the southern summer solstice in 2002 and the vernal equinox in 2009.

## 5.8 Haze particle candidates

### 5.8.1 Comparison with laboratory measurements of the refractive index

The optical and physical properties of tropospheric haze parametrised by the refractive complex index define the composition of the haze, and so can eventually lead to the identification of aerosol particles. Indeed, the real and imaginary parts of the refractive index can be directly compared to laboratory measurements of the index of haze candidates. The formation of haze is a complex process embracing microphysical reactions probably also coupled with photochemical reactions. Therefore, haze particle candidates potentially include all molecules present in Saturn's tropopsphere and stratosphere, as well as photochemical products such as diphosphine ($P_2H_4$), linear hydrocarbon chains ($C_{2n+2}H_2$) and polycyclic aromatic hydrocarbons (see Fig. 1.5). The complex refractive index of ammonia, ammonium hydrosulphide, hydrazine, methane and water (Hale and Query, 1973; Martonchik *et al.*, 1984; Martonchik and Orton, 1994; Howett *et al.*, 2007) are plotted in Fig. 5.24. In section 5.3.2, the best-fitting real and imaginary indexes are obtained mainly in the range 1.1-1.8 and 0-0.001 respectively. Note that refractive indices are measured for a few wavelength ranges within a larger near-infrared spectrum covering approximately the 0.5-6 $\mu$m spectral region. In particular, each 0.8-3.5 $\mu$m reflection spectrum gathers two sets of measurements made below and above $\sim$ 3 $\mu$m. The

measurement errors are larger at the edges of the wavelength intervals, however the feature at 3 $\mu$m is still real for all the candidates plotted. Indeed it is due to one of the bending modes of vibration common to all molecules with hydrogen (Dieke, 1958).

The measured complex refractive indices for ammonia are nearly constant over the whole near-infrared reflection spectrum, with real values in the range 1.40-1.45, except in the 3-$\mu$m band. The measured imaginary index is below the 0.001 threshold value at almost all spectral points, especially at lower wavelengths ($\leq 2\,\mu$m) where hazes mostly reflect the sunlight radiation. Therefore, the range of real and imaginary index values obtained from the analysis of VIMS 0.8-3.5 $\mu$m data is consistent with a haze made of ammonia particles. Ammonium hydrosulphide particles have a real refractive index between 1.7 and 2.4, significantly larger that the estimated value for Saturn's tropospheric haze. Similar conclusions as for ammonia particles can be drawn for water dopplets.

In conclusion, a direct comparison of the measured refractive indices with the values derived in this thesis rules ammonium hydrosulphide particles out as potential haze candidates. On the other hand, the values for ammonia and water are not in contradiction with the haze properties. Measurements of the complex refractive index for methane and hydrazine ($N_2H_4$) are also available and can be compared with the haze model. Methane's real and imaginary indexes at 0.8-2.0 $\mu$m are in the range 1.20-1.45 and $10^{-5}$-$10^{-3}$ respectively. The imaginary index increases above 2.0 $\mu$m with values higher than $10^{-3}$. As for ammonia and water, methane cannot be ruled out by simply focusing on the complex refractive index. Hydrazine is formed through the photolysis of ammonia and is expected to account for Jupiter's hazes as suggested by photochemical models (Atreya and Romani, 1985). The condensation of ammonia in Saturn's troposphere would greatly deplete its volume mixing ratio above the cloud base pressure level, preventing the photolysis of ammonia and subsequent formation of hydrazine. However, ammonia condenses in Jupiter's atmosphere too where hydrazine is a potential candidate for the Jovian haze. Therefore, comparisons with laboratory measurements of the imaginary refractive index or photochemical models, can be used instead to determine whether a hydrazine haze might also form in Saturn's atmosphere. The real refractive index of hydrazine has values in agreement with the 1.1-1.8 range, however the imaginary index is above 0.005 at all wavelengths. The hydrazine imaginary refractive index is thence larger than the best-fitting values for this parameter, suggesting that hydrazine is probably not a major component of Saturn's hazes.

The use of the complex refractive index as a way to identify Saturn's tropospheric haze can only

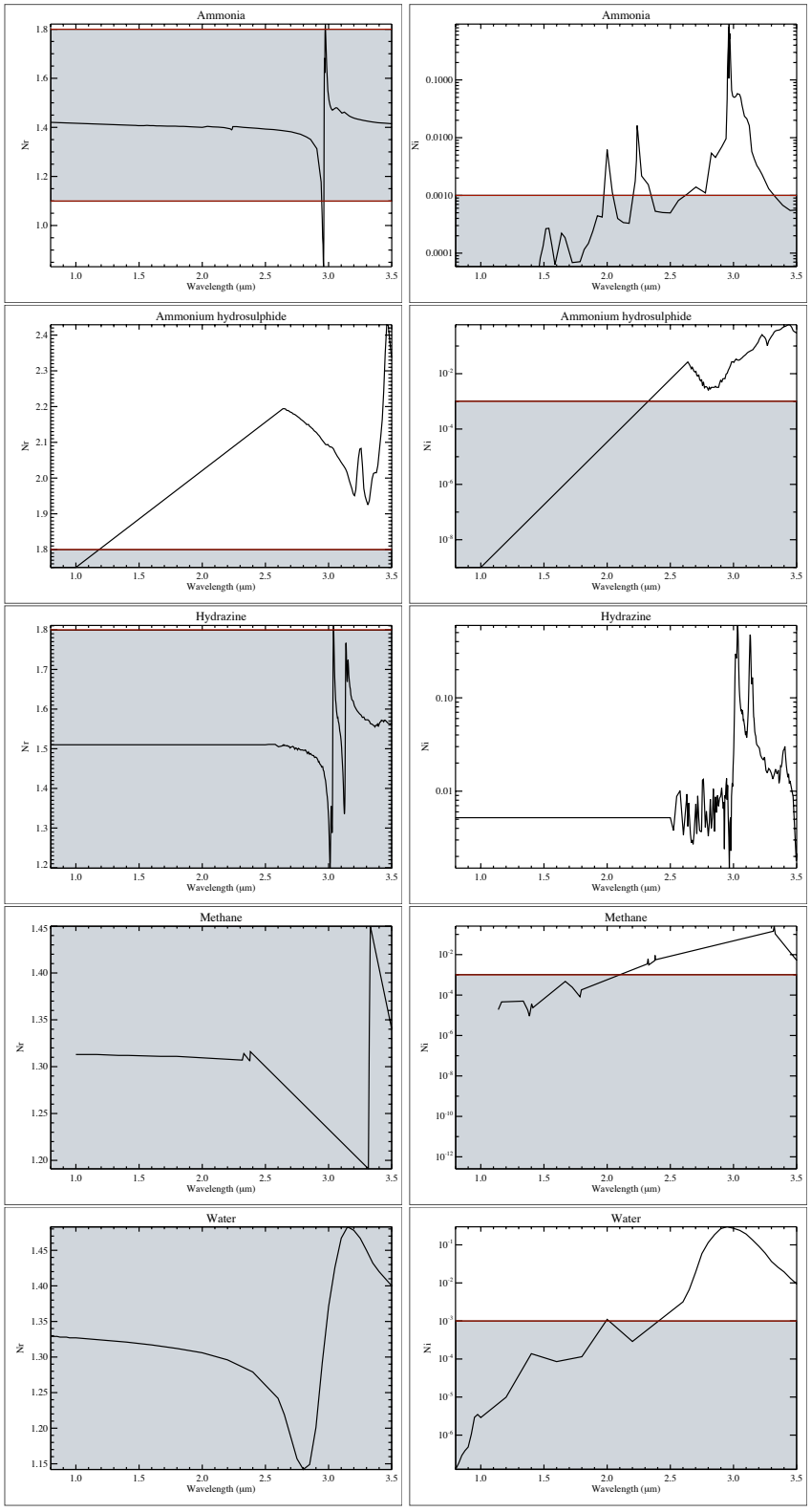



Figure 5.24: Known complex refractive indexes from laboratory measurements of the following tropospheric species: ammonia, ammonium hydrosulphide, hydrazine, methane and water (Hale and Query, 1973; Martonchik *et al.*, 1984; Martonchik and Orton, 1994; Howett *et al.*, 2007). Optimum values in the range 1.1-1.8 and 0-0.001 for the real and imaginary indexes respectively are found to best match VIMS near-infrared reflection data. The grey regions represent the best-fitting real and imaginary parts of the refractive index dtermined from the VIMS spectra.

be effective if the measured values of all haze candidates are known, and if the 0.8-3.5 $\mu$m reflection spectrum allows a fine retrieval of this parameter at each wavelength. First of all, only a range of values for the real and imaginary indexes is obtained from the analysis of VIMS data. In addition, laboratory measurements of many haze candidates are missing, which prevents a direct comparison with the haze model. However, the knowledge of this parameter is necessary in order to parametrise the haze optical and physical properties in the radiative transfer algorithm. Furthermore, it can rule out certain molecules such as ammonium hydrosulphide and hydrazine as haze candidates in Saturn's troposphere, and be eventually compared with future measurements of the index for other candidates. In addition to the complex refractive index, the vertical distribution of aerosols derived from VIMS data is also a valuable result for identifying the composition of Saturn's tropospheric haze. In the next section, the aerosol density profiles are compared with the outcomes of photochemical models developed by Moses *et al.* (2005).

### 5.8.2 Comparison with photochemical models

The haze vertical structure retrieved with NEMESIS from VIMS near-infrared data is compared in Fig. 5.25 with a photochemical model of Saturn's troposphere and stratosphere developed by Moses *et al.* (2005). The temperature profile used in this model was derived from CIRS infrared data measured at 27°S by Fletcher *et al.* (2007). Note that the photochemical model does not take into account seasonal variations, and so the solar flux is fixed at the vernal equinox. Finally, only the photochemistry of C-H-O-N-P species is considered in the model. Moses *et al.* (2005) assumed a methane volume mixing ratio of $4.7\times10^{-3}$ at the lower boundary based on the CIRS far-infrared rotational line analysis of Fletcher *et al.* (2009)[3]. The deep volume mixing ratios of ammonia and hydrogen sulphide were set respectively to $4.7\times10^{-4}$ and $3.7\times10^{-4}$, based on Briggs and Sackett (1989). Although sulphur chemistry is not included in the photochemical model, the hydrogen sulphide volume mixing ratio drops off due to the ammonium hydrosulphide cloud formation expected from thermochemical equilibrium theories. Both the ammonia and hydrogen sulphide mixing ratios drop off assuming saturation with respect to ammonium hydrosulphide in the cloud region, and then the remaining ammonia survives and eventually follows its saturation vapour density above the am-

[3]Note that a similar photochemical model developed by Moses *et al.* in 2005 is used here with updated temperature and abundances profiles obtained by Fletcher *et al.* in 2007 and 2009.

monia ice cloud, until photochemistry starts controlling the profile at higher altitudes. The phosphine volume mixing ratio was set to $6.4\times10^{-6}$ in the deep troposphere (Fletcher *et al.*, 2009). Phosphine is well shielded until it diffuses up above the ammonia cloud, where it is then very rapidly destroyed by photochemistry. The resulting photochemical profile for phosphine is very similar to what was derived from ISO data (Davis *et al.*, 1996). There is not a lot of photochemical coupling between ammonia and hydrocarbons. However, nitrogen-phosphorus photochemical coupling is prevalent in the upper troposphere. Moses *et al.* (2005) generated a photochemical profile of 124 species in gas phase including parent molecules, photochemical products, and the remaining major constituents in the troposphere and stratosphere of Saturn. The aerosol densities obtained from the analysis of VIMS spectra are in units of particle number per cubic centimetre of atmosphere. The abundance of the source for the peak of aerosol below the tropopause is estimated for each of the 124 species assuming a gamma size distribution with parameters 1-$\mu$m and 0.05, and with a density of 1.4 g.cm$^{-3}$. NEMESIS retrieves the aerosol specific density $\sigma_{Nemesis}$ in number of aerosol particle per gram of atmosphere. If $\rho_{atm}$ is the atmospheric density computed at each pressure level $P(T)$ where $T$ is the temperature from the hydrostatic equation, then the aerosol concentration in particle number per unit of volume $\rho_{haze}$ is given by:

$$\begin{cases} \rho_{atm} = \dfrac{Pm_a}{k_B T} \\ \\ \rho_{haze} = \sigma_{Nemesis} \cdot \rho_{atm} \end{cases}$$

where $m_a$ is the gaseous molecular weight and $k_B$ is the Boltzmann constant. If $\rho_{particle}$ is the constant particle density and $< r >$ the mean of the gamma distribution, the particle mass $m_{particle}$ is equal to:

$$m_{particle} = \frac{4}{3}\pi < r >^3 \cdot \rho_{particle}.$$

The number of molecules in one particle $N$ is obtained by dividing the particle mass with the molecular mass $m_{molecule}$:

$$N = \frac{m_{particle}}{m_{molecule}}.$$

The quantity above can be estimated for each haze candidate. The aerosol concentration in number of molecules $\rho$ per unit of volume is then given by:

$$\rho = N \cdot \rho_{haze}.$$

Only four species have abundances high enough to be the source of tropospheric haze: phosphine, ammonia, hydrogen sulphide and ethane. The photochemical profiles are compared in Fig. 5.25 with the estimated source abundances for the four species, as well as the main photochemical products of phosphine ($P_2H_2$, $P_2H_4$) and ammonia ($N_2H_4$) . The aerosol concentrations $\rho$ are estimated from the vertical profile retrieved with NEMESIS for each haze candidate. They are shown in dot-dashed lines in Fig. 5.25. The photochemical profiles are shown in solid lines. The hydrogen sulphide abundance is large enough at pressure levels below 2 bar to be a potential source for Saturn's aerosols. However the abundances drop off very quickly above the 2-bar level, and so hydrogen sulphide cannot account for the peak of aerosols.

Methane has enough abundance throughout the troposphere to form hazes although the vertical haze distribution is very different from the methane vertical profile. Methane is stable in Saturn's atmosphere and so only photochemical products could potentially form a haze layer. Only a full microphysical model of Saturn's troposphere and stratosphere could explain the haze distribution assuming hazes are formed mainly by methane photochemistry. Such a model was developed by Friedson *et al* (2002) for Jupiter's atmosphere, although similar processes are expected to extend to Saturn's atmosphere. Friedson's model predicts the formation of tiny primary particles at 0.1 mbar from the photochemical destruction of methane through homogeneous nucleation. At lower altitudes, the different primary particles heterogeneously nucleate to form larger particles. These particles grow by coagulation at around 1 mbar and eventually sediment out to the troposphere below the 100 mbar level. In this process, small particles are still present in the lower stratosphere, but they would not be detected at 0.8-3.1 $\mu$m because of the rapid decrease of Rayleigh scattering intensity with wavelength. Phosphine and ammonia are also candidates for parent molecules of Saturn's tropospheric haze. Among these two possibilities, phosphine is the most likely source of the aerosol component at the peak. It's more abundant than ammonia in this region, and the sharp cutoff at the appropriate pressure region must be balanced by production of some phosphorus-bearing species, probably $P_2H_2$ or $P_2H_4$ which promptly condenses in situ.

More conclusions can be drawn by comparing the spatial and temporal variations of haze concentration with the North-South distributions of the two possible parent molecules, phosphine and methane. Fletcher *et al.* (2009a, 2009b) retrieved the phosphine and methane abundances at all latitudes from Cassini/CIRS observations during the Prime Mission. Their results are shown in Fig.

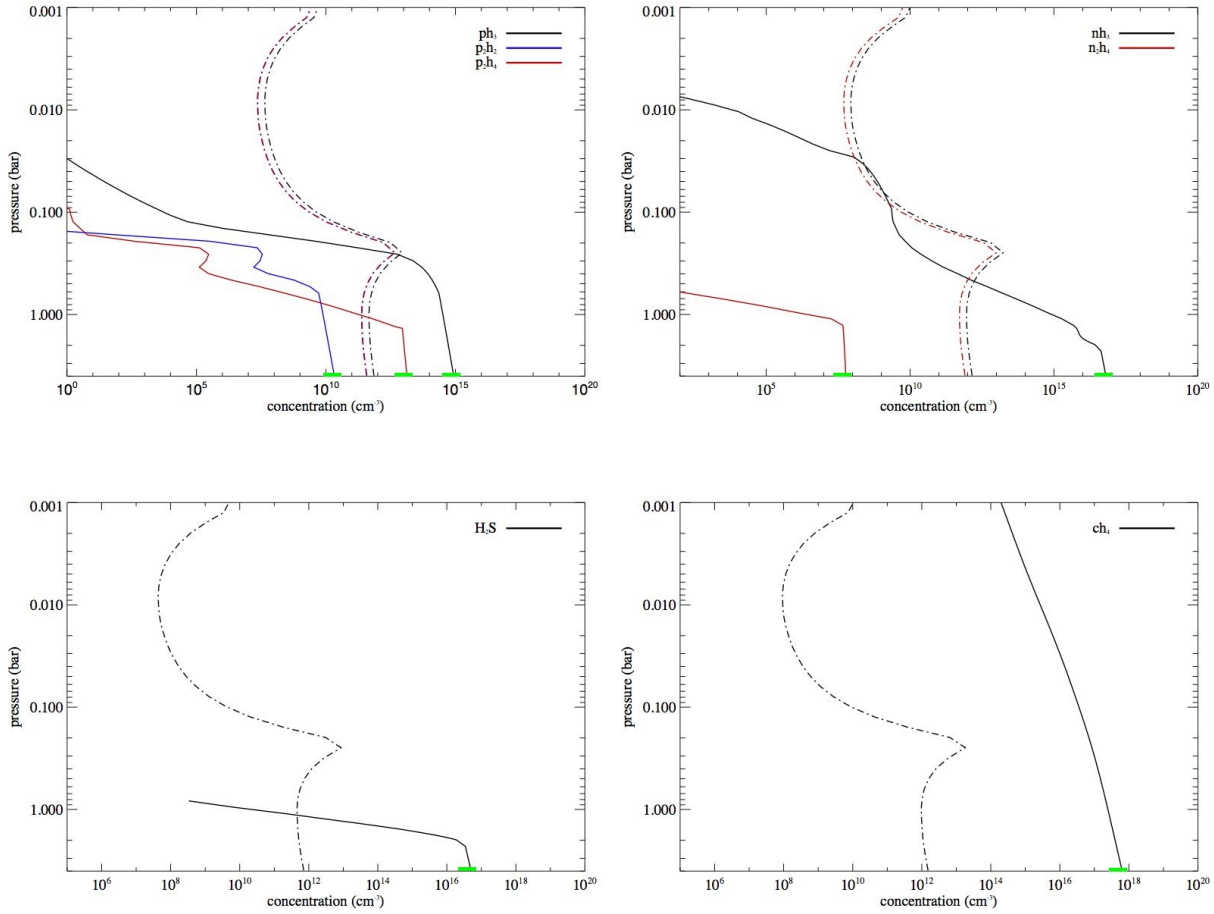



Figure 5.25: Comparison of the haze vertical structure with Saturn's photochemical model (Moses *et al.*, 2005) for the following species: $PH_3$, $P_2H_2$, $P_2H_4$ (*top-left*), $NH_3$, $N_2H_4$ (*top-right*), $H_2S$ (*bottom-left*) and $CH_4$ (*bottom-right*). The haze concentrations are given in units of number of molecules per cubic centimetre for each haze candidate, assuming a density of 1.4 g.cm$^{-3}$. They are shown in dot-dashed lines. The abundances of the sources and haze candidates derived from the photochemical model are shown in solide lines. Note that $P_2H_2$ and $P_2H_4$ have very similar molecular weight, and so the expected haze concentrations shown in dotted lines for these two molecules are nearly the same. The green bar at the bottom of each photochemical model shows the concentration offsets for a particle density between 1 and 2 g.cm$^{-3}$

5.26. Methane is homogeneously distributed across the whole surface of the planet. However, the results for phosphine show significant variations between the northern and southern hemispheres. At the location of the peak of haze concentration below the tropopause, the phosphine abundance is significantly enhanced in the northern hemisphere. In addition, phosphine is distributed higher up in the equatorial zone, at 42°S, 67°S and 83°S. Therefore, the presence of the haze layer at higher altitudes at the equator is coherent with the enhancement of phosphine abundance in the same zone.

Photochemical times for phosphine are negligible with respect to a Saturnian year (Kaye and Strobel, 1984 ; Sinclair *et al.*, 2013). As a result, long photochemical times cannot explain why

the aerosol concentration does not increase in the northern hemisphere in 2010 and 2011. However, assuming that phosphine contributes most to the haze formation in Saturn's troposphere, lower phosphine abundances in the northern hemisphere might reduce the efficiency of haze formation. On the other hand, the enhancement of phosphine abundance coupled with high insolation rates in the southern hemisphere during the period 2004-2008 before the equinox is likely to explain the higher aerosol concentrations.

In conclusion, the vertical and latitudinal distributions of phosphine are the most coherent with the haze vertical structure, and its latitudinal and temporal variations, suggesting $P_2H_2$ and $P_2H_4$ as trospospheric haze candidates. However, photochemical products of methane cannot be ruled out due to the high abundance of methane in the troposphere and stratosphere of the planet. Laboratory measurements of the complex refractive index of $P_2H_2$ and $P_2H_4$ , as well as a coupled photochemical-microphysical model of methane in Saturn's atmosphere are necessary in order to advance in the identification of haze particles.

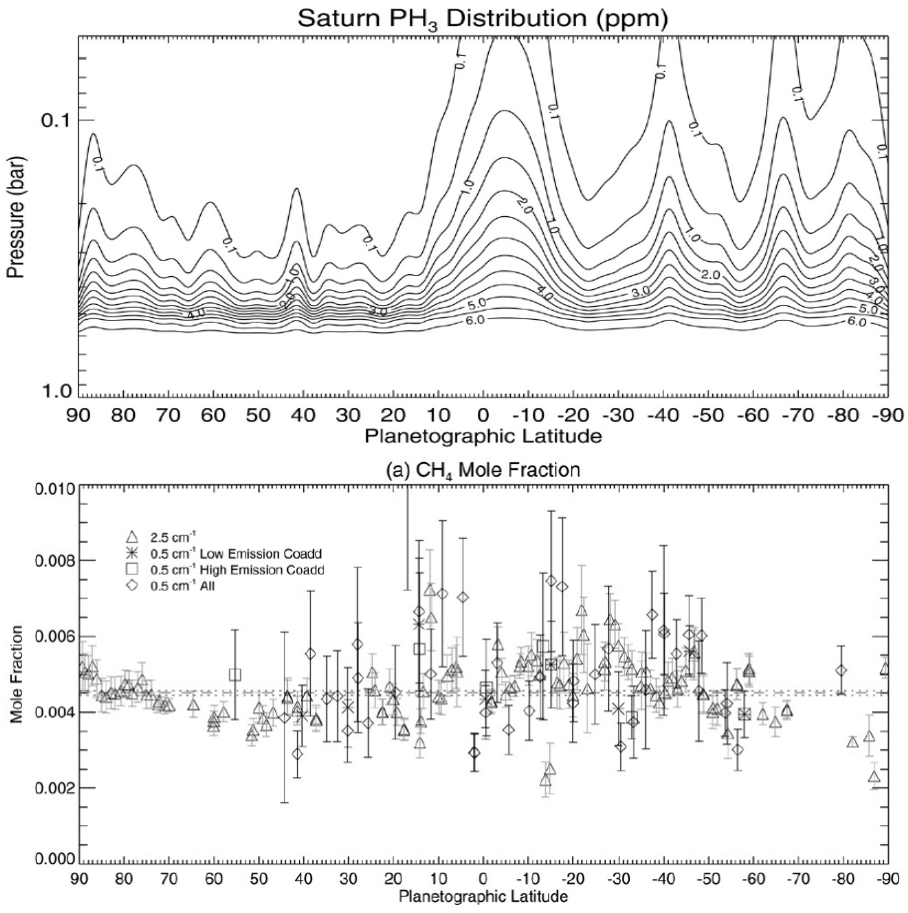



Figure 5.26: North-South distributions of 2001 phosphine and ammonia from Cassini/CIRS observations during the Prime Mission 2204-2008. Source: Fletcher *et al.* (2009a, 2009b).

## 5.9 Summary

The analysis of Saturn's near-infrared reflection spectra in the 0.8-3.5 $\mu$m wavelength range was carried out in this chapter. Such spectra are made by the reflection of sunlight by tropospheric and stratospheric hazes. Although gas particles deviate the sunlight through Rayleigh scattering, the contribution of gases to Saturn's spectra at 0.8-3.5 $\mu$m is negligible. The two-way transmission functions have shown that Saturn's reflection data are sensitive to aerosols located above the 1-bar level.

In the first part of this chapter, the optical and physical properties of Saturn's hazes were derived from VIMS near-infrared data observed at a latitude of 20°S. The haze can be characterised by the complex refractive index and the size distribution of the aerosol particles. The best-fitting values of the real refractive index, complex refractive index and aerosol particle size are found in the ranges 1.1-1.8, 0-0.001 and 0.5-5 $\mu$m respectively. A similar analysis was carried out for various viewing geometries, and coherent result were found all values of the emission and solar angles assuming that the solar angle is below 85° even for a high number of zenith angles in the radiative transfer algorithm. The haze properties were also obtained at all latitudes in the southern and northern hemispheres of Saturn. Although small variations weith latitude are observed, the retrieved values of the real refractive index, complex refractive index and aerosol particle size are all obtained in the ranges 1.1-1.8, 0-0.01 and 0.3-5 $\mu$m respectively.

The second part of the chapter focuses on the vertical distribution of aerosol density. The haze vertical profile is characterised by a peak of concentraton below the tropopause at around 200 mbar. The concentration decreases sharply above that level, in a region referred to as the opacity clearing. The concentration then increases at the 10-mbar level until 1 mbar. below the peak, the concentration also decreases until it relaxes to its *a priori* profile. The shape of the vertical profile is very similar for all best-fitting values of the real refractive index, complex refractive index and particle size. However, the absolute values of the aerosol concentration vary with the optical and physical parameters. The variation of the aerosol concentration with latitude was also assessed in this chapter. The shape of the vertical profile is similar at all latitudes, although the aerosol peak is retrieved at a higher altitude in the equatorial region. The north-south variations of the haze distribution are derived from VIMS data measured between the southern summer solstice in 2002 and the vernal equinox in 2009. At

these observation times, the aerosol concentration is significantly higher in the southern hemisphere than in the northern hemisphere. The haze distribution shows important temporal variations, with the hazes in southern hemisphere being significantly denser before the equinox in 2007. The northern hemisphere response to solar insolation in 2004-2012 is less efficient than in the southern hemisphere, and can be explain by the North-South variations of abundances of photochemical parents.

The third part of the chapter analyses the correlations between the haze distribution and a thermal feature refered to as the temperature knee. The temperature knee corresponds to a local increase of temperature below the tropopause and above the radiative-convective boundary. Cassini/CIRS mid- and far-infrared data have been analysed in order to derive Saturn's thermal structure in the troposphere and stratosphere. At first, the thermal structure is retrieved from Saturn's spectra measured at a latitude of 30°S. For such latitude, the temperature knee is clearly present at around 200 mbar. Although the *a priori* value has an effect on the curvature of the temperature knee, the knee is still retrieved for different *a priori* profiles. North-south variations of the temperature vertical profile are also observed. In particular, the knee is stronger at mid-latitudes in the southern hemisphere and is globally absent in the northern hemisphere and the equatorial region. There are significant variations between the thermal structure and the aerosol concentration profile. In particular, the aerosol peak is found slightly deeper than the temperature knee.

In the last part of the chapter, the haze properties retrieved from VIMS near-infrared reflection spectra are compared with laboratory experiments and a photochemical model in order to identify haze particle candidates. First, the real and imaginary parts of the complex refractive index were compared with laboratory measurements for various species present in Saturn's atmosphere. Such a comparison has shown that Saturn's hazes are unlikely to be made of ammonium hydrosulphide and hydrazine. However, no conclusion could be drawn for other species. Instead, the vertical distribution was compared with a photochemical model of Saturn's troposphere and stratosphere. The vertical distribution of aerosol concentration is coherent with a haze made of phosphorus-bearing species such as $P_2H_2$ and $P_2H_4$, although photochemical products of methane could not me ruled out. The refractive index data are still unknown for these two species and so no direct comparison with the best-ffiting values derived from VIMS data can be made. However, the comparison of the retrievals with the vertical and latitudinal variations of phosphine has led to the conclusion that phosphine is the most likely source of haze particles.

Chapter 6

# Consistency of the reflected sunlight and 5-$\mu$m analysis

*The analysis and results described in this chapter are entirely my own. Referenced contributions from external works are also included in order to allow further discussions on the results.*

## 6.1 Methodology: σ tests

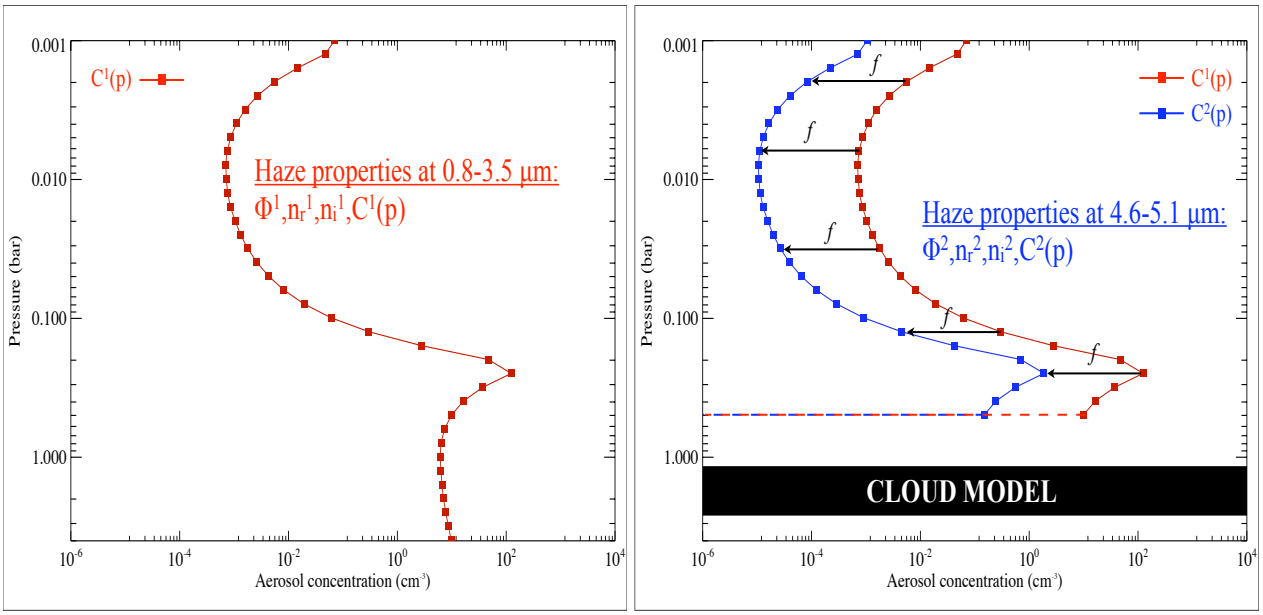



Figure 6.1: Update of the retrieval strategy at 4.6-5.1 $\mu$m using the results from the analysis at 0.8-3.5 $\mu$m.

In this chapter, results of the analysis of Saturn's reflection spectra in the 0.8-3.5 $\mu$m wavelength range are used in order to constrain the cloud properties, as well as the distribution of phosphine and ammonia at deeper tropospheric levels. In chapter 4, The limb-darkening analysis of Saturn's thermal emission spectra at 5 $\mu$m has shown that the tropospheric haze must be included in the atmospheric model in order to match the VIMS observations at low and high emission angles simultaneously. However, the haze vertical distribution is not entirely constrained by VIMS data at 5 $\mu$m.

In the previous chapter, the optical and physical properties, as well as the vertical profile of the tropospheric haze have been retrieved from VIMS near-infrared reflection spectra. Optimum values of the particle radius, real refractive index and complex refractive index have been found mostly in the ranges 0.5-5 $\mu$m, 1.1-1.8 and 0-0.001 respectively. The best-fitting values of the complex refractive index were obtained in the 0.8-3.5 $\mu$m wavelength range. However, the complex refractive index depends on the wavelength and so the optical properties of Saturn's hazes are likely to be different at 5 $\mu$m. The haze vertical profile is characterised by a higher concentration right below the tropopause and a sharp decrease of opacity at lower pressures. The aerosol opacity below the concentration peak becomes too large to allow the retrieval of atmospheric parameters at higher pressures. Therefore, Saturn's near-infrared spectra at 0.8-3.5 $\mu$m are not sensitive to the aerosol distribution at deep pressure levels below the 600-mbar pressure level.

The haze vertical structure down to the 600-mbar pressure level constrained by the analysis of VIMS reflection spectra is used in this section in order to update the aerosol model at 5 $\mu$m. VIMS data described in the next section consist of one dayside spectrum measured at 0.8-3.5 $\mu$m at a given latitude, and of nightside limb-darkening spectra at 4.6-5.1 $\mu$m measured at the same latitude and at a date not too far apart from the observations at 0.8-3.5 $\mu$m. The methodology used in this chapter is described below, with the goal of finding haze and cloud structures consistent with both the reflected sunlight and limb-darkening data.

*i.* The haze vertical profile is retrieved from the reflection spectrum at 0.8-3.5 $\mu$m for a particle size $\Phi^1$, a real refractive index $n_r^1$ and an imaginary refractive index $n_i^1$. The concentration in cm$^{-3}$ at each pressure level derived from the reflection spectrum is given by $C^1(p)$. *ii.* The haze density profile $C^1(p)$ down to the 600-mbar level is used as a reference profile for the analysis of VIMS limb-darkening spectra at 4.6-5.1 $\mu$m. The haze extinction coefficients and scattering albedos are evaluated

at 4.6-5.1 $\mu$m, assuming that the particle size, real refractive index and imaginary refractive index are respectively given by $\Phi^2$, $n_r^2$ and $n_i^2$. A cloud model is also assumed at deeper pressure levels. The scale factor $f$ of the reference haze profile $C^1(p)$, the cloud opacity and the deep volume mixing ratios of phosphine and ammonia are retrieved from the 5-$\mu$m limb-darkening data. The scaled haze density profile is given by $C^2(p)$ and is equal to the product of the retrieved scale factor $f$ with $C^1(p)$. *iii.* The standard deviation $\sigma_N$ between the two haze profiles obtained at 0.8-3.5 $\mu$m ($C^1(p)$) and 4.6-5.1 $\mu$m ($C^2(p)$) is calculated. This parameter is normalised by the mean haze concentration, and so is written as follows:

$$\begin{cases} \sigma = \sqrt{\dfrac{1}{N}\displaystyle\sum_{i=1}^{N}(C^1(i)-C^2(i))^2} \\ \nu = \dfrac{1}{2N}\displaystyle\sum_{i=1}^{N}C^1(i)+\dfrac{1}{2N}\sum_{i=1}^{N}C^2(i) \\ \sigma_N = \dfrac{\sigma}{\nu} \end{cases}$$

where $C^1(i)$ and $C^2(i)$ at the $i^{th}$ level are given in cm$^{-3}$, and $N$ is the number of pressure levels down to 600 mbar. The aim is to find haze properties matching both spectral regions with a minimal $\sigma_N$ value.

The value of $\sigma_N$ depends on the assumptions made for $\Phi^1$, $n_r^1$, $n_i^1$, $\Phi^2$, $n_r^2$, $n_i^2$, and the cloud model. Chapter 5 has shown that the haze vertical structure is similar within the period 2004-2012, and only the absolute concentrations in cm$^{-3}$ vary with time. If the 0.8-3.5 $\mu$m and 4.6-5.1 $\mu$m spectra are measured at times not too far apart, the number of aerosol particles per volume $C^2(p)$ is expected to vary little from $C^1(p)$, and as a result $\sigma_N$ should be small. In particular, the differences between $C^1(p)$ and $C^2(p)$ should be less than the seasonal variation of haze concentrations. In Fig. 5.19, haze concentrations in 2004-2012 are shown for $\Phi^1 = 1$ $\mu$m, $n_r^1$ = 1.4 and $n_i^1 = 10^{-7}$.

Upper boundary values of $\sigma_N$ can be estimated by calculating the variations in haze concentrations between two consecutive years (for instance between 2004 and 2005). In this calculation, $C^1(p)$ is the haze concentration in 2004 and $C^2(p)$ is the haze concentration in 2005, and is latitude-dependant. However, a rough estimation can be made and upper boundary values of $\sigma_N$ in the range 1-3 are obtained.

The same result is obtained for other consecutive years. If all the possible combinations of the particle size ($\Phi^1$) and complex refractive index ($n_r^1$,$n_i^1$) at 0.8-3.5 $\mu$m are tested, upper boundary

values of $\sigma_N$ are still obtained in the range 1-3. $\sigma_N$ tests (see section 6.1) can be undertaken to search for values of $\Phi^1$, $n_r^1$, $n_i^1$, $\Phi^2$, $n_r^2$, $n_i^2$ and a cloud model which minimise $\sigma_N$ or at least lead to $\sigma_N$ values below 1-3 between the reflected and 5-$\mu$m spectral fits. The aim is to find a haze and cloud structures consistent with both the reflected sunlight and limb-darkening analysis. The next section focuses on the values of $\Phi^2$, $n_r^2$, $n_i^2$ the most coherent with the analysis at 0.8-3.5 $\mu$m.

## 6.2 Parameterisation of the tropospheric haze at 5 $\mu$m

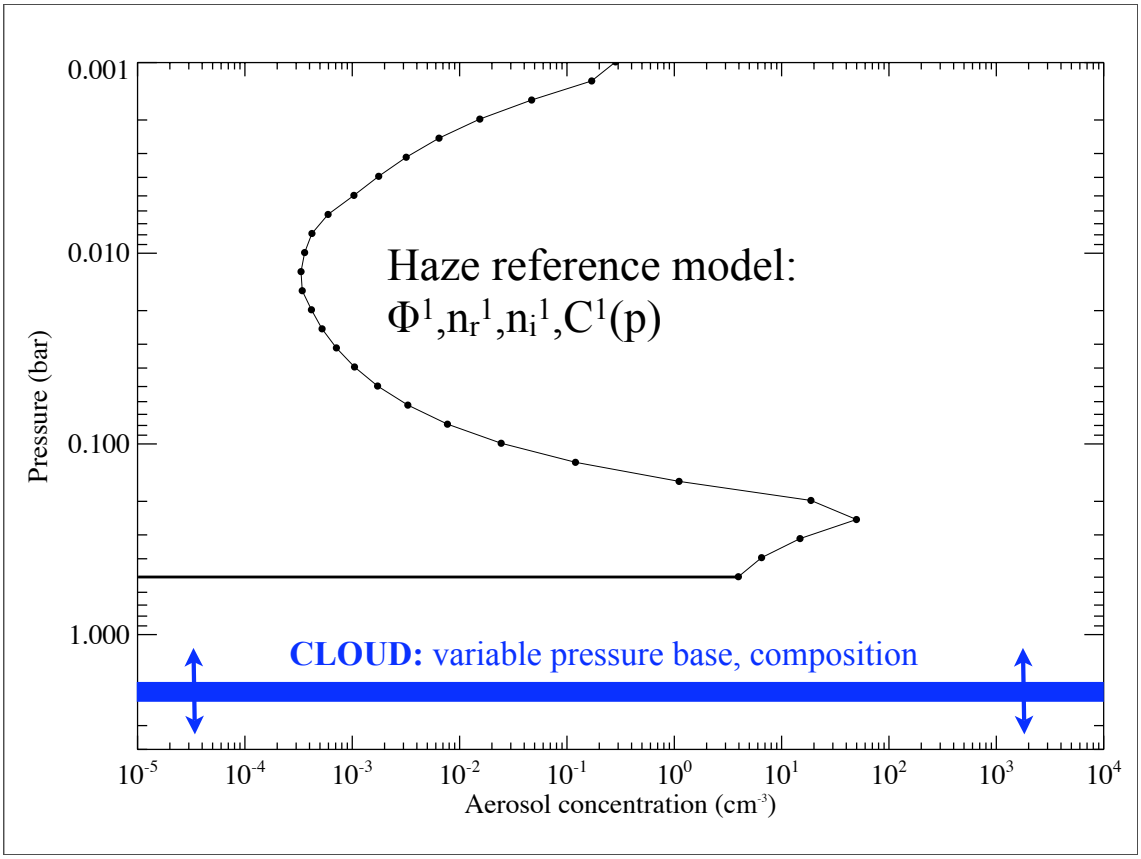



Figure 6.2: Aerosol reference model used for the limb-darkening analysis at 5 $\mu$m. The vertical distribution of trospospheric and stratospheric hazes is retrieved from VIMS reflection spectrum at 20°S in the spectral cube CM1519321223. The distribution is obtained for an aerosol particle size ($\Phi^1$) of 1 $\mu$m and a complex refractive index ($n_r^1$, $n_i^1$) of 1.4 + i$\times 10^{-7}$ although various values for these parameters are tested in this section.

The aerosol reference model used in this section is shown in Fig. 6.2. The VIMS 5-$\mu$m spectra at 20°S measured on 16 April 2006 at low (CM1523880874) and high (CM1523875542) emission angles, are used in this section. The low emission angle spectrum is measured at a latitude, longitude, emission angle of -19.14° ± 1.53°, 252.82° ± 1.48° and 24.35° ± 1.58° respectively. The high

emission angle spectrum is measured at a latitude, longitude, emission angle of -19.24° ± 1.54°, 257.42° ± 3.31° and 71.76° ± 3.24° respectively. The deep cloud is modelled with a compact scattering layer at a variable pressure level. In this section, the cloud is assumed to be made of ammonia ice with a 1-$\mu$m particle radius.

The haze vertical structure down to the 600-mbar pressure level is derived from the 0.8-3.5 $\mu$m spectrum extracted from the VIMS cube CM1519321223 acquired on 23 February 2006. The selected spectrum is measured at a latitude of -20.03° ± 2.13°, a longitude of 255.30° ± 1.75°, an emission angle 29.33° ± 2.22° and a solar angle of 40.02° ± 2.32°. The haze particle size ($\Phi^1$) and complex refractive index ($n_r^1$, $n_i^1$) at 0.8-3.5 $\mu$m are first assumed to be equal to 1 $\mu$m and 1.4 + i$\times 10^{-7}$ respectively. The haze vertical profile in the stratosphere and upper trosposphere retrieved from VIMS reflection spectrum is shown in black line in Fig. 6.2. The modelled spectrum at 0.8-3.5 $\mu$m is compared to VIMS reflection data in the left panel in Fig. 6.3.

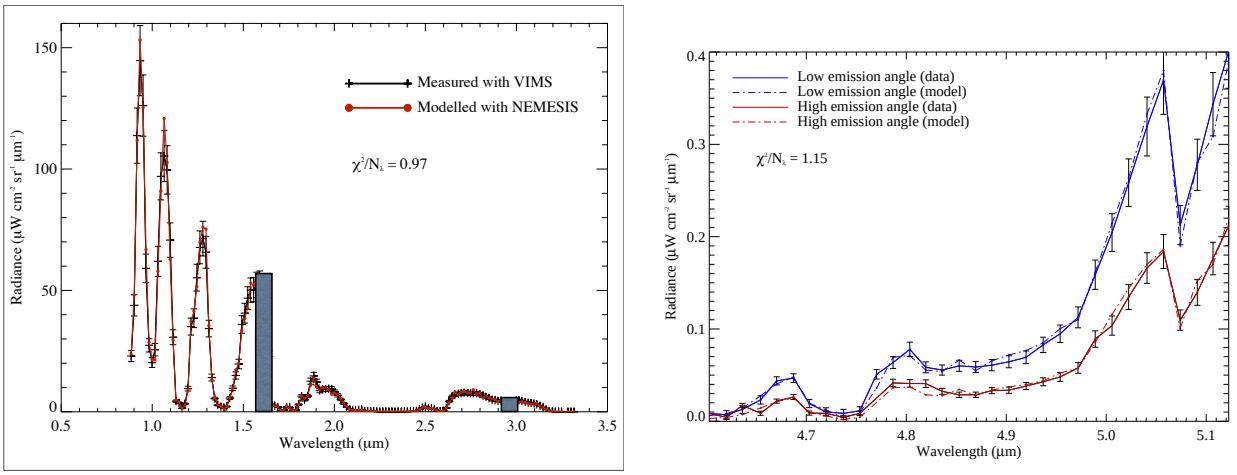



Figure 6.3: Limb-darkening analysis at 5 $\mu$m for a compact ammonia cloud and a haze vertical structure derived from VIMS data at 0.8-3.5 $\mu$m. The haze vertical profile in the stratosphere and upper troposphere down to the 600-mbar level is retrieved from VIMS near-infrared reflection spectrum. The haze particle size ($\Phi^1$) and complex refractive index ($n_r^1$, $n_i^1$) are assumed to be equal to 1 $\mu$m and 1.4 + i$\times 10^{-7}$ respectively. The measured and modelled reflection spectra are shown in the left panel. The aerosol model at 5 $\mu$m is updated by using the retrieved haze structure and a scattering ammonia cloud with variable base pressure. The haze particle size ($\Phi^2$) and complex refractive index ($n_r^2$, $n_i^2$) at 5 $\mu$m are also assumed to be equal to 1 $\mu$m and 1.4 + i$\times 10^{-7}$ respectively. The measured and modelled spectra at 5 $\mu$m are shown in the right panel for a cloud base pressure of 2.7 bar.

The effect of the haze optical and physical properties at 4.6-5.1 $\mu$m on the retrieved parameters from VIMS limb-darkening data is estimated as follows. For each value of the particle size ($\Phi^2$), real refractive index ($n_r^2$) and imaginary refractive index ($n_i^2$) in the range 0.5-5 $\mu$m, 1.0-2.0 and 0-0.1 respectively, the extinction coefficient and scattering albedo are calculated in the 4.6-5.1 $\mu$m spectral

range with a 0.05-$\mu$m step. The complex refractive index is allowed to vary between all typical values of known materials since this parameter varies with wavelength.

The cloud opacity, as well as the volume mixing ratios of phosphine and ammonia are retrieved with NEMESIS for each particle size ($\Phi^2$), real refractive index ($n_r^2$) and imaginary refractive index ($n_i^2$) of the haze, and for each pressure of the ammonia cloud base. The scaling factor $f$ of the haze concentration is also retrieved in order to account for the variation of haze concentrations between the observation times of CM1519321223, CM1523880874 and CM1523875542. Scattering was included in the model since non-scattering aerosols could not fit VIMS limb-darkening data at 5 $\mu$m.

The best fits are obtained for a compact ammonia cloud at 2.7 bar for all combinations of the particle size ($\Phi^2$) and complex refractive index ($n_r^2$, $n_i^2$) in the 4.6-5.1 $\mu$m wavelength range. The modelled and measured spectra at 4.6-5.1 $\mu$m, assuming that the haze particle size ($\Phi^2$) and complex refractive index ($n_r^2$, $n_i^1$) at 5 $\mu$m are equal to 1 $\mu$m and $1.4 + \mathrm{i}\times10^{-7}$ respectively, are similar within the measurement errors as it can be seen in the right panel in Fig. 6.3. This shows that the vertical structure of Saturn's haze is coherent in both wavelength ranges assuming that a scaling factor of the haze concentration is retrieved at 5 $\mu$m and given the particular particle size and complex refractive index of the haze.

Similar conclusions are drawn for all combinations of the the haze particle size ($\Phi^2$), real refractive index ($n_r^2$) and imaginary refractive index ($n_i^2$) at 5 $\mu$m in the range 0.5-5 $\mu$m, 1.0-2.0 and 0-0.1. As expected from chapter 4, none of these parameters are constrained at 5 $\mu$m and so any combination managed to fit VIMS limb-darkening data quite well. Note that a scaling factor $f$ of the haze concentration ($C^1$(p)) is retrieved with NEMESIS as well: the vertical shape remains the same although absolute concentrations are allowed to vary. The scaled haze concentrations ($C^2$(p)) depend on the optical and physical parameter values assumed at 5 $\mu$m. However, the haze opacity at 5 $\mu$m, which is a function of the haze concentration ($C^2$(p)), the haze extinction coefficient and optical path, remains very similar for all parameter values as it can be seen in Fig. 6.4.

In the top panel, the complex refractive index ($n_r^2$, $n_i^2$) is set at $1.4 + \mathrm{i}\times10^{-7}$ and the particle radius ($\Phi^2$) varies between 500 nm and 5 $\mu$m. The aerosol opacities at 5 $\mu$m and volume mixing ratios of phosphine and ammonia are similar within the retrieval errors for all the aerosol sizes ($\Phi^2$) tested here. The haze opacity averaged over the particle radius is equal to $0.74 \pm 0.21$. The standard deviation characterising the variation of the retrieved haze opacity with the radius is equal to 0.0025,

and so is significantly smaller than the mean retrieval errors.

Therefore, the choice of particle radius ($\Phi^2$) in the parametrisation of the tropospheric haze does not affect the retrieved value of the haze opacity within the modelling errors. The mean value and standard deviation of the cloud opacity are equal to $1.42 \pm 0.16$ and 0.0062. The deep volume mixing ratio of ammonia has a mean value of $(2.80 \pm 1.09)\times10^{-4}$ and a standard deviation of $6\times10^{-5}$. For these two parameters, the standard deviation is also smaller than the mean retrieval error.

Phosphine is the main gaseous absorber at 5 $\mu$m, and as a result its abundance is retrieved with low modelling errors. The deep volume mixing ratio of phosphine is equal to $(4.46 \pm 0.21)\times10^{-6}$ with a standard deviation of 0.19. The retrieved error and the standard deviation are of the same order, thus the variation of phosphine abundance due to the particle radius ($\Phi^2$) cannot be distinguished from the modelling errors. In conclusion, any particle radius ($\Phi^2$) between 500 nm and 5 $\mu$m leads to similar retrieved values of the cloud and haze opacities, and volume mixing ratios of phosphine and ammonia.

A similar analysis as above was carried out by varying the real refractive index ($n_r^2$) of the tropospheric haze at 4.6-5.1 $\mu$m. The particle radius ($\Phi^2$) and imaginary refractive index ($n_i^2$) were set to 1 $\mu$m and $10^{-7}$ respectively. The haze and cloud opacities at 5 $\mu$m, and the deep phosphine and ammonia abundances were retrieved for different values of the real refractive index between 1.0 and 2.0. The scattering ammonia cloud was found to provide a better fit to the observations for a cloud base pressure of 2.7 bar. The standard deviations of opacities and abundances due to the choice of real refractive index are similar or smaller than the modelling errors. Therefore, the values of the retrieved parameters are similar for all real refractive indices ($n_r^2$) within the modelling errors. The effect of the imaginary refractive index ($n_i^2$) was also estimated by varying its values between 0 and 0.1. The real refractive index ($n_r^2$) was set at 1.4 and the particle radius ($\Phi^2$) at 1 $\mu$m. As for the particle radius and the real refractive index, the variation of imaginary refractive index did not affect the retrievals. All best-fitting values of the cloud and haze opacities, and abundances of phosphine and ammonia are again similar within the retrieval errors.

Finally, the particle radius ($\Phi^2$), the real refractive index ($n_r^2$) and the imaginary refractive index ($n_i^2$) at 5 $\mu$m were tested simultaneously in the ranges 0.5-5 $\mu$m, 1.0-2.0 and 0-0.1 respectively. Similar conclusions as above can be drawn. The best fits were obtained for an ammonia cloud at the 2.7-bar pressure level in the scattering case. For each set of particle radius and complex refractive index, the

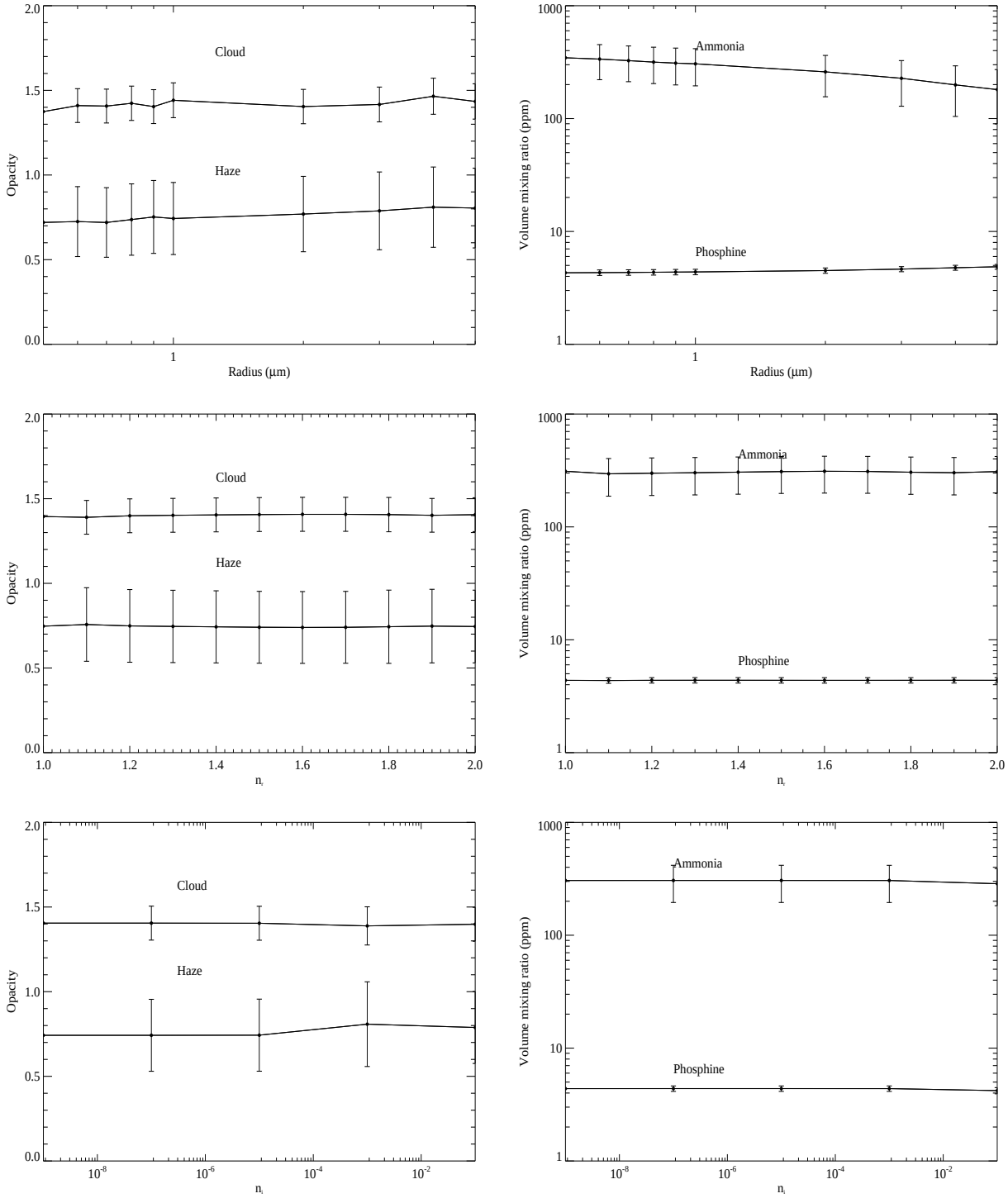



Figure 6.4: Effect of haze properties at 5 $\mu$m on the retrieved parameters. A deep scattering cloud made of ammonia ice with 1-$\mu$m particle size is placed at the 2.7-bar level. The haze and cloud opacities at 4.6-5.1 $\mu$m (*left panels*), and the volume mixing ratios of ammonia and phosphine in parts-per-million (*right panels*) are retrieved for various values of the particle radius $\Phi^2$ (*top panels*), real refractive index $n_r^2$ (*middle panels*) and imaginary refractive index $n_i^2$ (*bottom panels*) of the tropospheric haze at 5 $\mu$m.

modelling errors were larger than or similar to the standard deviation of the retrieved parameters. In conclusion, particle sizes between 0.5 and 5 $\mu$m, and all realistic values of the real refractive index and imaginary refractive index managed to fit VIMS limb-darkening spectra at 4.6-5.1 $\mu$m. In addition, all values of these three parameters ($\Phi^2$, $n_r^2$, $n_i^2$) led to similar values of the cloud base pressures, cloud and haze opacities, and deep volume mixing ratios of phosphine and ammonia.

So far, the haze properties at 0.8-3.5 $\mu$m have been fixed to $\Phi^1 = 1$ $\mu$m, $n_r^1 = 1.4$ and $n_i^1 = 10^{-7}$. The effect of the haze properties at 4.6-5.1 $\mu$m on the retrieved parameters from VIMS limb-darkening data is also tested for all combinations of $\Phi^1$, $n_r^1$ and $n_i^1$ in the ranges 0.5-5 $\mu$m, 1.1-1.8 and 0-0.001 respectively. Saturn's 5-$\mu$m data are only sensitive to the haze opacity, and not to optical and physical properties of the haze. Therefore, the choice of $\Phi^1$, $n_r^1$, $n_i^1$, $\Phi^2$, $n_r^2$ and $n_i^2$ does not affect the retrievals of the cloud and haze 5-$\mu$m opacities, and abundances of phosphine and ammonia from VIMS limb-darkening spectra at 4.5-6.1 $\mu$m. This is consistent with the results obtained in chapter 4 showing that Saturn's 5-$\mu$m window is only sensitive to the haze opacity and not its parameterisation.

A scaling factor $f$ of the haze distribution has been retrieved at 4.5-6.1 $\mu$m from the vertical structure ($C^1$(p)) retrieved at 0.8-3.5 $\mu$m. Saturn's hazes vary mostly with seasons and so any variation over a shorter timescale is expected to be smaller than the seasonal variations. The three cubes considered in this section are measured within about two months. Although the VIMS thermal spectrum is measured on the nightside, chapter 4 has shown that the haze lazer was still present at nighttime suggesting that the photochemical lifetimes are large enough to maintain the haze overnight.

The variation between the two haze concentrations retrieved at 0.8-3.5 $\mu$m ($C^1$(p)) and updated at 4.5-6.1 $\mu$m ($C^2$(p)) is assessed by calculating the parameter $\sigma_N$ described in section 6.1. For given values of $\Phi^1$, $n_r^1$, $n_i^1$, $\Phi^2$, $n_r^2$ and $n_i^2$, and for a specific cloud model, $\sigma_N$ should be less than the upper boundary values in the range 1-3. Note that the deep tropospheric cloud is assumed to be made of scattering ammonia ice. Other cloud models are considered in the next section. The parameter $\sigma_N$ is evaluated for all values of the particle size ($\Phi^2$) and complex refractive index ($n_r^2$, $n_i^2$) used to model the haze properties at 5 $\mu$m. The same haze profile as in Fig.6.2, derived from the VIMS reflection spectrum for a particle size ($\Phi^1$) of 1 $\mu$m and a complex refractive index ($n_r^1$, $n_i^1$) of $1.4 + i\times10^{-7}$ at 0.8-3.5 $\mu$m, is implemented in the reference model for the limb-darkening analysis at 5 $\mu$m. The results are presented in the top-right panel in Fig. 6.5 for a variable particle size ($\Phi^2$) and a fixed complex refractive index ($n_r^2$, $n_i^2$) at 4.5-6.1 $\mu$m equal to $1.4 + i\times10^{-7}$. Minimum values are obtained

for a particle size ($\Phi^2$) of 1 $\mu$m. Thus, the two haze distributions $C^1$(p) and $C^2$(p) are closer to each other for the same particle size at 0.8-3.5 $\mu$m and 4.5-6.1$\mu$m, that is to say for $\Phi^2 = \Phi^1$. $\sigma_N$ as a function of the imaginary refractive index ($n_i^2$) decreases whereas the variation of $\sigma_N$ with the real refractive index ($n_r^2$) appears more chaotic.

Similar conclusions as above can be drawn if the particle size ($\Phi^2$), real refractive index ($n_r^2$) and imaginary refractive index ($n_i^2$) are varied simultaneously. The two haze distributions are closer for a particle size ($\Phi^2$) of 1 $\mu$m and a larger imaginary refractive index ($n_i^2$). The results in Fig. 6.5 suggest that lower $\sigma_N$ values are obtained for an imaginary refractive index at 5 $\mu$m equal to 0.1. However, if all values of the real refractive index ($n_r^2$) are considered, the condition is less strict and the imaginary part ($n_i^2$) at 4.5-6.1 $\mu$m only needs to be higher than the value at 0.8-3.5 $\mu$m ($n_i^1$) equal to $10^{-7}$. Therefore, the two conditions $\Phi^2 = \Phi^1$ and $n_i^2 > n_i^1$ lead to minimum values of the $\sigma_N$ parameter. In that case, the scaled haze profile $C^2(p)$ is subject to minimum departure from the reference profile $C^1(p)$ derived from the analysis at 0.8-3.5 $\mu$m.

For lower values of $\sigma_N$, the scaled haze concentrations ($C^2(p)$) at 4.6-5.1 $\mu$m vary less from the reference haze profile ($C^1(p)$) derived from the analysis at 0.8-3.2 $\mu$m. If the modelled limb-darkening spectra are calculated without scaling the reference haze profile such as $C^2(p) = C^1(p)$, the model match the observations more closely for lower values of $\sigma_N$. This can be shown in the bottom-right panel in Fig. 6.5. The synthetic spectra is calculated assuming that the imaginary refractive index increases from $n_i^1 = 10^{-7}$ at 0.8-3.2 $\mu$m to $n_i^2 = 10^{-1}$ at 4.6-5.1 $\mu$m. The particle sizes and real refractive indices are assumed to stay the same in both wavelength ranges, that is to say $\Phi^2 = \Phi^1$ and $n_i^2 = n_i^1$. As it can be seen in the top-right panel in Fig. 6.5, this haze parametrisation corresponds to a $\sigma_N$ value of 0.07. The modelled and measured spectra at low and high emission angles are in good agreement within the measurement errors, with a $\chi^2/N_\lambda$ value of 3.52. If a scaling factor $f$ of the haze profile is retrieved, the $\chi^2/N_\lambda$ value drops to around 1 and the fit is very similar to what is observed in Fig. 6.3. If the modelled limb-darkening spectra are calculated for the same complex refractive index in both wavelength ranges ($n_r^2 = n_r^1$ and $n_i^2 = n_i^1$) but for a particle size ($\Phi^2$) of 800 nm at 4.6-5.1 $\mu$m, then $\sigma_N$ and $\chi^2/N_\lambda$ are respectively equal to 0.8 and 6.92 and the model does not fit VIMS data anymore. If all possible combinations of the haze parameters are tested, $\chi^2/N_\lambda$ values below the 5.0 threshold value are obtained for $\sigma_N$ values lower than approximately 0.5. Therefore, the haze parametrisations for which $\sigma_N$ is below 0.5 are coherent between VIMS

near-infrared data at 0.8-3.5 $\mu$m and at 4.6-5.1 $\mu$m, and the changes in the absolute values of the haze concentration are due to temporal variations between the three observations times.

So far, the haze optical and physical properties at 0.8-3.5 $\mu$m were assumed to consist of a particle size ($\Phi^1$) of 1 $\mu$m and a complex refractive index ($n_r^1$, $n_i^1$) of 1.4 + i$\times 10^{-7}$. Assuming minimum variation of the haze concentration over the three observation times, the haze distributions retrieved at 0.8-3.5 $\mu$m ($C^1(p)$) and then updated at 4.6-5.1 $\mu$m ($C^2(p)$) are coherent for a particle size ($\Phi^2$) of 1 $\mu$m and a higher imaginary refractive index ($n_i^2$) at 4.6-5.1 $\mu$m. If a similar analysis starts at 0.8-3.5 $\mu$m with a different particle size ($\Phi^1$), real refractive index ($n_r^1$) and complex refractive index ($n_i^1$) in the ranges 0.5-5 $\mu$m, 1.1-1.8 and 0-0.001, similar conclusions can be drawn. In Fig. 6.6, the particle sizes at 0.8-3.5 ($\Phi^1$) $\mu$m and 4.6-5.1 $\mu$m ($\Phi^2$) are varied simultaneously for a fixed refractive index of 1.4 + i$\times 10^{-7}$ ($n_r^2 = n_r^1 = 1.4$ and $n_i^2 = n_i^1 = 10^{-7}$). Lower values of $\sigma_N$ are observed for similar values of the particle size between the two wavelength ranges. The $\sigma_N$ map obtained by varying the imaginary refractive index at 0.8-3.5 $\mu$m ($n_i^1$) and 4.6-5.1 $\mu$m ($n_i^2$) confirms that increasing values of this parameter lead to lower $\sigma_N$ values. However, no specific trend is observed for the real imaginary index.

Considering all the possible combinations of the haze properties at both 0.8-3.5 $\mu$m and 4.6-5.1 $\mu$m wavelength ranges, the minimum $\sigma_N$ values are obtained around 0.1. Low $\sigma_N$ values are observed if the particle size is uniform across the two wavelength ranges, and if the imagniary refractive index increases at 4.6-5.1 $\mu$m. Note that VIMS data at 5$\mu$m are only sensitive to the haze opacity, and so even for large $\sigma_N$ values, the ammonia cloud pressure, the retrieved values of the haze and cloud opacities, and deep volume mixing ratios of ammonia and phosphine are similar for all haze models considered in this section. In conclusion, $\sigma_N$ only constrain the haze optical and physical parameters over the two wavelength ranges but not the retrieved cloud and haze opacities, and deep volume mixing ratios of ammonia and phosphine.

This section has shown that the haze vertical profile $C^1(p)$ retrieved at 0.8-3.5 $\mu$m fits VIMS limb-darkening observations at 4.6-5.1 $\mu$m if the scaled profile $C^2(p)$ stays close to $C^1(p)$, that is to say for lower $\sigma_N$ values. Minimum $\sigma_N$ values are obtained for $\Phi^2 = \Phi^1$ and $n_i^2 > n_i^1$. The deep tropospheric cloud is assumed to be made of scattering ammonia ice. A similar analysis is carried out for different cloud compositions in the next section.

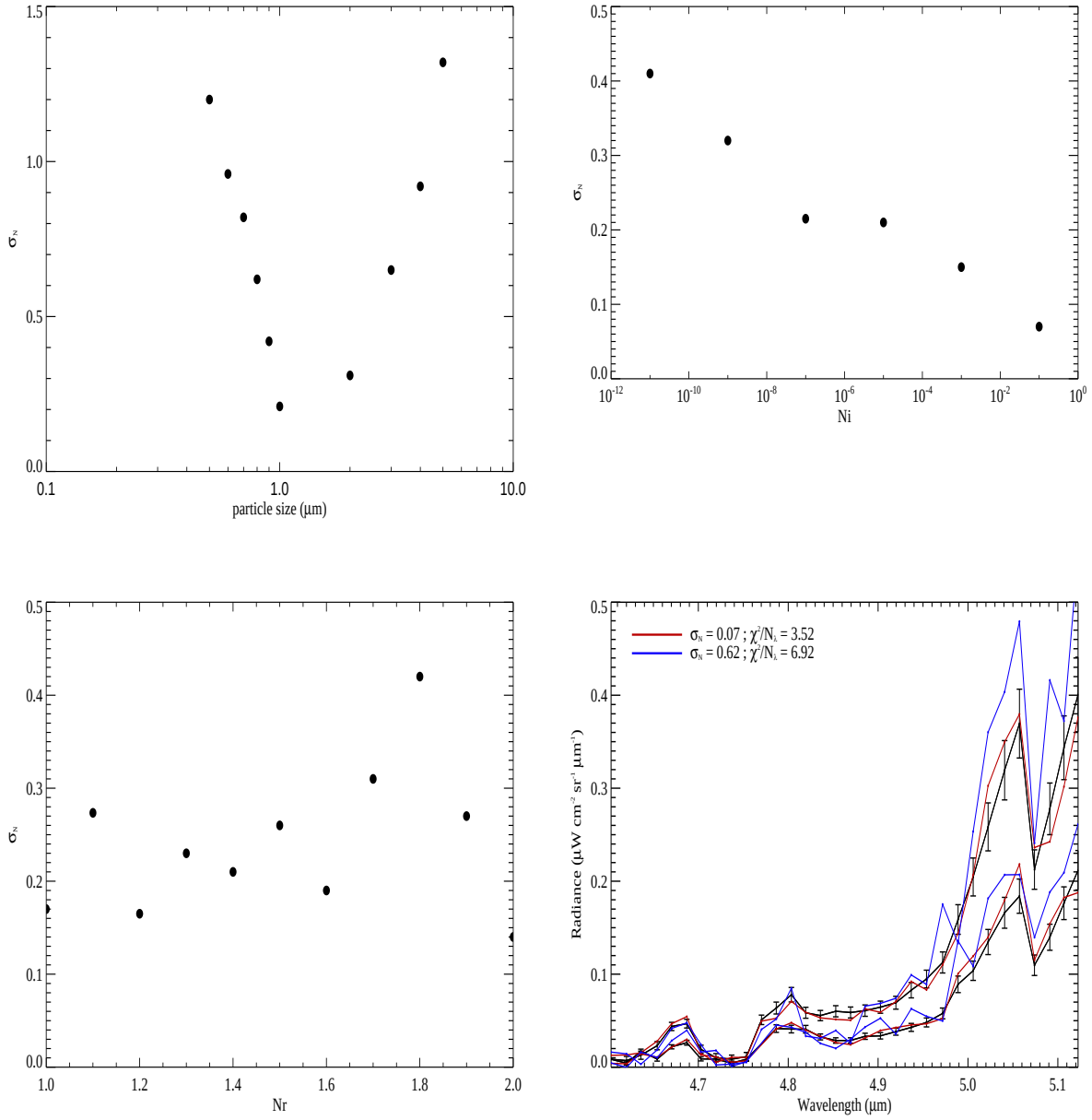



Figure 6.5: Standard deviation between the two haze vertical distributions at 0.8-3.5 $\mu$m ($C^1$(p)) and 4.5-5.1 $\mu$m ($C^2$(p)) for different optical and physical properties of Saturn's hazes at 5 $\mu$m. In the top-left panel, the variation of $\sigma_N$ is plotted against the particle size ($\Phi^2$) for a fixed complex refractive index ($n_r^2$, $n_i^2$) at 4.6-5.1 $\mu$m equal to 1.4 + i$\times 10^{-7}$. In the top-right panel, the variation of $\sigma_N$ is plotted against the imaginary refractive index ($n_i^2$) for a fixed real refractive index ($n_r^2$) of 1.4 and a particle size ($\Phi^2$) of 1 $\mu$m. In the bottom-left panel, the variation of $\sigma_N$ is plotted against the real refractive index ($n_r^2$) for a fixed imaginary refractive index ($n_i^2$) of $10^{-7}$ and a particle size ($\Phi^2$) of 1 $\mu$m. In the bottom-right panel, the modelled spectra at 4.5-6.1 $\mu$m are calculated without scaling the haze vertical profile retrieved at 0.8-3.2 $\mu$m, that is to say for $C^2$(p) = $C^1$(p). The results for a particle size ($\Phi^2$) of 1 $\mu$m and a complex refractive index ($n_r^2$, $n_i^2$) of 1.4 + i$\times 10^{-1}$ at 4.6-5.1 $\mu$m are shown in red line (this haze parametrisation corresponds to a $\sigma_N$ of 0.07). The results for a particle size ($\Phi^2$) of 0.8 $\mu$m and a complex refractive index ($n_r^2$, $n_i^2$) of 1.4 + i$\times 10^{-7}$ at 4.6-5.1 $\mu$m are shown in blue line ($\sigma_N$ is now equal to 0.62). Note that in both cases, optimum results are obtained and shown for a scattering ammonia cloud at 2.7 bar.

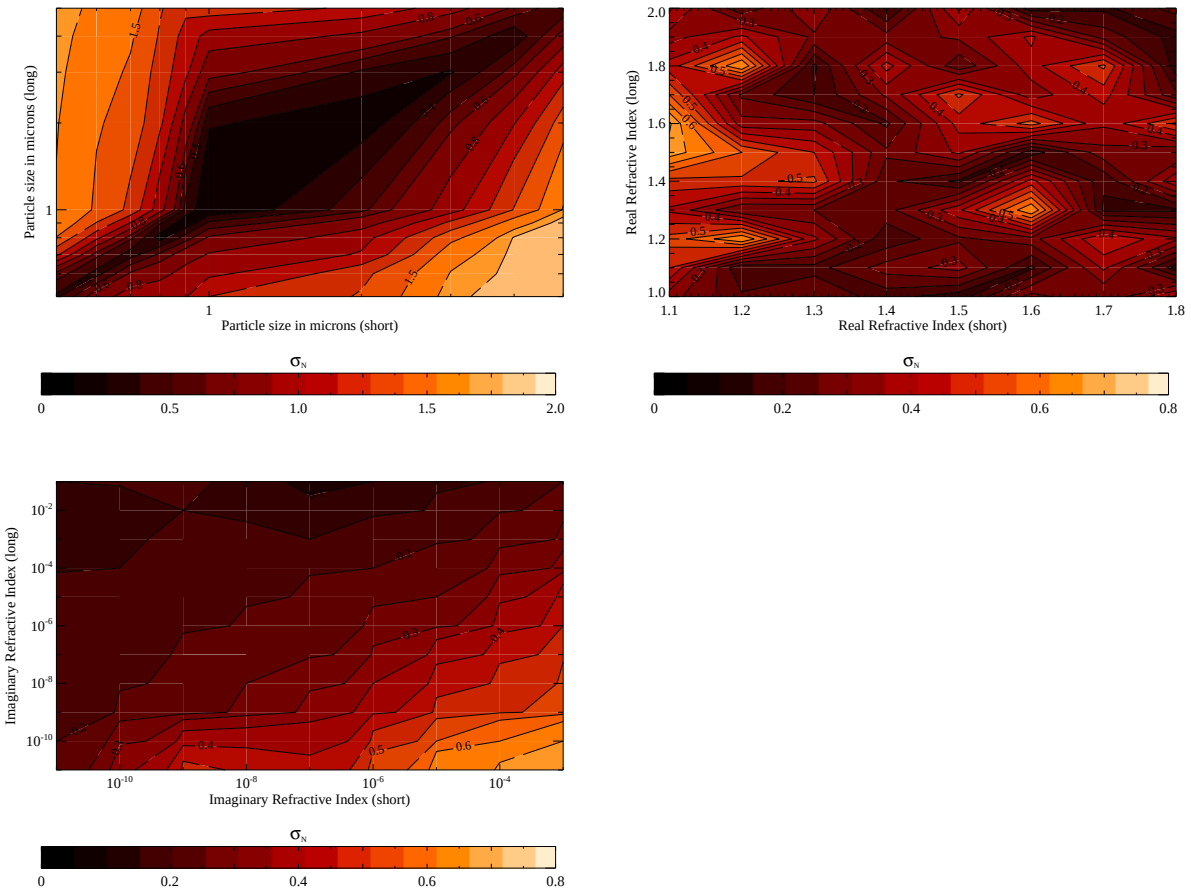



Figure 6.6: $\sigma_N$ maps as a function of the haze parameters at 0.8-3.5 $\mu$m and 4.5-6.1 $\mu$m. *Top-left:* The haze vertical profiles are retrieved from VIMS spectrum at 0.8-3.5 $\mu$m (short) for a fixed refractive index ($n_r^1$, $n_i^1$) of 1.4 + i$\times 10^{-7}$ and a variable particle size ($\Phi^1$) between 500 nm and 5 $\mu$m. The $\sigma_N$ is calculated assuming that the refractive index ($n_r^2$, $n_i^2$) at 4.6-5.1 $\mu$m (long) is 1.4 + i$\times 10^{-7}$ and the particle size ($\Phi^2$) varies between 500 nm and 5 $\mu$m. Lower $\sigma_N$ values are obtained for a similar particle size at 0.8-3.5 $\mu$m and 4.6-5.1 $\mu$m, that is to say for $\Phi^2 \sim \Phi^1$. *Top-right:* The particle size and imaginary refractive index in both wavelength ranges are fixed to 1 $\mu$m and $10^{-7}$ respectively. The real refractive index varies between 1.1 and 1.8 at 0.8-3.5 $\mu$m, and between 1.0 and 2.0 at 4.6-5.1 $\mu$m. *Left-bottom:* The particle size and real refractive index are fixed to 1 $\mu$m and 1.4 respectively. The $\sigma_N$ values are calculated as a function of the imaginary refractive indices assumed in each wavelength range. Lower $\sigma_N$ values are obtained for increasing values of the imaginary refractive index with wavelength.

## 6.3 Tropospheric model at 20°S

### 6.3.1 Cloud composition

The previous section has shown that the haze vertical distributions derived from the analysis of VIMS near-infrared reflection data is consistent with the haze needed by the 5-$\mu$m limb-darkening observations, but is better constrained vertically. The haze optical and physical properties are constrained by the condition that $\sigma_N$ should be small or at least inferior to the upper boundary range 1-3. Such a condition implies that the particle size is uniform across the two wavelength ranges and the imaginary refractive index increases with wavelength. The analysis in the previous section was made for a scattering ammonia cloud with a cloud particle size of 1 $\mu$m. The best fits to VIMS limb-darkening data were obtained for a cloud base pressure of 2.7 bar. In this section, the consistency between the haze structures retrieved at 0.8-3.5 $\mu$m and then updated at 4.6-5.1 $\mu$m is tested for other cloud models. Non-scattering cloud models fail at matching limb-darkening observations at 5 $\mu$m, therefore scattering is included in the all cloud models. Three scattering cloud models are considered here consisting of:

*i.* an ammonium hydrosulphide cloud since it is expected to form at pressure levels sounded by Saturn's 5-$\mu$m window.

*ii.* a simple grey cloud similar as in chapter 4 with a scattering albedo of 0.95 and an isotropic phase function.

*iii.* a cloud with a particle size and complex refractive index constant with wavelength. This model is tested for all values of the real and imaginary refractive index in the ranges 1-2 and 0-0.1 respectively. This model assumes that the cloud composition is completely unknown. As a result, the cloud is parametrised by the particle size and complex refractive index, assumed to be constant with wavelength at first approximation.

The three models are tested following a similar methodology as in the previous section assuming the same haze profile shown in Fig. 6.2 derived from VIMS near-infrared spectrum for a particle size ($\Phi^1$) of 1 $\mu$m and a complex refractive index ($n_r^1$, $n_i^1$) of $1.4 + \mathrm{i}\times 10^{-7}$. The variation of $\sigma_N$ with the particle size ($\Phi^2$) assumed at 4.6-5.1 $\mu$m is shown in the top-left panel in Fig. 6.7 for a compact ammonium hydrosulphide and compact grey clouds. The complex refractive index ($n_r^2$, $n_i^2$) at 4.6-5.1

$\mu$m is fixed to $1.4 + i\times10^{-7}$. The results are compared with the compact ammonia cloud studied in the previous section.

$\sigma_N$ values are higher for an ammonium hydrosulphide cloud than for an ammonia cloud with minimum values around 0.45. As for the ammonia cloud, the lowest $\sigma_N$ value is found also for an aerosol particle size ($\Phi^2$) of 1 $\mu$m. However, the $\sigma_N$ values for a grey cloud have significant larger values and are more randomly distributed. Indeed $\sigma_N$ are obtained in the range 3-8 and so are larger than $\sigma_N$ values characterising seasonal variations. As mentioned in section 6.1, $\sigma_N$ values are expected to be smaller than the upper boundary values in the range 1-3. Therefore the haze distributions at 0.8-3.5 $\mu$m ($C^1(p)$) and at 4.6-5.1 $\mu$m ($C^2(p)$) are not consistent with each other for the grey cloud model.

The $\sigma_N$ values are plotted against the imaginary refractive index ($n_i^2$) in the top-right panel in Fig. 6.7. For the ammonium hydrosulphide cloud, $\sigma_N$ slightly decreases with the imaginary index ($n_i^2$), however $\sigma_N$ values for a grey cloud do not follow a similar trend and are all above 4. The distribution of $\sigma_N$ with the real refractive index ($n_r^2$) is more chaotic for the three cloud models, although only the ammonia and ammonium hydrosulphide clouds have $\sigma_N$ values lower than the upper boundary values. Therefore, the haze concentrations retrieved from VIMS reflection data at 0.8-3.5 $\mu$m ($C^1(p)$) are not consistent with the haze concentrations updated at 4.6-5.1 $\mu$m ($C^2(p)$) for a grey cloud.

The grey cloud model can only VIMS limb-darkening spectra in the 4.6-5.1 $\mu$m for unrealistic variations of $C^2(p)$ with respect to $C^1(p)$. The $\sigma_N$ plots for an ammonium hydrosulphide follow a similar trend as for an ammonia although with larger absolute values. If all combinations of the haze properties at both wavelengths ($\Phi^1$, $n_r^1$, $n_i^1$, $\Phi^2$, $n_r^2$, $n_i^2$) are considered for the ammonium hydrosulphide and grey clouds, similar conclusions can be drawn. Only the ammonium hydrosulphide cloud in the scattering case is associated with $\sigma_N$ values lower than the upper boundary values, assuming that the haze particle size is constant and that the imaginary refractive index increases with wavelength.

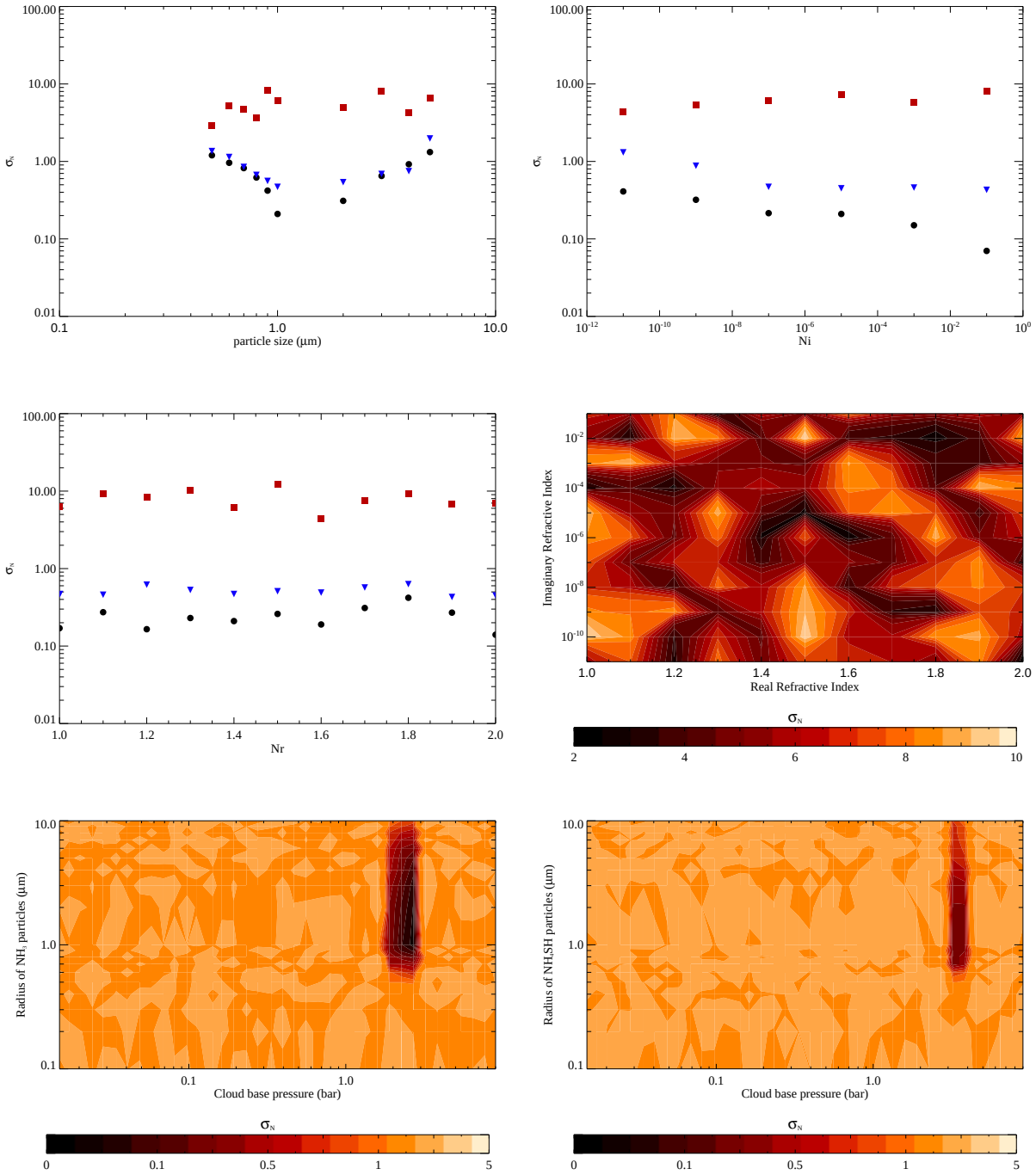



Figure 6.7: $\sigma_N$ tests (see section 6.1) for various compositions of the deep tropospheric cloud. In the top-left, top-right and middle left panels, a similar analysis as in Fig. 6.5 is carried out for an ammonium hydrosulphide cloud (blue triangles) and a grey cloud (red squares). The results are compared with an ammonia cloud (black circles). The particle size for the ammonium hydrosulphide and ammonia clouds is equal to 1 $\mu$m. In the middle-right panel, the minimum $\sigma_N$ values are calculated for a deep cloud parametrised by a constant complex refractive index over the 4.6-5.1 $\mu$m wavelength range. All possible combinations of the real and imaginary parts of the refractive index, in the ranges 1-2 and 0-0.1 respectively, are tested. The results are shown for a particle size of 1 $\mu$m. In the bottom-left panel, the minimum $\sigma_N$ values are calculated for an ammonia cloud with a variable pressure and a variable particle size. The same analysis is done for an ammonium hydrosulphide cloud in the bottom-right panel.

The same analysis is carried out for the third cloud model. For each complex refractive index characterising the deep cloud, the minimum $\sigma_N$ value is estimated by considering all the different haze properties at 0.8-3.5 $\mu$m and 4.6-5.1 $\mu$m. The minimum $\sigma_N$ values as a function of the real and imaginary parts of the refractive index for the cloud are shown in the middle-right panel in Fig. 6.7. These values are all in the range 2-9 and so are of the same order or above the values representing seasonal variations. In the bottom panels, the minimum $\sigma_N$ values are plotted for an ammonia cloud (left panel) and an ammonium hydrosulphide cloud (right panel) as a function of the cloud base pressure and cloud particle size. The lowest $\sigma_N$ values are obtained for an ammonia cloud at 2.7 bar and a particle size between 800 nm and 4 $\mu$m. For an ammonium hydrosulphide cloud, minimum $\sigma_N$ values of about 0.40 are obtained for a cloud base at 3.2 bar and a cloud particle size between 700 nm and 4 $\mu$m. Among all the cloud models tested in this section, only the scattering ammonia and ammonium hydrosulphide cloud models are associated with $\sigma_N$ values low enough for the haze parameters and vertical structure to be coherent at 0.8-3.5 $\mu$m and 4.6-5.1 $\mu$m. Although variations of the aerosol concentration in $cm^{-3}$ are likely to occur over the three observation times, they should be less than the seasonal variations. The grey cloud model and the cloud model with constant complex refractive index can only fit the limb-darkening data at 5 $\mu$m for unrealistic variation of the haze concentrations. Real clouds are unlikely to be modelled by these two simpler models. However, such models manage to fit VIMS limb-darkening data in the 4.6-5.1 $\mu$m wavelength range within the measurement errors if no assumptions are made on the haze vertical structure. $\sigma_N$ tests (see section 6.1) can be performed in order to descriminate between different cloud models. In particular, chapter 4 has showed that the grey cloud managed to fit VIMS thermal emission spectra in the 5-$\mu$m window. Chapter 5 has constrained the vertical distribution of the haze located above the deep tropospheric cloud. The deep cloud model assumed in the 5-$\mu$m limb-darkening analysis should satisfy the condition that the haze profiles $C^1(p)$ and $C^2(p)$ are consistent with each other. This section has shown that this is not the case for the grey cloud or a simple cloud model with a fixed refractive index. However, the scaled haze profile at 4.6-5.1 $\mu$m is consistent with the haze profile retrieved at 0.8-3.5 $\mu$m for an ammonia and ammonium hydrosulphide clouds. Therefore, these two cloud models can be validated as candidates for the deep tropospheric cloud. In the next section, the retrievals of VIMS limb-darkening spectra at 4.6-5.1 $\mu$m are then performed for an ammonia and ammonium hydrosulphide clouds.

### 6.3.2 Retrievals for an ammonia and ammonium hydrosulphide clouds

In this section, the limb-darkening analysis at 5 $\mu$m is undertaken for an ammonia and ammonium hydrosulphide clouds. Chapter 4 has shown that the haze must be included in the atmospheric model in order to fit limb-darkening data at 5 $\mu$m. However, the vertical distribution, as well as the optical and physical properties of the haze are not constrained at 5 $\mu$m. Instead, the haze structure is derived from the analysis of near-infrared reflection data and used as a reference profile for the analysis at 4.6-5.1 $\mu$m. The reference haze profile ($C^1(p)$) shown in Fig. 6.2 is retrieved from VIMS reflection data at 0.8-3.5 $\mu$m for a particle size ($\Phi^1$) of 1 $\mu$m and a complex refractive index ($n_r^1$, $n_i^1$) of 1.4 + i$\times 10^{-7}$. The extinction cross-section and scattering albedos at 4.6-5.1 $\mu$m for the tropospheric haze are calculated for an identical particle size and real refractive index but for an imaginary refractive index equal to $10^{-1}$, that is to say $\Phi^2 = \Phi^1 = 1$ $\mu$m, $n_r^2 = n_r^1 = 1.4$ and $n_i^2 = 10^{-1}$. The cloud opacity, and deep volume mixing ratios of phosphine and ammonia are retrieved for both deep cloud models. The scaling factor $f$ of the haze concentration is also retrieved in order to take into account the variation of haze concentration between the different oberving times. The cloud base pressure and cloud particle size are allowed to vary between 10 mbar and 10 bar, and between 100 nm and 10 $\mu$m respectively.

As expected, a non-scattering cloud cloud not match the observations and so scattering had to be included in the cloud model. The results are shown in Fig. 6.8 for a scattering ammonia cloud. The best fits to the observations are obtained for a cloud particle radius ranging between 500 nm and 5 $\mu$m. The lowest $\chi^2/N_\lambda$ value corresponds to a particle radius equal to 2 $\mu$m. For each particle radius, the ammonia cloud must be placed at the 2.7-bar level in order to match both the low and high emission angle spectra. In the top-right panel of Fig. 6.8, the synthetic spectra for a cloud base pressure of 2.7 bar and a particle radius of 2 $\mu$m are plotted against the limb-darkening measurements. Both synthetic spectra are in good agreement with VIMS data within the measurement errors. The same conclusion holds for any particle radius in the range 0.5-5 $\mu$m. The retrieved parameters are presented as a function of the cloud particle radius. Ammonia abundances and haze opacities are retrieved with error bars larger than the standard deviation due to the choice of aerosol radius. Phosphine abundances are very similar for all particle radii although they have very small retrieval errors. Therefore, the ammonia and phosphine volume mixing ratios and haze opacities are not affected by the aerosol

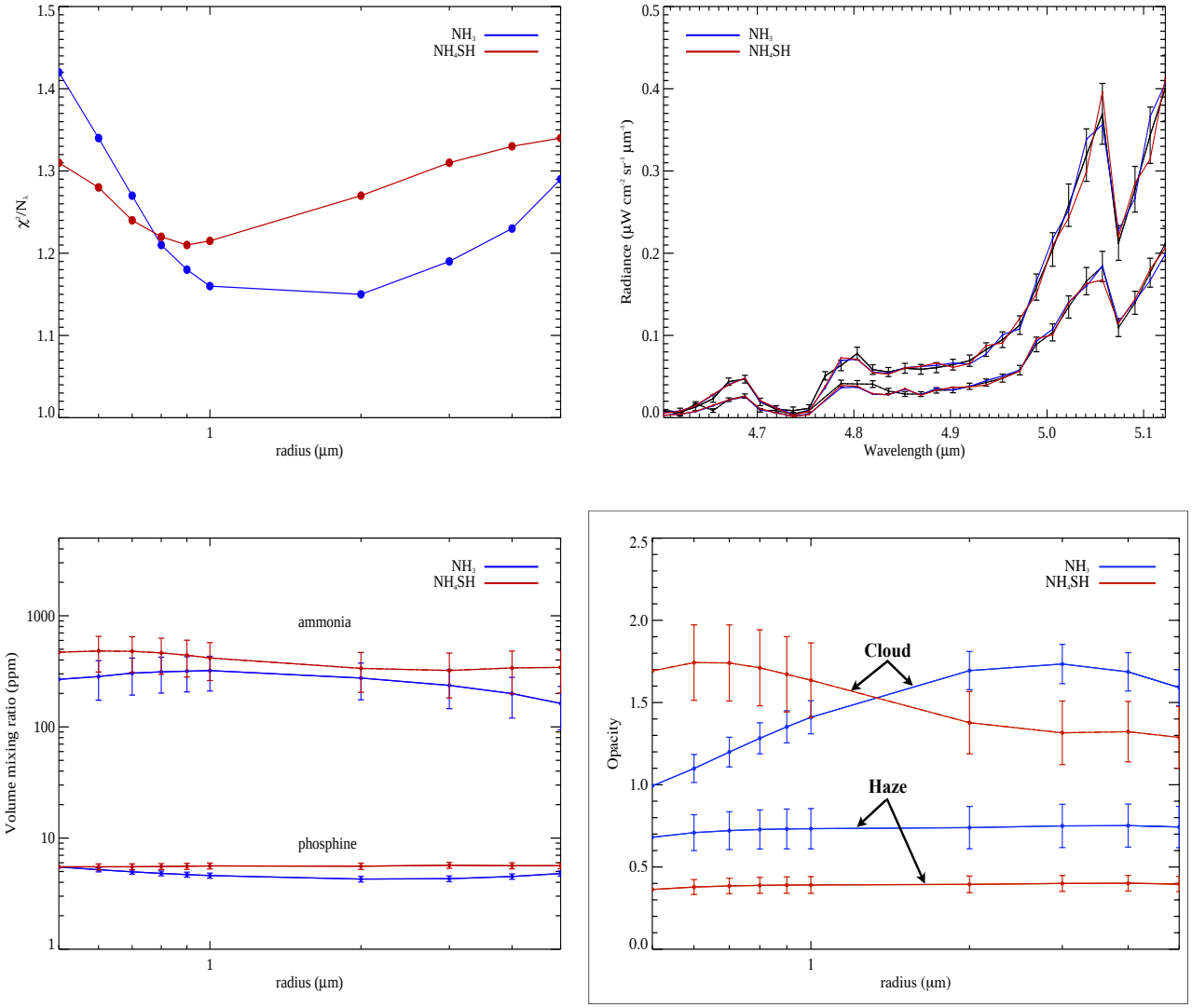



Figure 6.8: Limb-darkening analysis of Saturn's 5-$\mu$m window for a deep cloud made of ammonia and ammonium hydrosulphide particles. The troposheric haze is assumed to be made of scattering particles with a 1-$\mu$m radius ($\Phi^1$) and a complex refractive index ($n_r^1$, $n_i^1$) of $1.4 + \mathrm{i}\times 10^{-7}$ at 0.8-3.5 $\mu$m. The same haze particle size ($\Phi^2 = \Phi^1$) and real refractive index ($n_r^2 = n_r^1$), but higher imaginary refractive index ($n_i^2 = 10^{-1}$) are assumed in the 5-$\mu$m window. The pressure and particle radius of the deep cloud are allowed to vary in the range 0.1-10 $\mu$m and 0.01-10 bar respectively. The deep cloud is assumed to be made either of scattering ammonia ice ($NH_3$) or ammonium hydrosulphide particles ($NH_4SH$). The haze and cloud opacities at 5 $\mu$m (*bottom-right panel*), and the deep volume mixing ratios of phosphine and ammonia (*bottom-left panel*) are retrieved with NEMESIS. The best fits are obtained for an aerosol particle size between 500 nm and 5 $\mu$m for both cloud compositions. The model is in better agreement with VIMS limb-darkening data for a cloud base pressure at 2.7 bar and 3.2 bar for an ammonia and ammonium hydrosulphide cloud respectively. The goodness-of fit (*top-left panel*) and the retrieved parameters are thus shown for particles sizes in the range 0.5-5 $\mu$m. The modelled spectra for an ammonia cloud at 2.7 bar with 2-$\mu$m radius particles and an ammonium hydrosulphide cloud at 3.2 bar with 900-nm radius particles are compared with VIMS limb-darkening spectra (*top-right panel*).

particle radius. However, the cloud opacity increases with the particle size until a radius of 2 $\mu$m and then remains approximately constant. Although the cloud base pressure is well constrained for all particle radii, the cloud opacity can only be roughly estimated. A similar analysis as above was carried out for an ammonium hydrosulphide cloud. The best fits are obtained for a scattering cloud slightly deeper than the ammonia cloud at the 3.2-bar level. As can be seen in Fig. 6.8, the $\chi^2/N_\lambda$ has a minimum value for a cloud particle size of 900 nm. The modelled spectra for a cloud at 3.2 bar and a particle size of 900 nm are compared to VIMS near-infrared data at low and high emission angles. As for an ammonia cloud, the model matches the observations quite well within the measurement errors. The retrieved parameters are plotted for an aerosol particle size in the range 0.5-5 $\mu$m in Fig. 6.8. The variations of ammonia and phosphine abundances, and the variation of the haze opacity due to the change in particle size are similar or less than the measurement errors on each parameter. Therefore, the retrieval of these parameters is not significantly affected by the choice of cloud particle size. However, the retrieved cloud opacity is sensitive to the choice of cloud particle size. Note that a scale factor $f$ of the haze vertical profile ($C^1(p)$) is retrieved in this section. In the atmospheric model, the haze particle size was assumed to be uniform across the wavelength ranges 0.8-3.5 $\mu$m and 4.6-5.1 $\mu$m, and the imaginary refractive index was assumed to increase with wavelength. Such a model is characterised by low values of the $\sigma_N$ parameter. In that case, the scaled haze profile at 4.6-5.1 $\mu$m ($C^2(p)$) does not vary significantly for the reference profile ($C^1(p)$). Lower $\sigma_N$ values are obtained around 0.10 and 0.40 for an ammonia cloud and an ammonium hydrosulphide cloud respectively. If instead of retrieving a scale factor $f$ at 4.6-5.1 $\mu$m, ($C^2(p)$) is fixed to ($C^1(p)$), then $\chi^2/N_\lambda$ increases as expected. This is equivalent to the assumption that the scale factor is fixed to 1. The cloud and haze opacities, as well as the volume mixing ratios of phosphine and ammonia for an ammonia and ammonium hydrosulphide clouds are shown in Table 6.1. The results of the retrievals are shown for an ammonia cloud at 2.7 bar with a cloud particle size of 2 $\mu$m. If the scale factor $f$ of the haze verical profile $C^1(p)$ is retrieved, then $\chi^2/N_\lambda$ is equal to 1.15 and the model matches the observations quite well within the measurement errors. In that case, NEMESIS retrieves a haze opacity of 0.74 $\pm$ 0.19, a cloud opacity of 1.69 $\pm$ 0.12, a phosphine volume mixing ratio of 4.27 $\pm$ 0.25 an an ammonia volume mixing ratio of 275.22 $\pm$ 99.68. The $\sigma_N$ parameter is equal to 0.11 and so the scaled haze profile ($C^2(p)$) stays close to the reference profile ($C^1(p)$). For a fixed scale factor of 1, $\chi^2/N_\lambda$ is equal to 2.96 and so is still below the 5-threshold value. As a result, the

model still matches VIMS limb-darkening data within the measurement errors. The cloud opacity and volume mixing ratios of phosphine and ammonia retrieved with NEMESIS are very similar to the values obtained in the previous case. However, the haze opacity drops to 0.49. The variation in the haze opacity is mainly responsible for the larger $\chi^2/N_\lambda$ value.

| Ammonia cloud | | | | |
|---|---|---|---|---|
| | $\sigma_N$ = 0.11 | | $\sigma_N$ = 0.55 | |
| | retrieved $f$ | $f = 1$ | retrieved $f$ | $f = 1$ |
| $\chi^2/N_\lambda$ | 1.15 | 2.96 | 1.17 | 8.12 |
| Haze opacity | $0.74 \pm 0.19$ | 0.49 | $0.74 \pm 0.18$ | 0.23 |
| Cloud opacity | $1.69 \pm 0.12$ | $1.73 \pm 0.15$ | $1.67 \pm 0.13$ | $2.34 \pm 0.21$ |
| Phosphine (ppm) | $4.27 \pm 0.25$ | $4.22 \pm 0.24$ | $4.27 \pm 0.24$ | $11.56 \pm 0.34$ |
| Ammonia (ppm) | $275.22 \pm 99.68$ | $281.95 \pm 93.12$ | $277.09 \pm 98.99$ | $74.32 \pm 34.12$ |
| Ammonium hydrosulphide cloud | | | | |
| | $\sigma_N$ = 0.38 | | $\sigma_N$ = 1.04 | |
| | retrieved $f$ | $f = 1$ | retrieved $f$ | $f = 1$ |
| $\chi^2/N_\lambda$ | 1.21 | 3.12 | 1.23 | 11.54 |
| Haze opacity | $0.39 \pm 0.05$ | 0.58 | $0.38 \pm 0.05$ | 0.87 |
| Cloud opacity | $1.67 \pm 0.23$ | $1.60 \pm 0.19$ | $1.69 \pm 0.24$ | $4.23 \pm 0.24$ |
| Phosphine (ppm) | $5.58 \pm 0.37$ | $5.64 \pm 0.39$ | $5.56 \pm 0.36$ | $0.19 \pm 0.03$ |
| Ammonia (ppm) | $336.00 \pm 131.36$ | $323.42 \pm 138.01$ | $340.05 \pm 134.23$ | $613.00 \pm 249.64$ |

Table 6.1: Retrieved parameters at 4.6-5.1 $\mu$m for low and high $\sigma_N$ values. The haze and cloud opacities at 5 $\mu$m, and the volume mixing ratios of phosphine and ammonia in parts-per-million are shown with their retrieval errors for an ammonia and ammonium hydrosulphide clouds. The results are presented for an ammonia cloud at 2.7 bar with a 2-$\mu$m cloud particle size, and for an ammonium hydrosulphide cloud at 3.2 bar with a 900-nm cloud particle size. The low $\sigma_N$ value corresponds to a constant haze particle size of 1 $\mu$m, a constant real refractive index of 1.4 and an increasing imaginary index from $10^{-7}$ at 0.8-3.2 $\mu$m to $10^{-1}$ at 4.6-5.1 $\mu$m. The high $\sigma_N$ value corresponds to a constant refractive index of $1.4 + 10^{-7}$ and a decreasing cloud particle size from 1 $\mu$m at 0.8-3.2 $\mu$m to 700 nm at 4.6-5.1 $\mu$m.

The case for large $\sigma_N$ values is analysed in this section. The haze complex refractive index is fixed to $1.4 + \mathrm{i}\times 10^{-7}$ across the 0.8-3.2 $\mu$m and 4.6-5.1 $\mu$m wavelength ranges. However, the particle size is assumed to decrease from 1 $\mu$m at 0.8-3.2 $\mu$m ($\Phi^1$) to 700 nm at 4.6-5.1 $\mu$m ($\Phi^2$). As expected from the previous section, such a haze model is characterised by larger $\sigma_N$ value of about 0.55. If the scale factor $f$ is retrieved, NEMESIS adjusts the haze concentrations so as to obtain an integrated

haze opacity of 0.74 $\pm$ 0.18, similar to what is obtained for a $\sigma_N$ of 0.11. The retrieved values of the cloud opacity and volume mixing ratios of phosphine and ammonia are also very similar within the retrieval errors. This was expected from the results shown in Fig. 6.4. in Saturn's 5-$\mu$m window, NEMESIS retrieves similar aerosol opacities and gas abundances for all haze properties. This is also true for large values of $\sigma_N$. Even though the haze structure obtained at 4.6-5.1 $\mu$m ($C^2(p)$) is not consistent with the haze structure at 0.8-3.2 $\mu$m ($C^1(p)$), NEMESIS adjusts the haze opacity at 4.6-5.1 $\mu$m in order to fit VIMS limb-darkening data. However, if the scale factor is fixed to 1, the $\chi^2/N_\lambda$ value increases to 8.12 and the modelled spectra do not match the observations. Besides, NEMESIS the retrieved values of the cloud opacity and gas abundances are inconsistent with the previous estimations. The retrieved parameters for low and high values of $\sigma_N$ are also presented in Table 6.1 for an ammonium hydrosulphide cloud at 3.2 bar, assuming a cloud particle size of 900 nm. Similar conclusions can be drawn as for an ammonia cloud. For a low $\sigma_N$ value of about 0.38, the parameters retrieved at 4.6-5.1 $\mu$m are very similar within the retrieval errors for both a retrieved and fixed scale factors. For a high $\sigma_N$ value of about 1.04, retrieving a scale factor of the haze vertical profile leads to similar results as for a lower $\sigma_N$ value. If the scale factor is fixed, the model fails at matching VIMS limb-darkening data in the 5-$\mu$m window. The results shown in Table 6.1 can be generalised to any value of $\sigma_N$. For a haze structure consistent at 0.8-3.2 $\mu$m and 4.6-5.1 $\mu$m (low $\sigma_N$), the retrieved cloud opacity and volume mixing ratios of phosphine and ammonia are similar whether or not a scale factor is retrieved. For large values of $\sigma_N$, the retrieved parameters are similar to what is observed for low $\sigma_N$ values only if a scale factor is retrieved. This can be explained by the non-sensitivity of Saturn's 5-$\mu$m window to the haze optical and physical properties. In conclusion, the haze distribution is consistent at both 0.8-3.2 $\mu$m and 4.6-5.1 $\mu$m for a deep tropospheric cloud made of either scattering ammonia particles or scattering ammonium hydrosulphide particles. This is only observed for a constant value of the haze particle size[1] and for an increasing value of the imaginary refractive index with wavelength. In that case, fixing the haze profile $C^2(p)$ to $C^1(p)$ or retrieving a scale factor $f$ leads to similar retrieved values of the cloud opacity and deep volume mixing ratios of phosphine and ammonia. Section 2 and 3 have focused on observations made at 20°S. In the next section, a similar strategy is developed but at various latitudes.

[1]The results are shown for one particular size although they can be generalised for all particle sizes in the 0.5-5 $\mu$m range. The results are consistent for any particle size in this range assuming a constant size across the two wavelength ranges

## 6.4 Tropospheric model at all latitudes

### 6.4.1 $\sigma_N$ tests

In this section, VIMS limb-darkening data at 4.6-5.1$\mu$m are analysed at all latitudes in the range 60°S-60°N. Data at low emission angles are extracted from the VIMS spectral cube CM1517766319 acquired on 4 February 2006 at $17^h15^m38.888^s$. The 25 near-infrared spectra are measured at a similar longitude of $308.31° \pm 4.47°$ and at 5°-latitude from each other. VIMS image at 5.05 $\mu$m and the individuam pixels selected at each latitude are shown in Fig. 6.9. Spectra at the same longitude but observed at higher emission angle are extracted from the VIMS cube CM1517833752 measured on 5 February 2006 at $11^h59^m31.458^s$. The latitude, longitude and emission angles of each spectrum analysed in this section are presented in Table 6.2.

The haze vertical distribution between 60°S and 60°N is obtained from the two VIMS spectral cubes CM1518772354 and CM1518778752 measured on 16 February 2006 at $08^h42^m47.471^s$ and on 16 February 2006 at $10^h29^m24.433^s$ respectively. VIMS images at 1.07 $\mu$m in each cube are presented in Fig. 6.9. The near-infrared retrievals for a particle size ($\Phi^1$) of 1 $\mu$m and a complex refractive index ($n_r^1$, $n_i^1$) of $1.4 + \mathrm{i}\times10^{-7}$ are also shown in Fig. 6.9. In 2006, the ring shadows covered latitudes between approximately 15°N and 30°N, and so the haze concentrations are not retrieved in this latitudinal range.

The haze vertical profiles at each latitude shown in Fig. 6.9 are used as a reference model for the analysis of all VIMS limb-darkening data listed in Table 6.2, except between 15°N and 30°N. A scattering ammonia cloud with a cloud particle size of 1 $\mu$m is first asumed as a cloud model. The cloud opacity, scale factor $f$ of the reference haze profile ($C^1(p)$) and deep abundances of phosphine and ammonia are retrieved with NEMESIS. The cloud base is allowed to vary between 10 mbar and 10 bar. The haze extinction coefficients and scattering albedos at 4.6-5.1 $\mu$m are calculated for all combinations of the particle size ($\Phi^2$), real refractive index ($n_r^2$) and imaginary refractive index ($n_i^2$) in the ranges 0.5-5 $\mu$m, 1-2 and 0-0.1 respectively. For all combinations of ($\Phi^2$, $n_r^2$, $n_i^2$), the retrievals at 4.6-5.1 $\mu$m are performed and the $\sigma_N$ parameter between the scaled haze profile $C^2(p)$ and the haze reference profile $C^1(p)$ is evaluated. The best fits to VIMS limb-darkening observations in the 5-$\mu$m window within the measurement errors are obtained for a deep ammonia cloud between 2.3 and 2.7 bar, in the scattering case.

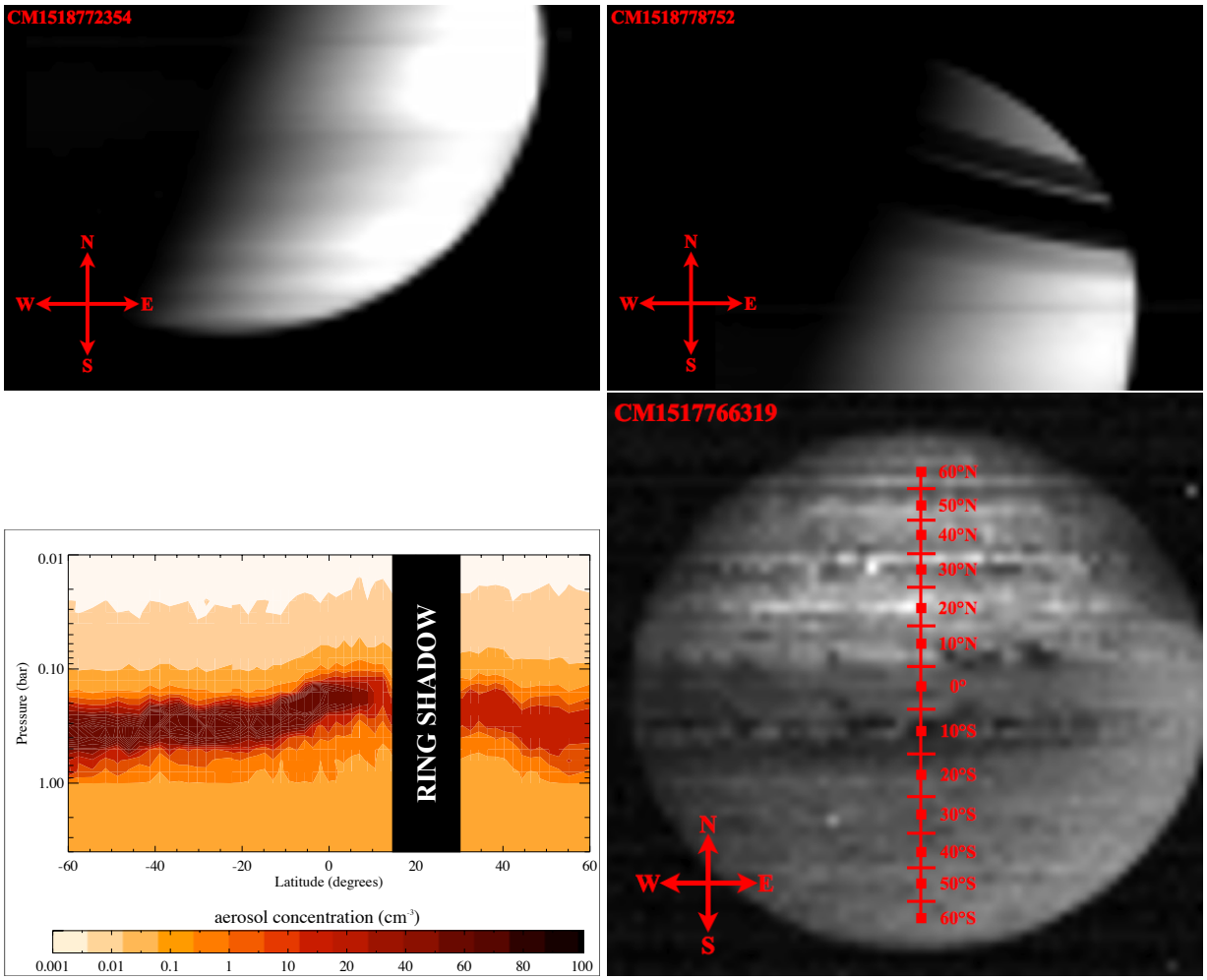



Figure 6.9: VIMS near-infrared cubes and haze distribution in February 2006 used in the update of the 5-$\mu$m analysis at all latitudes. The haze North-South distribution in February 2006 is presented in the bottom-left panel. The haze vertical distribution in the southern hemisphere is retrieved from VIMS near-infrared spectra at 0.8-3.5 $\mu$m in CM1518772354. The haze distribution in the northern atmosphere is retrieved from VIMS cube CM1518778752. VIMS images in the second reflection peak at 1.07 $\mu$m are shown in the top panels. The cube CM1518772354 and CM1518778752 were measured on 16 February 2006 at $08^h42^m47.471^s$ and on 16 February 2006 at $10^h29^m24.433^s$ respectively. The retrievals are performed for a particle size of 1 $\mu$m ($\Phi^1$) and a complex refractive index ($n_r^1$, $n_i^1$) of $1.4 + \mathrm{i}\times 10^{-7}$ at 0.8-3.5 $\mu$m. Low-emission angle spectra were extracted from the VIMS spectral cube CM1517766319 at nighttime. VIMS image at 5.05 $\mu$m in this cube is shown in the bottom-right. The spectral cube was acquired on 4 February 2006 at $17^h15^m38.888^s$. The spectra at lower emission angles are extracted at latitudes ranging from 60°S to 60°N with a step of 5°. The pixel positions of VIMS data extracted for the limb-darkening analysis are shown with the red squares and dashes.

| | LATITUDE | LONGITUDE | EMISSION ANGLE |
|---|---|---|---|
| 60°N | 60.53° ± 3.27° | 309.02° ± 5.65° | 61.09° ± 5.23° |
| | 62.08° ± 3.47° | 309.32° ± 5.42° | 79.11° ± 5.31° |
| 55°N | 55.12° ± 2.84° | 308.87° ± 4.54° | 49.23° ± 3.75° |
| | 54.23° ± 3.21° | 310.02° ± 5.12° | 78.23° ± 5.03° |
| 50°N | 50.12° ± 2.71° | 310.01° ± 4.33° | 45.45° ± 3.22° |
| | 49.51° ± 2.88° | 307.87° ± 4.87° | 77.11° ± 4.81° |
| 45°N | 46.02° ± 2.62° | 308.45° ± 4.10° | 39.23° ± 3.00° |
| | 45.23° ± 2.75° | 308.43° ± 4.45° | 75.23° ± 4.34° |
| 40°N | 41.02° ± 2.52° | 307.85° ± 3.23° | 31.92° ± 2.91° |
| | 40.74° ± 2.70° | 305.99° ± 3.65° | 71.32° ± 4.21° |
| 35°N | 35.67° ± 2.34° | 309.05° ± 3.19° | 29.56° ± 2.64° |
| | 35.12° ± 2.62° | 307.45° ± 3.51° | 69.34° ± 4.01° |
| 30°N | 29.65° ± 2.14° | 308.82° ± 3.17° | 28.93° ± 2.43° |
| | 30.11° ± 2.55° | 307.32° ± 3.54° | 67.43° ± 3.73° |
| 25°N | 24.67° ± 2.10° | 307.65° ± 2.67° | 25.34° ± 2.37° |
| | 25.21° ± 2.40° | 308.23° ± 2.99° | 66.23° ± 3.19° |
| 20°N | 20.45° ± 2.05° | 307.46° ± 2.29° | 23.23° ± 2.31° |
| | 20.53° ± 2.33° | 308.13° ± 2.56° | 65.34° ± 2.67° |
| 15°N | 15.00° ± 1.97° | 308.23° ± 2.13° | 21.55° ± 2.21° |
| | 15.21° ± 2.11° | 308.76° ± 2.33° | 64.12° ± 2.50° |
| 10°N | 10.04° ± 1.93° | 309.12° ± 2.03° | 20.12° ± 2.17° |
| | 10.10° ± 2.00° | 307.85° ± 2.17° | 63.21° ± 2.42° |
| 5°N | 5.05° ± 1.32° | 308.34° ± 2.00° | 18.53° ± 1.93° |
| | 5.12° ± 1.45° | 308.32° ± 2.09° | 62.74° ± 2.13° |
| 0° | 0.12° ± 1.21° | 308.43° ± 1.97° | 17.86° ± 1.78° |
| | 0.05° ± 1.34° | 307.34° ± 2.00° | 61.23° ± 1.89° |
| 5°S | -5.12° ± 1.27° | 309.00° ± 2.05° | 19.05° ± 1.87° |
| | -5.00° ± 1.38° | 308.72° ± 2.13° | 63.12° ± 2.22° |
| 10°S | -10.11° ± 1.93° | 309.12° ± 2.11° | 20.21° ± 2.05° |
| | -9.98° ± 2.03° | 308.45° ± 2.22° | 64.03° ± 2.50° |
| 15°S | -15.12° ± 2.02° | 308.76° ± 2.22° | 21.67° ± 2.17° |
| | -15.54° ± 2.20° | 307.67° ± 2.41° | 65.05° ± 2.73° |

| | LATITUDE | LONGITUDE | EMISSION ANGLE |
|---|---|---|---|
| 20°S | -20.87° ± 2.13° | 309.34° ± 2.41° | 23.56° ± 2.39° |
| | -20.17° ± 2.49° | 309.54° ± 2.61° | 65.98° ± 2.99° |
| 25°S | -25.11° ± 2.19° | 308.56° ± 2.84° | 24.96° ± 2.45° |
| | -25.25° ± 2.52° | 309.13° ± 3.00° | 66.50° ± 3.20° |
| 30°S | -30.12° ± 2.23° | 308.32° ± 2.95° | 27.07° ± 2.51° |
| | -29.94° ± 2.59° | 308.43° ± 3.33° | 67.34° ± 3.51° |
| 35°S | -35.27° ± 2.41° | 308.32° ± 3.23° | 28.85° ± 2.70° |
| | -35.05° ± 2.73° | 309.43° ± 3.73° | 70.03° ± 3.78° |
| 40°S | -40.65° ± 2.59° | 309.09° ± 3.41° | 30.65° ± 2.88° |
| | -40.06° ± 2.80° | 308.34° ± 3.88° | 71.75° ± 3.99° |
| 45°S | -45.12° ± 2.71° | 308.45° ± 3.76° | 35.45° ± 3.11° |
| | -45.54° ± 2.88° | 308.32° ± 4.13° | 74.34° ± 4.29° |
| 50°S | -50.23° ± 2.87° | 309.65° ± 4.12° | 42.45° ± 3.33° |
| | -50.49° ± 2.93° | 308.67° ± 4.85° | 75.39° ± 4.75° |
| 55°S | -55.21° ± 2.90° | 308.34° ± 4.59° | 48.34° ± 3.85° |
| | -56.04° ± 3.33° | 309.76° ± 5.06° | 77.54° ± 4.93° |
| 60°S | -60.41° ± 3.43° | 307.98° ± 4.99° | 60.12° ± 4.64° |
| | -62.71° ± 3.52° | 308.45° ± 5.32° | 78.45° ± 5.25° |

Table 6.2: Viewing geometries of VIMS data at various latitudes between 60°S and 60°N used for the update of the 5-$\mu$m analysis. The low and high emission angle spectra are extracted from VIMS spectral cubes CM1517766319 and CM1517833752 respectively.

As for the analysis at a latitude of 20°S in the previous sections, Saturn's limb-darkening spectra at 4.6-5.1 $\mu$m are only sensitive to the haze opacity and not to the vertical structure of the haze. As a result, for all values of the particle size ($\Phi^2$) and complex refractive index ($n_r^2$, $n_i^2$) at 4.6-5.1 $\mu$m, NEMESIS adjusts the haze concentrations in order to fit VIMS limb-darkening data within the measurement errors.

The $\sigma_N$ parameter can be estimated for each retrieval in order to the measure the correspondence between $C^1(p)$ and $C^2(p)$. In Fig. 6.10, $\sigma_N$ is plotted as a function of the haze properties assumed at 4.6-5.1 $\mu$m ($\Phi^2$, $n_r^2$, $n_i^2$) for seven latitudes: 60°N, 45°N, 0°, 15°S, 30°S, 45°S and 60°S. In the top-left panel, the complex refractive index ($n_r^2$, $n_i^2$) is fixed and the particle size ($\Phi^2$) at 4.6-5.1 $\mu$m varies between 500 nm and 5 $\mu$m. Minimum $\sigma_N$ values are observed at all latitudes for a particle

size ($\Phi^2$) of 1 $\mu$m, that is to say for $\Phi^2 = \Phi^1$. In the top-right panel, $\sigma_N$ is calculated as a function of the imaginary refractive index ($n_i^2$) at 4.6-5.1 $\mu$m for a fixed particle size ($\Phi^2$) and real refractive index ($n_r^2$). Lower $\sigma_N$ values are obtained for $n_i^2$ values higher than $n_i^1$. In the bottom-left panel, the variation of $\sigma_N$ with the real refractive index $n_r^2$ shows no specific trend. Similar results are obtained at other latitudes. For all combinations of the particle size ($\Phi^2$), real refractive index ($n_r^2$) and imaginary refractive index ($n_i^2$) at 4.6-5.1 $\mu$m, similar conclusions can be drawn. Optimum values of $\sigma_N$ are observed for a particle size ($\Phi^2$) of 1 $\mu$m and a complex refractive index ($n_i^2$) larger than $10^{-7}$, while no particular values of the real refractive index ($n_r^2$) stand out.

Note that the haze reference profiles were generated from VIMS near-infrared reflection spectra for a particle size ($\Phi^1$) of 1 $\mu$m and a complex refractive index ($n_r^1$, $n_i^1$) of $1.4 + \mathrm{i}\times 10^{-7}$ at 0.8-3.5 $\mu$m. A similar analysis was carried out at all latitudes for all combinations of the particle size ($\Phi^1$), real refractive index ($n_r^1$) and imaginary refractive index ($n_i^1$) in the ranges 0.5-5 $\mu$m, 1.1-1.8 and 0-0.001 respectively. For each set ($\Phi^1$, $n_r^1$, $n_i^1$), the haze density profile was retrieved with NEMESIS from VIMS near-infrared spectra at 0.8-3.5 $\mu$m, and used as a reference profile for the limb-darkening analysis at 4.6-5.1 $\mu$m. The retrievals were performed and the $\sigma_N$ parameter evaluated for all haze properties ($\Phi^2$, $n_r^2$, $n_i^2$) at 4.6-5.1 $\mu$m. Optimum values of $\sigma_N$ are obtained for a constant haze particle size and an increasing imaginary refractive index at 0.8-3.5 $\mu$m and 4.6-5.1 $\mu$m. In conclusion, the results on the haze properties obtained at 20°S can be generalised to all latitudes: If $\Phi^2 = \Phi^1$ and $n_i^2 > n_i^1$, the haze structure at 4.6-5.1 $\mu$m ($C^2(p)$) is consistent with the haze structure at 0.8-3.5 $\mu$m ($C^1(p)$) at all latitudes between 60°S and 60°N, except in the latitudinal range 15°N- 30°N where no signal is measured because of the ring shadows. The deep tropospheric cloud was assumed to be made of scattering ammonia ice. The ammonia cloud model matches VIMS 5-$\mu$m limb-darkening observations for a cloud base pressure between 2.3 and 2.7 bar.

The same analysis as above was also carried out for the three other cloud models described in section 6.31 consisting of an ammonium hydrosulphide cloud, a grey cloud and a cloud with a constant complex refractive index. For all haze properties at 0.8-3.5 $\mu$m ($\Phi^1$, $n_r^1$, $n_i^1$) and 4.6-5.1 $\mu$m ($\Phi^2$, $n_r^2$, $n_i^2$), the minimum $\sigma_N$ values are evaluated for each cloud composition and latitude except between 15°N and 30°N. The results are shown in Fig. 6.11. For an ammonia and ammonium hydrosulphide clouds, minimum $\sigma_N$ values are approximately equal to 0.07 and 0.33 respectively, below the upper boundary values in the range 1-3. Therefore, the haze vertical profiles retrieved

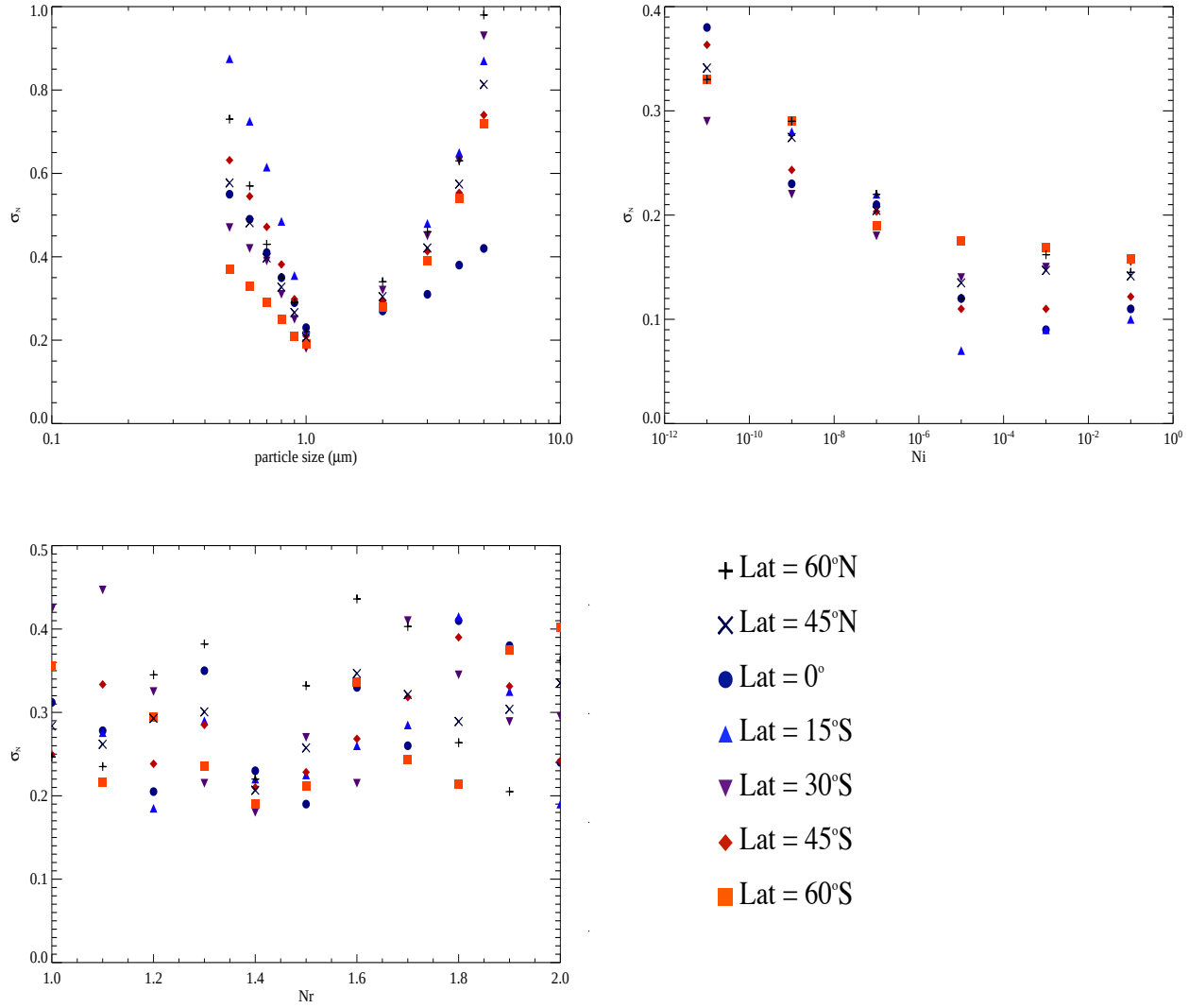



Figure 6.10: $\sigma_N$ tests (see section 6.1) at multiple latitudes. The haze vertical profiles retrieved at each latitude from VIMS near infrared spectra at 0.8-3.5 $\mu$m are used as a reference profile for the limb-darkening analysis at 4.6-5.1 $\mu$m. At 0.8-3.5 $\mu$m, a particle size of 1 $\mu$m ($\Phi^1$) and a complex refractive index ($n_r^1$, $n_i^1$) of $1.4 + \mathrm{i}\times10^{-7}$ are assumed for the haze optical and physical properties. The deep tropospheric cloud is assumed to be made of scattering ammonia ice with a cloud particle size of 1 $\mu$m and a variable base pressure between 0.01 and 10 bar. The cloud opacity, scale factor of the haze profile and deep volume mixing ratios of phosphine and ammonia are retrieved from VIMS 4.6-5.1 $\mu$m limb-darkening data at each latitude. The haze extinction coefficient and scattering albedos at 4.6-5.1 $\mu$m are calculated for all combinations of the particle size ($\Phi^2$) and complex refractive index ($n_r^2$, $n_i^2$). The retrievals are performed and the coefficient $\sigma_N$ is evaluated for each set of particle size ($\Phi^2$) and complex refractive index ($n_r^2$, $n_i^2$). In the top-left panel, the complex refractive index ($n_r^2$, $n_i^2$) at 4.6-5.1 $\mu$m is fixed to $1.4 + \mathrm{i}\times10^{-7}$ and the particle size ($\Phi^2$) is allowed to vary between 500 nm and 5 $\mu$m. In the top-right panel, the particle size ($\Phi^2$) and real refractive index ($n_r^2$) at 4.6-5.1 $\mu$m are fixed to 1 $\mu$m and 1.4 respectively, while the imaginary refractive index ($n_i^2$) varies in the range 0-0.1. In the bottom-left panel, the particle size ($\Phi^2$) and imaginary refractive index ($n_i^2$) at 4.6-5.1 $\mu$m are fixed to 1 $\mu$m and $10^{-7}$ respectively, and the real refractive index ($n_r^2$) varies from 1 to 2. The results are shown at seven latitudes: 60°N, 45°N, 0°, 15°S, 30°S, 45°S and 60°S.

at 0.8-3.5 $\mu$m ($C^1(p)$) and updated 4.6-5.1 $\mu$m ($C^2(p)$) are consistent with each other for these two cloud compositions at all latitudes. The ammonium hydrosulphide cloud is retrieved slightly deeper than the ammonia cloud between 3.2 and 3.5 bar at all latitudes. Also minimum $\sigma_N$ values for the ammonium hydrosulphide cloud correspond to a tropospheric haze with a uniform particle size ($\Phi^2 = \Phi^1$) and increasing imaginary refractive index at 0.8-3.5 $\mu$m and 4.6-5.1 $\mu$m ($n_i^2 > n_i^1$).

However, the grey cloud model is associated with larger $\sigma_N$ values above 3, and so this model can only fit VIMS limb-darkening data in the 5-$\mu$m window for unrealistic variations of the haze concentrations. The cloud model consisting of a constant refractive index is also considered here. The real and imaginary refractive indices are allowed to vary simultaneously between 1 and 2, and between 0 and 0.1 respectively. The minimum $\sigma_N$ values as a function of the cloud refractive index are presented in Fig. 6.11 at five latitudes: 60°N, 35°N, 0°, 35°S and 60°S. $\sigma_N$ values are observed in the range 2-10 and so are of the same order or larger than the upper boundary values. Similar results are also obtained at other latitudes. As a result, the cloud model with constant refractive index leads to inconsistent haze profiles between 0.8-3.5 $\mu$m and 4.6-5.1 $\mu$m.

The generalisation of the $\sigma_N$ tests (see section 6.1) at all latitudes has shown that the haze vertical profiles at 0.8-3.5 $\mu$m and 4.6-5.1 $\mu$m are consistent with each other for a deep tropospheric cloud made of either scattering ammonia ice or ammonium hydrosulphide particles. The update of the haze distribution from the analysis of Saturn's near-infrared reflection spectra has shown that simpler cloud models lead to unrealistic variations of the haze concentrations, larger than the seasonal variations. For both the ammonia and ammonium hydrosulphide clouds, lower $\sigma_N$ values are observed for the same particle size across the two wavelenth ranges, and an increasing value of the imaginary refractive index between 0.8-3.5 $\mu$m and 4.6-5.1 $\mu$m.

Saturn's spectra at 4.6-5.1 $\mu$m are only sensitive to the haze opacity which is a function of the aerosol concentration, extinction cross-section and optical path. Therefore, the retrieved values of the cloud and haze opacities, and deep abundances of phosphine and ammonia are similar within the retrieval errors for all assumptions of the haze optical and physical properties, that is to say for all combinations of $\Phi^1$, $n_r^1$, $n_i^1$, $\Phi^2$, $n_r^2$ and $n_i^2$. However, the retrieved parameters depend on the cloud composition and the cloud particle size as it can be seen in Fig. 6.8. In the next section the cloud and haze opacities, as well as the deep volume mixing ratios of phosphine and ammonia are retrieved at all latitudes for an ammonia and ammonium hydrosulphide clouds in the scattering case.

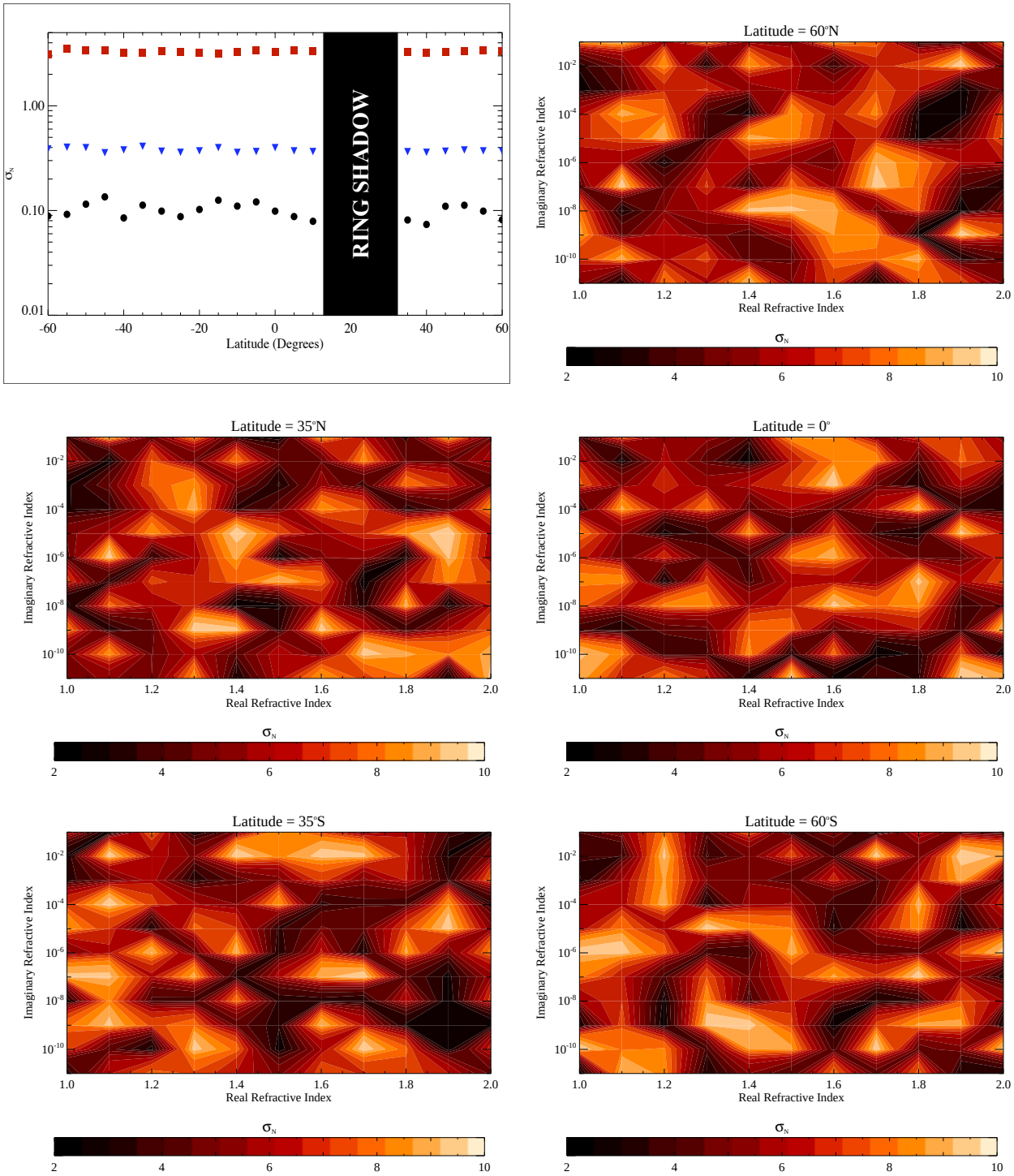



Figure 6.11: Minimum $\sigma_N$ values for various cloud compositions and latitudes. In the top-left panel, the minimum $\sigma_N$ values are plotted for an ammonia cloud (black circle), ammonium hydrosulphide cloud (blue triangle) and grey cloud (red square). The minimum $\sigma_N$ values are also shown in the other panels for a cloud with a constant complex refractive index at 4.6-5.1 $\mu$m at 60°N, 35°N, 0°, 35°S and 60°S. All combinations of the cloud real refractive index in the range 1-2 and imaginary refractive index in the range 0-0.1 are tested at different latitudes, except where the ring shadows are visible. Only the ammonia and ammonium hydrosulphide clouds have $\sigma_N$ values lower than the upper boundary values in the range 1-3.

### 6.4.2 Retrievals at all latitudes for an ammonia and ammonium hydrosulphide cloud

In this section, VIMS limb-darkening spectra at 60°S-60°N are analysed using scattering ammonia and ammonium hydrosulphide clouds after updating the haze reference profiles with the results obtained at 0.8-3.5 $\mu$m. The haze reference profiles at each latitude, except those between 15°N and 30°N, are retrieved from the 0.8-3.5 $\mu$m spectra in the CM1519321223 cube described in section 6.2. The haze particle size ($\Phi^1$), real refractive index ($n_r^1$) and imaginary refractive index ($n_i^1$) are assumed to be equal to 1 $\mu$m, 1.4 and $10^{-7}$ respectively. The extinction cross-sections and scattering albedos in the 4.6-5.1 $\mu$m wavelength range are calculated for $\Phi^2 = \Phi^1$, $n_r^2 = n_r^1$ and $n_i^2 = 10^{-1}$. The scaling factor $f$ of the haze density profile, the cloud opacity and deep volume mixing ratios of phosphine and ammonia are retrieved from the 5-$\mu$m limb-darkening data. The cloud base pressure and cloud particle size are allowed to vary between 10 mbar and 10 bar, and between 100 nm and 10 $\mu$m respectively. The best fits to the observations are obtained for a cloud particle size of around one micrometre. The results for an ammonia and ammonium hydrosulphide cloud are presented in Fig. 6.12 for a cloud particle size of 1 $\mu$m.

The $\chi^2/N_\lambda$ values observed at all latitudes are below the 5-0 threshold value and the modelled spectra manage to fit the observations quite well within the measurement errors. The $\chi^2/N_\lambda$ values are slightly smaller for an ammonia cloud especially at lower latitudes and in the northern hemisphere. The best fits to VIMS data are obtained for an ammonia cloud between 2.3 and 2.7 bar. The ammonium hydrosulphide cloud is retrieved to lie slightly deeper between 3.2 and 3.5 bar. The ammonia volume mixing ratio is enhanced in the equatorial region between $-10^\circ$ and $+10^\circ$ and is uniform at higher latitudes in the southern and northern hemispheres of the planet. This is observed for both an ammonia cloud and an ammonium hydrosulphide cloud. The ammonia volume mixing ratios for an ammonia cloud are obtained mostly in the range 200-300 ppm at higher latitudes and reach a maximum value of about 550 ppm at the equator. Therefore the ammonia abundances at higher latitudes are consistent with the upper tropospheric abundances from previous studies (see Table 4.3). Ammonia abundances at the equator are also similar to the (480 $\pm$ 100) ppm abundance at 25 bar estimated by Briggs and Sackett (1989). The ammonia volume mixing ratios retrieved for an ammonium hydrosulphide cloud are larger than for an ammonia cloud. Ammonia abundances

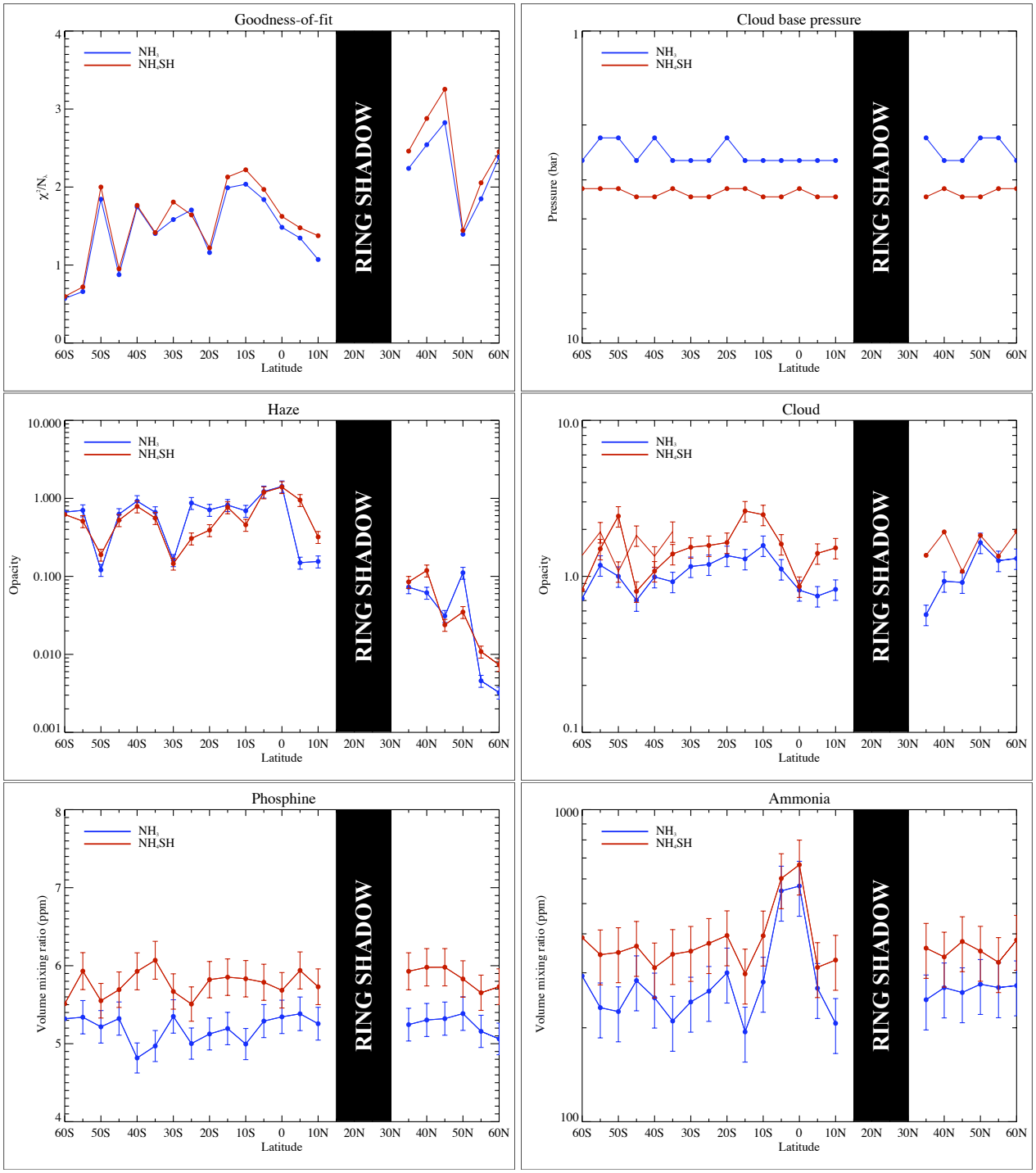



Figure 6.12: Limb-darkening analysis of Saturn's 5-$\mu$m window at latitudes in the range 60°S-60°N for a scattering ammonia (blue line) and ammonium hydrosulphide (red line) clouds. The 5-$\mu$m spectra are extracted from the VIMS spectral cubes CM1517766319 and CM1517833752 acquired respectively on 4 February 2006 at $17^h15^m38.888^s$ and on 5 February 2006 at $11^h59^m31.458^s$. The goodness-of-fit (*top-left panel*), haze (*middle-left panel*) and cloud (*middle-right panel*) opacities at 5 $\mu$m, and volume mixing ratios of phosphine (*bottom-left panel*) and ammonia (*bottom-right panel*) are shown for the best-fitting cloud base pressure (*top-right panel*) at all latitudes and for a cloud particle size of 1 $\mu$m.

are obtained in the range 300-400 ppm at higher latitudes, and have a maximum value of about 640 ppm for an ammonium hydrosulphide cloud. The ammonia abundances for an ammonium hydrosulphide are then larger than the estimations from previous studies. This is consistent with Chapter 4 which has shown that the retrievals at 5 $\mu$m depend on the cloud model. As a result, an ammonia and ammonium hydrosulphide clouds lead to different values of the retrieved parameters. However, the enhancement at the equator and the north-south symmetry at higher latitudes are observed for both cloud compositions. The enhancement of ammonia coincides with the diffuse region seen in Fig. 6.9. Fletcher *et al.* (2011) suggested that the advection of ammonia-rich air at the equator from depths below the ammonia cloud into the upper troposphere was responsible for the enhacement of gaseous ammonia. At higher latitudes, the ammonia abundances would be depleted due to the condensation of ammonia. Such a scenario is thus consistent with a tropospheric cloud made of ammonia ice.

The deep volume mixing ratio of phosphine is symmetrically distributed between the southern and northern hemispheres. The phosphine abundances are obtained in the range 4.7-5.4 ppm for an ammonia cloud, and in the range 5.5-6.1 for an ammonium hydrosulphide cloud. As for the ammonia abundances, the phosphine abundances depend on the cloud composition and have larger values for an ammonium hydrosulphide cloud. However, the phosphine volume mixing ratios retrieved here are consistent with the 4.5-7.5 ppm deep tropospheric abundances estimated by Noll and Larson (1990), Orton *et al.* (2000) and Burgdorf *et al.* (2004). The vertical mixing processes of disequilibrium species such as phosphine are not expected to vary with season, which is consistent with the phosphine distribution retrieved here. North-south variations are also not present in the cloud opacities suggesting that the cloud formation is not seasonally variable. Local minima of the cloud opacity are due to cloud clearing processes and coincide with the white bands seen in VIMS 5-$\mu$m images. However, the haze opacity decreases significantly in the northern hemisphere due to lower haze concentrations in the winter northern hemisphere. This is consistent with the larger haze concentrations observed in the summer southern hemisphere from the analysis of 0.8-3.5 $\mu$m spectra in chapter 5.

Note that the analysis above was carried out for specific values of the haze particle size and complex refractive index: $\Phi^2 = \Phi^1 = 1$ $\mu$m, $n_r^2 = n_r^1 = 1.4$, $n_i^2 = 10^{-7}$ and $n_i^2 = 10^{-1}$. The particle size is then uniform across the 0.8-3.5 $\mu$m and 4.6-5.1 $\mu$m wavelength ranges and the imaginary refractive index increases with wavelength. Therefore, this parametrisation of the tropospheric haze leads to scaled haze profiles $C^2(p)$ at 4.6-5.1 $\mu$m consistent with the reference haze profiles $C^1(p)$

retrieved from the 0.8-3.5 $\mu$m spectra. If the same analysis is undertaken for all possible combinations of ($\Phi^1$, $n_r^1$, $n_i^1$, $\Phi^2$, $n_r^2$, $n_i^2$), the retrieved values of the cloud and haze opacities, and phosphine and ammonia abundances are similar within the retrieval errors for both the ammonia cloud and ammonium hydrosulphide cloud. Indeed, Saturn's 5-$\mu$m window is only sensitive to the haze opacity and but not the optical and physical parameters of the haze. Therefore, NEMESIS scales the haze reference profile so as to obtain similar haze opacities as the opacities shown in the middle-left panel in Fig. 6.12. However, the haze concentrations $C^1(p)$ and $C^2(p)$ are consistent with each other only for a constant haze particle size ($\Phi^2 = \Phi^1$) and increasing value of the imaginary refractive index ($n_i^2 > n_i^1$).

Minimum $\chi^2/N_\lambda$ values are obtained for a cloud particle size around of one micrometre for both an ammonia and ammonium hydrosulphide clouds. As it can be seen in Fig. 6.8, the retrieved parameters of the haze opacity, and deep volume mixing ratios of phosphine and ammonia are similar within the retrieval errors for all cloud particle size. However, the cloud opacity varies with the cloud particle size. The results obtained in Fig. 6.8 at a latitude of 20°S can be generalised at all latitudes. The cloud opacity increases with the cloud particle size for an ammonia cloud, while it decreases for an ammonium hydrosulphide cloud. However, the variation of cloud opacity with latitude shown in the middle-right panel in Fig. 6.12 is similar for all cloud particle sizes. North-south variations of the cloud opacity are not observed and minimum cloud opacities coincide with the bright spots seen in VIMS 5-$\mu$m images. The ranges of retrieved parameters at 5 $\mu$m comprising all the cloud particle sizes between 500 nm and 5 $\mu$m are shown in Table 6.3 for an ammonia cloud and an ammonium hydrosulphide cloud. The deep volume mixing ratios of phosphine and ammonia are compared with estimations from previous studies. The cloud pressure base and opacity depend on the cloud model assumption and so the retrieved parameters vary for an ammonia cloud and an ammonium hydrosulphide cloud. This is also observed for the retrieved values of phosphine and ammonia abundances. However, the ranges of values obtained for the mixing ratios are expected to be consistent with the previous estimations. This is clearly the case for the phosphine abundances: volume mixing ratios are within the 4.5-7.5 range for both an ammonia cloud and ammonium hydrosulphide cloud. However, the ammonia volume mixing ratios at higher latitudes and at the equator only match the previous estimations for an ammonia cloud. Also, minimum $\sigma_N$ values are reported in Table 6.3 for the two cloud compositions. Lower $\sigma_N$ values are obtained for an ammonia cloud.

| | $NH_3$ cloud | | $NH_4SH$ cloud | |
|---|---|---|---|---|
| | Merlet | Previous studies | Merlet | Previous studies |
| Min($\sigma_N$) | 0.06-0.15 | | 0.33-0.44 | |
| $\chi^2/N_\lambda$ | 0.59-2.80 | | 0.61-3.27 | |
| Cloud base pressure (bar) | 2.3-2.7 | | 3.2-3.5 | |
| Haze opacity | 0.0032-1.31 | | 0.0065-1.32 | |
| Cloud opacity | 0.57-1.73 | | 0.83-2.43 | |
| Phosphine (ppm) | 4.7-5.4 | 4.5-7.5 | 5.5-6.1 | 4.5-7.5 |
| HL Ammonia (ppm) | 200-300 | 70-300 | 300-400 | 70-300 |
| E Ammonia (ppm) | 550 | 380-580 | 640 | 380-580 |

Table 6.3: Retrieved parameters at 4.6-5.1 $\mu$m for an ammonia cloud and an ammonium hydrosulphide cloud. The haze and cloud opacities at 5 $\mu$m, and the volume mixing ratios of phosphine and ammonia in parts-per-million are shown with their retrieval errors for both cloud models. The values of the ammonia volume mixing ratio at higher latitudes (HL) and at the equator (E) are both presented here. The ranges of values for the retrieved parameters comprise all the cloud particle sizes between 500 nm and 5 $\mu$m. The retrieved phosphine and ammonia abundances are compared with estimations from previous studies.

In conclusion, both the ammonia and ammonium hydrosulphide clouds are associated with $\sigma_N$ values below the 1-3 upper boundary values. Lower $\sigma_N$ values are obtained for an ammonia cloud. Thus, the haze concentrations obtained at 0.8-3.5 $\mu$m ($C^1(p)$) and at 4.6-5.1 $\mu$m ($C^2(p)$) are more consistent with each other for a tropospheric cloud made of scattering ammonia ice. In addition, lower $\chi^2/N_\lambda$ are observed for an ammonia cloud and so the modelled spectra match the limb-darkening observations more closely than for this cloud composition. The ammonia cloud is retrieved to be between the 2.3- and 2.7-bar pressure levels at all latitudes. The phosphine and ammonia abundances for an ammonia cloud are also in good agreement with previous estimations of these parameters. Finally, a north-south variation of the tropospheric haze is observed at 5 $\mu$m, which is consistent with the results in chapter 5.

## 6.5 Summary

Chapter 6 analyses the consistency of the haze vertical profiles at 0.8-3.5 $\mu$m and 4.6-5.1 $\mu$m for various haze and cloud models. Constraints on the haze vertical structure and on the optical and physical properties of the haze have been obtained in chapter 5 from the analysis of VIMS reflection spectra at 0.8-3.5 $\mu$m. VIMS-limb darkening observations at 4.6-5.1 $\mu$m are sensitive to the haze opacity. However, these data cannot be analysed independently in order to retrieve the haze properties. Instead the haze concentrations obtained in each wavelength range are compared so that the haze and cloud properties can simultaneously constrained.

The haze vertical profiles retrieved at 0.8-3.5 $\mu$m are used as reference profilesfor the 5-$\mu$m limb-darkening analysis. A scale factor of the reference haze profile is retrieved at 4.6-5.1 $\mu$m. In addition, the cloud opacity, as well as the deep volume mixing ratios of phosphine and ammonia are also retrieved from VIMS limb-darkening data.

The scaled haze profile is expected to vary little from the reference profile, or at least less than the seasonal variations of haze concentrations. The difference between the two haze profiles is characterised by the $\sigma_N$ parameter. Upper boundary values of this parameter can be estimated by measuring the variation of haze concentrations between consecutive years. Upper boundary values are found in the range 1-3 at all latitudes and comprise all combinations of the haze properties. Therefore, in this chapter the haze and cloud properties with $\sigma_N$ values below the 1-3 range are investigated.

The haze properties at 0.8-3.5 $\mu$m are parameterised by the haze particle size and complex refractive index. The haze extinction cross-section and scattering albedo must be evaluated at 4.6-5.1 $\mu$m. Therefore, assumptions on the haze particle size and complex refractive index must be made at 4.6-5.1 $\mu$m. The first part of chapter 6 focuses on VIMS reflection and limb-darkening data at a latitude of 20°S and a tropospheric cloud made of ammonia ice. Lower $\sigma_N$ values are obtained for a constant particle size and an increasing imaginary index. However, the variations of the real refarctive index between the two wavelength ranges are not constrained. The haze particle size is indeed not expected to vary with wavelength for consistent haze models. Because Saturn's 5-$\mu$m is only sensitive to the haze opacity, NEMESIS adjusts the reference profile in order to obain similar opacities for all combinations of the haze properties. As a result, the retrieved values of the cloud opacity, and deep abundances of phosphine and ammonia are also similar for all particle sizes and

complex refractive indices of the haze.

Different cloud composition are tested in this chapter, including an ammonium hydrosulphide cloud, a grey cloud, and a cloud model with constant refractive index. Only the ammonia and ammonium hydrosulphide cloud are associated with $\sigma_N$ values below the 1-3 upper boundary values. Thus, the $\sigma_N$ tests have ruled out the two other cloud models and have confirmed the ammonia and ammonium hydrosulphide clouds as likely candidates for the deep tropospheric cloud. Note that in the Mie scattering frame, only spherical shapes are assumed in the model (see chapter 3 section 3), although thermochemical models suggest that the deep troposphoric clouds could be made of ammonia ices. The next step would be to integrate a scattering model for icy particles in the radiative transfer algorithm and run a series of sigma tests based on this assumption.

The results at 20°S can be generalised at all latitudes where similar constraints on the haze properties and cloud composition are obtained. The haze concentrations at 0.8-3.5 $\mu$m and 4.6-5.1 $\mu$m are again more consistent with an ammonia cloud and ammonium hydrosulphide cloud. The haze particle size must be uniform across the two wavelength ranges and the imaginary refractive index increases with wavelength. The retrieved parameters at 4.6-5.1 $\mu$m depend on the cloud compositions. The ammonia abundances retrieved for an ammonia cloud are more consistent with previous students, also $\sigma_N$ are slightly lower for this cloud composition. This is observed at all latitudes. The consistency of the haze concentrations at short and long near-infrared wavelengths and the retrieved ammonia abundances lead toward the conclusion that the main 5-$\mu$m absorbing cloud in Saturn's atmosphere is most probably composed of ammonia ice, lying at pressure levels between 2.3 and 2.7 bar.

Chapter 7

# Conclusions and future work

## 7.1 Thesis results

This thesis investigates the haze and cloud properties in the upper troposphere and lower stratosphere of Saturn from Cassini/VIMS near-infrared data. Clouds are expected to condense from thermochemical equilibrium theories in the upper troposphere of the planet, while photochemical and microphysical models predict the formation of hazes above the cloud layers. In particular, thermochemical equilibrium models lead toward an ammonia cloud at 2 bar and an ammonium hydrosulphide cloud at 6 bar.

There are numerous haze candidates including hydrocarbons and phosphorus-bearing molecules. However, none of these species have been spectrally detected so far in the troposphere and so indirect methods must be used in order to constrain the cloud and haze compositions. In particular, this work focuses on the interaction between infrared radiation and aerosol particles so as to draw conclusions on the cloud properties.

The infrared channel of the VIMS instrument covering the spectral range 0.85-5.1 $\mu$m sounds pressure levels where the clouds and hazes are likely to form. The Cassini mission has investigated the Saturnian system since 2004 and so VIMS spectra are available for various observation times, latitudes, longitudes and viewing geometries. The atmospheric properties are derived from VIMS spectra by using the numerical model NEMESIS, which comprises a radiative transfer algorithm and a retrieval algorithm. The radiative transfer algorithm RADTRANS computes the modelled spectrum for a reference atmosphere. The retrieval agorithm adjusts the reference atmosphere so as to minimise

the discrepancies between the modelled and VIMS spectra.

Most of the published works on VIMS have focused on retrieving atmospheric properties for single spectra in the visible and infrared. In this thesis, we show that the use of multiple spectra can further enhance our knowledge of Saturn's atmosphere. Besides, new methodologies are also developed in order to combine these results and obtain a model of the planet's troposphere and lower stratosphere consistent at 0.8-3.2 $\mu$m and at 4.6-5.1 $\mu$m.

### 7.1.1 5-$\mu$m limb-darkening analysis

Saturn's thermal emission spectra at 4.6-5.1 $\mu$m measured with VIMS were analysed in order to retrieved the cloud properties and deep abundances of phosphine and ammonia in the upper troposphere. Only nightside spectra are considered in this thesis so that the effects of sunlight reflection by tropospheric aerosols can be ignored. The tropospheric cloud and gases absorb and scatter the thermal infrared radiation emitted from deeper tropospheric levels. The contribution weighting functions have shown than Saturn's 5-$\mu$m window is sensitive to opacity sources located between the 1-bar and 5-bar pressure levels. Among the gaseous absorbers, phosphine contributes the most to the extinction of thermal radiation, with a minor contribution from ammonia.

Single spectra acquired for a specific viewing geometry were first analysed for three cloud compositions: an ammonia cloud, an ammonium hydrosulphide cloud and a grey cloud in the scattering and non-scattering cases. The cloud was modelled as either a compact cloud at variable pressure level or an extended cloud with variable pressure level and vertical extension. The cloud particle radius was also allowed to vary between 100 nm and 10 $\mu$m. The cloud opacity and the volume mixing ratios of phosphine and ammonia were retrieved for all cloud models. Most of the cloud models provided a good fit to the observations within the measurement errors for both scattering and non-scattering conditions.

The results obtained from single VIMS spectra are consistent with recent publications (see Fletcher *et al.*). However, the analysis of single spectra did not manage to rule out many of the cloud models tested in the retrieval algorithm. In particular, although the best fits to the thermal emission spectra are obtained for a two-aeroso-layers model, the one-cloud model cloud not be excluded. Finally, the model was in good agreement with the observations for both scattering and non-scattering conditions.

Therefore, the limb-darkening analysis was carried out instead in this thesis.

Also, the cloud particle size and base pressure are both poorly constrained especially in the non-scattering case. The retrieved values of the cloud opacity and gas abundances depend on the assumptions made on the cloud model and the inclusion of scattering in the reference atmosphere. Therefore, nightside limb-darkening spectra at 5 $\mu$m were considered instead of single spectra in order to constrain the cloud properties.

The limb-darkening data consist of one spectrum measured at low emission angle, and one other spectrum measured at the same latitude and longitude, but at higher emission angle. As the planet rotates around its own axis, the VIMS instrument takes measurements from the same area of the planet, but at different viewing geometries. Consecutive VIMS data are selected in order to minimise the gap between the two observation times. As a result, the same cloud structure can be observed at low and high emission angles. If the high emission angle is large enough, approximately above 60°, the two spectra can be seen as independent measurements of the same physical quantity and so can be analysed simultaneously. By increasing the number of measurements, further constraints on the cloud properties can then be obtained.

The cloud opacity and gas abundances were retrieved simultaneously from the low and high emission angle spectra, for both scattering and non-scattering conditions. None of the compact cloud models consisting of only one cloud layer managed to fit the limb-darkening data. The extended cloud model in the scattering case could fit the limb-darkening observations, but only for a cloud extension over 25 kilometres. Such a large extension is in contradiction with the cloud vertical structure expected from thermochemical equilibrium models. However, this suggests that another opacity source above the cloud is necessary in order to fit VIMS spectra at low and high emission angles. This assumption was tested by considering an aerosol model consisting of one deep tropospheric cloud and one grey aerosol layer at higher altitude. Both the cloud and haze layers have variable pressure bases.

The fit to the limb-darkening observations greatly improved if a scattering haze layer located above the 500-mbar level was included in the atmospheric model. However, the optical and physical properties, and vertical distribution of the haze are not constrained at 5 $\mu$m. This result was confirmed by retrieving a continuous aerosol profile: two scattering sources are retrieved, one in the upper troposphere corresponding to the condensing cloud and one at higher altitude corresponding to the

haze layer. Similar conclusions are drawn at all latitudes in the northern and southern hemispheres of the planet. Saturn's 5-$\mu$m window is sensitive to the haze opacity, but not the vertical distribution, as well as the optical and physical properties of the haze. Therefore, Saturn's spectra at shorter wavelengths are analysed in order to constrain the haze properties.

This is the first limb-darkening analysis of VIMS thermal emission spectra on Saturn. However, Roos-Serote and Irwin (2006) analysed limb-darkening data of Jupiter and could only fit the data in scattering conditions.

### 7.1.2 Saturn's haze properties

Saturn's near-infrared reflection spectra in the 0.8-3.5 $\mu$m wavelength range were also analysed in order to study the haze structure in the upper troposphere and lower stratosphere of the planet. These dayside spectra are characterised by six peaks formed by the reflection of sunlight radiation by the haze. The low radiances between the peaks correspond mainly to the absorption of methane. Saturn's reflection spectra are sensitive to opacity sources located above the 1-bar pressure level.

The tropospheric and stratospheric hazes are parameterised by the aerosol particle size and complex refractive index. The analysis of each reflection peak does not constrain the haze physical and optical properties. Thus, the full 0.8-3.5 $\mu$m spectrum is retrieved instead assuming a constant refractive index at all wavelengths. The analysis was first carried out at a latitude of 20°S. The best-fitting parameters of the haze particle size, real refractive index, and imaginary refractive index are obtained in the ranges 0.5-5 $\mu$m, 1.1-1.8, and 0-0.001 respectively. The haze properties retrieved for various viewing geometries are similar assuming that the solar angle is below 85°. The haze optical and physical properties vary very little with latitudes and similar ranges of the particle size and complex refractive index are obtained in the northern and southern hemispheres of the planet.

The haze vertical structure is characterised by a peak of concentration below the tropopause at around 200 mbar. The concentration drops above that level in a stratospheric region referred to as the opacity-clearing region. The validity of the opacity-clearing region was assessed by considering a "block model" with variable bottom and top pressure levels. Such a model is also consistent with a low opacity region right above the tropopause. Below the concentration peak, the concentration decreases until it relaxes to the *a priori* profile. The shape of the vertical profile is very similar for

all best-fitting values of the haze particle size and complex refractive index.

The seasonal changes in the haze distribution are investigated by analysing VIMS spectra measured between 2004 and 2012. The haze vertical shape does not vary with time. However, changes in the haze concentrations are observed. In particular, the haze densities are larger in the summer southern hemisphere of the planet in 2004-2007 before Saturn's equinox in 2007. On the other hand, the northern hemisphere response to solar insolation in 2007-2012 is less efficient, which is very likely due to the north-south variations of photochemical parent abundances.

The haze vertical structure is compared with a thermal structure referred to as the "temperature knee" seen in Cassini/CIRS observations (Fletcher *et al.*, 2007). Such a feature is characterised by a local increase of temperature below the tropopause. A few assumptions have been made on the mechanism responsible for the formation of the knee. In particular, the absorption of visible sunlight by the haze might trigger the local heating of the upper troposphere and the subsequent formation of the knee. The temperature profiles at all latitudes are retrieved from Cassini/CIRS mid- and far-infrared spectra. The knee is present at mid-latitudes in the southern hemisphere and is generally absent at the equator and in the northern hemisphere. The haze concentrations drop in the northern hemisphere, however the concentration peak is retrieved at the equator. In addition, the temperature knee is found slightly higher up in the atmosphere than the haze concentration peak. Although there are correlations between the thermal and haze density profiles, a solar heating model will need to be developed in order to explain the differences between the two profiles.

The haze properies derived from the analysis of Saturn's reflection spectra are compared with laboratory measurements of the complex refractive index and photochemical models. The aim is to search for haze particle candidates that are in better agreement with both the VIMS analysis and theoretical models. The comparison with experimental values of the complex refractive index has excluded hydrazine and ammonium hydrosulphide as potential haze candidates. However, most theoretical models predict the formation of hazes made of hydrocarbons or photochemical products of phosphine.

The measurements for these species are however missing and so direct comparison with the VIMS-derived values could not be made. The haze vertical structure was compared with a photochemical model including most haze candidates present in Saturn's atmosphere. The comparison has shown that phosphorus-bearing species, such as $P_2H_2$ and $P_2H_4$, are the best haze candidates,

although photochemical products of methane could not be definitely excluded. Indeed, the methane concentration is large enough to reproduce the haze concentrations obtained in this thesis. However, the vertical shape of the haze and especially the concentration peak below the tropopause are more consistent with a haze made from the photodissociation of phosphine.

The photochemical model should be combined with a microphysical model in order to fully understand the haze vertical profile retrieved from VIMS near-infrared reflection spectra. Friedson *et al.* (2010) developed a microphysical model for Jupiter, although similar reactions are expected on Saturn as well. In particular, such a model would be very helpful in order to validate the concentration peak below the tropopause.

### 7.1.3 Saturn's haze and cloud model consistent with the reflection and 5-$\mu$m VIMS data

The consistency of the reflected sunlight and 5-$\mu$m analysis is finally assessed in the last part of this thesis, leading to further constraints on the cloud and haze properties. The haze density profiles retrieved at 0.8-3.5 $\mu$m are used as reference profiles in the 5-$\mu$m limb-darkening analysis. The scale factor of the reference haze profile, cloud opacity, and deep volume mixing ratios of phosphine and ammonia are then retrieved from VIMS 5-$\mu$m data. The haze reference profiles derived from the analysis of reflection spectra and the scaled haze profiles at 5-$\mu$m are expected to vary very little, or at least less than the seasonal variations. The differences between the two profiles are estimated by the $\sigma_N$ parameter. In particular, the $\sigma_N$ values should be less than the 1-3 upper boundary values characterising the seasonal variations.

At first, a scattering ammonia cloud is considered as the cloud model. $\sigma_N$ tests are undertaken for all combinations of the haze particle size and complex refractive index assumed at 0.8-3.5 $\mu$m and 4.6-5.1 $\mu$m. These tests have demonstrated that the haze particle size must be constant as expected, and that the imaginary refractive index increases with wavelength. Different cloud compositions are also tested, including an ammonium hydrosulphide cloud, a grey cloud and a cloud with constant complex refractive index. Only the ammonia and ammonium hydrosulphide clouds in the scattering case are associated with $\sigma_N$ values below the 1-3 range, with the lowest $\sigma_N$ values observed for the ammonia cloud. Lower $\sigma_N$ values are also observed for a constant particle size and increasing

imaginary refractive index for an ammonium hydrosulphide cloud. However, the $\sigma_N$ tests ruled out the two other cloud models since they both lead to unrealistically large $\sigma_N$ values.

The $\sigma_N$ tests were undertaken at all latitudes for a ammonia cloud and ammonium hydrosulphide cloud in the scattering case. The ammonia cloud is retrieved between the 2.3- and 2.7-bar pressure levels, while the ammonium hydrosulphide cloud is retrieved slightly deeper between the 3.2- and 3.5-bar pressure levels. Optimum cloud particle sizes are obtained at about one micrometre. These two models are associated with low $\chi^2/N_\lambda$ values below the 5-threshold value and low $\sigma_N$ values below the 1-3 upper boundary values. The haze opacity decreases in the winter northern hemisphere as expected from the analysis of Saturn's reflection spectra. No such north-south variations are observed for the cloud opacity, and lower cloud opacity coincides with opacity clearing regions present in both the southern and northern hemispheres of Saturn.

The deep phosphine and ammonia abundances are also similar in the two hemispheres, however the ammonia mixing ratio is larger at the equator. Both the scattering ammonia and ammonium hydrosulphide clouds lead to retrieved phosphine abundances in good agreement with the estimations from previous studies. Only the ammonia abundances retrieved for an ammonia cloud are consistent with previous studies, while larger abundances are observed for an ammonium hydrosulphide cloud. The enhancement of ammonia at the equator was also observed by Fletcher *et al.* who concluded that it was due to the advection of ammonia-rich air from depths below the cloud layers.

This scenario is consistent with a tropospheric cloud made of ammonia ice: the lower ammonia abundances at higher latitudes are due to the condensation of ammonia ice at 2.3-2.7 bar while the higher abundances at the equator are similar to the abundances below the cloud-forming region. In conclusion, the 5-$\mu$m cloud is most probably composed of scattering ammonia ice. For this cloud model, the best-fitting values of phosphine abundances are in the range 4.7-5.4 ppm, those for the ammonia abundances at higher latitudes are in the range 200-300 ppm, and a larger ammonia abundance of about 550 ppm is obtained at the equator.

The $\sigma_N$ tests were developed in this thesis and combined with the results from the limb-darkening analysis on Saturn. As mentioned before, the limb-darkening analysis was already carried out on Jupiter by Roos-Serote and Irwin (2006). Therefore, the next step will be probably to test the reproducibility of the $\sigma_N$ methodology on other Jovian planets.

## 7.2 Next steps

This thesis has brought new constraints on the haze and cloud properties by analysing Cassini/VIMS data at near-infrared wavelengths. In particular, the thesis results lead toward a scattering ammonia cloud located below a scattering haze layer made of $P_2H_2$ or $P_2H_4$. The next steps following this work will be to:

*i.* study the vertical structure, as well as the optical and physical properties of the upper stratospheric haze by analysing VIMS data at visible wavelengths.

*ii.* obtain laboratory measurements of the complex refractive index of $P_2H_2$ or $P_2H_4$, and compare them to the VIMS-derived values obtained in this thesis.

*iii.* further constrain the haze and cloud properties by analysing Saturn's 5-$\mu$m spectra at daytime.

*iv.* track specific cloud features by analysing VIMS data measured at high spatial resolution.

*v.* continue to search for seasonal changes of the haze distribution by analysing VIMS reflection data until the last stages of the Cassini mission in 2017 when Saturn's northern hemisphere enters summer.

*vi.* develop a solar heating model at visible wavelengths so as to determine if the haze structure observed in Saturn's upper troposphere might generate the temperature knee retrieved with Cassini/CIRS specra.

*vii.* Carry out a similar analysis for non-spherical aerosol particles and see how it compares with the Mie theory scheme.

*vii.* Generalise the $\sigma_N$ tests to other Jovian planets.

The key points above sum up the most immediate area of research which should follow the work done in this thesis. In the meantime, several techniques used in the analysis of VIMS data, such as the limb-darkening analysis or the $\sigma_N$ tests, have been efficient to constrain the haze and cloud properties. By developing similar techniques that combine various datasets, further constraints on the input parameters can be obtained and our understanding of Saturn's climate improved.

# Bibliography


[1] AMELIN, Y., KROT, A. N., HUTCHEON, I. D., AND ULYANOV, A. A. Lead isotopic ages of chondrules and calcium-aluminium-rich inclusions. Science 297, 5587 (2002), 1678–1683.

[2] ANDERSON, J. A., SIDES, S. C., SOLTESZ, D. L., SUCHARSKI, T. L., AND BECKER, K. J. Modernization of the integrated software for imagers and spectrometers. Lunar and Planetary Science XXXV (2004).

[3] ANDREWS, D. G. An introduction to atmospheric physics, $2^{nd}$ ed. Cambridge University Press, 2000.

[4] ATREYA, S. K. The Outer Planets and their Moons. In Atmospheres and Ionospheres of the Outer Planets and their Satellites. Springer-Verlag, 1986.

[5] ATREYA, S. K., AND ROMANI, P. N. Photochemistry and clouds of Jupiter, Saturn and Uranus. In Planetary Meteorology. Cambridge University Press, 1985, pp. 17–68.

[6] ATREYA, S. K., AND WONG, A. S. Coupled clouds and chemistry of the giant planets - a case for multiprobes. Space Sci. Rev. 116 (2005), 121–136.

[7] ATREYA, S. K., WONG, M. H., OWEN, T. C., MAHAFFY, P. R., NIEMANN, H. B., DE PATER, I., DROSSART, P., AND ENCRENAZ, T. A comparison of the atmospheres of Jupiter and Saturn: deep atmospheric composition, cloud structure, vertical mixing, and origin. Plan. & Space Sci. 47 (1999), 1243–1262.

[8] BAINES, K. H., DROSSART, P., MOMARY, T. W., FORMISANO, V., GRIFFITH, C., BELLUCI, G., BIBRING, J. P., BROWN, R. H., BURATTI, B. J., CAPACCIONI, F., CERRONI,

P., CLARK, R. N., CORADINI, A., COMBES, M., CRUIKSHANK, D. P., JAUMANN, R., LANGEVIN, Y., MATSON, D. L., MCCORD, T. B., MENNELLA, V., NELSON, R. M., NICHOLSON, P. D., SICARDY, B., AND SOTIN, C. The atmospheres of Saturn and Titan in the Near-Infrared: First Results of Cassini/VIMS. Earth, Moon, and Planets 96 (2006), 1–29.

[9] BAINES, K. H., MOMARY, T., FLETCHER, L., SHOWMAN, A. P., DELITSKY, M., BROWN, R. H., BURATTI, B. J., CLARK, R. N., NICHOLSON, P. D., AND SOTIN, C. The evolution of Saturn's northern storm of 2010 and environs as viewed by Cassini/VIMS. In American Geophysical Union (2011).

[10] BAINES, K. H., MOMARY, T. W., FLETCHER, L. N., SHOWMAN, A. P., ROOS-SEROTE, M., BROWN, R. H., BURATTI, B. J., CLARK, R. N., AND NICHOLSON, P. D. Saturn's north polar cyclone and hexagon at depth revealed by CASSINI/VIMS. Plan. & Space Sci. 57 (2009), 1671–1681.

[11] BAINES, K. H., MOMARY, T. W., ROOS-SEROTE, M., AND THE CASSINI/VIMS SCIENCE TEAM. North vs South on Saturn: Discovery of a Pronounced Hemispherical Asymmetry in Saturn's 5-Micron Emission and Associated Deep Cloud Structure by Cassini/VIMS. B.A.A.S. 38 (2006), 488.

[12] BERK, A., BERNSTEIN, L. S., ANDERSON, G. P., ACHARYA, P. K., ROBERTSON, D. C., CHETWYND, J. H., AND ADLER-GOLDEN, S. M. MODTRAN cloud and multiple scattering upgrades with application to AVIRIS. Remote Sens. Environ. 65 (1998), 367–375.

[13] BÉZARD, B. The thermal structure of Saturn's atmosphere. In The atmosphere of Saturn and Titan. ESA SP-241, European Space Agency, Paris, 1985.

[14] BÉZARD, B., DROSSART, P., ENCRENAZ, T., AND FEUCHTGRUBER, H. Benzene on the giant planets. Icarus 154 (2001), 492–500.

[15] BÉZARD, B., DROSSART, P., LELLOUCH, E., TARRAGO, G., AND MAILLARD, J. P. Detection of arsine in Saturn. Astrophys. J. 346 (1989), 509–513.

[16] BÉZARD, B., GREATHOUSE, T., LACY, J., RICHTER, M. J., MOSES, J., AND GRIFFITH, C. High spectral resolution observations of Jupiter and Saturn near 10 micron: Ethylene and the $CH_3D/CH_4$ ratio . In paper presented at the conference Jupiter after Galileo and Cassini (Lisbon, 17-21 June 2002).

[17] BODENHEIMER, P., HUBICKYJ, O., AND LISSAUER. Models of the in situ formation of detected extrasolar giant planets. Icarus 143 (2000), 2–14.

[18] BOSS, A. P. Formation of gas and ice giant planets. Earth Planet. Sci. Lett. 202 (2002), 513–523.

[19] BOSS, A. P. The solar nebula. In Treatise on Geochemistry, vol. 1 of Meteorites, Comets and Planets. Elsevier, 2007.

[20] BRIGGS, F. H., AND SACKETT, P. D. Radio observations of Saturn as a probe of its atmosphere and cloud structure. Icarus 80 (1989), 77–103.

[21] BROOKE, T. Y., KNACKE, R. F., ENCRENAZ, T., DROSSART, P., CRISP, D., AND FEUCHTGRUBER, H. Models of the ISO 3-$\mu$m reflection spectrum of Jupiter. Icarus 136 (1998), 1–13.

[22] BROWN, R. H., BAINES, K. H., BELLUCCI, G., BIBRING, J. P., BURATTI, B. J., CAPACCIONI, F., CERRONI, P., CLARK, R. N., CORADINI, A., CRUIKSHANK, D. P., DROSSART, P., FORMISANO, V., JAUMANN, R., LANGEVIN, Y., MATSON, D. L., MCCORD, T. B., MENNELLA, V., MILLER, E., NELSON, R. M., NICHOLSON, P. D., SICARDY, B., AND SOTIN, C. The *Cassini* Visual and Infrared Mapping Spectrometer (VIMS) investigation. Space Science Reviews 115 (2004), 111–168.

[23] BURGDORF, M. J., ORTON, G. S., ENCRENAZ, T., DAVIS, G. R., LELLOUCH, E., SIDHER, S. D., AND SWINYARD, B. M. Far-infrared spectroscopy of the giant planets: measurements of ammonia and phosphine at Jupiter and Saturn and the continuum of Neptune. Advances in Space Research 34 (2004), 2247–2250.

[24] CAMERON, A. G. W. Physics of primitive solar accretion disk. Moon and the Planets 18 (1978), 5–40.

[25] CHANDRASEKHAR, S. Radiative transfer, $1^{st}$ ed. Oxford University Press, 1950.

[26] CHEN, F., JUDGE, D. L., WU, C. Y. R., CALDWELL, J., WHITE, H. P., AND WAGENER, R. High-resolution low-temperature photoabsorption croos sections of $C_2H_2$, $PH_3$, $AsH_3$, and $GeH_4$, with application to Saturn's atmosphere. J. Geophys. Res. 96 (1991), 17519–17527.

[27] CHOI, D. S., SHOWMAN, A. P., AND BROWN, R. H. Cloud features and zonal wind measurements of Saturn's atmosphere as observed by Cassini/VIMS. Journal of Geophysical Research (Planets) 114 (2009), 4007.

[28] COLINA, L., BOHLIN, R. C., AND CASTELLI, F. The 0.12-2.5 micron absolute flux distribution of the Sun for comparison with solar analog stars. Astron. J. 112 (1996), 307–315.

[29] CONRATH, B. J., AND GAUTIER, D. Saturn helium abundance: A reanalysis of Voyager measurements. Icarus 144 (2000), 124–134.

[30] CONRATH, B. J., GAUTIER, D., HANEL, R. A., AND HORNSTEIN, J. S. The helium abundance of Saturn from Voyager measurements. Astrophys. J. 282 (1984), 807–815.

[31] CONRATH, B. J., GIRASCH, P. J., AND USTINOV, E. A. Thermal structure and para hydrogen fraction on the outer planets from Voyager IRIS measurements. Icarus 135 (1998), 501–517.

[32] CONRATH, B. J., HANEL, R. A., AND SAMUELSON, R. E. Thermal structure and heat balance of the outer planets. In Origin and evolution of planetary and satellite atmospheres. University of Arizona press, 1989.

[33] COURTIN, R., GAUTIER, D., MARTEN, A., BÉZARD, B., AND HANEL, R. The composition of Saturn's atmosphere at northern temperate latitudes from Voyager IRIS spectra - $NH_3$, $PH_3$, $C_2H_2$, $C_2H_6$, $CH_3D$, $CH_4$, and the Saturnian D/H isotopic ratio. Astrophys. J. 287 (1984), 899–916.

[34] COX, A. N. Allen's astrophysical quantities, $4^{th}$ ed. Springer, 2000.

[35] CUZZI, J. N., CLARK, R. N., FILACCHIONE, G., FRENCH, R., JOHNSON, R., MAROUF, E. A., AND SPILKER, L. J. Ring particle composition and size distribution. In Saturn from Cassini-Huygens. 2009, pp. 459–509.

[36] DANA, V., J.-Y., M., TARRAGO, G., OLSON, W. B., AND BÉZARD, B. Absolute infrared intensities in the fundamentals $\nu_1$ and $\nu_3$ of arsine. Journal of molecular spectroscopy 159 (1993), 468–480.

[37] DE GRAAUW, T., FEUCHTGRUBER, H., BÉZARD, B., DROSSART, P., ENCRENAZ, T., BEINTEMA, D. A., GRIFFIN, M., HERAS, A., KESSLER, M., LEECH, K., LELLOUCH, E., MORRIS, P., ROELFSEMA, P. R., ROOS-SEROTE, M., SALAMA, A., VANDENBUSSCHE, B., VALENTIJN, E. A., DAVIS, G. R., AND NAYLOR, D. A. First results of ISO-SWS observations of Saturn: detection of $CO_2$, $CH_3C_2H$, $C_4H_2$ and tropospheric $H_2O$. Astron. Astrophys. 321 (1997), L13–L16.

[38] DEL GENIO, A. D., ACHTERBERG, R. K., BAINES, K. H., FLASAR, F. M., READ, P. L., SÁNCHEZ-LAVEGA, A., AND SHOWMAN, A. P. Saturn atmospheric structure and dynamics . In Saturn from Cassini-Huygens. Springer, 2009, pp. 113–159.

[39] DIEKE, G. H. The molecular spectrum of hydrogen and its isotopes. Journal of molecular spectroscopy 2 (1958), 494–517.

[40] DURISEN, R. H., BOSS, A. P., MAYER, L., NELSON, A. F., QUINN, T., AND RICE, W. K. M. Gravitational instabilities in gaseous protoplanetary disks and implications for gas planet formation. In Protostars and Planets V. University of Arizona Press, 2007, pp. 607–622.

[41] ESPAILLAT, C., CALVET, N., D'ALESSION, P., HERNÁNDEZ, J., QI, C., HARTMANN, L., FURLAN, E., AND WATSON, D. M. On the diversity of the Taurus transitional disks: UX Tauri A and LkCa 15. Astrophysical Journal 670 (2007), L135–L138.

[42] ESTRADA, P. R., AND MOSQUEIRA, I. A gas-poor planetesimal capture model for the formation of giant planet satellite systems. Icarus 181 (2006), 486–509.

[43] FEGLEY, B., AND PRINN, R. G. Equilibrium and nonequilibrium chemistry of Saturn's atmosphere: Implications for the observability of $PH_3$, $N_2$, CO, and $GeH_4$. Astrophys. J. 299 (1985), 1067–1078.

[44] FESTOU, M. C., AND ATREYA, S. K. Voyager ultraviolet stellar occultation measurements of the composition and thermal profiles of the Saturnian upper atmosphere. Geophys. Res. Lett. 9 (1982), 1147–1150.

[45] FINK, U., AND LARSON, H. P. Deuterated methane observed on Saturn. Science 201 (1978), 343–345.

[46] FINK, U., LARSON, H. P., BJORAKER, G. L., AND JOHNSON, J. R. The $NH_3$ spectrum in Saturn's 5 micron window. ApJ 268 (1983), 880–888.

[47] FLASAR, F. M., KUNDE, V. G., ABBAS, M. M., ACHTERBERG, R. K., ADE, P., BARUCCI, A., BÉZARD, B., BJORAKER, G. L., BRASUNAS, J. C., CALCUTT, S., CARLSON, R., CÉSARSKY, C. J., CONRATH, B. J., CORADINI, A., COURTIN, R., COUSTENIS, A., EDBERG, S., EDGINGTON, S., FERRARI, C., FOUCHET, T., GAUTIER, D., GIERASCH, P. J., GROSSMAN, K., IRWIN, P., JENNINGS, D. E., LELLOUCH, E., MAMOUTKINE, A. A., MARTEN, A., MEYER, J. P., NIXON, C. A., ORTON, G. S., OWEN, T. C., PEARL, J. C., PRANGÉ, R., RAULIN, F., READ, P. L., ROMANI, P. N., SAMUELSON, R. E., SEGURA, M. E., SHOWALTER, M. R., SIMON-MILLER, A. A., SMITH, M. D., SPENCER, J. R., SPILKER, L. J., AND TAYLOR, F. W. Exploring the Saturn system in the thermal infrared: The composite infrared spectrometer. Space Science Reviews 115 (2004), 169–297.

[48] FLETCHER, L. N., BAINES, K. H., MOMARY, W., SHOWMAN, A. P., IRWIN, P. G. J., ORTON, G. S., ROOS-SEROTE, M., AND MERLET, C. Saturn's tropospheric composition and clouds from Cassini/VIMS 4.6-5.1 $\mu$m nightside spectroscopy. Icarus 214 (2011), 510–533.

[49] FLETCHER, L. N., IRWIN, P. G. J., TEANBY, N. A., ORTON, G. S., PARRISH, P. D., CALCUTT, S. B., DE KOK, R., HOWETT, C., BOWLES, N., AND TAYLOR, F. W. Characterising Saturn's vertical temperature structure from Cassini/CIRS. Icarus 189 (2007), 457–478.

[50] FLETCHER, L. N., ORTON, G. S., TEANBY, N. A., AND IRWIN, P. G. J. Phosphine on Jupiter and Saturn from Cassini/CIRS. Icarus 202 (2009a), 543–564.

[51] FLETCHER, L. N., ORTON, G. S., TEANBY, N. A., IRWIN, P. G. J., AND BJORAKER, G. L. Methane and its isotopologues on Saturn from Cassini/CIRS observations. Icarus 199 (2009b), 351–367.

[52] FLETCHER, L. N., SWINYARD, B., SALJI, C., POLEHAMPTON, E., FULTON, T., SIDHER, S., LELLOUCH, E., MORENO, R., ORTON, G., CAVALIÉ, T., COURTIN, R., RENGEL, M., SAGAWA, H., DAVIS, G. R., HARTOGH, P., NAYLOR, D., WALKER, H., AND LIM, T. Sub-millimetre spectroscopy of Saturn's trace gases from Herschel/SPIRE. Astronomy & Astrophysics 539 (2012).

[53] FRIEDSON, A. J., WONG, A. S., AND YUNG, Y. L. Models for polar haze formation in Jupiter's stratosphere. Icarus 158 (2002), 389–400.

[54] GADIS, L., ANDERSON, J., BECKER, K., BECKER, T., COOK, D., EDWARDS, K., ELIASON, E., HARE, T., KIEFFER, H., LEE, E. M., MATHEWS, J., SODERBLOM, L., SUCHARSKI, T., AND TORSON, J. An overview of the integrated software for imaging spectrometer (ISIS). Lunar and Planetary Science XXVIII (1997), 387–388.

[55] GOLDREICH, P., LITHWICK, Y., AND R., S. Final stages of planet formation. Astrophysical Journal 614 (2004), 497–507.

[56] GOMES, R., LEVISON, H. F., TSIGANIS, K., AND MORBIDELLI, A. Origin of the cataclysmic late heavy bombardment period of the terrestrial planets. Nature 435 (2005), 466–469.

[57] GREATHOUSE, T., MOSES, J., BÉZARD, B., GRIFFITH, C., LACY, J., KNEZ, C., AND RICHTER, M. Latitudinal variations of temperature, $C_2H_2$ and $C_2H_6$ in Saturn's stratosphere along with the detection of propane. Bull. Am. Astron. Soc. 35 (2003), 50.07.

[58] GREVESSE, N., ASPLUND, M., AND SAUVAL, A. J. The solar chemical composition. Space Sci. Rev. 130 (2007), 105–114.

[59] GRIFFIN, M. J., NAYLOR, D. A., DAVIS, G. R., ADE, P. A. R., OLDHAM, P. G., SWINYARD, B. M., GAUTIER, D., LELLOUCH, E., ORTON, G. S., ENCRENAZ, T., DE GRAAW, T., FURNISS, I., SMITH, H., ARMAND, C., BURGDORF, M., DI GIORGIO, A., EWART, D., GRY, C., KING, K. J., LIM, T., MOLINARI, S., SIDHER, S., SMITH, A., TEXIER, D.,

TRAMS, N., UNGER, S. J., AND SALAMA, A. First detection of the 56-$\mu$m rotational line of HD in Saturn's atmosphere. Astron. Astrophys. 315 (1996), 389–392.

[60] GUILLOT, T. Interiors of giant planets inside and outside our solar system. Science 286 (1999), 72–77.

[61] GUILLOT, T. The interiors of giant planets. Ann. Rev. Earth Planet. Sci. 33 (2005), 493–530.

[62] HANEL, R., CONRATH, B., FLASAR, F. M., KUNDE, V., MAGUIRE, W., PEARL, J., PIRRAGLIA, J., SAMUELSON, R., HERATH, L., ALLISON, M., CRUIKSHANK, D., GAUTIER, D., GIERASCH, P., HORN, L., KOPPANY, R., AND PONNAMPERUMA, C. Infrared observations of the Saturnian system from Voyager 1. Science 212 (1981), 192–200.

[63] HANSEN, J. E., AND TRAVIS, L. D. Light scattering in planetary atmospheres. Space Sci. Rev. 16 (1974), 527–610.

[64] HOWETT, C. J. A., CARLSON, R. W., IRWIN, P. G. J., AND CALCUTT, S. B. Optical constants of ammonium hydrosulphide ice and ammonia ice. Journal of the Optical Society of America B Optical Physics 24 (2007), 126–136.

[65] HUBBARD, W. B., BURROWS, A., AND LUNINE, J. I. Theory of giant planets. Ann. Rev. Astrono. Astrophys. 40 (2002), 103–136.

[66] HUBICKYJ, O., BODENHEIMER, P., AND LISSAUER, J. J. Accretion of the gaseous enveloppe of Jupiter around a 5-10 Earth-mass core. Icarus 179 (2005), 415–431.

[67] HUFFMAN, D. R., AND BOHREN, C. F. Infrared absorption spectra of nonspherical particles treated in the Rayleigh-ellipsoid approximation. In Light scattering by irregularly shaped particles in Jupiter. Plenum, 1980, pp. 103–111.

[68] HURLEY, J., FLETCHER, L. N., IRWIN, P. G. J., CALCUTT, S. B., SINCLAIR, J. A., AND MERLET, C. Latitudinal variation of upper tropospheric $NH_3$ on Saturn derived from Cassini/CIRS far-infrared measurements. Planetary and Space Science 73 (2012), 347–363.

[69] IDA, S., AND LIN, D. N. C. Toward a deterministic model of planetary formation. I. A desert in the mas and semimajor axis distributions of extrasolar planets. Astrophysical Journal 604 (2004), 388–413.

[70] IRWIN, P. G. J. Giant planets of our solar system, $2^{nd}$ ed. Springer, 2009.

[71] IRWIN, P. G. J., SROMOVSKY, L. A., STRONG, E. K., SIHRA, K., TEANBY, N. A., BOWLES, N., CALCUTT, S. B., AND REMEDIOS, J. J. Improved near-infrared methane band models and *k*-distribution parameters from 2000 to 9500 $cm^{-1}$ and implications for interpretation of outer planet spectra. Icarus 181 (2006), 309–319.

[72] IRWIN, P. G. J., TEANBY, N. A., DE KOK, R., FLETCHER, L. N., HOWETT, C. J. A., TSANG, C. C. C., WILSON, C. F., CALCUTT, S. B., NIXON, C. A., AND PARRISH, P. D. The NEMESIS planetary atmosphere radiative transfer and retrieval tool. J. Quant. Spectrosc. Radiat. Trans. 109 (2008), 1136–1150.

[73] JACQUINET-HUSOON, N., SCOTT, N. A., CHÉDIN, A., K., G., ARMANTE, R., A., C. A., BARBE, A., BIRK, M., BROWN, L. R., CAMY-PEYRET, C., CLAVEAU, C., CLERBAUX, C., COHEUR, P. F., DANA, V., DAUMONT, L., DEBACKER-BARILLY, M. R., FLAUD, J. M., GOLDMAN, A., HAMDOUNI, A., HESS, M., JACQUEMART, D., KOPKE, P., MANDIN, J.-Y., MASSIE, S., MIKHAILENKO, S., NEMTCHINOV, V., NIKITIN, A., NEWNHAM, D., PERRIN, A., PEREVALOV, V. I., RÉGALIA-JARLOT, L., RUBLEV, A., SCHREIER, F., SCHULT, L., SMITH, K. M., TASHKUN, S. A., TEFFO, J. L., TOTH, R. A., TYUTEREV, V. G., VANDER AUWERA, J., VARANASI, P., AND WAGNER, G. The 2003 edition of the GEISA/IASI spectroscopic database. J. Quant. Spectrosc. Radiat. Trans. 95 (2005), 429–467.

[74] JACQUINET-HUSSON, N., CREPEAU, L., ARMANTE, R., BOUTAMMINE, C., CHÉDIN, A., SCOTT, N. A., CREVOISIER, C., CAPELLE, V., BOONE, C., POULET-CROVISIER, N., BARBE, A., CAMPARGUE, A., BENNER, D. C., BENILAN, Y., BÉZARD, B., BOUDON, V., BROWN, L. R., COUDERT, L. H., COUSTENIS, A., DANA, V., DEVI, V. M., FALLY, S., FAYT, A., FLAUD, J. M., GOLDMAN, A., HERMAN, M., HARRIS, G. J., JACQUEMART, D., JOLLY, A., KLEINER, I., KLEINBOHL, A., KWABIA-TCHANA, F., LAVRENTIEVA, N., LACOME, N., XU, L.-H., LYULIN, O. M., MANDIN, J.-Y., MAKI, A., MIKHAILENKO,

S., MILLER, C. E., MISHINA, T., MOAZZEN-AHMADI, N., MULLER, H. S. P., NIKITIN, A., ORPHAL, J., PEREVALOV, V., PERRIN, A., PETKIE, D. T., PREDOI-CROSS, A., RINSLAND, C. P., REMEDIOS, J. J., ROTGER, M., SMITH, M. A. H., SUNG, K., TASHKUN, S., TENNYSON, J., TOTH, R. A., VANDAELE, A.-C., AND AUWERA, J. A. The 2009 edition of the GEISA spectroscopic database. JQSRT 112 (2011), 2395–2445.

[75] KARKOSCHKA, E., AND TOMASKO, M. G. Saturn's upper troposphere 1986-1989. Icarus 97 (1992), 161–181.

[76] KARKOSCHKA, E., AND TOMASKO, M. G. Saturn's upper tropospheric hazes observed by the Hubble Space Telescope. Icarus 106 (1993), 421–441.

[77] KARKOSCHKA, E., AND TOMASKO, M. G. Saturn's vertical and latitudinal cloud structure 1991-2004 from HST imaging in 30 filters. Icarus 179 (2005), 195–221.

[78] KAYE, J. A., AND STROBEL, D. F. Phosphine photochemistry in the atmosphere of Saturn. Icarus 59 (1984), 314–335.

[79] KEROLA, D. X., LARSON, H. P., AND G., T. M. Analysis of the Near-IR spectrum of Saturn: A comprehensive radiative transfer model of its middle and upper troposphere. Icarus. 127 (1997), 190–212.

[80] KILLEN, R. M. Longitudinal variations in the Saturnian atmosphere. Icarus 73 (1988), 227–247.

[81] KIM, J. H., KIM, S. J., GEBALLE, T. R., KIM, S. S., AND BROWN, L. R. High-resolution spectroscopy of Saturn at 3 microns: $CH_4$, $CH_3D$, $C_2H_2$, $C_2H_6$, $PH_3$, clouds and haze . Icarus. 185 (2006), 476–486.

[82] LACIS, A. A., AND OINAS, V. A description of the correlated-*k* distribution method for modelling nongray gaseous absorption, thermal emission, and multiple scattering in vertically inhomogeneous atmospheres. J. Geophys. Res. 96 (1991), 9027–9063.

[83] LARSON, H. P. Infrared spectroscopic observations of the outer planets, their satellites, and the asteroids. Annual Review of Astronomy and Astrophysics 18 (1980), 43–75.

[84] LELLOUCH, E., BÉZARD, E., FOUCHET, T., ENCRENAZ, T., FEUCHTGRUBER, H., AND DE GRAAUW, T. The deuterium abundance in Jupiter and Saturn from ISO-SWS observations. Astron. Astrophys. 370 (2001), 610–622.

[85] LEVISON, H. F., MORBIDELLI, A., GOMES, R., AND BACKMAN, D. Planet migration in planetesimal disks. In Protostars and Planets V. University of Arizona Press, 2007, pp. 669–684.

[86] LEVISON, H. F., MORBIDELLI, A., GOMES, R., AND BACKMAN, D. Origin of the structure of the Kuiper belt during a dynamical instability in the orbits of Uranus and Neptune. Icarus 196 (2008), 258–273.

[87] LEWIS, J. S. The clouds of Jupiter and the $NH_3$-$H_2O$ and $NH_3$-$H_2S$ systems. Icarus 10 (1969), 365–378.

[88] LI, L., CONRATH, B. J., GIERASCH, P. J., ACHTERBERG, R. K., NIXON, C. A., SIMON-MILLER, A. A., FLASAR, F. M., BANFIELD, D., BAINES, K. H., WEST, R. A., INGERSOLL, A. P., VASAVADA, A. R., DEL GENIO, A. D., PORCO, C. C., MAMOUTKIN, A. A., SEGURA, M. E., BJORAKER, G. L., ORTON, G. S., FLETCHER, L. N., IRWIN, P. G. J., AND READ, P. L. Saturn's emitted power. J. Geophys. Res. 115 (2010).

[89] LINDAL, G. F., SWEETNAM, D. N., AND ESHLEMAN, V. R. The atmosphere of Saturn: an analysis of the Voyager radio occultation measurements. Astron. J. 90 (1985), 1136–1146.

[90] LISSAUER, J. J. Planet Formation. Ann. Rev. Astron. Astrophys. 31 (1993), 129–173.

[91] MANDIN, J. Line Positions and Intensities in the Vibrational System $2\nu2/\nu2 + \nu4/2\nu4/\nu1/\nu3$ of Arsine. Journal of Molecular Spectroscopy 172 (1995), 319–329.

[92] MARTONCHIK, J. V., ORTON, G. S., AND APPLEBY, J. F. Optical properties of NH3 ice from the far infrared to the near ultraviolet. Applied Optics 23 (1984), 541–547.

[93] MATSON, D. L., SPILKER, L. J., AND LEBRETON, J. P. The Cassini/huygens mission to the Saturnian system. Space Science Reviews 104 (2002), 59–100.

[94] MEYER, M. R., BACKMAN, D. E., WEINBERGER, A. J., AND WYATT, M. C. Evolution of circumstellar disks around normal stars: Placing our solar system in context. In Protostars and Planets V. University of Arizona Press, 2007, pp. 573–588.

[95] MILLER, E., KLEIN, G., JUERGENS, D., MEHAFFEY, K., PSEAS, J., GARCIA, R., GIANDOMENICO, A., IRIGOYEN, B., R., H., ROSING, D., SOBEL, H., BRUCE, C., FLAMINI, E., DEVIDI, R., REININGER, F., DAMI, M., SOUFFLOT, A., LANGEVIN, Y., AND HUNTZINGER, G. The Visual and Infrared Mapping Spectrometer for Cassini. SPIE 2803 (1996), 206.

[96] MORBIDELLI, A., LEVSON, H. F., TSIGANIS, K., AND GOMES, R. Chaotic capture of Jupiter's Trojan asteroids in the early solar system. Nature 435 (1967), 462–465.

[97] MOSES, J. I., BÉZARD, B., LELLOUCH, E., GLADSTONE, G. R., FEUCHTGRUBER, H., AND ALLEN, M. Photochemistry of Saturn's atmosphere. I. Hydrocarbon chemistry and comparisons with ISO observations. Icarus 143 (2000), 244–298.

[98] MOSES, J. I., AND GREATHOUSE, T. Latitudinal and seasonal models of stratospheric photochemistry on Saturn: Comparison with infrared data from IRTF/TEXES. J. Geophys. Res. 110 (2005).

[99] NICHOLSON, P., HEDMAN, M. M., GIERASCH, P. J., AND TEAM, C. V. Probing Saturn's atmosphere with Procyon. Bull. Amer. Astron. Soc. 38 (2006), 555.

[100] NOLL, K. S., GEBALLE, T. R., AND KNACKE, R. F. Arsine in Saturn and Jupiter. Astrophys. J. 338 (1989), L71–L74.

[101] NOLL, K. S., KNACKE, R. F., GEBALLE, T. R., AND TOKUNAGA, A. T. Detection of carbon monoxide in Saturn. ApJ Letters 309 (1986b), L91–L94.

[102] NOLL, K. S., KNACKE, R. F., GEBALLE, T. R., AND TOKUNAGA, A. T. Evidence for germane in Saturn. Icarus 75 (1988), 409–422.

[103] NOLL, K. S., KNACKE, R. F., TOKUNAGA, A. T., LACY, J. H., BECK, S., AND SERABYN, E. The abundances of ethane and acetylene in the atmospheres of Jupiter and Saturn. Icarus 65 (1986a), 257–263.

[104] NOLL, K. S., AND LARSON, H. P. The spectrum of Saturn from 1990 to 2230 cm−1 : Abundances of $AsH_3$, $CH_3D$, CO, $GeH_4$, $NH_3$ and $PH_3$. Icarus 89 (1991), 168–189.

[105] ORTON, G. S., BAINES, K. H., CRUIKSHANK, CUZZI, J. N., KRIMIGIS, S. M., MILLER, S., AND LELLOUCH, E. Review of knowledge prior to the Cassini-Huygens mission and concurrent research. In Saturn from Cassini-Huygens. Springer, 2009.

[106] PASQUINI, L., BONIFACIO, P., RANDICH, S., GALLI, D., GRATTON, R. G., AND WOLFF, B. Beryllium abundance in turn-off stars of NGC 6752. Astronomy & Astrophysics 464 (2007), 601–607.

[107] PORCO, C. C., BAKER, E., BARBARA, J., BEURLE, K., BRAHIC, A., BURNS, J. A., CHARNOZ, S., COOPER, N., DAWSON, D. D., DEL GENIO, A. D., DENK, T., DONES, L., DYUDINA, U., EVANS, M. W., GIESE, B., GRAZIER, K., HELFENSTEIN, P., INGERSOLL, A. P., JACOBSON, R. A., JOHNSON, T. V., MCEWEN, A., MURRAY, C. D., NEUKUM, G., OWEN, W. M., PERRY, J., ROATSCH, T., SPITALE, J., SQUYRES, S., THOMAS, P., TISCARENO, M., TURTLE, E., VASAVADA, A. R., VEVERKA, J., WAGNER, R., AND WEST, R. Cassini imaging science: Initial results on Saturn's atmosphere. Science 307 (2005), 1243–1247.

[108] PRESS, W. H., TEUKOLSKY, S. A., VETTERLING, W. T., AND FLANNERY, B. P. Numerical recipes in Fortran, second ed. Cambridge University Press, 1992.

[109] READ, P. L., DOWLING, T. E., AND SCHUBERT, G. Saturn's rotation period from its atmospheric planetary-wave configuration. Nature 460 (2009), 608–610.

[110] REININGER, F., DAMI, M., PAOLINETTI, R., PIERI, S., AND FALUGIANI, S. The Visual and Infrared Mapping Spectrometer-VISible channel (VIMS-VIS). SPIE 2198 (1994), 239–250.

[111] RODGERS, C. D. Inverse methods for atmospheric sounding: theory and practice, $2^{nd}$ ed. World Scientific, 2000.

[112] ROOS-SEROTE, M., AND IRWIN, P. G. J. Scattering properties and location of the jovian 5-micron absorber from Galileo/NIMS limb-darkening observations. Journal of Quantitative Spectroscopy & Radiative Transfer 101 (2006), 448–461.

[113] ROTHMAN, L. S., GORDON, I. E., BARBE, A., BENNER, D. C., BERNATH, P. F., BIRK, M., BOUDON, V., BROWN, L. R., CAMPARGUE, A., CHAMPION, J. P., CHANCE, K., COUDERT, L. H., DANA, V., DEVI, V. M., FALLY, S., FLAUD, J. M., GAMACHE, R. R., GOLDMAN, A., JACQUEMART, D., KLEINER, I., LACOME, N., LAFFERTY, W. J., MANDIN, J. Y., MASSIE, S. T., MIKHAILENKO, S. N., MILLER, C. E., MOAZZE-AHMADI, N., NAUMENKO, O. V., NIKITIN, A. V., ORPHAL, J., PEREVALOV, V. I., PERRIN, A., PREDOI-CROSS, A., RINSLAND, C. P., ROTGER, M., SIMECKOVA, M., SMITH, M. A. H., SUNG, K., TASHKUN, S. A., TENNYSON, J., TOTH, R. A., VANDAELE, A. C., AND AUWERA, J. V. The HITRAN 2008 molecular spectroscopic database. J. Quant. Spectrosc. Radiat. Trans. 110 (2008), 533–572.

[114] S., O. G., AND INGERSOLL, A. P. Saturn's atmospheric temperature structure and heat budget. J. Geophys. Res. 85 (1980), 5871–5881.

[115] S., O. G., SERABYN, E., AND LEE, Y. T. Vertical distribution of $PH_3$ in Saturn from observations of its 1-0 and 3-2 rotational lines. Icarus 146 (2010), 48–59.

[116] SADA, P. V., BJORAKER, G. L., JENNINGS, D. E., ROMANI, P. N., AND MCCABE, G. H. Observations of $C_2H_6$ and $C_2H_2$ in the stratosphere of Saturn. Icarus 173 (2005), 499–507.

[117] SAFRONOV, V. S. Protoplanetary cloud and its evolution. Soviet Astronomy AJ USSR 10 (1967), 650–658.

[118] SAFRONOV, V. S. Kuiper prize lecture - some problems in the formation of the planets. Icarus 94 (1991), 260–271.

[119] SAFRONOV, V. S., AND RUSKOL, E. L. Formation and evolution of planets. Astrophysics and Space Science 212 (1994), 13–22.

[120] SÁNCHEZ-LAVEGA, A. An introduction to planetary atmospheres, $2^{nd}$ ed. Taylor & Francis, 2010.

[121] SÁNCHEZ-LAVEGA, A., ROJAS, J. F., AND SADA, P. V. Saturn's zonal winds at cloud level. Icarus 147 (2000), 405–420.

[122] SIHRA, K. Laboratory measurements of near-infrared methane bands for remote sensing of the Jovian atmosphere. PhD thesis, University of Oxford, 1998.

[123] SINCLAIR, J. A., IRWIN, P. G. J., FLETCHER, L. N., MOSES, J. I., GREATHOUSE, T. K., FRIEDSON, A. J., HESMAN, B., HURLEY, J., AND MERLET, C. Seasonal variations of temperature, acetylene and ethane in Saturn's atmosphere from 2005 to 2010, as observed by Cassini-CIRS. Icarus 225 (2013), 257–271.

[124] SMITH, G. R., SHEMANSKY, D. E., HOLBERG, J. B., BROADFOOT, A. L., SANDEL, B. R., AND MCCONNELL, J. C. Saturn's upper atmosphere from the Voyager 2 EUV solar and stellar occultations. J. Geophys. Res. 88 (1983), 8667–8678.

[125] SNELL, H. E., MONCET, J. L., ANDERSON, G. P., CHETWYND, J. H., MILLER, S., AND WANG, J. G. FASCODE for the environment (FASE). Proc. SPIE 2471 (1995), 88–95.

[126] SPERGEL, D. N., BEAN, R., DORÉ, O., NOLTA, M. R., BENNETT, C. L., DUNKLEY, J., HINSHAW, G., JAROSIK, N., KOMATSU, E., PAGE, L., PEIRIS, H. V., VERDE, L., HALPERN, M., HILL, R. S., KOGUT, A., LIMON, M., MEYER, S. S., ODEGARD, N., TUCKER, G. S., WEILAND, J. L., WOLLACK, E., AND WRIGHT, E. L. Three-year Wilkinson Microwave Anisotropy Probe (WMAP) observations: Implications for cosmology. Astrophysical Journal Supplement Series 170 (2007), 377–408.

[127] SROMOVSKY, L. A., AND FRY, P. M. The source of widespread 3-$\mu$m absorption in Jupiter's clouds: Constraints from 2000 Cassini VIMS observations. Icarus 210 (2010), 230–257.

[128] STAMNES, K., TSAY, S., WISCOMBE, W., AND JAYAWEERA, K. Numerically stable algorithm for discrete-ordinate-method radiative transfer in multiple scattering and emitting layered media. Appl. Opt. 27 (1998), 2502–2509.

[129] STRONG, E. K., TAYLOR, F. W., CALCUTT, S. B., REMEDIOS, J. J., AND BALLARD, J. Spectral parameters of self- and hydrogen-broadened methane from 2000 to 9500 $cm^{-1}$ for remote sounding of the atmosphere of Jupiter. . Journal of Quantitative Spectroscopy & Radiative Transfer 50 (1993), 309–325.

[130] TOKUNAGA, A. T., CALDWELL, J., GILLETT, F. C., AND NOLT, I. G. Spatially resolved infrared observations of Saturn: II. The temperature enhancement at the south pole of Saturn. Icarus 36 (1978), 216–222.

[131] TOMASKO, M. G., AND DOOSE, L. R. Polarimetry and photometry of Saturn from Pioneer 11: Observations and constraints on the distribution and properties of cloud and aerosol particles. Icarus 63 (1984), 1–34.

[132] TORSON, J. M., AND J., B. K. ISIS - A software architecture for processing planetary images. Lunar and Planetary Science XXVIII (1997), 1443–1444.

[133] TRAFTON, L. Long-term changes in Saturn's troposphere. Icarus 63 (1985), 374–405.

[134] TSIGANIS, K., GOMES, R., MORBIDELLI, A., AND LEVISON, H. F. Origin of the orbital architecture of the giant planets of the solar system. Nature 435 (2005), 459–461.

[135] WARD, W. R. Density waves in the solar nebula - Differential lindblad torque. Icarus 67 (1986), 164–180.

[136] WARD, W. R. Protoplanet migration by nebula tides. Icarus 126 (1997), 261–281.

[137] WEIDENSCHILLING, S. J., AND LEWIS, J. S. Atmospheric and cloud structures of the jovian planets. Icarus 20 (1973), 465–476.

[138] WEISSTEIN, E. W., AND SERABYN, E. Detection of the 267 GHz J = 1 - 0 rotational transition of $PH_3$ in Saturn with a new fourier transfer spectrometer. Icarus 109 (1994), 367–381.

[139] WEST, R. A., BAINES, K. H., KARKOSCHKA, E., AND SÁNCHEZ-LAVEGA, A. Clouds and aerosols in Saturn's atmosphere. In Saturn from Cassini-Huygens. Springer, 2009.

[140] WEST, R. A., STROBEL, D. F., AND TOMASKO, M. G. Clouds, aersols, and photochemistry in the jovian atmosphere. Icarus 65 (1986), 161–217.

[141] WETHERILL, G. W. Formation of the terrestrial planets. Annual Review of Astronomy and Astrophysics 18 (1980), 77–113.

[142] WETHERILL, G. W., AND STEWART, G. R. Formation of planetary embryos - effects of fragmentation, low relative velocity, and independent variation of eccentricity and inclination. Icarus 106 (1993), 190–209.

[143] WINKELSTEIN, P., CALDWELL, J., KIM, S. J., COMBES, M., HUNT, G. E., AND MOORE, V. A determination of the composition of the saturnian stratosphere using the IUE. Icarus 54 (1983), 309–318.

[144] WONG, A.-S., YUNG, Y. L., AND FRIEDSON, A. J. Benzene and haze formation in the polar atmosphere of Jupiter. Geophys. Res. Lett. 30 (2003).

[145] WONG, M., BJORAKER, G., SMITH, M., FLASAR, D., AND NIXON, C. Identification of the 10-$\mu$ ammonia ice feature on Jupiter. Planet. Space Sci. 52 (2004), 385–395.

[146] YANAMANDRA-FISHER, P. A., ORTON, G. S., FISHER, B. M., AND SANCHEZ-LAVEGA, A. Saturn's 5.2-$\mu$m cold spots: Unexpected cloud variability. Icarus 150 (2001), 189–193.

[147] YUNG, Y. L. Photochemistry of Planetary Atmospheres, $1^{st}$ ed. Oxford University Press, 1998.

THE POSSESSION OF KNOWLEDGE DOES NOT KILL THE SENSE OF WONDER AND MYSTERY.

THERE IS ALWAYS MORE MYSTERY.

Anaïs Nin